2011

CP violating anomalous top-quark coupling in ppbar collision at $\sqrt{s}$ = 1.96 TeV

Sehwook Lee
Iowa State University

CP violating anomalous top-quark coupling in $p\bar{p}$ collision at $\sqrt{s} = 1.96$ TeV

by

Sehwook Lee

A dissertation submitted to the graduate faculty

in partial fulfillment of the requirements for the degree of

DOCTOR OF PHILOSOPHY

Major: High Energy Physics

Program of Study Committee:
John Hauptman, Major Professor
German Valencia
James Cochran
Charles Kerton
Young-Jin Lee

Iowa State University

Ames, Iowa

2011

TABLE OF CONTENTS

LIST OF TABLES

LIST OF FIGURES

ACKNOWLEDGEMENTS

For the last six years, I have sought to do my best each day. At times, it was a fight against myself. Sometimes, I wanted to give up everything. But many precious people encourage me to keep doing my graduate education. Indeed, I could not complete my graduate education without their help and support. I would like to express my thanks to those who helped me.

First and foremost, Dr. John Hauptman for his huge advice, guidance, patience and support. It is the best luck for me to be a student of Dr. John Hauptman. I have learned how I must behave as a physicist and human, from his passion and his way of life as a scholar. I would like to thank my parents Hae-Yong Lee, Kyung-Soon Park, grand parents-in-law Jong-Hae Lee, Oke Park, father-in-law Seung-Bong Lee, uncle and aunt-in-law Yoon-Shik Lee, Young-Sook Lee, cousin Dong-A Yoo, and wife, Eun-Ah Lee. Without their support and sacrifice for me, it was impossible for me to complete my graduate education. I thank Monk Pyung-Jung who is my spiritual mentor and teaches how to live, with the way of his life. I would also like to thank my committee members for their efforts: Dr. James Cochran, Dr. German Valencia, Dr. Charles Kerton and Dr. Young-Jin Lee. I should not forget to express my thanks to Dr. Richard Wigmans, Dr. Nural Akchurin, Dr. Sung-Won Lee and Dr. Alan Sill who taught me a lot about calorimetry and greeted me with kindness. I thank my good friends: Dong-Wook Jang and his wife Sung-Won Park, Hyun-Wook Choi, Sung-Woong Cho, Ho-jin Lee, Woo-Chan Jun, Hwidong Yoo, Hyejin Ryu and Jeyoun Dong. It is great delight in my life that I have those good friends. I have to express my thanks to Linda Shuck and Lori Hockett for their kind help.

ABSTRACT

We conduct the first study of the T-odd correlations in $t\bar{t}$ events produced in $p\bar{p}$ collision at the Fermilab Tevatron collider that can be used to search for CP violation. We select events which have lepton+jets final states to idenfiy $t\bar{t}$ events and measure counting asymmetries of several physics observables. Based on the result, we search the top quark anomalous couplings at the production vertex at the Tevatron. In addition, Geant4 development, photon identification, the discrimination of a single photon and a photon doublet from π^0 decay are discussed in this thesis.

CHAPTER 1. Introduction

The discovery of the top quark in 1995 gave credence to the standard model. The studies of the top quark properties have been the major goal of top quark physics study after the discovery of the top quark. Moreover, the heavy mass of the top quark is enough to provide interesting new physics beyond the Standard Model. It opens new questions to particle physics whether the observed mass results from an unknown fundamental particle and whether it can be the key to find how particle masses are given by the electroweak symmetry breaking because the energy scale at which the electroweak symmetry breaking occur is close to the top quark mass. Understanding of the top quark mass with other electroweak processes can be used to predict the Higgs boson mass since the masses of the top quark, the Higgs boson, and the W boson are related in various physics processes. Also, an interesting property of the top quark is its anomalous chromoelectric dipole moment (CEDM) which affects the production of the top quark system. The CEDM causes CP violation in top pair production. In this chapter, the Standard Model and the CP violating effect of the CEDM in the top-pair production will be discussed.

1.1 The Standard Model

The Standard Model describes that matter is made of structureless and point-like elementary particles: mediators, leptons and quarks. The leptons are classified acording to electron, muon, tau numbers and their charge: e^- and ν_e, μ and ν_μ, τ and ν_τ. They have spin $\frac{1}{2}$ and classified as three generations. Table 1.1 shows that the flavor of leptons and their properties.

The quark has also six different flavors, which are up, down, charm, strange, top and bottom. They are grouped into three generations and all have spin $\frac{1}{2}$. Quarks carry three

Table 1.1: Lepton Classification [1].

Generation	l	Mass[MeV/c^2]	Q	L_e	L_μ	L_τ	L
1	e	0.511±0.000	-1	1	0	0	1
	ν_e	$< 2 \cdot 10^{-6}$	0	1	0	0	1
2	μ	105.658±0.000	-1	0	1	0	1
	ν_μ	< 0.19	0	0	1	0	1
3	τ	1776.84±0.17	-1	0	0	1	1
	ν_τ	< 18.2	0	0	0	1	1

color charges: Red, Blue and Green. The characteristics for quarks are shown in Table 1.2.

Table 1.2: Quark Classification

Generation	q	Mass	Q(Charge)	B(Baryon Number)
1	u	1.7 to 3.3 MeV/c^2	$+\frac{2}{3}$	$\frac{1}{3}$
	d	4.1 to 5.8 MeV/c^2	$-\frac{1}{3}$	$\frac{1}{3}$
2	c	$1.27\ ^{+0.07}_{-0.09}$ GeV/c^2	$+\frac{2}{3}$	$\frac{1}{3}$
	s	$101\ ^{+0.29}_{-0.21}$ MeV/c^2	$-\frac{1}{3}$	$\frac{1}{3}$
3	t	172.0 ± 0.9 ± 1.3 GeV/c^2	$+\frac{2}{3}$	$\frac{1}{3}$
	b	$4.19\ ^{+0.18}_{-0.06}$ GeV/c^2	$-\frac{1}{3}$	$\frac{1}{3}$

Quarks and Leptons have their antiparticles which have opposite charges and the same masses. The antiquarks are written as $\bar{d}$, $\bar{u}$ etc. and the antileptons are e^+, μ^+, τ^+. Moreover, the Standard Model postulates that four fundamental forces act between leptons and quarks by quantized fields. Elementary particles interact by the exchange of quantized fields which mediate the forces. The electromagnetic force is mediated by the photon (γ), and the weak interaction, which for example participates in the nuclear beta decay, is mediated by $W^\pm$ and Z^0. The eight gluons mediate the strong force which makes nuclei stable. Gravitation is mediated by the graviton. The general theory of relativity describes gravitation and it is not included in the Standard Model. Although the gravitational force is very weak compared with the other forces such as the electromagnetic force, the weak force and the strong force, it acts on all particles which have mass or energy. The quantum gauge field theory explains the electromagnetic force, the weak force and the strong force. The quanta of these fields have spin 1, so are called gauge bosons. The photon (γ) and the eight gluons are massless but $W^\pm$ and Z^0

have rest masses of 80.399 ± 0.023 GeV/c^2 and 91.1876 ± 0.0021 GeV/c^2, respectively. Leptons feel the weak force and the charged leptons participate in the electromagnetic interaction. But they don't participate in the strong interaction. Quarks take part in the strong, the weak and the electromagnetic interactions. The characteristic of the four forces is summarized in Table 1.3.

Table 1.3: The characteristic of the four forces and their gauge bosons [2].

Force	Acts on	Gauge bosons	Characteristic
Gravity	All particles	Graviton	Massless, Spin 2
Electromagnetism	All charged particles	Photon (γ)	Massless, Spin 1
Weak interaction	Quarks, Leptons, Electroweak gauge bosons	$W^{\pm}$, Z^0	Heavy, Spin 1
Strong interaction (QCD)	Quarks and Gluons (all colored particles)	Eight gluons (g)	Massless, Spin 1

1.1.1 Electroweak interactions

Quantum field theory represents leptons and quarks as spinor fields Ψ. The spinor fields are functions of x_μ which is the space-time coordinate. The left-handed particles couple to the weak interaction. To consider this, $\Psi_L = \frac{1}{2}(1-\gamma_5)$ (left-hand field) and $\Psi_R = \frac{1}{2}(1+\gamma_5)$ (right-handed field) are introduced. The left-handed states form isospin doublets Ψ_L and the right-handed states form singlets Ψ_R. For example, the electron and its neutrino can be denoted,

$$\Psi_L = \begin{pmatrix} \nu_e \\ e^- \end{pmatrix}_L, \quad \Psi_R = e_R^-$$

For quarks,

$$\Psi_L = \begin{pmatrix} u \\ d \end{pmatrix}_L, \quad \Psi_R = u_R, \ or \ d_R$$

The weak isospin for doublet and singlet are $T = \frac{1}{2}$ and $T = 0$, respectively. The Standard Model omits the right-handed neutrino since its mass is assumed to be 0. The free particle Lagrangian for the electromagnetic and weak forces can be written,

$$\mathcal{L}_0 = i\bar{\Psi}\gamma^\mu \partial_\mu \Psi \tag{1.1}$$

By taking $SU(2) \times U(1)$ transformations, the left- and right-handed fields become

$$\Psi_L \rightarrow e^{ig\alpha(x)\cdot\mathbf{T}+ig'\beta(x)Y}\Psi_L \quad \text{and} \quad \Psi_R \rightarrow e^{ig'\beta(x)Y}\Psi_R \tag{1.2}$$

In Eq. 1.2, $\alpha(x)$ is an arbitrary three-component vector, $\beta(x)$ is referred to a one-dimensional function of x and $\mathbf{T}$ is considered as the weak-isospin operator. T_i is the matrix expression which is defined as $\frac{1}{2}\tau_i$. τ_i is the Pauli matrices. Since τ_i does not commute, T_i is not commutative either. Thus, $SU(2)_L$ group is called non-Abelian group. Y is the generator of $U(1)_Y$ group of gauge transformation and the weak hypercharge. The relation between the electromagnetic charge and the weak hypercharge can be written as $Q = T_3 + \frac{Y}{2}$. By requiring the invariance of $\mathcal{L}_0$ under the local gauge transformations of $SU(2)_L \times U(1)_Y$, the additional terms which are about four vector fields (spin 1) should be included in the free particle Lagrangian. The four vector fields are the isotriplet $\mathbf{W}_\mu = (W_{1\mu},\ W_{1\mu},\ W_{1\mu},)^t$ for $SU(2)_L$ and the singlet B_μ for $U(1)_Y$. The invariance of the $\mathcal{L}_0$ under the local gauge transformations can be done by replacing the covariance derivative,

$$D_\mu = \partial_\mu + ig\mathbf{W}_\mu \cdot \mathbf{T} + ig'\frac{1}{2}B_\mu Y \tag{1.3}$$

and adding terms for the kinetic energy of the $\mathbf{W}_\mu$ and B_μ gauge fields, which are $-\frac{1}{4}\mathbf{W}_{\mu\nu} \cdot \mathbf{W}^{\mu\nu} - \frac{1}{4}B_{\mu\nu} \cdot B^{\mu\nu}$. Where $\mathbf{W}_{\mu\nu} = \partial_\mu \mathbf{W}_\nu - \partial_\nu \mathbf{W}_\mu - g \cdot \mathbf{W}_\mu \times \mathbf{W}_\nu$ and $B_{\mu\nu} = \partial_\mu B_\nu - \partial_\nu B_\mu$. Revisited electroweak Lagrangian by demanding an $SU(2)_L \times U(1)_Y$ invariance led to

$$\begin{aligned} \mathcal{L}_1 \quad = \quad & i\bar{\Psi}_L\gamma^\mu \left[\partial_\mu + ig\mathbf{W}_\mu \cdot \mathbf{T} + ig'Y_L\frac{1}{2}B_\mu\right]\Psi_L + \\ & i\bar{\Psi}_R\gamma^\mu \left[\partial_\mu - g'Y_R\frac{1}{2}B_\mu\right]\Psi_R - \frac{1}{4}\mathbf{W}_{\mu\nu} \cdot \mathbf{W}^{\mu\nu} - \frac{1}{4}B_{\mu\nu} \cdot B^{\mu\nu} \end{aligned} \tag{1.4}$$

The last two terms are the self-interaction and kinetic energy of the W_μ fields, and the kinetic energy of the B_μ field. These W_μ and B_μ fields are called gauge fields since these vector fields are adopted by the gauge transformations. The quantized W_μ and B_μ fields are gauge bosons [3].

1.1.2 Strong interaction

Quantum chromodynamics (QCD) describes the strong interaction of particles which have three different colors: Red, Green and Blue. The flavor of quarks doesn't change under the

strong interaction. The strong interaction is mediated by the eight gluons which carry one unit of color and one of anticolor. The eight massless gauge bosons (gluons) are yielded by requiring the local gauge invariance under the phase transformation of the non-Abelian gauge group $SU(3)_C$. The gauge symmetry is not broken like the weak interactions. The strong force forms bound-state by binding quarks, and the bound-states by the strong interaction are called hadron. Hadrons are classified into two groups, meson and baryon. Meson is composed of a quark and an antiquark and baryons consist of either three quarks or three antiquarks. All hadrons are assumed to be colorless, so that they are color singlet states. Quarks are confined in hadrons and can not exist as free particles [3].

1.2 Top Quark Pair Production

1.2.1 The total cross section for $t\bar{t}$ production

The top quark pair can be produced by the $q\bar{q}$ annihilation and gluon fusion processes at the Tevatron which is a proton-antiproton collider. At the Tevatron, the $q\bar{q}$ annihilation and gluon fusion contribute 85% and 15% to the production of the $t\bar{t}$ production at $\sqrt{s} = 1.96$ TeV, respectively. Figure 1.1 shows the Feynman diagrams for $t\bar{t}$ production.

The standard perturbative QCD theory calculates the invariant cross section for the inclusive production of a heavy quark which has momentum p and energy E as follows,

$$\frac{Ed^3\sigma}{d^3p} = \sum_{i,j} \int dx_i dx_j \left[\frac{Ed^3\hat{\sigma}_{ij}\left(x_i P_i, x_j P_j, p, m, \mu\right)}{d^3p} \right] F_i^A\left(x_i, \mu\right) F_j^B\left(x_j, \mu\right) \tag{1.5}$$

where the indices i, j are the interacting light partons such as gluons, light quarks and antiquarks. The functions F_i are the Parton Distribution Function(PDF) which give the probability density for a parton at a given momentum fraction and a scale μ. μ is know as the renormalization and factorization scale. x_i and x_j are the momentum fractions that the partons i and j carry. The $\hat{\sigma}$ represents the short distance cross section which is derived from the cross section of parton scattering by eliminating the long distance cross section. Removing the long distance cross section is necessary since the cross section calculated perturbatively has contribution from interactions before the hard scattering. By integrating Eq. 1.5 and feeding

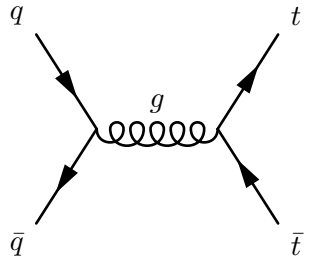

(a) $q\bar{q}$ annihilation

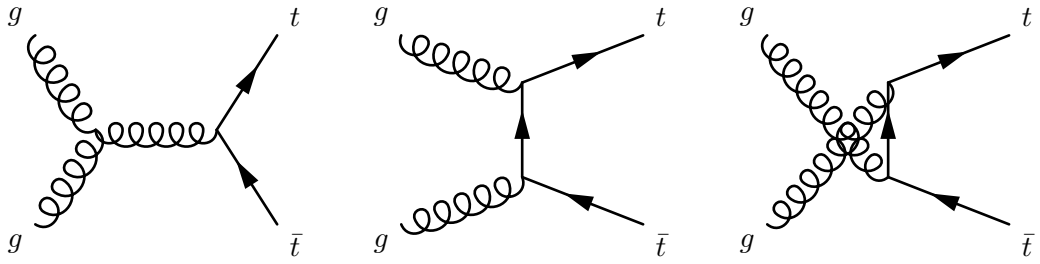

(b) gluon fusion

Figure 1.1: $t\bar{t}$ production in the lowest order.

variables for $t\bar{t}$ mass and PDF for $p\bar{p}$ collision, we get the total cross section for $p\bar{p} \to t\bar{t}$ at the center of mass energy $\sqrt{s}$ as follow [4],

$$\sigma(s) = \sum_{i,j} \int dx_i dx_j \hat{\sigma}_{ij} \left(x_i x_j s, m_t^2, \mu^2\right) F_i^p \left(x_i, \mu\right) F_j^{\bar{p}} \left(x_j, \mu\right) \tag{1.6}$$

where s is the square of the center of mass energy of the colliding p and $\bar{p}$. The short distance cross section $\hat{\sigma}$ for the $t\bar{t}$ inclusive production by interacting partons i, j can be written as,

$$\hat{\sigma}\left(s, m_t^2, \mu^2\right) = \frac{\alpha_s^2(\mu^2)}{m_t^2} f_{ij}\left(\rho, \frac{\mu^2}{m_t^2}\right) \tag{1.7}$$

where $\rho = 4m_t^2/s$ and s is the square of the center of mass for interacting parton i, j. The f_{ij} are the dimensionless functions which can be expanded as follow,

$$f_{ij}\left(\rho, \frac{\mu^2}{m_t^2}\right) = f_{ij}^{(0)}(\rho) + g^2(\mu^2)\left[f_{ij}^{(1)}(\rho) + \bar{f}_{ij}^{(1)}(\rho) ln\left(\frac{\mu^2}{m_t^2}\right)\right] + O(g^4) \tag{1.8}$$

The strong coupling constant can be written as $\alpha_s = g^2/4\pi$. From Eq. 1.7 and Eq. 1.8, the first term $f_{ij}^{(0)}(\rho)$ corresponds to the Leading Order (LO) contribution ($O(\alpha_s^2)$), and the second

terms $f_{ij}^{(1)}(\rho)$ and $\bar{f}_{ij}^{(1)}$ are referred to the Next-to-Leading-Order (NLO) contributions ($O(\alpha_s^3)$). Reference [4] describes the functions $f_{ij}^{(0)}$ as

$$f_{q\bar{q}}^{(0)} = \frac{\pi\beta\rho}{27}\left[2+\rho\right] \tag{1.9}$$

$$f_{g\bar{g}}^{(0)} = \frac{\pi\beta\rho}{192}\left[\frac{1}{\beta}\left(\rho^2+16\rho+16\right) ln\left(\frac{1+\beta}{1-\beta}\right) - 28 - 31\rho\right] \tag{1.10}$$

$$f_{gq}^{(0)} = f_{g\bar{q}}^{(0)} = 0, \tag{1.11}$$

$\beta = \sqrt{1-\rho}$. The quantities $f^{(1)}$ and $\bar{f}^{(1)}$ don't have analytical forms. Thus, fitting is conducted as a numerical calculation and provides a fit function. The fit functions for the $f^{(1)}$ and $\bar{f}^{(1)}$ are described in reference [4]. Using Eq. 1.6, 1.7 and 1.8, the total $t\bar{t}$ cross section by NLO correction can be derived. In 2008, S. Moch and P. Uwer published theoretical $t\bar{t}$ cross section by Next-to-Next-to-Leading-Order (NNLO) correction and obtained $\sigma_{t\bar{t}} = 7.46^{+0.48}_{-0.67}$ pb at $m_t = 172.5$ GeV. Table 1.4 shows the total cross section for $t\bar{t}$ at several m_t, which are estimated by the NNLO (approx) QCD prediction.

Table 1.4: The $t\bar{t}$ total cross section by NNLO (approx) QCD prediction for CTEQ6.5 and MRST-2006 NNLO PDF sets [5].

		Only scale uncertainty			Only pdf uncertainty			Total uncertainty		
PDF	m_t	Min.	Max.	δ [%]	Min.	Max.	δ [%]	Min.	Max.	δ [%]
CTEQ6.5	170	7.90	8.26	3	7.73	8.65	6	7.46	8.70	8
	172	7.42	7.76	3	7.26	8.12	6	7.01	8.18	8
	175	6.76	7.08	3	6.62	7.4	6	6.39	7.45	8
MRST-2006 NNLO	170	8.16	8.59	3	8.28	8.73	3	7.94	8.81	6
	172	7.65	8.06	3	7.77	8.19	3	7.45	8.27	6
	175	6.95	7.34	3	7.07	7.45	3	6.77	7.52	6

1.2.2 Top Quark Decay

Top quark has a short life time of $\tau_t \approx 0.5\times10^{-24}$ s. The life time of top quark is shorter than the hadron formation time Λ_{QCD}^{-1}, so that top mesons are not able to form. The top quark is anticipated to decay before the hadronization to top-flavored hadrons or $t\bar{t}$-quarkonium-bound states. In the top decay, the Wb final state is predominant because the square of the matrix elements V_{td} and V_{ts} in the CKM matrix suppresses the Wd and Ws final states. Thus, the

top quark decays to a W boson and a b quark predominantly ($t \to Wb$). The W boson can have both leptonic and hadronic final states. Table 1.5 describes the decay modes and their branching ratios.

Table 1.5: The decay modes and their branching ratios in the W boson decay [6].

Decay Modes of W	Branching Ratios
W $\to e\nu_e$	10.75 ± 0.13 %
W $\to \mu\nu_\mu$	10.57 ± 0.15 %
W $\to \tau\nu_\tau$	11.25 ± 0.20 %
W $\to$ hadrons	67.60 ± 0.27 %

Since the top quark decay is dominated by the $t \to Wb$, the top decay modes are exactly the same as the W decay modes plus a b quark. Considering W decay modes, the $t\bar{t}$ final states can be classified into three classes [6].

A. $t\bar{t} \to W^+bW^-\bar{b} \to q\bar{q}'\ b\ q''\bar{q}'''\ \bar{b}$, (46.2 %)

B. $t\bar{t} \to W^+bW^-\bar{b} \to q\bar{q}'bl\bar{\nu}_l\bar{b} + \bar{l}\nu_l bq\bar{q}'\bar{b}$, (43.5 %)

C. $t\bar{t} \to W^+bW^-\bar{b} \to \bar{l}\nu_l\ b\ l'\bar{\nu}_{l'}\ \bar{b}$. (10.3 %)

Processes A represent both W bosons decaying hadronically, which is called "all-hadronic" channel. Processes B describe lepton+jets channel where one W boson has e, μ or τ and their neutrino as final states, and the other W boson decays hadronically. Processes C are dilepton channels with both W bosons decaying leptonically. The branching ratio of each channel for $t\bar{t}$ production can be found by the product of the branching ratios of W boson decay channels, for example,

1. e+jets channel

$$Br(t\bar{t} \to e + jets) = Br(W^+ \to e^+\nu_e) \times Br(W^- \to hadrons) + Br(W^- \to e^-\bar{\nu}_e) \times Br(W^+ \to hadrons)$$
$$= 10.75\ \% \times 67.60\ \% + 10.75\ \% \times 67.60\ \% = 14.53\ \%$$

2. μ+jets channel

$$Br(t\bar{t} \to \mu + jets) = Br(W^+ \to \mu^+\nu_\mu) \times Br(W^- \to hadrons) +$$

$$Br(W^- \to \mu^- \bar{\nu}_\mu) \times Br(W^+ \to hadrons)$$
$$= 10.57\ \% \times 67.60\ \% + 10.57\ \% \times 67.60\ \% = 14.29\ \%$$

1.3 CP violating anomalous top-quark couplings

1.3.1 Introduction

One interesting question in particle physics is the phenomenon that the universe is made mainly of matter instead of equal amounts of matter and antimatter. This phenomenon can be understood through violations of CP symmetry. In 1964, Christenson, Cronin, Fitch and Turlay showed that the K_L, being called the long-lived kaon, could decay to 2π with a branching ratio [8],

$$Br(K_L \to 2\pi) = 3.00 \pm \times 10^{-3} \tag{1.12}$$

In detail, considering the Kaon's are pseudoscalars,

$$CP \mid K^0\rangle = - \mid \bar{K}^0\rangle, \quad CP \mid \bar{K}^0\rangle = - \mid K^0\rangle \tag{1.13}$$

The normalized eigenstates of CP are

$$\mid K_1\rangle = \frac{1}{\sqrt{2}} \left(\mid K^0\rangle - \mid \bar{K}^0\rangle \right) \text{ and } \mid K_2\rangle = \frac{1}{\sqrt{2}} \left(\mid K^0\rangle + \mid \bar{K}^0\rangle \right) \tag{1.14}$$

$$CP \mid K_1\rangle = \mid K_1\rangle \text{ and } CP \mid K_2\rangle = - \mid K_2\rangle \tag{1.15}$$

From Eq. 1.14, 1.15, the eigenstates of K_1 and K_2 are $CP = +1$ and $CP = -1$, respectively. If CP is conserved in the weak interaction, K_1 must decay to the two-pion system and K_2 must have the three-pion configuration because both have $C = +1$, K_1 and K_2 have $P = +1$ and $P = -1$, respectively. Also, since the 2π decay has greater energy than the 3π decay, the decay of K_1 is faster. Therefore the lifetime of K_1 is much shorter than that of K_2. The lifetimes of K_1 and K_2 were measured experimentally by Lederman and collaborators at Brookhaven in 1956.

$$\begin{aligned} \tau_{K_1} &= 0.89 \times 10^{-10} \text{ sec} \\ \tau_{K_2} &= 5.2 \times 10^{-8} \text{ sec} \end{aligned} \tag{1.16}$$

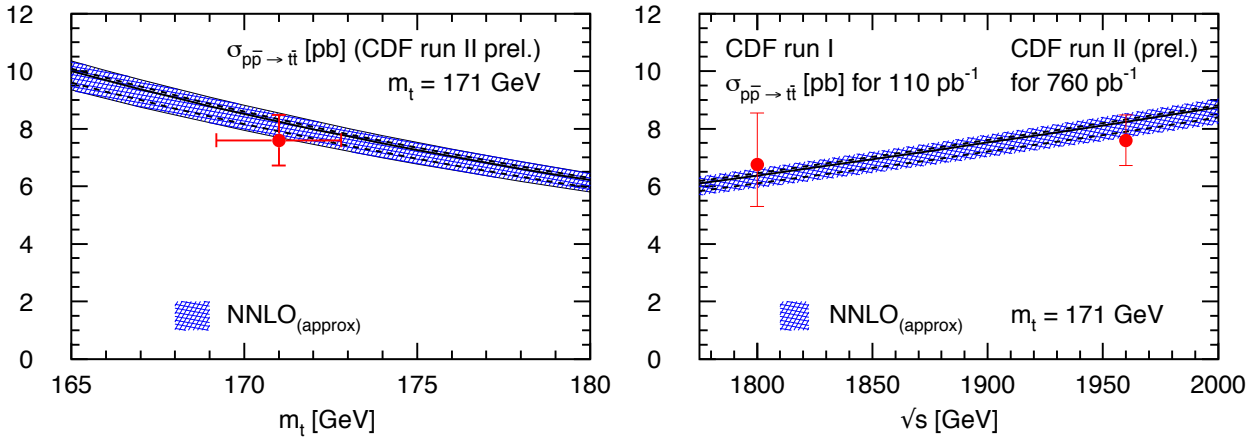

Figure 1.2: The $t\bar{t}$ total cross section at Tevatron by the NNLO (approx) QCD prediction and CDF data with $m_t = 171$ GeV (left). The left is the total cross section at $\sqrt{s} = 1.96$ TeV as function of m_t and the right is the $t\bar{t}$ total cross section as function of $\sqrt{s}$. The $t\bar{t}$ total cross section are estimated for $\mu = m_t$ (the solid line), $\mu = 2m_t$ (the lower dashed line) and $\mu = m_t/2$ (the upper dashed line) [5].

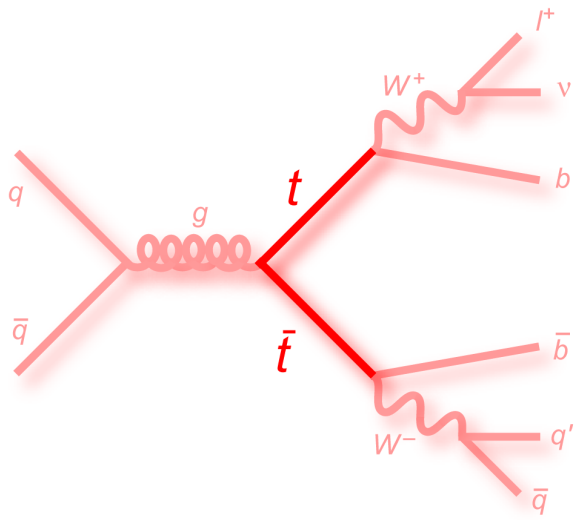

Figure 1.3: The lepton+jets channel of $t\bar{t}$ production event [7].

Cronin, Fitch and Turlay reported the observation of the 2π decay of the long-lived neutral kaon, expressed with a formula as

$$\mid K_L\rangle = \frac{1}{\sqrt{1+|\epsilon^2|}}\left(\mid K_2\rangle + \epsilon \mid K_1\rangle\right) \tag{1.17}$$

The magnitude of the coefficient ϵ was measured to be about 2.3×10^{-3} experimentally. This demonstrates that the long-lived kaon can decay to the 2π system and violates CP eigenstate of it [1].

1.3.2 CPT Theorem

CPT theorem states that any consecutive operation of charge conjugation (C), parity operation (P) and time reversal (T) doesn't break an exact symmetry of any interaction. The order of CPT operation can be taken in any order. This property implies that particles and antiparticles have the same lifetime, mass, magnetic moments but the opposite electric charge. The Table 1.6 is quoted from the book [9]. It shows the experimental results of the CPT theorem and the CPT theorem is well satisfied.

Table 1.6: Test of the CPT theorem [9].

Measured quantity	Limit or value
$(M_{K^0} - M_{\bar{K}^0})/(M_{K^0} + M_{\bar{K}^0})$	$< 10^{-19}$
$(M_{e^+} - M_{\bar{e}^-})/(M_{e^-} + M_{\bar{e}^+})$	$< 4 \times 10^{-8}$
$(M_\Lambda - M_{\bar{\Lambda}})/(M_\Lambda + M_{\bar{\Lambda}})$	$(-5 \pm 5) \times 10^{-6}$
$(Q_p - Q_{\bar{p}})/e$	$< 2 \times 10^{-5}$
$\left(\frac{Q_p}{M_p} - \frac{Q_{\bar{p}}}{M_{\bar{p}}}\right) / \left(\frac{Q_p}{M_p} + \frac{Q_{\bar{p}}}{M_{\bar{p}}}\right)$	$(8 \pm 6) \times 10^{-10}$
$(\mu_{e^+} - \mu_{e^-})/(\mu_{e^+} + \mu_{e^-})$	$-(3 \pm 5) \times 10^{-13}$
$(\tau_{\mu^+} - \tau_{\mu^-})/(\tau_{\mu^+} + \tau_{\mu^-})$	$< 10^{-4}$

1.3.3 CP violating anomalous top-quark couplings

Top quark has shorter lifetime than the hadronization time due to its large mass. So, the complicated theory of non-perturbative and bound state physics does not affect the dynamics of top production and decay. The top quark decays are very effective spin analyzers and this can be used to detect CP violation effectively. By the way, CP violation in the top physics is very

small in the Standard Model. Nevertheless, there are two motivations for CP violation study using top quark events. First is that the study of CP violation using top quark is another source of CP violation which can explain why the universe is made mainly of matter. The second is the the observation of CP violation in top quark physics is explicit evidence of new physics beyond the Standard Model because the Standard Model predicts that CP violation in the top quark system is very small.

Let us review how CP violation occur in the ttg vertex. To get an idea how Chromo Electric Dipole Moment (CEDM) behaves, let us first investigate the characteristic of Electric Dipole Moment (EDM). An EDM vector has to be aligned along the direction of spin vector since any component of any other direction would be cancelled out due to the spin rotation of the particle. The EDM vector of a particle is even under time reversal and odd under parity operation while the spin vector of the particle is axial vector so it is even under parity operation and odd under time reversal. Therefore, a permanent EDM of elementary particles would violate time reversal (T) and parity (P) symmetries. Figure 1.4 shows the charge distribution and spin of a particle and the behavior of a EDM under T (time reversal), P (Parity) operations. The Hamiltonian for the interaction between the spin and the EDM can be written as,

$$H_E = -d_E \vec{S} \cdot \vec{E} \tag{1.18}$$

where $\vec{S}$ and $\vec{E}$ are the spin and the electric field vectors, respectively [13], and d_E is the electric dipole moment strength. As the interaction Hamiltonian shows, when the vectors of the EDM and the spin are in the same direction, the potential energy is least and the EDM is in the equilibrium state ((a) in Figure 1.4). Under Parity operation, the axial vector $\vec{S}$ is even while $\vec{E}$ is odd ((b) in Figure 1.4). Time reversal changes the sign of the spin vector whereas the sign of the EDM vector is unchanged ((c) in Figure 1.4). In the cases of both (b) and (c) in Figure 1.4, if d_E exists, the interaction Hamiltonian would violate the symmetries for time reversal and parity.

Similarly, Chromo-Electric Dipole Moment (CEDM) is formed by the color charge distribution within a top quark. In the Standard Model, the CEDM of top quark is induced at three-loop level, but Higgs model and SUSY model enhance giving a rise to CEDM. The mech-

anism for CEDM is well described in References [8]. With this idea for CEDM, an example for the CP-violating interaction in the $t\bar{t}$ production near threshold will be given to show how CP violation occur by CEDM. Near $t\bar{t}$ threshold region, top quark pairs are produced almost at rest. Thus $t\bar{t}$ are produced at a distance $r \sim 1/m_t$, where r is a distance between top and anti-top quark. Then they move apart non-relativistically. When the distance between top and anti-top quarks reach the order of Bohr radius ($r \sim (\alpha_s m_t)^{-1}$), top and anti-top quarks form a color coulomb potential. This $t\bar{t}$ system starts to decay via electroweak interaction once the distance between top and anti-top quarks reach $r \sim (m_t\Gamma_t)^{-1/2}$. The hadronization scale Λ_{QCD}^{-1} is much larger than two scales $(\alpha_s m_t)^{-1}$ and $(m_t\Gamma_t)^{-1/2}$. Table 1.7 shows that the magnitudes of $(\alpha_s m_t)^{-1}$ and $(m_t\Gamma_t)^{-1/2}$ are similar and they are very much smaller than the hadronization scale (Λ_{QCD}^{-1}). To calculate Bohr radius of $t\bar{t}$ system, 0.375 is used for α_s [10]. Since top quark pairs are produce almost at rest, the momentum transfer Q would be very small value. Table 1 in reference [10], the α_s for Υ decay is 0.217. Since the Q is very small value and according to the α_s formula in the book [12], α_s for $t\bar{t}$ system will be larger than α_s for Υ decay. Thus the measured α_s 0.375 is chosen, whose Q is smallest in table. The width Γ_t is 13.1 GeV which comes from reference [6]. Reference [11] gives $\Lambda_{QCD} \simeq 200$ MeV.

Table 1.7: Comparison of Bohr radius of $t\bar{t}$ system ($(\alpha_s m_t)^{-1}$), the distance that a $t\bar{t}$ system starts decaying ($(m_t\Gamma_t)^{-1/2}$) and Hadronization scale (Λ_{QCD}^{-1}).

Bohr radius $((\alpha_s m_t)^{-1}$	$(m_t\Gamma_t)^{-1/2})$	Hadronization scale (Λ_{QCD}^{-1})
3.1×10^{-3} F	4.2×10^{-3} F	1.0 F

In this $t\bar{t}$ system, both spins of top and anti-top quarks are along the beam direction or in a state that the combination of the two spin makes $S = 1$ state. At this state, the orbital angular momentum is 0 ($L = 0$), thus the total spin and PC eigenstates of this $t\bar{t}$ system can be represented as $J^{PC} = 1^{--}$. When top and anti-top quarks are apart by the Bohr radius ($(\alpha_s m_t)^{-1}$)), top and anti-top quarks exchange multiple gluons and the anomalous top-gluon coupling forms a color coulomb potential with Eq. 1.19 and the color factor $C_F = 4/3$ which is the color singlet state. In other words, the top quarks and gluons are confined within color

singlet states. The color coulomb potential

$$V(r) = -C_F \frac{\alpha_s \hbar c}{r} \tag{1.19}$$

aligns both CEDMs of top and antitop quarks in the direction of the field. In other words, the spins of top and antitop quarks are aligned antiparallel. In the previous paragraph, the EDM vector of a particle is aligned along its spin. In case of CEDM, it can be considered as the EDM and this aligns the spins of t and $\bar{t}$ quarks into the antiparallel direction along the color electric field. Figure 1.5 shows the alignment of the spins of the top and antitop quarks in the chromo electric field. After the interaction with the potential, the $J^{PC} = 1^{--}$ ($L = 0$ and $S = 1$) turns into $J^{PC} = 1^{+-}$ ($L = 1$ and $S = 0$). The CP eigenstates of this $t\bar{t}$ system before and after the interaction relating to the CEDM have -1 and +1 and this means that CP violation occurs by the top-gluon anomalous coupling [14].

CP violation via anomalous top quark coupling is parametrized for Tevatron energies. The interaction between the chromo-electric dipole moment of the top quark and gluon modifies the $t\bar{t}$ production. The interaction Lagrangian can be written as Eq. 1.20.

$$\mathcal{L}_{cedm} = -ig_s \frac{\tilde{d}}{2} \bar{t} \sigma_{\mu\nu} \gamma_5 G^{\mu\nu} t \tag{1.20}$$

where $\tilde{d}$ is CP violating anomalous coupling, g_s and $G^{\mu\nu}$ are the strong coupling constant and the field strength tensor, respectively, and $\sigma_{\mu\nu} = \frac{i}{2}[\gamma_\mu, \gamma_\nu]$. The top quark coupling to gluons in the Standard Model is modified by the Lagrangian. The vertex factors for ttg and $ttgg$ are written as Eq. 1.21.

$$\begin{aligned} gt\bar{t} &\rightarrow -ig_s \frac{\lambda_a}{2} \left(\gamma_\mu + \tilde{d} \sigma_{\mu\nu} q^\nu \gamma_5 \right) \\ ggt\bar{t} &\rightarrow i\pi\alpha_s [\lambda^b, \lambda^c] \tilde{d} \sigma_{\mu\nu} \gamma_5 \end{aligned} \tag{1.21}$$

Figure 1.6 shows 5 diagrams for the possible CP violating vertices. Figure 1.6 (a) is $q\bar{q}$ annihilation channel and (b) shows s-channel, t-channel, u-channel and seagull channel in gluon fusion. The seagull channel is involved as a CP violating channel and is needed to preserve gauge invariance [8, 15]. The CP asymmetry can be calculated by considering the $t\bar{t}$ production processes in Figure 1.6 in the parton CM frame, using a mixed method of helicity

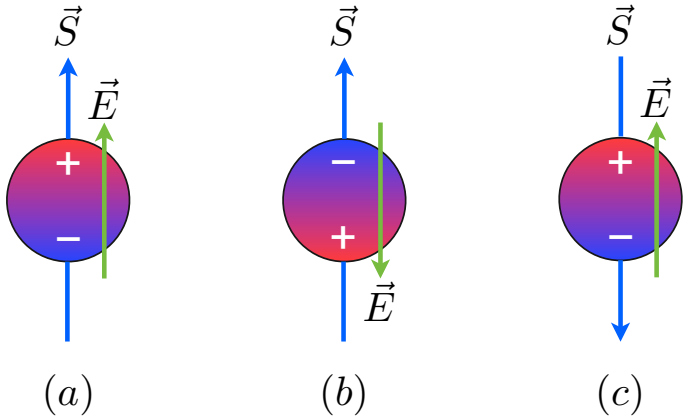

Figure 1.4: The Electric Dipole Moment (EDM) of a elementary particle. (a) The EDM vector (or electric field vector by the EDM) is aligned in the direction of the spin of a particle. (b) After parity (P) operation, the charge distribution and the electric field flip but the spin direction does not change (axial vector) $\vec{S} = \vec{r} \times \vec{p}$. (c) The charge distribution and the direction of the electric field are unchanged but the spin rotation reverses after time reversal (T).

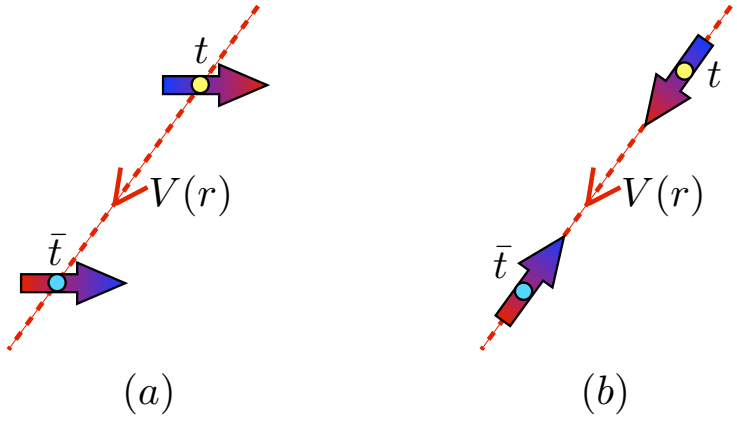

Figure 1.5: The directions of the top and antitop spins (a) before and (b) after the interaction with the color electric field.

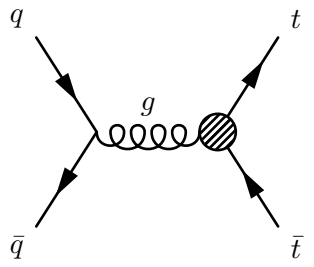

(a) $q\bar{q}$ annihilation

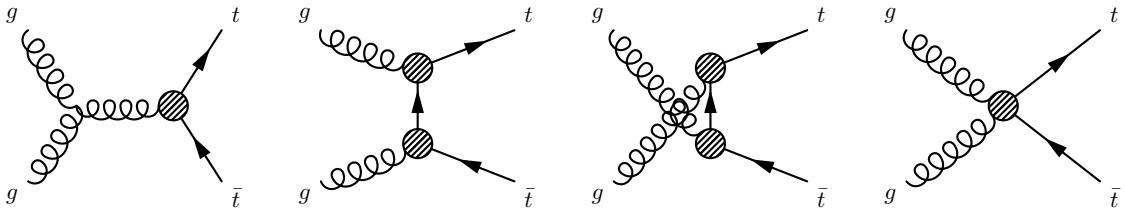

(b) gluon fusion

Figure 1.6: CP violation in $t\bar{t}$ production vertices via (a) $q\bar{q}$ annihilation and (b) gluon fusion: s, t, u and seagull channels.

amplitudes and traces of Dirac matrices for the $t\bar{t}$ production processes. The matrix elements for the CP-odd in $gg \to t\bar{t}$ process is written as Eq. 1.22 [15]. In the following formulae, $\epsilon(a,b,c,d)$ is the Levi-Civita tensor which is defined as $\epsilon(a,b,c,d) \equiv \epsilon_{\mu\nu\alpha\beta}\alpha^{\mu}b^{\nu}c^{\alpha}d^{\beta}$. The sign convention $\epsilon_{0123} = 1$ is used. And s,t,u are the Mandelstam variables of interacting partons.

$$\begin{aligned} |\mathcal{M}|^2_{CP} &= C_1(s,t,u)q\cdot(p_{\bar{t}}-p_t)\epsilon(p_{\bar{t}},p_t,p_D,p_{\bar{D}}) \\ &+ C_2(s,t,u)(P\cdot p_t\epsilon(p_D,p_{\bar{D}},p_{\bar{t}},q)+P\cdot p_{\bar{t}}\epsilon(p_D,p_{\bar{D}},p_t,q)) \\ &+ C_3(s,t,u)(P\cdot p_D\epsilon(p_{\bar{D}},p_t,p_{\bar{t}},q)+P\cdot p_{\bar{D}}\epsilon(p_D,p_t,p_{\bar{t}},q)) \end{aligned} \tag{1.22}$$

Where $P \equiv p_1 + p_2$ and $q \equiv p_1 - p_2$. P and q mean the sum and difference of two incoming parton four-momentum. The form factors in Eq. 1.22 are defined as follow

$$C_i(s,t,u) = C_i^s(s,t,u) + C_i^{tu}(s,t,u) + C_i^{tu-s}(s,t,u) \tag{1.23}$$

The contributions from s channel amplitude is

$$C_1^s(s,t,u) = C_2^s(s,t,u) = C_3^s(s,t,u) = \frac{3}{2}\tilde{d}Km_t\frac{t-u}{s^2} \tag{1.24}$$

The t and u channels contribution are

$$\begin{aligned}
C_1^{tu}(s,t,u) &= \frac{1}{48}\tilde{d}K\frac{m_t}{s^2(t-m_t^2)^2(u-m_t^2)^2}[9(t-u)^5-2(5s-36m_t^2)s(t-u)^3 \\
&+ s^2(s^2-22sm_t^2+144m_t^4)(t-u)+\frac{14m_t^2s^4(s+8m_t^2)}{(t-u)}] \\
C_2^{tu}(s,t,u) &= \frac{1}{48}\tilde{d}K\frac{m_t}{s^2(t-m_t^2)^2(u-m_t^2)^2}[9(t-u)^5-2(5s-9m_t^2)s(t-u)^3 \\
&+ s^2(s^2+46sm_t^2)(t-u)] \\
C_3^{tu} &= C_2^{tu}(s,t,u)
\end{aligned} \tag{1.25}$$

The interference of the s channel amplitude and the amplitudes for the t and u channels are

$$\begin{aligned}
C_1^{tu-s}(s,t,u) &= -\frac{3}{4}\tilde{d}K\frac{m_t(t-u)}{s^2(t-m_t^2)(u-m_t^2)}\left(-4sm_t^2+s^2-(t-u)^2\right) \\
C_2^{tu-s}(s,t,u) &= -3\tilde{d}Km_t\frac{t-u}{s^2} \\
C_3^{tu-s} &= C_2^{tu-s}(s,t,u)
\end{aligned} \tag{1.26}$$

For one W decay into a lepton, the form factors and the four-momentum p_D and $p_{\bar{D}}$ are considered for two final states $bl^+\nu W^-$ or $\bar{b}l^-\bar{\nu}W^+$ separately. For the final state $bl^+\nu W^-$,

$$p_D \to p_{l^+},\ p_{\bar{D}} \to p_{\bar{b}} \tag{1.27}$$

and the factor K in the form factor C_i is

$$\begin{aligned}
K_{lb} &\equiv 4(\pi^2\alpha_s^2g^6)(p_b\cdot p_\nu)\left(2-\frac{m_t^2}{M_W^2}\right)\left(\frac{\pi}{m_t\Gamma_t}\right)^2\left(\frac{\pi}{M_W\Gamma_W}\right) \\
&\times \delta(p_t^2-m_t^2)\delta(p_{\bar{t}}^2-m_t^2)\delta(p_{W^+}^2-M_W^2)
\end{aligned} \tag{1.28}$$

For the final state $\bar{b}l^-\bar{\nu}W^+$,

$$p_D \to p_b,\ p_{\bar{D}} \to p_{l^-} \tag{1.29}$$

and the factor K in the form factor C_i is

$$\begin{aligned}
K_{bl} &\equiv 4(\pi^2\alpha_s^2g^6)(p_{\bar{b}}\cdot p_{\bar{\nu}})\left(2-\frac{m_t^2}{M_W^2}\right)\left(\frac{\pi}{m_t\Gamma_t}\right)^2\left(\frac{\pi}{M_W\Gamma_W}\right) \\
&\times \delta(p_t^2-m_t^2)\delta(p_{\bar{t}}^2-m_t^2)\delta(p_{W^-}^2-M_W^2)
\end{aligned} \tag{1.30}$$

So far, CP violation in the production vertex has been reviewed. The other source of CP violation in the $t\bar{t}$ system is the decay vertices $t \to bW^+$ and $\bar{t} \to \bar{b}W^-$ via anomalous coupling f. The general vertices are written as follows,

$$\begin{aligned}
\Gamma^{\mu}_{W_{tb}} &= -\frac{g}{\sqrt{2}} V^*_{tb} \bar{u}(p_b)[\gamma_\mu P_L - i\tilde{f} e^{i(\phi_f+\delta_f)} \sigma^{\mu\nu}(p_t - p_b)_\nu P_R] u(p_t) \\
\bar{\Gamma}^{\mu}_{W_{tb}} &= -\frac{g}{\sqrt{2}} V_{tb} \bar{v}(p_{\bar{t}})[\gamma_\mu P_L - i\tilde{f} e^{i(-\phi_f+\delta_f)} \sigma^{\mu\nu}(p_{\bar{t}} - p_{\bar{b}})_\nu P_L] \bar{v}(p_{\bar{b}})
\end{aligned} \tag{1.31}$$

The P_L and P_R are chiral projection operators which are defined as $P_L = \frac{1}{2}(1-\gamma^5)$ and $P_R = \frac{1}{2}(1+\gamma^5)$. Also the phase of $\tilde{f}$ is separated into a CP violating phase ϕ_f and a CP conserving phase δ_f. From these vertices, the matrix element square for the T-odd triple product correlation is

$$|\mathcal{M}|^2 = \tilde{f} sin(\phi_f + \delta_f)\epsilon(p_t, p_b, p_{l^+}, Q_t) + \tilde{f} sin(\phi_f - \delta_f)\epsilon(p_{\bar{t}}, p_{\bar{b}}, p_{l^-}, Q_{\bar{t}}) \tag{1.32}$$

The Q_t and $Q_{\bar{t}}$ have different result for each W decay channel and are described well in the references [15, 16]. Detailed calculations for CP violating amplitudes for both production vertex and decay vertex are explained very well in reference [15].

The $q\bar{q} \to t\bar{t}$ process contributes 85 % of $t\bar{t}$ production in Tevatron so the $q\bar{q}$ annihilation is main contribution for CP violation in $t\bar{t}$ system at Tevatron. The matrix elements for CP violation in the production vertex is

$$|\mathcal{M}|^2_{CP} = C_1(s,t,u)\mathcal{O}_1 + C_2(s,t,u)\mathcal{O}_2 + C_3(s,t,u)\mathcal{O}_3 \tag{1.33}$$

$\mathcal{O}_i$ is written as Eq. 1.34

$$\begin{aligned}
\mathcal{O}_1 &= \epsilon(p_t, p_{\bar{t}}, p_D, p_{\bar{D}}) \\
\mathcal{O}_2 &= (t-u)\epsilon(p_D, p_{\bar{D}}, P, q) \\
\mathcal{O}_3 &= (t-u)\epsilon(P \cdot p_D \epsilon(p_{\bar{D}}, p_t, p_{\bar{t}}, q) + P \cdot p_{\bar{D}} \epsilon(p_D, p_t, p_{\bar{t}}, q))
\end{aligned} \tag{1.34}$$

The form factors C_i are

$$\begin{aligned}
C_1^{q\bar{q}}(s,t,u) &= -\frac{16}{9}\tilde{d}K m_t \left(\frac{(t-u)^2}{s^2} + 4\frac{m_t^2}{s} \right) \\
C_3^{q\bar{q}}(s,t,u) &= -\frac{16}{9}\tilde{d}K \frac{m_t}{s^2} \\
C_2^{q\bar{q}}(s,t,u) &= \frac{2}{s} C_3^{q\bar{q}}(s,t,u)
\end{aligned} \tag{1.35}$$

For the decay channel $t\bar{t} \to l^+\nu_l\ b\ q\bar{q}'\ \bar{b}$, $p_D, p_{\bar{D}}$ and K become

$$\begin{aligned} p_D &\to p_{l^+} \text{ and } p_{\bar{D}} \to p_d \\ K &\equiv 48(\pi^2\alpha_s^2 g^8)(p_b \cdot p_\nu)(p_{\bar{b}} \cdot p_{\bar{u}}) \left(\frac{\pi}{m_t\Gamma_t}\right)^2 \left(\frac{\pi}{M_W\Gamma_W}\right)^2 \\ &\times \delta(p_t^2 - m_t^2)\delta(p_{\bar{t}}^2 - m_t^2)\delta(p_{W^+}^2 - M_W^2)\delta(p_{W^-}^2 - M_W^2) \end{aligned} \tag{1.36}$$

And for the channel $t\bar{t} \to l^-\bar{\nu}_l\ \bar{b}\ q\bar{q}'\ b$,

$$\begin{aligned} p_D &\to p_{\bar{d}} \text{ and } p_{\bar{D}} \to p_{l^-} \\ K &\equiv 48(\pi^2\alpha_s^2 g^8)(p_b \cdot p_u)(p_{\bar{b}} \cdot p_{\bar{\nu}}) \left(\frac{\pi}{m_t\Gamma_t}\right)^2 \left(\frac{\pi}{M_W\Gamma_W}\right)^2 \\ &\times \delta(p_t^2 - m_t^2)\delta(p_{\bar{t}}^2 - m_t^2)\delta(p_{W^+}^2 - M_W^2)\delta(p_{W^-}^2 - M_W^2) \end{aligned} \tag{1.37}$$

The matrix element form for CP violation in the decay vertex which is produced by $q\bar{q}$ annihilation is same as Eq. 1.32. The Q_t and $Q_{\bar{t}}$ can be written Eq. 1.38.

$$\begin{aligned} Q_t^{q\bar{q}} &= K\frac{16m_t}{9s^2}\{(4sm_t^2 + (t-u)^2 - s^2)p_{l^-} + 2(sp_{l^-} \cdot (p_t - p_{\bar{t}}) - (t-u)p_{l^-} \cdot q)p_{\bar{t}} \\ &+ 2((t-u)p_{l^-} \cdot (p_t + p_{\bar{t}}) - sp_{l^-} \cdot q)q\} \\ Q_{\bar{t}}^{q\bar{q}} &= K\frac{16m_t}{9s^2}\{(4sm_t^2 + (t-u)^2 - s^2)p_{l^+} - 2(sp_{l^+} \cdot (p_t - p_{\bar{t}}) - (t-u)p_{l^+} \cdot q)p_t \\ &- 2((t-u)p_{l^+} \cdot (p_t + p_{\bar{t}}) + sp_{l^+} \cdot q)q\} \end{aligned} \tag{1.38}$$

To obtain the relevant results for $t\bar{t} \to l^+\nu_l\ b\ q\bar{q}'\ \bar{b}$ and $t\bar{t} \to l^-\bar{\nu}_l\ \bar{b}\ q\bar{q}'\ b$ channels, p_{l^-}, p_{l^+} in Eq. 1.32 and K in Eq. 1.38 are needed to be replaced as follows,

For the channel $t\bar{t} \to l^+\nu_l b q\bar{q}'\bar{b}$,

$$\begin{aligned} &p_{l^-} \to p_d \\ &K \text{ is the } K \text{ in Eq. 1.36} \end{aligned} \tag{1.39}$$

For the channel $t\bar{t} \to l^-\bar{\nu}_l\bar{b}q\bar{q}'b$,,

$$\begin{aligned} &p_{l^+} \to p_{\bar{d}} \\ &K \text{ is the } K \text{ in Eq. 1.37} \end{aligned} \tag{1.40}$$

From the matrix elements for the production vertex and the decay vertex, physics observables are derived for lepton+jets channel. Eq. 1.41 are physics observables for lepton+jets

channel [16].

$$\begin{aligned}
\mathcal{O}_1 &= \epsilon(p_t, p_{\bar{t}}, p_b, p_{\bar{b}}) \xrightarrow{t\bar{t}\ CM} \propto \vec{p}_t \cdot (\vec{p}_b \times \vec{p}_{\bar{b}}) \\
\mathcal{O}_2 &= \epsilon(P, p_b + p_{\bar{b}}, p_l, p_{j_1}) \xrightarrow{lab} \propto (\vec{p}_b + \vec{p}_{\bar{b}}) \cdot (\vec{p}_l \times \vec{p}_{j1}) \\
\mathcal{O}_3 &= Q_l \epsilon(p_b, p_{\bar{b}}, p_l, p_{j_1}) \xrightarrow{b\bar{b}\ CM} \propto Q_l \vec{p}_b \cdot (\vec{p}_l \times \vec{p}_{j1}) \\
\mathcal{O}_4 &= Q_l \epsilon(P, p_b - p_{\bar{b}}, p_l, p_{j_1}) \xrightarrow{lab} \propto Q_l (\vec{p}_b - \vec{p}_{\bar{b}}) \cdot (\vec{p}_l \times \vec{p}_{j1}) \\
\mathcal{O}_7 &= \tilde{q} \cdot (p_b - p_{\bar{b}}) \epsilon(P, \tilde{q}, p_b, p_{\bar{b}}) \xrightarrow{lab} \propto \vec{p}_{beam} \cdot (\vec{p}_b - \vec{p}_{\bar{b}}) \vec{p}_{beam} \cdot (\vec{p}_b \times \vec{p}_{\bar{b}})
\end{aligned} \tag{1.41}$$

In these equations, the sum of the proton and antiproton four-momenta is denoted as P, and $\tilde{q}$ represent the difference of the proton and antiproton four-momenta. Q_l is the lepton charge. p refers to the four-momentum and the subscripts t, b and l denotes top quark, b quark jet and lepton. p_{j1} is the hardest jet four-momentum between two jets coming from hadronic W decay. Also, T-odd but CP-even correlation can be induced by strong interaction (unitary) phase. Eq. 1.42 are established to measure CP conserving contamination in the CP-odd signal.

$$\begin{aligned}
\mathcal{O}_a &= \epsilon(P, p_b - p_{\bar{b}}, p_l, p_{j_1}) \xrightarrow{lab} \propto (\vec{p}_b - \vec{p}_{\bar{b}}) \cdot (\vec{p}_l \times \vec{p}_{j1}) \\
\mathcal{O}_b &= Q_l \epsilon(P, p_b + p_{\bar{b}}, p_l, p_{j_1}) \xrightarrow{lab} \propto Q_l (\vec{p}_b + \vec{p}_{\bar{b}}) \cdot (\vec{p}_l \times \vec{p}_{j1})
\end{aligned} \tag{1.42}$$

Using physics observables in Eq. 1.41 and 1.42, the integrated counting asymmetry is constructed to measure CP-odd violating asymmetry.

$$A_i \equiv \frac{N_{events}(\mathcal{O}_i > 0) - N_{events}(\mathcal{O}_i < 0)}{N_{events}(\mathcal{O}_i > 0) + N_{events}(\mathcal{O}_i < 0)} \tag{1.43}$$

Eq. 1.20 - 1.43 are written based on References [15, 16].

In this thesis, only the CP violation in the production vertex is considered and e+jets and μ+jets channels that contain the contributions of e+jets and μ+jets coming from τ+jets channel are discussed, which consist of one isolated lepton, missing transverse energy, two b-quark jets and two light quark jets from W decay as final state. Figure 1.3 shows the lowest order of lepton+jets channel for $t\bar{t}$ production event.

CHAPTER 2. Tevatron and DØ Detector

The Fermi National Accelerator Laboratory (FNAL or Fermilab) has led high energy physics as the energy frontier for the past twenty years in the world. In particular, the Tevatron accelerator complex makes collisions of proton-antiproton ($p\bar{p}$) at a center of mass energy of almost 2 TeV, the DØ and the CDF detectors at the Fermi National Accelerator Laboratory, have been the center of great developments in high energy physics. The Run I operation, which achieved about 130 pb^{-1} of delivered luminosity at a center of mass energy $\sqrt{s} = 1.8$ TeV from 1992 to 1996, led to the discovery of the top quark in 1995. From 1996 to 2001, the Tevatron and the DØ detector were upgraded to prepare for the next operation called Run II and the upgrade for the Tevatron achieved a center of mass energy $\sqrt{s} = 1.96$ TeV. The Run II operation began to take data since 2002 and data taking is ongoing as of 2010. During the Run II operation, lots of interesting physics researches have been conducted not only in the Standard Model but also beyond the Standard Model, such as the study of Top quark properties, Electroweak physics, New phenomena and Higgs searches. The big milestone of the Run II operation is the discovery of the single top quark production. In this chapter, the Tevatron accelerator complex and the DØ detector for Run II will be described

2.1 Tevatron

The Tevatron accelerator complex is comprised of the Pre-accelerator, LINAC, Booster, Main Injector, Recycler, Tevatron, Debuncher and Accumulator as shown in Figure 2.1. Debuncher and Accumulator are known as the antiproton source. The Tevatron is the collider which uses proton and antiproton sources. First off, we may wonder how the proton source is made. The simple way is to strip off an electron from hydrogen atom by accelerating hydro-

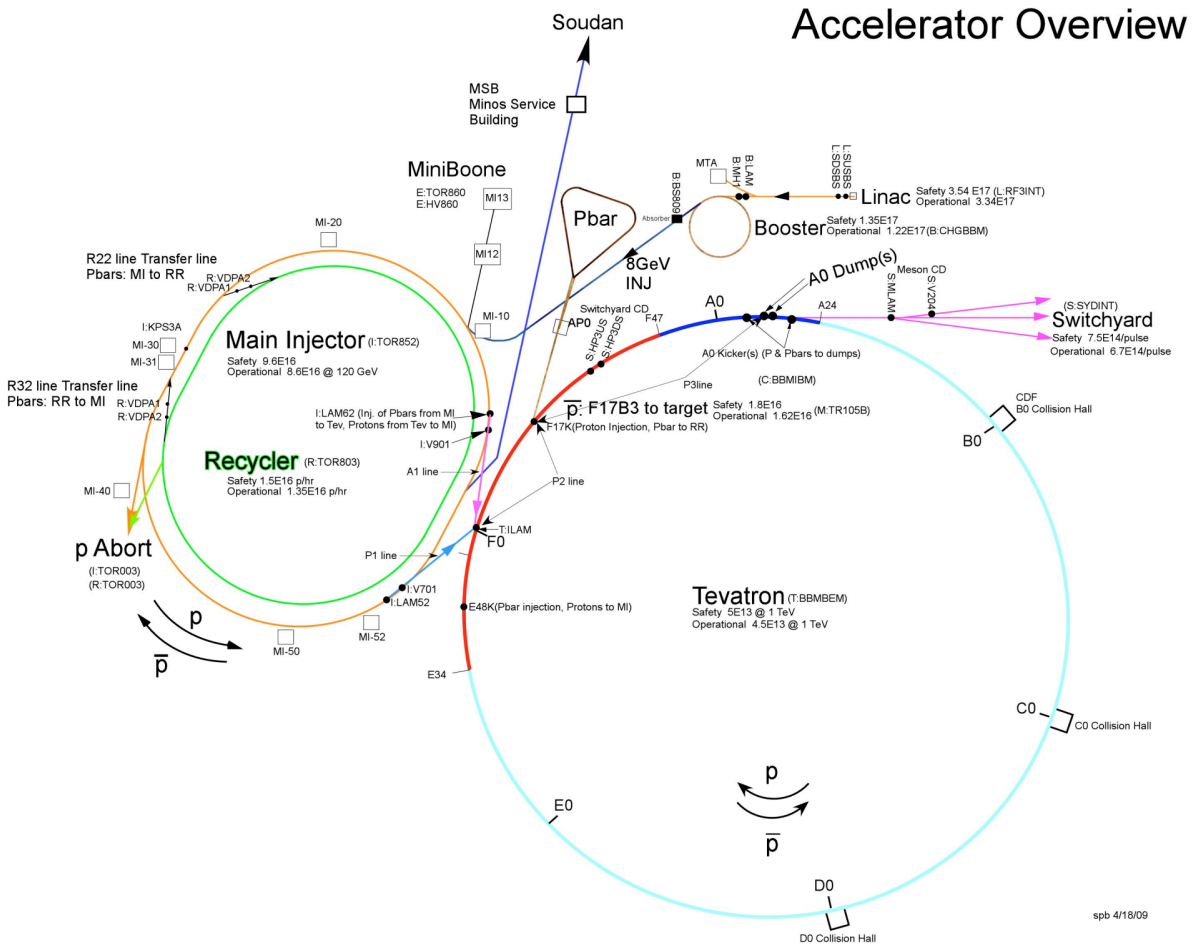

Figure 2.1: The overview of the accelerator complex [18].

gen atom and passing it through a carbon foil since hydrogen consists of one proton and one electron. However, hydrogen atom is electrically neutral so it can not be accelerated until it is ionized.

2.1.1 Production of H^- ions

Figure 2.2 is a diagram to explain how H^- ions are made. The negative molybdenum cathode (Mo) and positive anode result in an electric field. Hydrogen atoms are sent into this electric field and an electron is stripped away from a hydrogen atom. Protons congregate on the surface of the cesium cathode. Cesium is added to lower the surface work function of the cathode thereby increasing the electron capture probability. Proton captures an electron

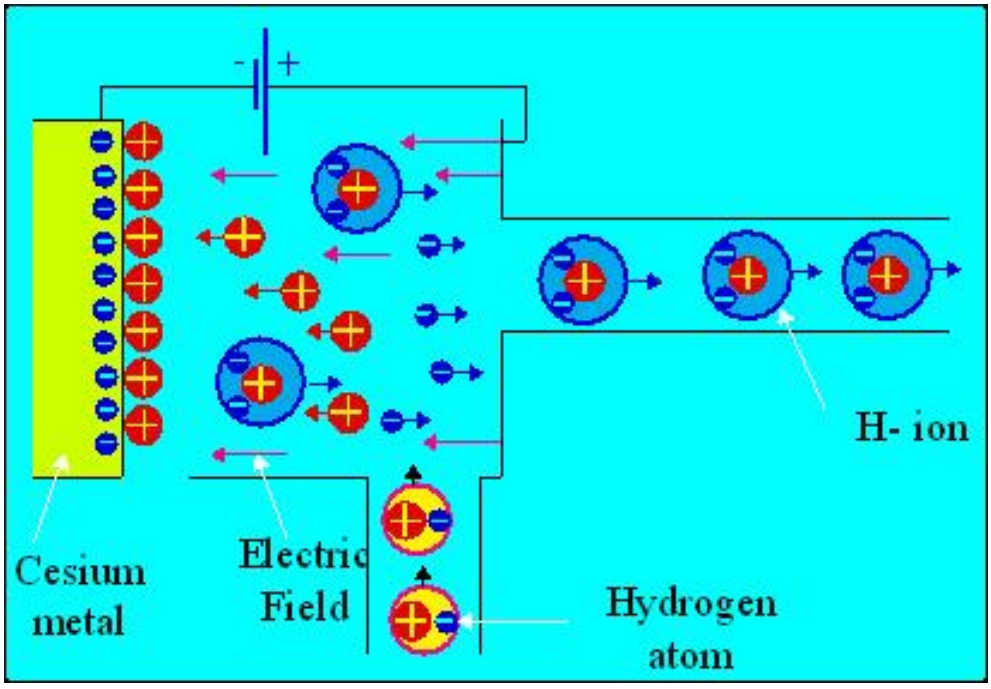

Figure 2.2: Producing H^- ions [19].

from the cathode easily and occasionally, an incoming proton smacks a proton which captured two electrons off the metal wall. Due to the negative charge of ionized hydrogen, the H^- ions go away from the cathode surface [19].

2.1.2 Pre-accelerator

The Pre-accelerator is designed to produce and accelerate the negatively charged hydrogen (H^-) to an energy of 750 keV. It ionizes hydrogen gas to negatively charged hydrogen gas. Ionized hydrogen gas is housed in the electrically charged dome. A potential of -750 kV is applied to the dome. The Cockcroft-Walton accelerator supplies a 750 kV DC voltage, which is voltage multipliers consisting of capacitors and diodes, and the maximum voltage is restricted by how much air can stand off before sparking. It generates a potential of -750 kV between the dome and the grounded wall. The ionized hydrogen gas has an energy of 750 keV while it is accelerated from the charged dome to the grounded wall. Every 66 millisecond, the Pre-accelerator repeats acceleration of beam. After the ionized hydrogen gas exits Cockcroft-Walton accelerator, it passes through a transfer line and then enters the Linac [18].

2.1.3 Linac

Linac is the Linear Accelerator which takes the hydrogen ions with an energy of 750 keV from the Pre-Accelerator and then accelerates the ions to an energy of 400 MeV. The Linac consists of the drift tube Linac (DTL) and the side coupled cavity Linac (SCL). The drift tube Linac has five RF stations and the side coupled cavity Linac has seven RF stations. Figure 2.3 explains how negatively charged hydrogen ions are accelerated in the DTL.

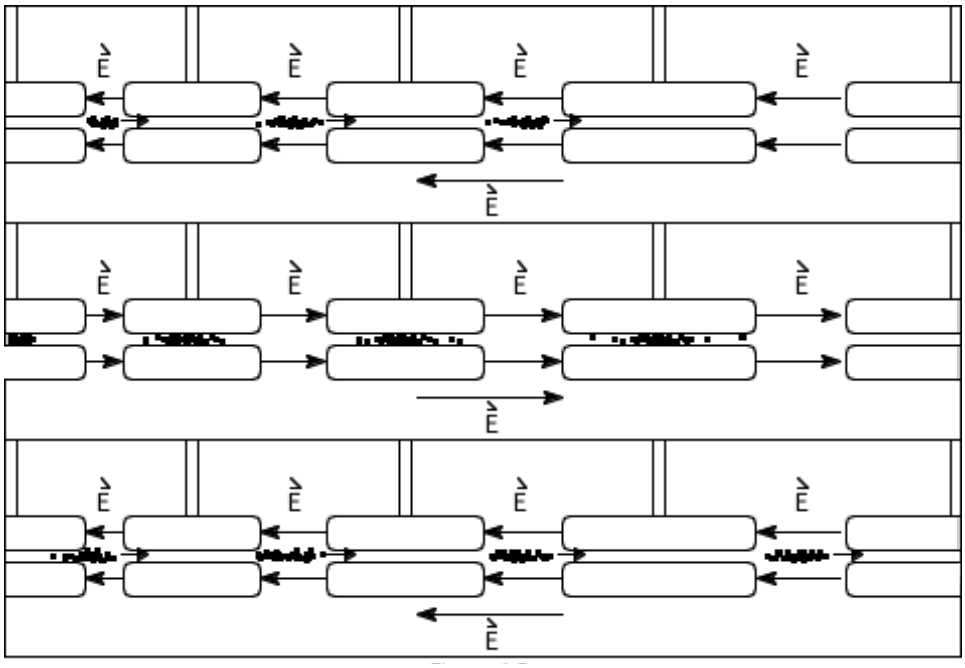

Figure 2.3: The drift tube Linac (DTL) [20].

When H^- ions are passing the gap between drift tubes, the electric field vector is pointing in the direction to accelerate H^- ions and when the H^- ions traverse in the interior of the drift tubes, the drift tubes shields the electric field which is in the deceleration direction. The H^- ions get increased energy and velocity whenever they cross every gap. The 5 drift tube cavities accelerates H^- ions beam to an energy of 116 MeV. Figure 2.4 (a) is a general diagram for the side coupled cavity Linac.

Each side coupled cavity module is comprised of 4 sections. Each section contains 16 accelerating cells and 15 coupling cells. Each accelerating cell is coupled to other cells in the module. The module contains several separate cavities. Figure 2.4 (b) is a diagram which

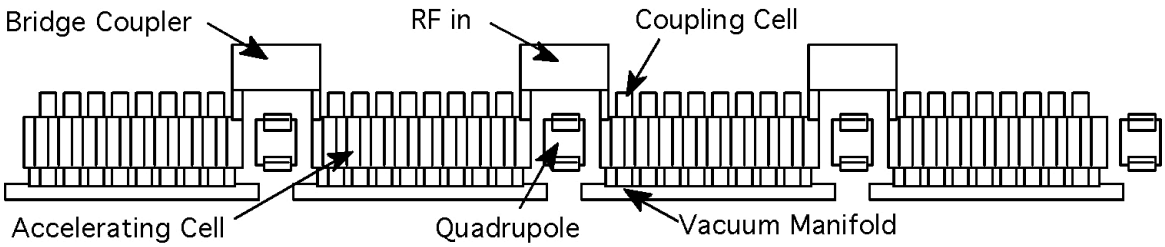

(a) The side coupled cavity Linac(SCL)

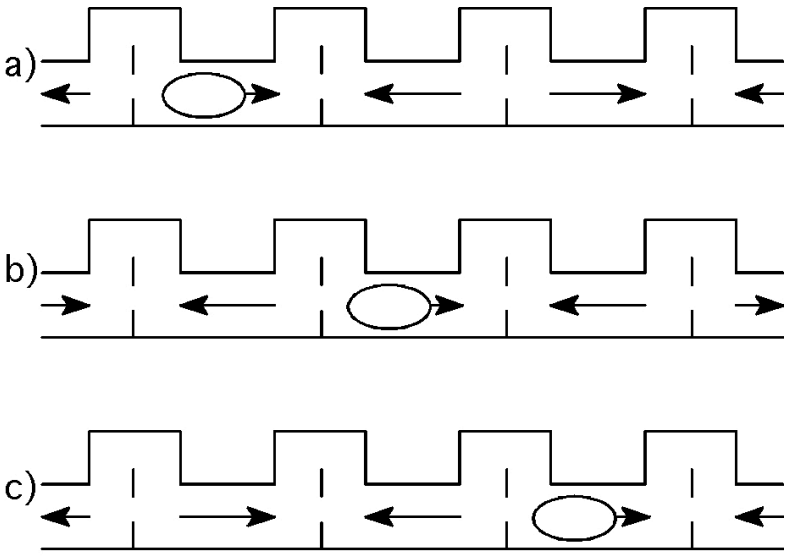

(b) The acceleration of beam in the cells of SCL

Figure 2.4: The side coupled cavity Linac (SCL) [20].

briefly explains how the side coupled cavity Linac accelerates beam. When beam enters the first accelerating cell, the field points in the direction to accelerate beam. While beam is passing between accelerating cells, the field direction changes into the other direction and the field direction of second accelerating cell is ready to accelerate beam. As beam enters the second cell, the beam is accelerated by the field while the field of the first cell is in the decelerating direction. Also, no beam goes into the first cell so there is nothing to be decelerated in the first cell. While the beam passes through the cavities, beam is accelerated by the field. The side coupled cavity Linac receives 116 MeV beam and accelerates beam to an energy of 400 MeV. The difference between DTL and SCL is to use different resonating frequencies. The 201 MHz RF signal is used to accelerate beam in the DTL but the SCL uses 804 MHz ($= 4 \times 201$ MHz).

After H^- ions go through the Linac, 750 keV of H^- ions are accelerated to 400 MeV [20].

2.1.4 Booster

Booster is the first circular accelerator (synchrotron) in the chain of accelerators. The circumference of the Booster is 475 meters. It is made up of 96 magnets in a series of 24 repeating periods with 17 RF cavities interspersed. The negatively charged hydrogen ions with 400 MeV are sent to the Booster and H^- ions are merged with protons circulating in the Booster since they have opposite charge. While the combined beam pass through a carbon foil, the electrons of H^- ions are stripped off and only proton bunches exist in the Booster. The RF cavities accelerate the protons up to 8 GeV. The protons with an energy of 8 GeV are transferred to the Main Injector [18].

2.1.5 Main Injector

The Main Injector is a synchrotron whose circumference is seven times the Booster circumference. The Main Injector has 18 accelerating cavities. 8 GeV protons transferred from the Booster are accelerated to either 120 GeV or 150 GeV by the Main Injector. In the case that beam is injected to the Tevatron, the Main Injector accelerates beam to 150 GeV. When it stacks antiproton or sends beam to NuMI, beam is accelerated up to 120 GeV. The Main Injector can accept antiprotons from Antiproton Source as well as protons from the Booster [18].

2.1.6 Antiproton Source

The Antiproton Source is made up of a Target station, Debuncher and Accumulator and the transport lines between Debuncher and Accumulator and the Main Injector. The target station accepts 120 GeV protons from the Main Injector. A beam of 120 GeV protons strike a nickel alloy target every 1.5 sec. These 120 GeV protons striking the nickel alloy target create a spray of secondary particles. Only about twenty 8 GeV antiprotons are produced for one million protons on the target. A Lithium lens focuses the beam containing many different particles as well as antiprotons. The bend magnet distinguishes 8 GeV antiprotons from the

spray of secondary particles (Figure 2.5). These antiprotons are transferred to the Debuncher.

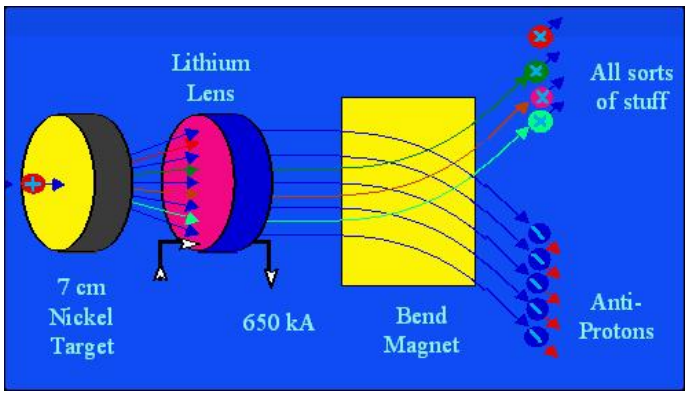

Figure 2.5: The target station [21].

The Debuncher is outer one of the two synchrotrons which have rounded triangular-shape in Figure 2.6, and its mean radius is 90 meters. It accepts not only 8 GeV antiprotons from the target station but also 8 GeV proton from Main Injector for beam studies. The Debuncher captures the large energy spread antiprotons which come off the target and changes them into narrow energy spread antiprotons. Antiprotons are cooled by the Debuncher to make them more manageable and transferred to the Accumulator. The Accumulator is a triangular-synchrotron whose radius is 75 meters. It stores antiprotons at 8 GeV until generated antiprotons are a sufficient amount to be transferred into the Main Injector [18].

2.1.7 Tevatron

Tevatron is a circular synchrotron with a radius of 1 km. It receives both protons and antiprotons from Main Injector and its eight accelerating cavities accelerate them from 150 GeV to 980 GeV. It make collisions with a center of mass energy 1.96 TeV. Superconducting niobium/titanium alloy magnets produce a magnetic field of 4.2 Tesla to bend proton and antiproton beams along the circumference and are needed to maintain cold temperature ($\tilde{4}$ K). 36 bunches of both protons and antiprotons travel in the beam pipe in opposite directions and share the same beam pipe. Proton and Antiproton beams collide at DØ and CDF with 396 ns time interval [18].

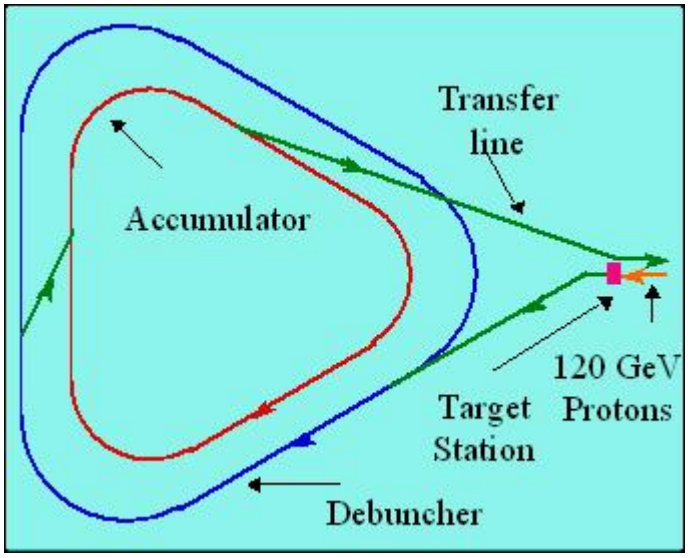

Figure 2.6: The target station [21].

Luminosity can be defined as a measurement of the rate of particle interactions, which refers to the chance that a proton and an antiproton make a collision. Luminosity gives how many proton-antiproton inelastic scattering occur per unit area per unit time ($\mathrm{cm}^{-2}\mathrm{s}^{-1}$). The RunII project began in 2001. The RunII operation is divided into two periods, RunIIa and RunIIb. RunIIa achieved 1.0 fb^{-1} until April 2006 and RunIIb began in June 2006 and data are being taken as of January 2011. Fig. 2.7 shows that the Tevatron delivered an integrated luminosity 10.08 fb^{-1} and DØ recorded 9.01 fb^{-1}.

2.2 DØ Detector

This section is written based on Reference [17]. The DØ experiment is designed to study high mass states and large p_T phenomena. The DØ experiment has lead to the top quark discovery and measurement of top quark mass, the measurement of the W boson mass and search of new phenomena using the DØ detector. The DØ detector consists of several major subdetector systems such as central tracking detectors, uranium/liguid-argon calorimeters, and a muon spectrometer.

Figure 2.8 shows an overview of the DØ detector system which is viewed from inside the Tevatron ring. The central tracking detectors are located on top of the beam line, a

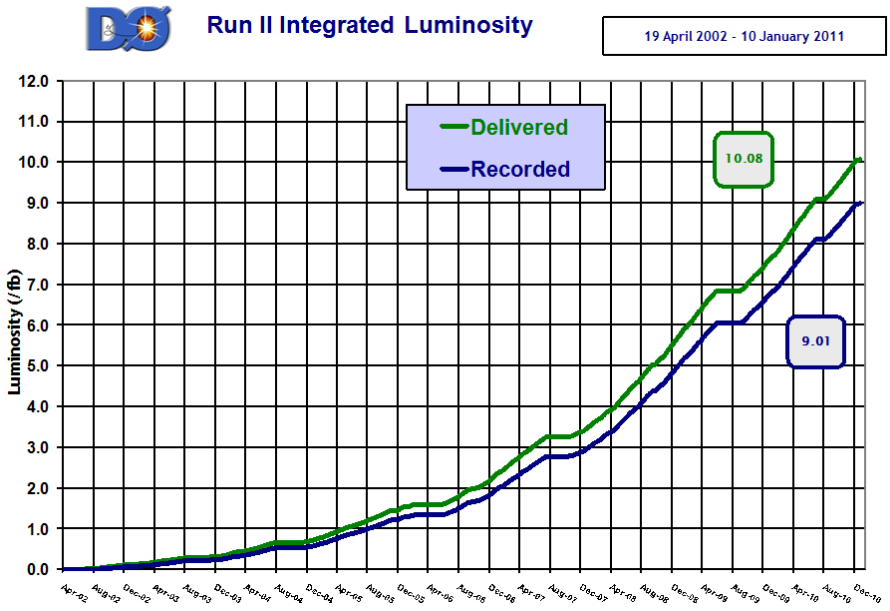

Figure 2.7: Integrated luminosity delivered and recorded to DØ during RunII (April 2002 - January 2011) [22].

solenoid magnet wraps the central tracking systems and forms a magnetic field of ∼2 T, the calorimeter is outside the solenoid, the toroidal magnet lies between the calorimeter and the muon spectrometer system, and the muon detector is located at the outermost DØ detector system. In this section, subdetectors forming the DØ detector are introduced.

2.2.1 Coordinate System

The coordinate system of the DØ experiment is right-handed. The positive z-axis is set to the direction that the protons travel, the y-axis is upward and the x-axis points outward from the center of Tevatron. The cartesian coordinate system (x, y, z) can be converted to the spherical coordinate system (r, θ, ϕ) and it is useful through this analysis.

$$\begin{aligned} r &= \sqrt{x^2 + y^2} \\ \theta &= \arccos\left(\frac{z}{\sqrt{x^2 + y^2 + z^2}}\right) \\ \phi &= \arctan\left(\frac{y}{x}\right) \end{aligned} \tag{2.1}$$

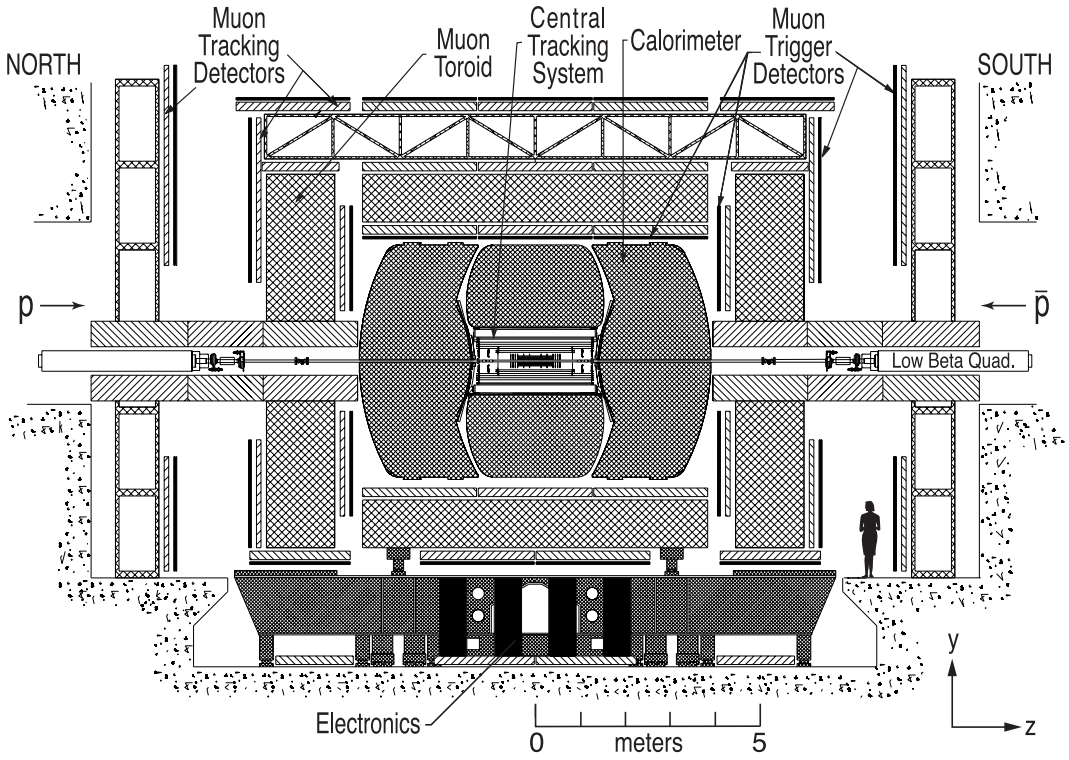

Figure 2.8: Diagram of the upgraded DØ detector for Run II operation. It is drawn as viewed from inside the Tevatron ring [17].

where the θ and ϕ are the polar and azimuthal angles, respectively. Using pseudorapidity is more convenient than using the polar angle for relativistic particles. It is defined:

$$\eta = -\ln\left[\tan\left(\frac{\theta}{2}\right)\right] \tag{2.2}$$

where θ is referred to the angle that the momentum $\vec{p}$ and the beam axis form. The pseudorapidity can be approximated to the true rapidity for the particle which travels close to the speed of light, namely at the regime that the particle mass is nearly as small as zero.

$$\eta = \frac{1}{2}\ln\left[\frac{E+p_z}{E-p_z}\right] \tag{2.3}$$

In a proton-antiproton collision, the inelastic collision point can be moved along the beam pipe. There exists a big difficulty to measure the z component of a particle momentum. Therefore transverse momentum and energy are more convenient to use, which are the projection of momentum and energy onto the x-y plane perpendicular to the z-axis (the beam axis). They

can be written as:

$$\begin{aligned} p_T &= p \cdot sin\theta \\ E_T &= E \cdot sin\theta \end{aligned} \tag{2.4}$$

2.2.2 Central Tracking Detectors

The central tracking system consists of the Silicon Microstrip Tracker (SMT) and the Central Fiber Tracker (CFT), which are the innermost detectors of the DØ detector. A superconducting solenoidal magnet generates a magnetic field of 2.0 T and surrounds the central track system. When charged particles pass through the tracker, the SMT and the CFT find their helical trajectories and their momentum can be measured using information about helical trajectories and magnetic field. These tracking detectors have an ability to measure the

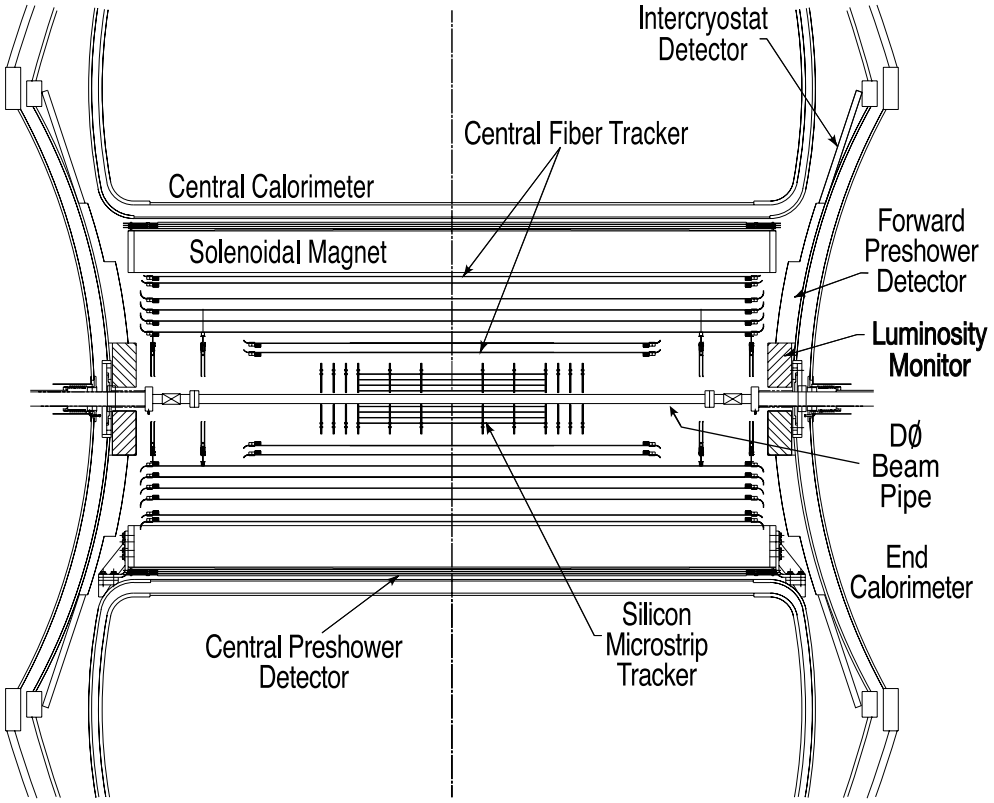

Figure 2.9: The view of the central tracking system [17].

position of the primary inelastic interaction vertex with a resolution about 35 μm along the

beamline. They are able to tag jets originating from b-quark decay with an impact parameter resolution of better than 15 μm in the r-ϕ plane for particles whose transverse momentum p_T is greater than 10 GeV/c at $|\eta| = 0$. Figure 2.9 shows the cross-sectional view of the central tracking system.

Silicon Microstrip Tracker (SMT)

The SMT establishes tracks of charged particles and finds vertices. It covers nearly all η range that calorimeter and muon detector cover. The SMT is made up of 12 F-disks, 4 H-disks and 6 barrels. The barrel detectors measure the r-ϕ coordinates of particles at small η and the disk detectors measure r-z and r-ϕ coordinates at high η.

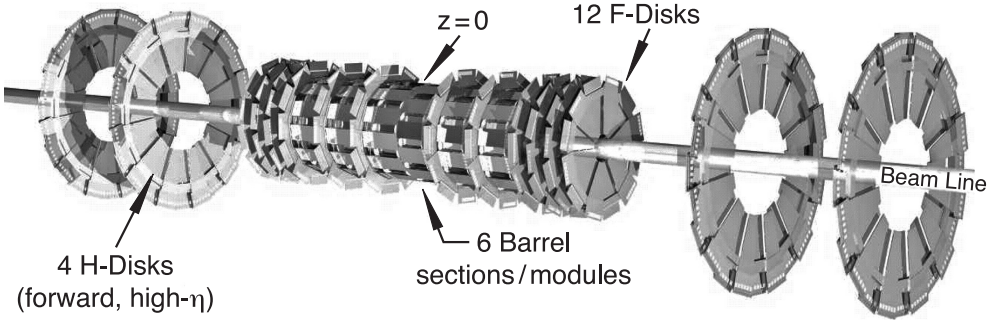

Figure 2.10: A 3-D view of the Silicon Microstrip Detector [17].

Figure 2.10 shows a 3-D view of the SMT. In 6 barrels, each barrel consists of four silicon readout layers. Each silicon module is called "ladder" and 12 ladders are in each layer 1 and 2. Each layer 3 and 4 is made up of 24 ladders. A total of 432 ladders are 2.7 cm $< r <$ 10.5 cm and $|z| <$ 38 cm. Twelve double-sided wedges make up of one F-disk and the F-disks are located at $|z|$=12.5, 25.3, 38.2, 43.1 48.1 and 53.1 cm. At $|z|$=100.4, 121.0 cm, large-diameter disks, called H-disks, are placed to track charged particles which travel high $|\eta|$ region. Each H-disk has 24 full wedges mounted on it and each wedge is comprised of two back-to-back single-sided wedges. The axial hit resolution is 10 μm and the z hit resolution is 35 μm.

Central Fiber Tracker (CFT)

The CFT is placed in the radial space from 20 to 52 cm from the center of the beam pipe. The

CFT consists of eight concentric support cylinders on which scintillating fibers are mounted. Two inner cylinders and six outer cylinders are 1.66 m and 2.52 m long, respectively. The outer cylinder covers $|\eta| \lesssim 1.7$. Each cylinder has two doublet layers. One doublet layer of fibers is parallel to the beam direction and the second doublet layer is at a stereo angle of $\pm$ 3° The scintillating fibers are connected to fiber waveguides that transport the scintillation light to visible light photon counters (VLPCs) for read out. The fiber diameter is 835 μm and the doublet layer made of this fiber gives a resolution of about 100 μm.

2.2.3 Calorimeter

"A calorimeter is designed for the total absorption of a particle's energy, that is, a particle enters, interacts, its secondaries reinteract, and so on, until all byproducts are reduced by dE/dx to zero energy [23]." With this principle, the DØ calorimeter provides energy measurement of electrons, photons and jets. Also, it plays a role to help electrons, photons, jets, and muons be identified and the transverse energy balance be measured.

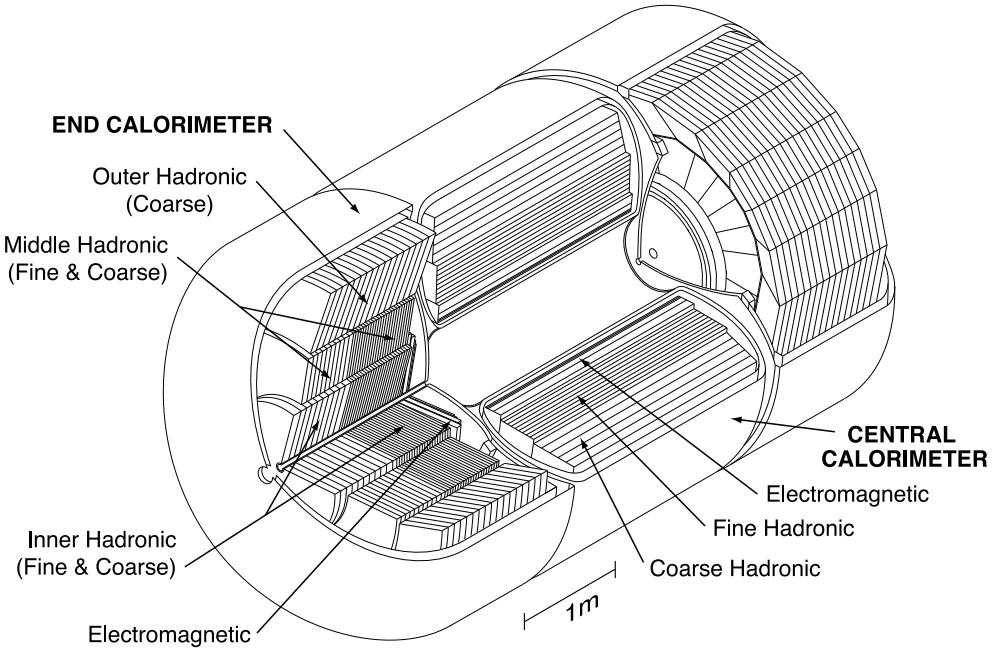

Figure 2.11: Isometric view of the central and two end calorimeters [17].

The central and two end calorimeters are shown in Figure 2.11. The central calorimeter

(CC) covers $|\eta| \lesssim 1.0$ and the coverage of two end calorimeters (EC) is extended to $|\eta| \approx 4$. An electromagnetic section and hadronic section consisting of fine and coarse spatial segmentation are contained in each central and end calorimeter. Each of CC and EC calorimeter is placed within its own cryostat that keeps the temperature of detector at approximately 90 K. The intercryostat detector (ICD) is installed to minimize the degradation of the energy resolution in the region between the central and end calorimeters ($0.8 < |\eta| < 1.4$). The electromagnetic calorimeter is made from thin depleted uranium plates (3 or 4 mm in the CC and EC, respectively). The find hadronic (FH) sections are built with 6-mm-thick uranium-niobium (2%) alloy. The coarse hadronic (CH) modules are made from 46.5-mm-thick plates of copper in the CC and stainless steel in the EC.

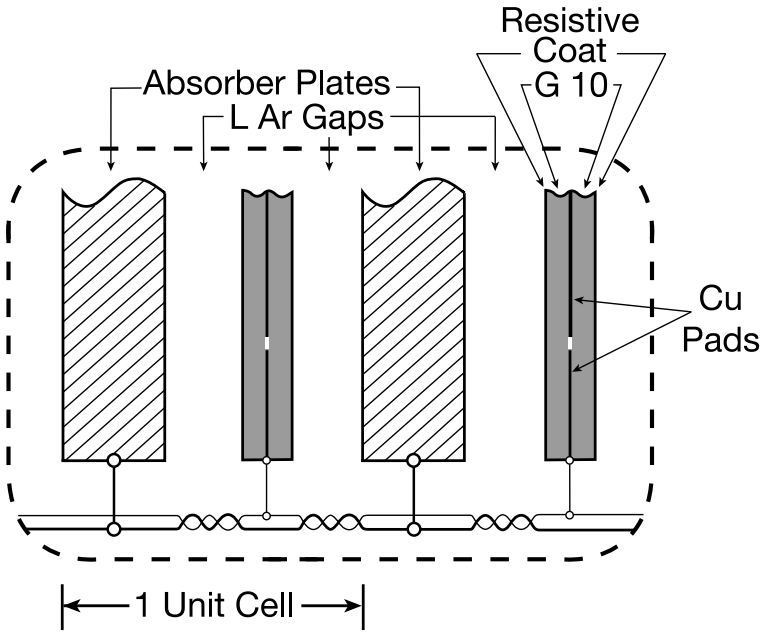

Figure 2.12: Unit cell consisting of the liquid argon gap and signal board for the calorimeter [17].

A schematic view of the unit cell for the calorimeter is shown in Figure 2.12. In the CC, 4 EM readout layers, 3 FH layers and 1 CH layer are built by the combination of the cells. EC consists of 4 EM layers, 4 FH layers and 1 CH layer. The readout cells, called "Tower", in the EM, FH and CH layers cover $\delta\eta \times \delta\phi = 0.1 \times 0.1$ but the third layer of the EM calorimeter at the EM shower maximum covers $\delta\eta \times \delta\phi = 0.5 \times 0.5$ to measure more precise location of EM

shower centroid.

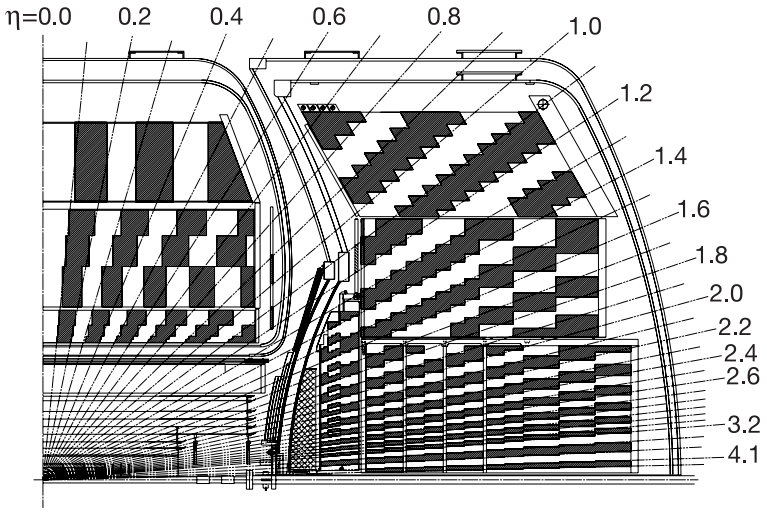

Figure 2.13: Schematic view of the DØ calorimeters showing the transverse and logitudinal segmentation pattern [17].

Figure 2.13 shows the transverse and longitudinal segmentation pattern. The shading pattern is groups of cells for signal readout. The numbers and rays indicate pseudorapidity intervals from the center of detector.

2.2.4 Muon Detector

The central muon system consists of proportional drift tubes (PDTs), toroidal magnets and central scintillation counters. It provides coverage for $|\eta| \lesssim 1.0$. The forward muon systems used mini drift tubes (MDTs), scintillation counters and beam pipe shielding and extends the coverage for muon detection to $|\eta| \approx 2.0$.

Figure 2.14 and 2.15 show exploded view of the muon wire chambers and scintillation detectors. In the central muon system, a toroidal magnet generates a magnetic field of 1.9 T in the iron absorber and PDTs of A layer are located under the central toroidal magnet and B, C layers are outside of the toroid. The PDTs measure the electron drift time and the charge deposition to determine the hit position along the wire. They give a drift distance resolution of $\sigma \approx 1$ mm. In the forward muon system, end toroidal magnets produce approximately 2.0

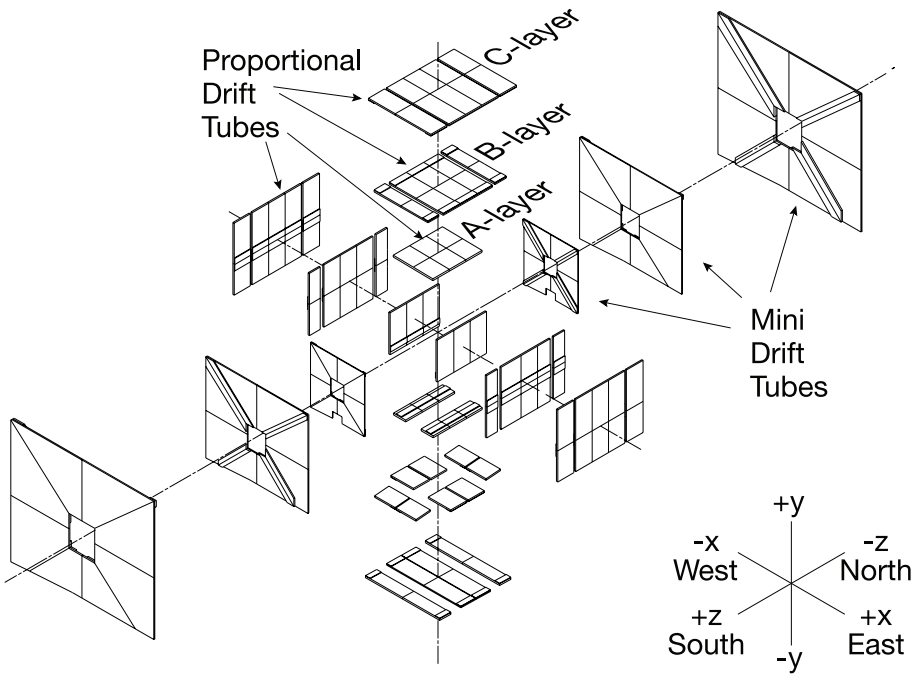

Figure 2.14: Exploded view of the muon wire chambers [17].

T and the MDTs of A layer are arranged inside toroidal magnets, and those for B, C layers are located outside the toroidal magnets in order to reconstruct muon tracks. The three layers of scintillation counters are also placed inside (layer A) and outside (layers B and C) of the toroidal magnet to trigger events which include muon. The MDT coordinate resolution is $\sim$ 0.7 mm per hit. The stand-along momentum resolution is $\sim$ 20% for muon momentum below 40 GeV/c, a combination of multiple scattering in the iron and MDT resolution on the bend angle.

2.2.5 Luminosity Monitor

The Tevatron luminosity at the DØ interaction region is determined with the luminosity shown in Figure 2.16. It detects inelastic $p\bar{p}$ collisions, measures beam halo rates and finds the z coordinate of the interaction vertex. Two Luminosity Monitor (LM) counters are placed at north and south. Each LM counter consists of 24 plastic scintillation wedges and 24 photo-multipliers (PMT) mounted on the scintillation wedges for readout. The LM counters provide a coverage of $2.7 < |\eta| < 4.4$ and located at $z = \pm 140$ cm as shown in Figure 2.17.

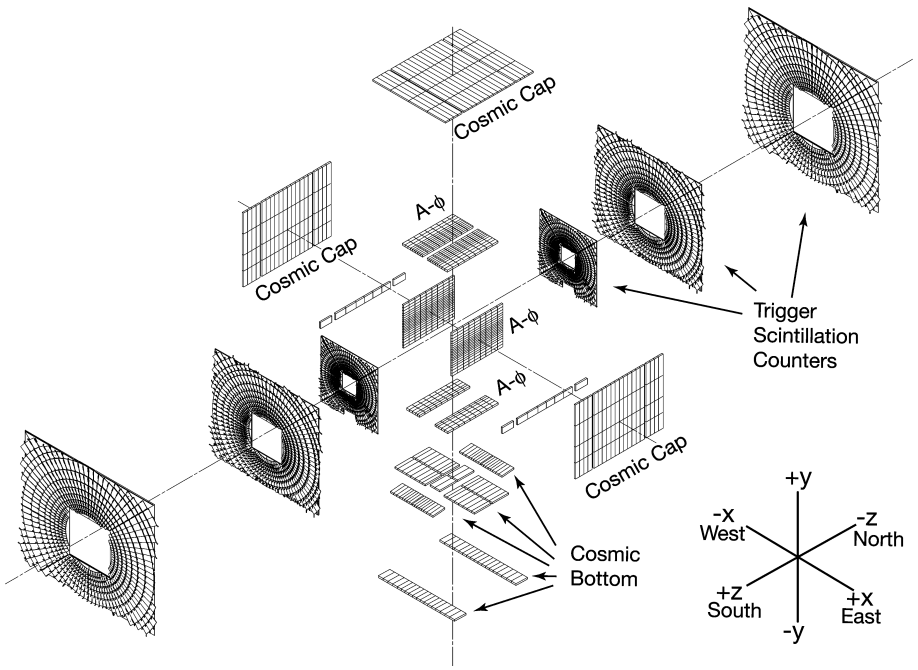

Figure 2.15: Exploded view of the muon scintillation detectors [17].

For accurate measurement of the luminosity, it is necessary to discriminate inelastic $p\bar{p}$ interactions and the beam halo backgrounds. The time-of-flight measurements of particles can separate $p\bar{p}$ interaction from the beam halo. Eq. 2.5 gives the z position of the interaction vertex z_v.

$$z_v = \frac{c}{2}(t_- - t_+) \tag{2.5}$$

where t_+ and t_- are the time-of-flight for particles hitting the LM detectors which are placed at ± 140 cm. Beam halo particles can be removed by requiring $|z_v| < 100$ cm since they give $|z_v| \approx 140$ cm.

The luminosity $\mathcal{L}$ is calculated using the average number of inelastic collisions per beam crossing $\bar{N}_{LM}$ and the effective cross section that takes into account the acceptance and efficiency of the LM detector.

$$\mathcal{L} = \frac{f\bar{N}_{LN}}{\sigma_{LM}} \tag{2.6}$$

where f is the beam crossing frequency.

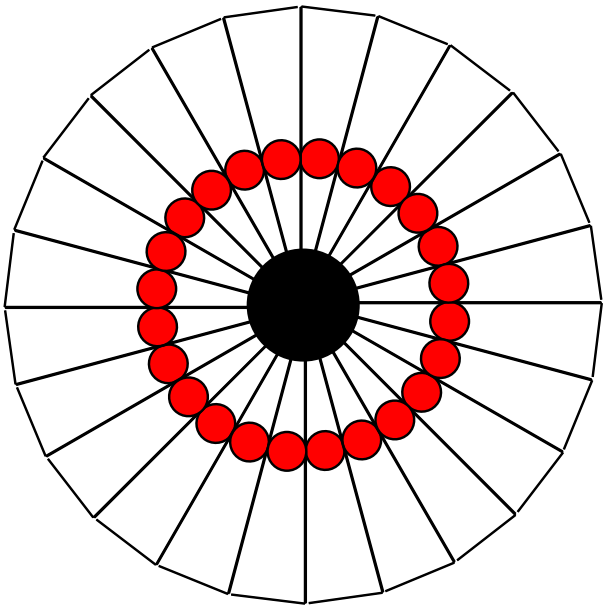

Figure 2.16: The geometry of the luminosity monitor and the location of the PMTs (red solid dots) [17].

2.2.6 Trigger System

In the Tevatron, proton and antiproton collide every 396 ns and the data rate from detector is 1.7 MHz. The initial data from the DØ detector include low p_T background and the DØ data acquisition system cannot record all of 1.7 MHz rate of data due to its limited ability. Thus, it is necessary that data that we are not interested in be filtered and reduced in rate to about 50 Hz so that the DØ data acquisition system can process and record it. We use a three level trigger system, called L1, L2 and L3 (Level 1, Level 2 and Level 3). An overview of the

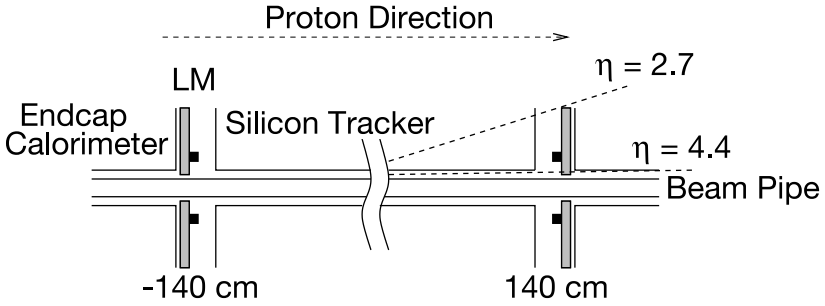

Figure 2.17: The location of the LM detectors [17].

DØ trigger and data acquisition system is shown in Figure 2.18.

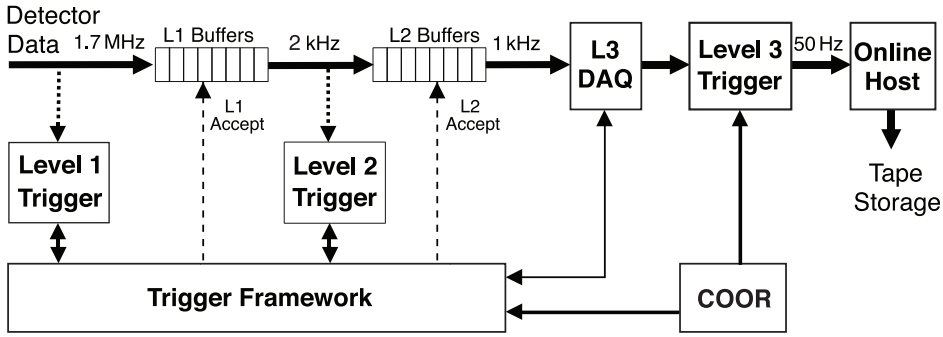

Figure 2.18: Overview of the DØtrigger and DAQ systems [17].

L1 trigger

Hardware trigger elements constitute the L1 trigger. It reduces the initial data rate of 1.7 MHz to 2 kHz. The L1 trigger consists of the calorimeter trigger (L1Cal), the central track trigger (L1CTT) and the muon trigger (L1Muon). The L1Cal decision is made with the trigger inputs which consist of electromagnetic and hadronic trigger tower energies. The trigger tower energies are made up by sums of the deposited energies in $\delta\eta \times \delta\phi = 0.2 \times 0.2$. The L1CTT reconstructs the trajectories of charged particles using data taken by the central fiber tracker and the central and forward preshower detectors in order to make trigger decision. The L1Muon trigger finds patterns consistent with muons using information from muon wire chamber, muon scintillation counters, and tracks from the L1CTT for trigger decision. The Level 1 trigger decision should be made to the trigger framework within 3.5 μs.

L2 trigger

The L1 trigger rate of 2 kHz is input to the L2 trigger. The L2 trigger reduces the L1 trigger rate to a maximum accept rate of 1 kHz. The L2 trigger includes the L2CAL, L2CTT, L2MUO, L2PS (PreShower), L2STT and L2Global systems. The preprocessors of the L2 trigger system reconstructs physics objects collecting and analyzing data from the front-ends and the L1 trigger system to make trigger decisions. The fired L1 triggers are sent to the L2Global

system and the L2Global matches the fired L1 triggers to L2 triggers. This means that if a L1 trigger is matched to a related L2 trigger, the L2 trigger will be passed.

L3 trigger and L3DAQ

The L3 trigger receives candidates passed through the L1 and L2 triggers and it reduces the 1 kHz input rate to 50 Hz so that events can be recorded for offline analysis. A farm of microprocessors constitutes the L3 trigger. It performs a limited reconstruction of physics objects in events and reduces the input rate. The L3 trigger decision is made based on complete physics objects and the relationships between objects. Input, event building and output take 15 ms per event. Unpacking, reconstruction and filtering take about 235 ms. The L3DAQ system transports detector component data from the VME readout crates to the L3 trigger filtering farm. The bandwidth of the L3DAQ is 250 MB/s and it corresponds to an average event size of about 200 kB at an L2 trigger accept rate of 1 kHz.

More detail information about DØ detectors is in Reference [17].

CHAPTER 3. Object Reconstruction and Correction for Monte Carlo Simulation

In high energy physics experiments, we discover a new particle, or study the properties of fundamental particles, through its, or their, final state objets such as electron, muon, tau, jet, missing transverse energy $\not\!\!E_T$, tracks and primary vertices. The physics objects are detected by the detectors and reconstructed using information from detectors. This chapter describes algorithms to reconstruct and identify physics objets in DØ.

3.1 Track Reconstruction

When charged particles pass through the SMT and CFT under the magnetic field produced by the solenoid, they leave trajectories that are the shape of helical trajectories. Charged particles generate electric signals through ionization process, called hits, when they traverse silicon strips of the SMT and scintillation fibers of the CFT. Hits from adjacent silicon strips or scintillating fibers form a cluster. These hits are used to reconstruct tracks using a track algorithm. A global track reconstruction (GTR) algorithm combined with the Histogramming Track Finding (HTF) [24] and the Alternative Algorithm (AA) [25, 26] constitutes the track finding. The HTF is the method to reduce the number of possible combinations of the hits with the Hough transformation. Figure 3.1 shows an example of the histogramming technique using the Hough transformation for a single 1.5 GeV muon track with 5 hits. The Hough transformation transforms the hits in (x, y) plane into (ρ, ϕ) plane. The Hough transformation makes random combinations of hits distributed uniformly but produce a peak for a track candidate by the hits in the ϕ vs ρ histogram. The result from the HTF is processed with a 2D Kalman filter to discard fake tracks and find precise track parameters. The Alternative

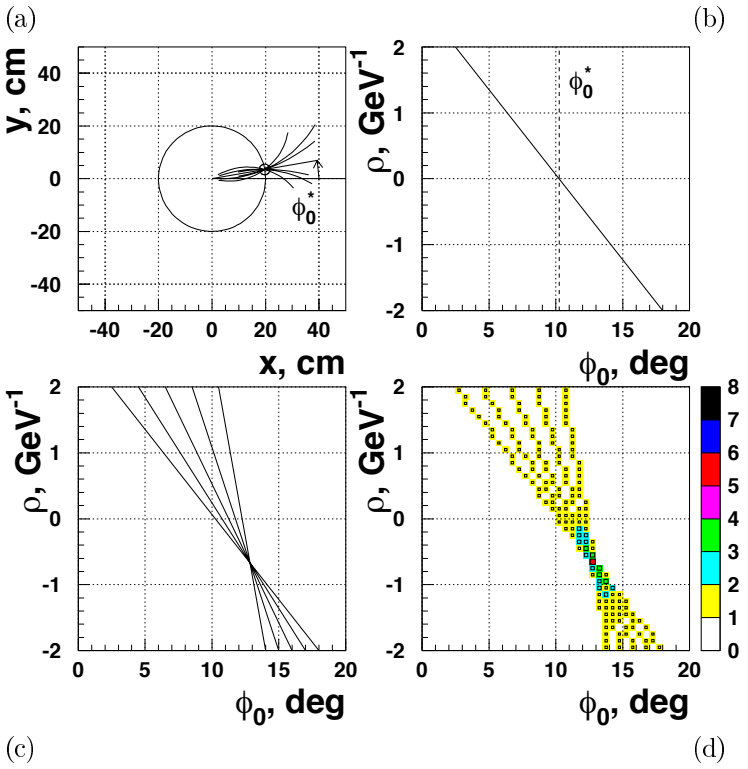

Figure 3.1: The histogramming technique for a single 1.5 GeV muon track with 5 hits. (a) The family of trajectories passing through the hit at radius r=20 cm . (b) This family of trajectories corresponds to the line in (ρ, ϕ) coordinate. (c) All five hits can be transformed to five lines and these five lines are crossed in one point. (d) A peak is seen at the point of intersection in the (ρ, ϕ) histogram [24].

Algorithm (AA) keeps the track reconstruction efficiency high and suppresses the rate of fake tracks with pattern recognition. Both low and high momentum tracks are reconstructed by the AA. The AA constructs all possible combinations of 3 hits from the SMT layers and hits in the next layer of the SMT or CFT are extrapolated using possible track candidates. Hits associated with the track candidates can be found by the χ^2 requirement. If the number of hits is less than 3 in the SMT, the AA finds "CFT only" tracks.

3.2 Primary Vertex Reconstruction

The Primary Vertex (PV) is the interaction point where the inelastic $p\bar{p}$ collision occurs. Its position information is very important quantity to calculate kinematic variables in particle

physics experiment. The primary vertex reconstruction and identification is performed by the adaptive vertex fitting which consists of the three steps [27]: 1. Track selection, 2. Vertex fitting, 3. Vertex selection. The requirements for track selection are to have $p_T > 0.5$ GeV/c^2 and 2 or more SMT hits. Tracks must belong to the same interaction. The z-clustering algorithm clusters tracks within 2 cm of each other. This clustering identifies whether tracks come from a same interaction or different interactions. First, the Kalman Filter vertex fitting algorithm determines the location and width of the beam. The Kalman Filter vertex fitting algorithm removes tracks with the largest χ^2 contribution to the vertex in turn until the total vertex χ^2 per degree of freedom becomes smaller than 10. This fits all selected tracks within each z-cluster into a common vertex and determines the location and width of the beam. Second, tracks in each z-cluster are selected by the distance of closest approach (dca) to the beam spot requirement. The position and error of the beam spot are determined in the previous step and the dca to the beam spot cut requires $dca/\sigma(dca) < 5$. Tracks that pass this selection are fitted into a common vertex using the adaptive fitting algorithm. The adaptive fitting algorithm reweights track errors with the function 3.1

$$w_i = \frac{1}{1 + e^{(\chi_i^2 - \chi_{cutoff}^2)/2T}} \tag{3.1}$$

where χ_i^2 is the χ^2 contribution of track i to the vertex, χ_{cutoff}^2 is the χ^2 contributio to the vertex where the weight function drops to 0.5 and T is a parameter that controls the sharpness of the function. The third and last step is the vertex selection. The hard-scatter vertex is selected by the minimum bias probability selection algorithm [28].

3.3 Electron Reconstruction

An electron produced from some physics process flies through the tracking system and stops in the ElectroMagnetic (EM) calorimeter. While it flies through the tracking system, it leaves traces in the SMT and CFT and these traces can be reconstructed as the track of the electron. In addition, when electron enters the calorimeter, its energy is deposited in the calorimeter and it is fully absorbed. Track matching with energy cluster in the calorimeter distinguishes electron from photon since photon which is neutral does not leave hits in the tracking system.

Thus, these two features can be used to reconstruct electrons. The energy deposits of electron in the calorimeter are reconstructed as towers in the $\eta \times \phi$ space. These towers are sorted by E_T. The highest E_T tower is defined as a seed. Then, all towers within a cone of $\Delta R < 0.2$ around a seed are added and become an EM cluster. Parameters for each EM cluster derived with calorimeter information and track matching are used to identify electrons.

1. EM fraction (f_{em}): This is defined as the energy ratio of the cluster in the EM calorimeter to the total energy deposited in the calorimeter.

$$f_{em} = \frac{E_{em}(\Delta R < 0.2)}{E_{tot}(\Delta R < 0.2)} \tag{3.2}$$

   EM clusters in this analysis are required to have EM fractions larger than 0.9 ($f_{em} > 0.9$).

2. Isolation: EM objets should be isolated in η space. A variable for isolation of EM objets is defined as Eq. 3.3

$$f_{iso} = \frac{E_{tot}(\Delta R < 0.4) - E_{em}(\Delta R < 0.2)}{E_{em}(\Delta R < 0.2)} \tag{3.3}$$

   where $E_{em}(\Delta R < 0.2)$ is the energy of EM object within $\Delta R < 0.2$ and $E_{tot}(\Delta R < 0.4)$ is the total energy deposited in the calorimeter within $\Delta R < 0.4$. $f_{iso} < 0.15$ is required.

3. The χ^2 of H-matrix: The shower development of an electron in the calorimeter is different from hadronic particles. A 7×7 H-matrix quantifies how the shower development of a EM object is similar to an electron. It is computed using seven correlated variables: the fraction of energy in each of the four EM layers, the shower width in ΔR, the log of the total shower energy, the z position of the primary vertex. The χ^2 of the H-matrix (χ^2_{Hmtx}) is required to be smaller than 50 ($\chi^2_{Hmtx} < 50$).

4. Track matching: One reconstructed track with $p_T > 5$ GeV/c must match to an EM cluster in the third EM layer within $\Delta\eta \times \Delta\phi < 0.05 \times 0.05$. For this matching, χ^2_{EM-trk} is established as Eq. 3.4 and calculated using the difference between the track and the EM cluster in the third EM layer in ϕ and z coordinates as well as the square of the significance for the transverse energy of the EM cluster over the transverse momentum

of the track.

$$\begin{aligned} \chi^2_{EM-trk} &= \left(\frac{\Delta\phi}{\sigma_\phi}\right)^2 + \left(\frac{\Delta z}{\sigma_z}\right)^2 + \left(\frac{E_T/p_T - 1}{\sigma_{E_T/p_T}}\right)^2 \\ &= \chi^2_{spatial} + \left(\frac{E_T/p_T - 1}{\sigma_{E_T/p_T}}\right)^2 \end{aligned} \tag{3.4}$$

The χ^2 probability $P(\chi^2_{EM-trk})$ should be larger than zero in this analysis.

5. Electron Likelihood: The likelihood ratio for electron is defined as Eq. 3.5

$$\mathcal{L} = \frac{P_{sig}(x)}{P_{sig}(x) + P_{bkg}(x)} \tag{3.5}$$

where P_{sig} and P_{bkg} are the probabilities for EM clusters to be signal and background, respectively. This is calculated with 7 variables: EM fraction, the fraction of the transverse energy of the cluster in the calorimeter over the transverse momentum of the matched track, H-matrix, the χ^2 probability of track matching, distance closest approach, the total number of track within a cone of $\Delta R < 0.05$, and sum of p_T of all tracks. This analysis requires $\mathcal{L} > 0.85$.

If an EM object satisfies the criteria 1, 2, 3 and 4, this EM object is defined as a "loose isolated" (Top_loose) electron. A "tight isolated" (Top_tight) electron passes all of the five criteria in the above [47, 60, 66].

For Monte Carlo events, the electron selection efficiency is different from that in data. The scale factors to correct this difference are derived in [30] and parameterized in detector η and ϕ. The selection efficiencies in MC for both Top_loose and Top_tight are corrected by scale factors.

3.4 Muon Reconstruction

The muon reconstruction and identification are performed using information from the central tracking and muon systems. The muon detector provides the identification of muon. The central tracking system measures the muon momentum precisely and finds muon tracks with a high efficiency in the angular region which is comparable to that of the muon detector. When

a muon passes through the muon system, the muon leaves wire and scintillator hits in A, B, C layers. These wire hits form track line segments and if there exist matched scintillator hits for these segments, this track line is identified as a "local" muon. Then, this local muon has to be matched to a track reconstructed by the central tracking system. This muon is called a central track-matched muon. In this analysis, central track-matched muons are required. A muon can be classified into different qualities of muon in accordance with the number of hits in the muon system and the quality of matched track. This analysis uses "MediumNseg3" muon which requires the following criteria:

- $n_{seg} = 3$ requires that the "local muon" must have hits in all of A, B and C layers.
- The "medium" muon quality requires (1) at least two wire hits and one or more scintillator hits in the A layer, and (2) at least two wire hits and at least one scintillator hit in the B or C layer.
- To veto cosmic muons, the time of flight between the hard scattering and the A layer should be less than 10 ns ($t_A < 10$ ns) and that between the hard scattering and the BC layers has to be less than 10 ns ($t_B < 10$ ns and $t_C < 10$ ns).
- The muon must be a central track-matched muon.
- The quality of the central track match is "trackmedium" which requires that the dca (distance of closest approach) in (x, y) between the track and the primary vertex must be smaller than 0.04 cm ($|dca| < 0.04$ cm) if there is at least one SMT hit, or $|dca| < 0.2$ cm if there is no SMT hit. $\chi^2/ndf < 4$ is required, where χ^2/ndf comes from the central track fitting.
- The muon must be isolated. To find isolated muon, the ΔR between the central track of muon and any of the good jets with corrected $p_T > 15$ GeV/c must be bigger than 0.5 ($\Delta R > 0.5$). This is called "deltaR" isolation.

These requirements in the above are to select "loose isolated muons". By fulfilling the following additional criteria, "tight isolated muons" can be selected, which is referred to "Top-

ScaledTight".

- $\mathcal{I}^{cal}_{0.1<\Delta R<0.4}/p_T < 0.1$: $\mathcal{I}^{cal}_{0.1<\Delta R<0.4}$ is the scalar sum of transverse energies of all calorimeter clusters within a hollow cone $0.1 < \Delta R(cluster, \mu) < 0.4$ around the muon track.

- $\mathcal{I}^{trk}_{\Delta R<0.5}/p_T < 0.1$: $\mathcal{I}^{trk}_{\Delta R<0.5}$ is defined as the scalar sum of transverse momentum of all tracks inside a cone of $\Delta R(\mu, track) < 0.5$ around the muon track except the muon track itself. To avoid additional tracks from pile-up, $\Delta z_0(\mu, track) < 2$ cm is required.

All of these criteria are required to select muons for this analysis [31, 47].

For Monte Carlo events, the muon selection efficiency is different from that in data and corrected by the data/MC scale factors derived for the RunIIb1-2 data set [31]. Several scale factors for muon quality, track quality and isolation are considered to correct muon efficiency in MC. For the muon quality, the scale factor is parameterized in the muon η_{det} and ϕ. The scale factor for the track quality is a function of the z position of muon track (z_0) and η_{CFT} and also parameterized in $|\eta_{CFT}|$ and luminosity. The scale factor for the deltaR isolation ($\Delta R(\mu, closest\ jet) > 0.5$) is derived for the parameters luminosity and $|\eta_{CFT}|$. For the Top-ScaledTight isolation, the scale factor is parameterized in $|\eta_{CFT}|$, p_T and $\Delta R(\mu, closest\ jet)$.

3.5 Jet Reconstruction

Quarks and gluons produced with large momentum will emit a gluon and produce quark pair. For this process, there is a relatively large momentum transfer, so that this can be explained perturbatively. As the showering is developed, the process becomes a long-distance interaction which involves the growth of the coupling. This process becomes, and is referred to as, non-perturbative. While this non-perturbative process progresses, the color-charged quarks make groups and they turn into color-neutral hadrons. This process is referred to hadronization and the shower of hadrons is defined as a jet. These hadrons enter into the calorimeter and deposit energy in the calorimeter. Jets are reconstructed by clustering these energy deposits with the Run II cone algorithm [32]. To treat the calorimeter noise uniformly, the T42 algorithm removes the 3D-isolated calorimeter cells which have low energies [33]. After

removing noise cells, the jet algorithm starts grouping remained cells into pseudo-projective towers ($\delta\eta \times \delta\phi = 0.1 \times 0.1$). The towers with $p_T > 1$ GeV are utilized as seeds to seek preclusters. Adding towers within $\Delta R < 0.3$ around the seed towers forms preclusters. Then, protojets are constructed using the preclusters as seeds. A cone of $\Delta R < 0.5$ is constructed around the protojet. All towers within the cone around the protojet are summed together to construct a new protojet candidate until the original and the candidate are inside $\Delta R < 0.001$. This process is fulfilled until no more seeds to consider exist. The next step is to confirm that a tower is not shared with more than one jet. By comparing two jets that overlap, if the low p_T jet shares more than half of its energy with the higher p_T of jet, then the two jets are merged, otherwise, they become two individual jets and shared towers between two jets are assigned to the jet they are closer to. After jets are merged or split, jets with $p_T > 6$ GeV/c are selected [66].

Jets in Monte Carlo have different efficiencies from data for jet reconstruction, jet energy scale, and jet energy resolution. They need to be corrected for:

1. the reconstruction and identification efficiency.
2. the energy resolution in data which is worse than the simulation.
3. different calorimeter response.
4. the vertex confirmation efficiency. The vertex confirmation requires two or more tracks within the jet originated from the primary vertex.

The efficiency correction is performed through shifting, smearing and removal (SSR) procedure [41]. The SSR procedure smears the jet p_T in MC to make worse jet energy resolution as in the data. The jet energy shifting in the SSR procedure is turned on for Monte Carlo samples which have predominant gluon jets but it is turned off for the $t\bar{t}$ sample. This shifting procedure is needed since the Jet Energy Scale is derived using γ+jets sample which has predominant by quark jets. The different jet identification and vertex confirmation efficiencies between data and Monte Carlo are corrected using the scale factors supplied in the packages $jetid\_eff\ v03{-}01{-}03$ for e+jets and $jetid\_eff\ v03{-}01{-}04$ for μ+jets.

Jet Energy Scale

To measure more precise jet momenta, the relationship between the true jet energy and the measured jet energy in the calorimeter, we determine a scale using events with a photon and a jet as final state in order to compensate the energy difference between those two jets. The photon and the jet are produced back to back in the ϕ space. This scale calibrates jets in data and Monte Carlo simulation [34]. The Jet Energy Scale (JES) correction is performed using Eq. 3.6

$$E_{jet}^{corrected} = \frac{E_{jet}^{measured} - E_O}{R_{jet} S_{jet}} \tag{3.6}$$

- $E_{jet}^{corrected}$: the corrected jet energy.
- $E_{jet}^{measured}$: the measured jet energy in the calorimeter.
- E_O: the offset energy correction not related to the jet. The offset energy is referred to the energy deposits of the underlying events in the calorimeter jet cone. The underlying events come from multiple parton interaction or beam remnants.
- R_{jet}: the response correction and shows how calorimeter responds to the jet in the energy measurement.
- S_{jet}: the showering correction and makes correction for energy loss by showering out of cone.

3.6 Missing Transverse Energy

Weakly interacting particles such as neutrino and the lightest supersymmetric particle are not detected in the DØ detector. These invisible particles cause a momentum imbalance although the vector sum of all final state particles should be zero. At the Tevatron, we don't know the initial momentum of interacting partons along the beam axis, therefore we can not measure of the total missing energy. But the initial transverse energies of interacting partons are zero. Thus, the vector sum of final state particles in the transverse plane perpendicular to

the beam axis should be zero. The weakly interacting particles cause a momentum imbalance in the transverse plane. This missing energy in the transverse plane indicates Missing Transverse Energy. $\not\!\!E_T$, reconstructed by the vector sum of the transverse momentum of corrected EM objects, jets and muons [35].

$$\vec{\not\!\!p}_T = -\sum \vec{p}_T \tag{3.7}$$

3.7 b-tagging

In $t\bar{t}$ production, one of the distinct features in the $t\bar{t}$ events is that the final state of the $t\bar{t}$ production has two b quarks. Thus, an efficient b-quark jets selection will suppress the backgrounds significantly and enable us to make purer $t\bar{t}$ events samples. This pure $t\bar{t}$ events sample will minimize effect of the backgrounds. This analysis suppresses the backgrounds using b-quark jet tagging.

The b quark has a long lifetime so this is the distinct signature of b quark. The b-quark jet tagging using the long lifetime of b quark is called "lifetime tagging". In DØ experiment, three b-quark jet tagging algorithms based on lifetime tagging: Counting Signed Impact Parameters (CSIP) [36], Jet Lifetime Probability (JLIP) [37] and Secondary Vertex Tag (SVT) [38]. To improve the efficiency of b-tagging, the DØ experiment trains a neural network using these three b-tagging algorithms and builds b-tagger based on the weights from the trained neural network. This is called the Neural Network (NN) b-tagger [39]. The b-quark jet tagging efficiency is improved significantly compared to the other individual b-quark jet taggers as shown in Figure 3.2. The NN tagger is trained with 7 input variables described in Table 3.1.

Figure 3.3 shows the distribution of NN output for b- and $udsg$-jets. From the output distribution of NN training, b-tagging operating points are determined and introduced in Table 3.2. The NN is trained using QCD $b\bar{b}$ and light-jet Monte Carlo samples, so there exists a difference between the b-tagging efficiencies in data and Monte Carlo. To correct this difference, b-tagging efficiency is determined on data with the **System8** method [39], the scale factor is found with two b-tagging efficiencies derived on data and Monte Carlo and applied to the b-tagging efficiency in Monte Carlo. The fake rate is estimated using the negative tag rate

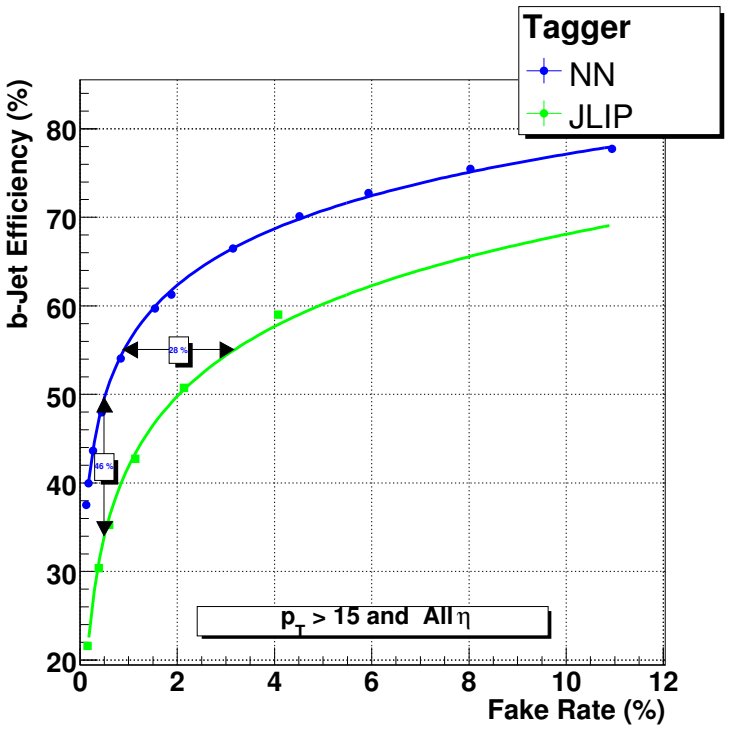

Figure 3.2: Performance of the NN and JLIP taggers [40].

(NTR) and it is used to assign to the light-flavor quarks tagging.

Figure 3.4 shows muonic b-jet tagging efficiency in data and MC as well as the data/MC scale factor parameterized in p_T and η for Medium operating point. The TagRateFunction (TRF) for b-jet is derived by the product of the scale factor and the b-tagging efficiency as Eq. 3.8.

$$TRF \text{ (TagRateFunction)} = \text{(scale factor)} \times (b\text{−jet tagging efficiency in MC}) \tag{3.8}$$

Figure 3.5 shows the inclusive b-tagging efficiency and the TRF for Medium operating point parametrized in p_T and η. In this analysis, b-quark jets are selected using these efficiencies and makes very pure $t\bar{t}$ events samples.

Table 3.1: NN input variables ranked in order of power [39].

Rank	Variable	Description
1	SVT_{SL} DLS	Decay Length Significance of the Secondary Vertex
2	CSIP Comb	Weighted combination of the tracks' Impact Parameter (IP) significancies
3	JLIP Prob.	Probability that the jet originates from the Primary Vertex (PV)
4	SVT_{SL} χ^2_{dof}	χ^2 per degree of freedom of the Secondary Vertex
5	SVT_L N_{tracks}	Number of track used to reconstruct the Secondary Vertex
6	SVT_{SL} Mass	Mass of the Secondary Vertex
7	SVT_{SL} Num	Number of the Secondary Vertex in the jet

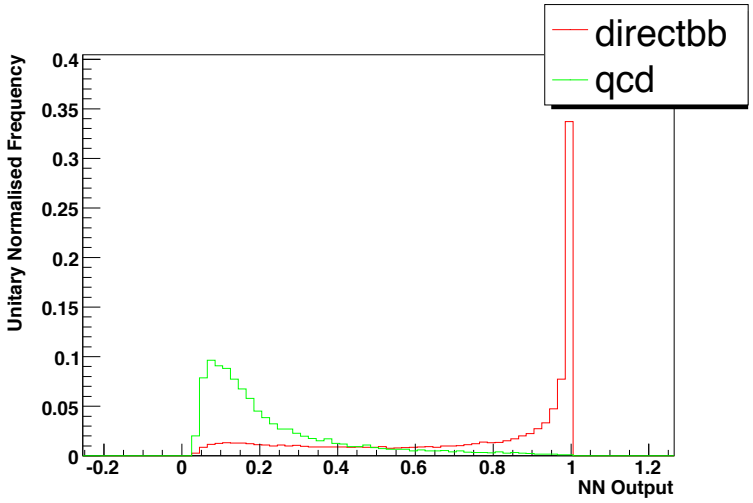

Figure 3.3: NN output for b (red) and $udsg$-jets (green) [39].

Table 3.2: The NN tagger's operating points [39].

Name	MegaTight	UltraTight	VeryTight	Tight	Medium	oldLoose
NN Cut	> 0.925	> 0.9	> 0.85	> 0.775	> 0.65	> 0.5
Name	Loose	L2	L3	L4	L5	L6
NN Cut	> 0.45	> 0.325	> 0.25	> 0.2	> 0.15	> 0.1

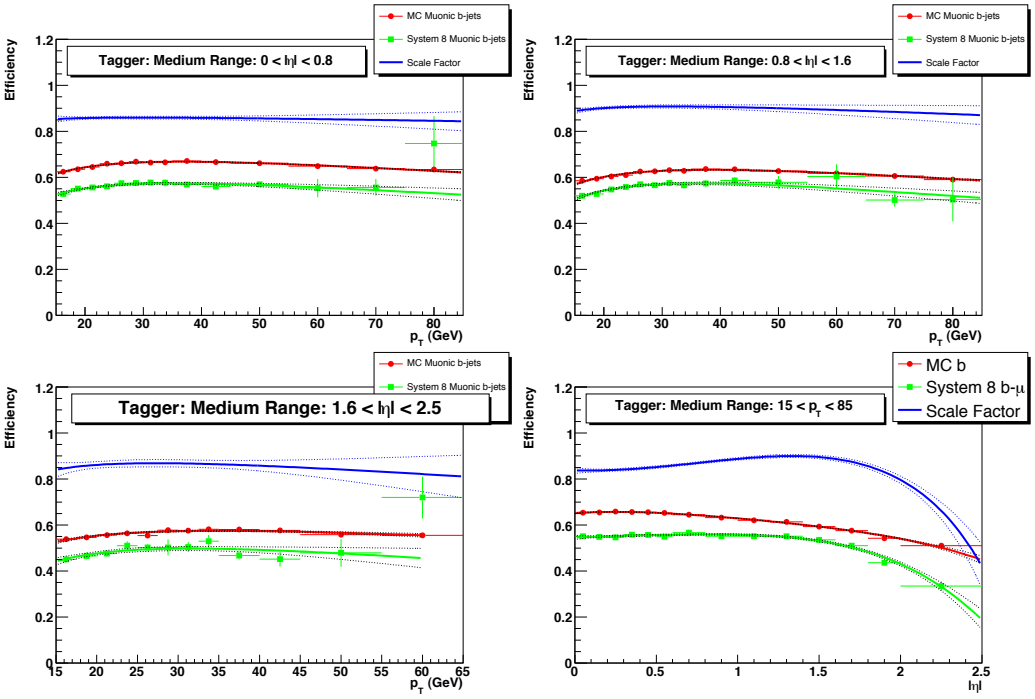

Figure 3.4: Muonic b-jet tagging efficiency measured in MC (red) and data (green) and the data/MC scale factor (blue) for Medium operating point parameterized in p_T in the CC (top left), ICR (top right) and EC (bottom left) and as function of η (bottom right). The black dotted curves are the fit error [39].

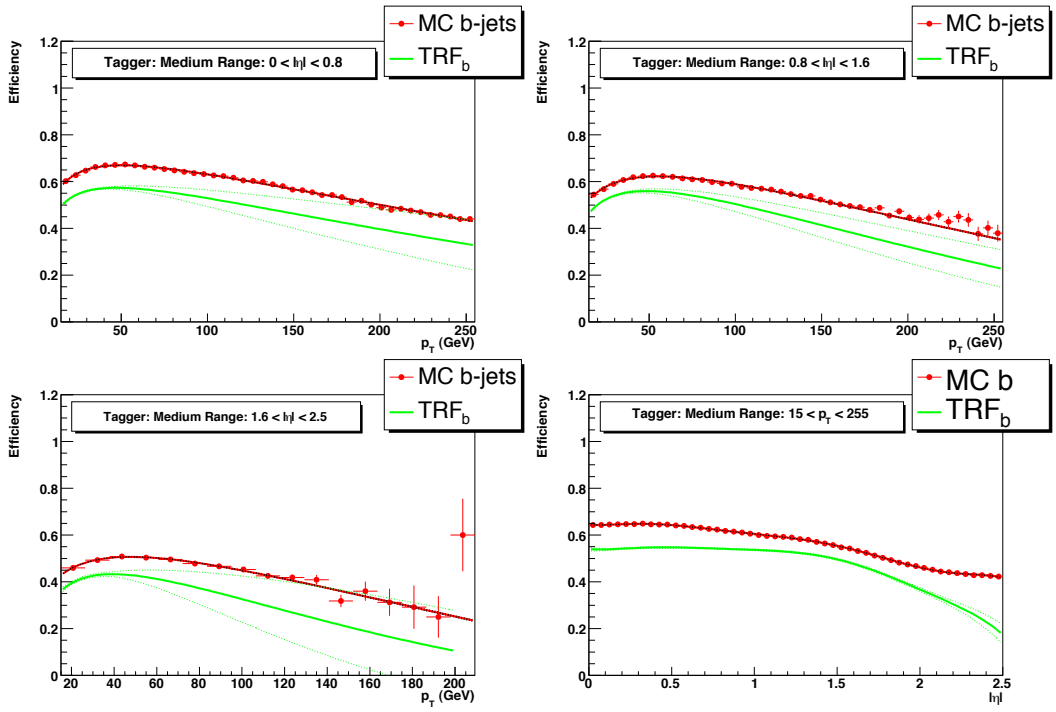

Figure 3.5: The inclusive b-jet tagging efficiency measured in MC (red) and TRF$_b$ (green) for Medium operating point parameterized in p_T in the CC (top left), ICR (top right) and EC (bottom left) and as function of η (bottom right). The green dotted curves are the one standard deviation uncertainty of the TRF$_b$ [39].

CHAPTER 4. Data and Monte Carlo Samples

4.1 Data Sample

This analysis is conducted with the data sample collected from April 2006 to June 2009, whose run range is 221,989-252,918. The total integrated luminosity is 4281.66 pb^{-1} shown in Table 4.1. Common Sample Group (CSG) [42] processed the data samples using Common Analysis Format (CAF) and the V+jets group provided the subskims that were used actually in this analysis [43]. The data were selected by the standard data quality selection performed by the official D0 data quality tools (caf_dq p21-br-03, dq_util p21-br-03 and dq_defs v2009-12-31). The data quality selection removed bad luminosity blocks caused by bad offline calorimeter quality, bad runs brought by bad SMT, CFT, muon or online calorimeter quality, and events with noise in the calorimeter [44]. The selection by the same "bad event quality" removal is performed in the Monte Carlo (MC) samples.

Table 4.1: Integrated luminosity analysed for e+jet and μ+jets.

Triggerlist version	Trigger	Integrated luminosity [pb^{-1}]
V 15.0 - V 15.99	JT125_L3J125	1619.77
V 16.0 - V 16.99	JT125_L3J125	2661.89
Total		4281.66

4.2 Monte Carlo Sample

The $t\bar{t}$ MC used to model the signal in this analysis is generated with ALPGEN [45] and PYTHIA [46] simulates the parton shower. The top quark mass is set to 172.5 GeV/c^2 and the CTEQ6L1 parton distribution function is used. The CTEQ6L1 parton distribution function

is used for all MC generation.

The W+jets samples which are a dominant background in the l+jets channel are generated with ALPGEN and the parton shower is simulated with PYTHIA. The W+jets samples include events in which one W boson decays to lepton and neutrino via an electroweak interaction and additional partons from QCD processes. The W+jets samples are comprised of four subsamples of parton flavors: Wbb+jets, Wcc+jets, Wc+jets and Wlp+jets, where "lp" stands for "light parton" (u, d, g). The contribution of these four kinds of events can not be estimated by the cross section that ALPEN supplies since their cross section does not take the NLO (next-to-leading order) correction into account. Especially, the cross sections for Wbb+jets and Wcc+jets by NLO correction are expected to be different from LO (leading order). Thus, the heavy flavor scale factor 1.47 with 15% uncertainty [47] multiplies the Wbb+jets and Wcc+jets samples to attain good agreement between data and background model. For the Wc+jets, the heavy flavor scale factor 1.27 with 12% uncertainty is applied, which is estimated from NLO correction. Also, there is no reliable NLO correction to normalize W+jets to its cross section accurately. Therefore, the normalization for W+jets is conducted using data and uses only the shape derived from the W+jets MC simulation. In other words, the normalization of W+jets background before b-tagging is performed by subtracting the number of $t\bar{t}$ signal and all MC background events from the number of data in each jet bin. Table 4.2 shows W+jets normalization factor for each channel and each jet bin. The default normalization factor 1.3 for W+light jets is not applied and W+jets normalization factor strongly depends on the measured $t\bar{t}$ cross section. The measured cross section 8.13 pb is applied to the $t\bar{t}$ signal.

Table 4.2: W+jets normalization factor. The default normalization factor 1.3 is not applied

	e+jet	μ+jets
1 jet	1.066	1.084
2 jets	1.216	1.305
3 jets	1.297	1.366
4 jets	1.073	1.747

Diboson (WW, WZ, ZZ) events, single top (s- and t-channels) events and Z($\rightarrow ee, \mu\mu, \tau\tau$)+jets events can have similar final states to the $t\bar{t}$ signal which decays to lepton+jets channel, and

are taken into account as other physics backgrounds. Thus, these physics processes are simulated. PYTHIA is used to generate WW, WZ and ZZ samples and MCFM [48] calculates their NLO cross sections. The cross sections of WW, WZ and ZZ are 12.0 pb, 3.68 pb and 1.42 pb, respectively, and an uncertainty of 7% is assigned, which is half of the difference between NLO and LO prediction. These processes are normalized to their NLO cross sections.

The MC samples for the single top processes are generated with the COMPHEP generator [49]. The NLO cross sections of s- and t-channels are 1.04 pb and 2.26 pb, respectively, and an uncertainty of 12.6% is assigned to their cross sections. These contributions of s- and t-channels are normalized using the NLO cross sections. The top quark mass for single top samples is set to 172.5 GeV/c^2. Since the single top contribution is very small in this analysis, the effect of the top mass is negligible and not considered.

Z+jets samples contain one Z boson decay to two electrons, muons and taus and additional partons. The Z+jets samples consist of three subsamples of parton flavors like W+jets samples: Zbb+jets, Zcc+jets and Zlp+jets. These samples are generated with ALPGEN and PYTHIA simulates the parton shower. The Z boson p_T reweighting is performed with the standard reweighting [50] in order to accomplish agreement of Z p_T distributions between simulated samples and data. Moreover, additional scale factors are applied to the normalization for the Z+jets background. The Z+light jets cross section is corrected by the k-factor 1.3 which stands for the ratio of NLO cross section to LO cross section. For the Z+cc and Z+bb samples, the heavy scale factors 1.67 and 1.52 are multiplied, repectively [51].

CHAPTER 5. Event Selection and Background Estimation

5.1 Event Selection

This analysis is based on the lepton+jets channel. The final state event signature of the $t\bar{t}$ signal consists of one isolated high p_T lepton, a large missing transverse energy $\not\!\!E_T$ from a undetected neutrino, and 4 jets: two jets come from the top quark decays and the other two jets are the products of the hadronic W decay. We select $t\bar{t}$ signal candidates based on this event signature. The following describes the event selection criteria for both e+jets and μ+jet channels.

- Good quality event. Bad luminosity block and ban runs are removed to retain only good quality of events.
- Good reconstructed vertex within the SMT fiducial region: $|z_{PV}| < 60$ cm. At least 3 tracks should exist associated with the primary vertex.
- Exactly 4 jets with $p_T > 20$ GeV/c and $|\eta_{det}| < 2.5$ are required. All jets must have at least two tracks within the jet cone which comes from the primary vertex.
- To suppress W+jets background without a large signal loss, leading jet $p_T > 40$ GeV/c is required.

The following cuts are applied to only e+jets channel:

- The electron must originate from the primary vertex: $|\Delta z(e, PV)| < 1cm$.
- One tight electron (Top_tight) must satisfy the tight electron requirement and have $p_T >$ 20 GeV/c and $|\eta_{det}| < 1.1$. The tight electron requirement is described in section 3.3.

- Events with a second tight electron with $p_T > 15$ GeV/c and $|\eta_{det}| < 2.5$ are vetoed. This requirement keeps orthogonality (non-overlapping event samples) with the dielectron channel. To ensure orthogonality with the electron-muon channel, events with a tight isolated muon with $p_T > 15$ GeV/c and $|\eta_{det}| < 2.0$ are rejected.

- The missing transverse energy $\not\!\!E_T > 20$ GeV.

- To reject multijet events in which a mis-reconstructed jet fakes an isolated lepton, the triangle cut $\Delta(e, \not\!\!E_T) > 0.7 \cdot \pi - 0.0045 \cdot \not\!\!E_T$ is required. More detail explanation about the triangle cut is in section 5.1.1.

- In data, each event should fire at least one single electron triggers or e+jets triggers. This trigger is called SuperOR trigger.

The event selection criteria for μ+jets are:

- $|\Delta z|$ between muon and primary vertex should be less than 1 cm: $|\Delta z(\mu, PV)| < 1$ cm. This requirement confirms a muon comes from the primary vertex.

- One isolated tight muon with $p_T > 20$ GeV/c and $|\eta_{det}| < 2.0$. The tight muon criteria are explained in section 3.4.

- Invariant mass of the leading muon and any second isolated muon with $p_T > 15$ GeV/c and $|\eta_{det}| < 2.0$ is reconstructed. If the invariant mass is between 70 GeV/c^2 and 110 GeV/c^2, the event is thrown away to reject $Z \to \mu\mu$+jets event.

- No second muon with $p_T > 15$ GeV/c, $|\eta_{det}| < 2.0$, medium track quality and $nseg = 3$ is allowed to keep orthogonality with the dimuon channel. In addition, to keep the orthogonality with the electron-muon channel, events which include a tight electron with $p_T > 15$ GeV/c and $|\eta_{det}| < 2.5$ are rejected.

- The missing transverse energy $\not\!\!E_T$ should be larger than 25 GeV: $\not\!\!E_T > 25$ GeV.

- The triangle cut is required to reject multijet events: $\Delta(\mu, \not\!\!E_T) > 2.1 - 0.0035 \cdot \not\!\!E_T$.

- To avoid mismeasured muons, we reject events containing $\not\!\!E_T > 250$ GeV and transverse mass of W > 250 GeV.

- In data, each event should fire at least one single muon trigger. This trigger is referred to as SingleMuon OR trigger.

After event selection with these criteria, the main background is W+jets. We conducted reweighting procedures and applied scale factors in luminosity profiles, z vertex distribution, and so on, to compensate differences between Data and Monte Carlo.

Luminosity reweighting The instantaneous luminosity difference between the zero bias events and the real data taking exists. Thus, we reweight the luminosity profile of each MC sample to that of the actual data set [52].

z vertex distribution The z vertex distribution is reweighted to correct for the difference between Monte Carlo and Data [53].

b fragmentation The e^+e^- experiments such as ALEPH, OPAL and DELPHI performed precise measurements of b-quark into heavy hadrons. But the default b fragmentation model for Monte Carlo simulation does not agree with the measurements from the e^+e^- experiments. The b fragmentation function is reweighted to match a function which is consistent with the measurements from ALEPH, OPAL and DELPHI [54].

Zp_T reweighting The p_T distribution of Z+jets from Monte Carlo simulation is reweighted to correct the difference from the distribution in data [50].

Lepton and jet identification scale factors Monte Carlo simulation and Data have different efficiencies for jet and lepton identification. To compensate the difference, we apply scale factors to Monte Carlo simulation.

W+jets η reweighting The jet η and $dR(jet, jet)$ of the W+jets in ALPGEN does not describe the same kinematic distributions in data accurately. To correct the kinematic distributions, these distributions are reweighted [55].

The reweights that change the shapes of generator level distributions such as luminosity reweight, beam position reweight and Zp_T reweight should change only the shapes but do not affect the total number of events before event selection. So, we normalize the sum of all weights being applied before event selection so that the sum of weights has to be same as the total number of events [47].

The top and anti-top quarks are reconstructed by their decay products using HITFIT [56] kinematic fitter. The fitter varies possible combinations of detected objects to reconstruct top and anti-top quarks by constraining the masses of both W bosons to 80.4 GeV, two b-quark jets tagging, and reconstruct top and anti-top quark with the combination of detected objects which gives minimum χ^2 value.

5.1.1 Triangle Cut

The multijet events are considered as the instrumental background in DØ. The multijet background, which has same final states as the $t\bar{t}$ signal, results from a jet which is mis-idenfied as a lepton, or an energetic jet which penetrates calorimeter and hits muon detector, or a real muon from semileptonic b-quark decay with non-reconstructed b-quark jet. To eliminate multijet background while suppressing the signal loss, "Triangle Cut" was invented and is applied to this analysis.

The Figures 5.1 and 5.2 show how multijet events obtained by inverting the tight electron and muon isolation criteria populate sace of $\delta\phi(e, \not\!\!E_T)$ and $\not\!\!E_T$. In principle, mismeasurements of jet energies due to the finite jet energy resolution can result in $\not\!\!E_T$ and those events by this mismeasurement tend to distribute in the low $\delta\phi(e, \not\!\!E_T)$ region and $\not\!\!E_T$ which moves towards higher $\not\!\!E_T$. Therefore, multijet events are suppressed more effectively by applying $\delta\phi(e, \not\!\!E_T)$ cut which is function of $\not\!\!E_T$ than flat $\not\!\!E_T$ cut. The black solid lines represent the triangle cut and the flat $\not\!\!E_T$ cut and show the triangle cut removes multijet events more efficiently [60].

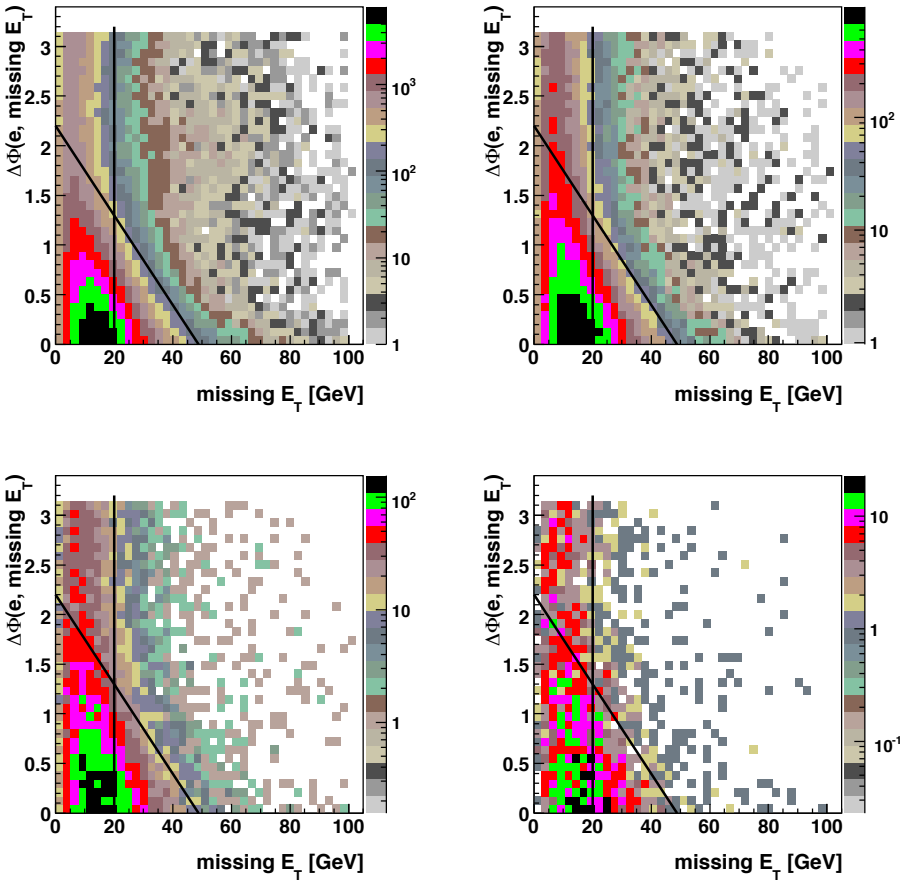

Figure 5.1: Distributions of $\Delta\Phi(e, \not\!\!E_T)$ vs $\not\!\!E_T$ for e+jets in data by inverting tight electron isolation cuts. From top left to bottom right, these plots correspond to 1 jet (top left), 2 jets (top right), 3 jets (bottom left) and $\geq$ 4 jets (bottom right) [57].

5.2 Background Estimation

Using event selection criteria in section 5.1, we extract the $t\bar{t}$ signal and background contributions. The background are classified as two types.

Instrumental background For e+jets channel, a jet with high electromagnetic fraction and a photon reconstructed with a random track can fake an electron. For μ+jets channel, punch-through or real muons from semileptonic b-quark decay with non-reconstructed b-jet can fake an isolated muon.

Physics background Physics backgrounds come from physics processes which have similar final states to the $t\bar{t}$ signal.

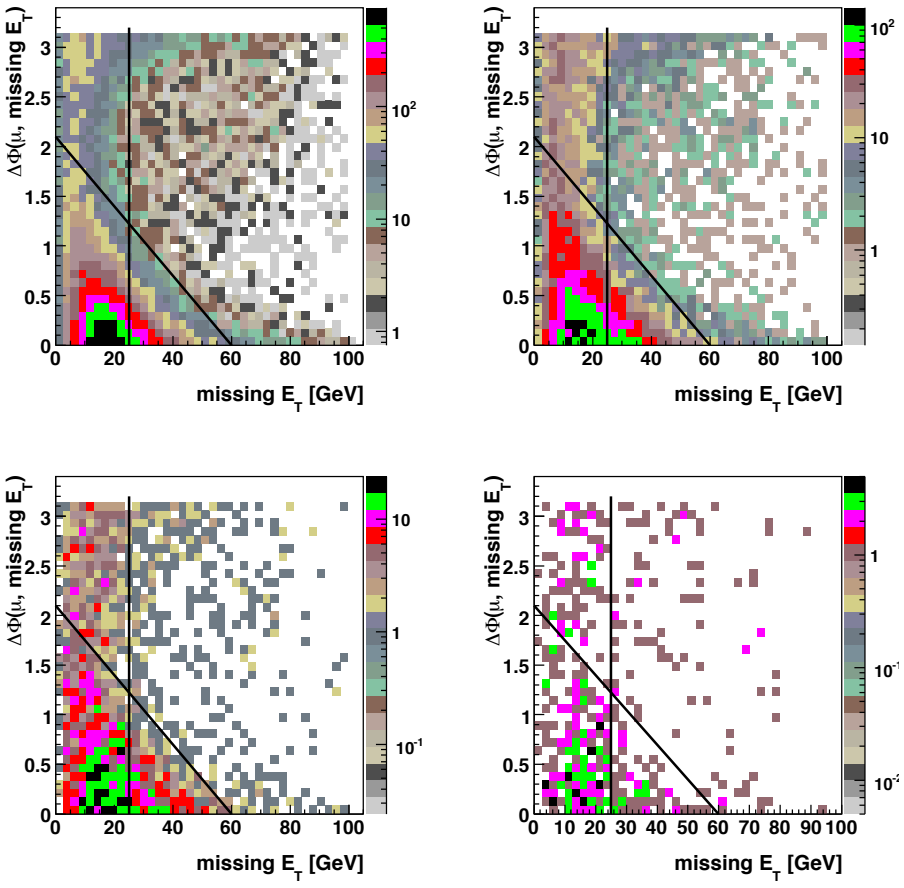

Figure 5.2: Distributions of $\Delta\Phi(\mu, \not\!\!E_T)$ vs $\not\!\!E_T$ for μ+jets in data by inverting tight electron isolation cuts. From top left to bottom right, these plots correspond to 1 jet (top left), 2 jets (top right), 3 jets (bottom left) and $\geq$ 4 jets (bottom right) [57].

W+jets is the dominant physics background after event selection in this analysis. Other physics backgrounds are diboson (WW, WZ, ZZ), single top(s-, t-channels), and $Z(\rightarrow \tau\tau, ee, \mu\mu)$+jets processes.

5.2.1 Instrumental Background

The "Matrix Method" enables us to estimate the contribution of multijet backgrounds from data. For the matrix method, tight and loose samples are needed. The former is a set of events which pass all event selection criteria described in section 5.1 and a subset of the loose sample. The latter is a set of events which pass the same event selection criteria as tight sample except the tight isolation cut for lepton. For the loose sample, the loose isolation cut for lepton is

required, which is described in section 3.4. The number of loose and tight events:

$$\begin{aligned} N_l &= N_l^{W+t\bar{t}} + N_l^{QCD} \\ N_t &= N_t^{W+t\bar{t}} + N_t^{QCD} \\ &= \epsilon_{sig} N_l^{W+t\bar{t}} + \epsilon_{qcd} N_l^{QCD} \end{aligned} \tag{5.1}$$

where $N_l^{W+t\bar{t}}$ and $N_t^{W+t\bar{t}}$ represent the total number of $t\bar{t}$ signal and physics background in the loose and the tight samples, respectively. The number of multijet events for the loose and the tight samples are denoted as N_l^{QCD} and N_t^{QCD}. ϵ_{sig} and ϵ_{qcd} are the efficiencies for a true and a fake isolated lepton to pass the tight lepton selection, respectively. The efficiency measurements for ϵ_{sig} and ϵ_{qcd} are described in [58]. Table 5.1 shows ϵ_{sig} and ϵ_{qcd} values used to estimate multijet background. If we solvie simultaneous equations for N_l^{QCD} and $N_l^{W+t\bar{t}}$,

Table 5.1: ϵ_{sig} and ϵ_{qcd} values for Run IIb dataset. The uncertainties are sum of statistical and systematic uncertainties in quadrature [47].

	e+jets	μ+jets
ϵ_{qcd}	0.124±0.0015	0.219±0.043
ϵ_{sig} (= 1 jet)	0.822±0.118	0.922±0.042
ϵ_{sig} ($\geq$ 2 jets)	0.813±0.045	0.896±0.021

then

$$N_l^{W+t\bar{t}} = \frac{N_t - \epsilon_{qcd} N_l}{\epsilon_{sig} - \epsilon_{qcd}} \quad \text{and} \quad N_l^{QCD} = \frac{\epsilon_{sig} N_l - N_t}{\epsilon_{sig} - \epsilon_{qcd}} \tag{5.2}$$

The efficiency ϵ_{sig} can be measured by obtaining the ratio of events passing the tight lepton selection to events passing the loose lepton selection using W+jets and $t\bar{t}$ samples. ϵ_{qcd} can be obtained by requiring $\not\!\!E_T < 10$ GeV to data where the multijet events are enriched and calculating the fraction of the number of events in the tight lepton sample to the number of events in the loose lepton sample. Using the efficiency ϵ_{sig} and ϵ_{qcd}, finally we can obtain $N_t^{W+t\bar{t}}$ and N_t^{QCD} for the before b-tagging events in the tight sample.

$$N_t^{W+t\bar{t}} = \epsilon_{sig} \frac{N_t - \epsilon_{qcd} N_l}{\epsilon_{sig} - \epsilon_{qcd}} \quad \text{and} \quad N_t^{QCD} = \epsilon_{qcd} \frac{\epsilon_{sig} N_l - N_t}{\epsilon_{sig} - \epsilon_{qcd}} \tag{5.3}$$

The estimation of multijet contribution for the b-tagged sample can be performed in the same way. The following gives estimated multijet contribution in the b-tagged sample.

$$\begin{aligned} N_l^{b-tag} &= N_l^{b-tag,W+t\bar{t}} + N_l^{b-tag,QCD} \\ N_t^{b-tag} &= N_t^{b-tag,W+t\bar{t}} + N_t^{b-tag,QCD} \\ &= \epsilon_{sig} N_l^{b-tag,W+t\bar{t}} + \epsilon_{qcd} N_l^{b-tag,QCD} \end{aligned}$$

$$N_l^{b-tag,W+t\bar{t}} = \frac{N_t^{b-tag} - \epsilon_{qcd} N_l^{b-tag}}{\epsilon_{sig} - \epsilon_{qcd}} \quad \text{and} \quad N_l^{b-tag,QCD} = \frac{\epsilon_{sig} N_l^{b-tag} - N_t^{b-tag}}{\epsilon_{sig} - \epsilon_{qcd}}$$

$$N_t^{b-tag,W+t\bar{t}} = \epsilon_{sig} \frac{N_t^{b-tag} - \epsilon_{qcd} N_l^{b-tag}}{\epsilon_{sig} - \epsilon_{qcd}} \quad \text{and} \quad N_t^{b-tag,QCD} = \epsilon_{qcd} \frac{\epsilon_{sig} N_l^{b-tag} - N_t^{b-tag}}{\epsilon_{sig} - \epsilon_{qcd}} \tag{5.4}$$

where "b-tag" stands for the b-tagged sample. Table 5.1 gives the values of ϵ_{sig} and ϵ_{qcd} used for multijet estimation in b-tag sample. Because the correlation between the sample before b-tagging and the b-tagged sample by the lepton selection is not expected to exist, we can use same ϵ_{sig} and ϵ_{qcd} values for the b-tagged sample. The uncertainty calculation for the matrix method is described in [59].

5.2.2 Physics Background

Section 4.2 introduced cross section information for physics backgrounds to be normalized, heavy flavor scale factors for W+jets and Z+jets and the method for W+jets normalization.

$$N_i^{presel} = \epsilon_i^{presel} \cdot Br_i \cdot \sigma_i \cdot \mathcal{L} \tag{5.5}$$

Eq. 5.5 is used to estimate the contribution of physics backgrounds other than W+jets for the preselected samples. The preselected samples refer to the samples which pass the event selection criteria enumerated in section 5.1. In Eq. 5.5 , the superscript "presel" denotes preselection, i represents each physics background, ϵ_i^{presel} is preselection efficiency, Br_i is branching ratio and σ_i and $\mathcal{L}$ denote cross section and integrated luminosity, respectively. In this analysis, the contributions of diboson (WW, WZ, ZZ), single top (s- and t-channels) and Z+jets are estimated using Eq. 5.5. The contribution of the W+jets, the main physics background, is

found by normalizing the number of the W+jets events to the number of data events. First, we subtract the $t\bar{t}$ signal, the other physics backgrounds and multijet contribution from the number of events for the tight data sample (Eq. 5.6).

$$N_{W+jets}^{presel} = N_t^{data} - N_{t\bar{t}}^{presel} - \sum_i N_i^{presel} - N_t^{QCD} \tag{5.6}$$

where i denotes physics backgrounds except W+jets. Second, from the W+jets simulation using ALPGEN, the contributions of Wlp+jets, Wbb+jet, Wcc+jets and Wc+jets are known by the ALPGEN cross sections. Also, we assign heavy flavor scale factors introduced in section 4.2. If we write an equation to find a normalization factor for W+jets,

$$f_{norm} = \frac{N_{W+jets}^{presel}}{\mathcal{N}_{Wlp}^{presel} + k_{Wbb} \cdot \mathcal{N}_{Wbb}^{presel} + k_{Wcc} \cdot \mathcal{N}_{Wcc}^{presel} + k_{Wc} \cdot \mathcal{N}_{Wc}^{presel}} \tag{5.7}$$

where k_{Wbb}. k_{Wcc} and k_{Wc} are heavy flavor scale factor for Wbb+jets, Wcc+jets and Wc+jets samples, respectively. $\mathcal{N}_{Wlp}^{presel}$, $\mathcal{N}_{Wbb}^{presel}$, $\mathcal{N}_{Wcc}^{presel}$ and $\mathcal{N}_{Wc}^{presel}$ represent the number of events estimated using Eq. **??**. This W normalization factor f_{norm} is multiplied to each Wlp+jets, Wbb+jets, Wcc+jets and Wc+jets sample. We get formulas for the estimation of W+jets contribution as in Eq. 5.8.

$$\begin{aligned} N_{Wlp}^{presel} &= f_{norm} \cdot \mathcal{N}_{Wlp}^{presel} \\ N_{Wbb}^{presel} &= f_{norm} \cdot k_{Wbb} \cdot \mathcal{N}_{Wbb}^{presel} \\ N_{Wcc}^{presel} &= f_{norm} \cdot k_{Wcc} \cdot \mathcal{N}_{Wcc}^{presel} \\ N_{Wc}^{presel} &= f_{norm} \cdot k_{Wc} \cdot \mathcal{N}_{Wc}^{presel} \end{aligned} \tag{5.8}$$

The W normalization f_{norm} for each jet multiplicity calculated with this method is shown in Table 4.2. For b-tagged sample, the background contributions are found by multiplying the preselected events by the b-tagging probability as in Eq. 5.9.

$$N_i^{b-tag} = N_i^{presel} \cdot P_i^{b-tag} \tag{5.9}$$

where i means each background considered in this analysis and the b-tagging probability is denoted as P_i^{b-tag}. The next section explains how the b-tagging probability is calculated.

5.3 b-tag Probability

To reduce the contributions of backgrounds and raise $t\bar{t}$ signal purity, the b-quark jet identification method is applied to data, the $t\bar{t}$ signal and all of the other backgrounds. The b-quark jet identification is performed with the Neural Network (NN) b-tagging algorithm and "MEDIUM" operating point is used since it gives the best $S/\sqrt{S+B}$ ratio, where S is the number of signal events and B denotes the number of background events. The detailed explanation to choose an operating point of the NN tagger is given in [60]. The NN b-tagging algorithm is described in section 3.7. In this analysis, at least two b-tags are required to data, the $t\bar{t}$ signal and all backgrounds in order to reduce background for measuring asymmetry.

"Direct b-tagging method" is applied in this analysis. For data, we pick jets which are b-tagged or not b-tagged by the NN tagger. Simply, if NN output of a jet in data is greater than an operating point of the NN tagger which is chosen for an analysis, this jet becomes b-tagged jet. This is direct b-tagging. Direct b-tagging method means that this direct b-tagging is applied to Monte Carlo too. We require b-tagged or not b-tagged jets in Monte Carlo and apply scale factors depending on jet flavor to them in order to compensate the difference of b-tagging efficiency between data and simulated jets. In order that a jet is b-tagged, the jet should be taggable. When a track jet which is reconstructed with simple cone jet algorthm [61] match a calorimeter jet by requiring $\Delta R < 0.5$ between two jets, this jet is taggable. There exists also difference of the efficiency for jets to be taggable between data and Monte Carlo. A taggability scale factor [63] is applied to account for this differences. If we apply the NN tagger to taggable jets in a event, we can get the b-tag scale factor per jet and calculate b-tag probability of a event using Eq. 5.10.

$$P_{event}^{b-tag} = \prod_{i=1}^{N_{jets}^{b-tagged}} SF_i \prod_{j=1}^{N_{jets}^{not\ b-tagged}} \overline{SF}_j \tag{5.10}$$

SF and $\overline{SF}$ in Eq. 5.10 are the tag scale factor and the not-tag scale factor, respectively. These scale factors are found by the output of the TagRateFunction(TRF) described in section 3.7.

$$SF = \frac{TRF_{Data}(\alpha) - TRF_{Data}(\beta)}{TRF_{MC}(\alpha) - TRF_{MC}(\beta)} \tag{5.11}$$

where α and β are the looser and the tighter b-tag operating points. If we set $TRF^{\alpha}_{Data} = TRF^{\beta}_{MC} = 1.0$ in Eq. 5.11, we can derive the not-tag scale factor [47].

5.4 Efficiencies and Event Yields

From the event selection criteria, instrumental and physics backgrounds estimation, and the b-tagging probability calculation, events yields for data, the $t\bar{t}$ signal and all backgrounds are derived. First off, to derive the preselection efficiency which is not contaminated by fake leptons, we select semileptonic $t\bar{t}$ events which decay to one electron, muon or leptonically decaying tau using parton level information. This procedure is done by the MCPraticleSelector in caf_mc_util select semileptonic $t\bar{t}$ events using Monte Carlo truth information before the selection efficiency calculation. Table 5.2 shows the branching ratios of the semileptonic $t\bar{t}$ and the dileptonic $t\bar{t}$ channel. These branching ratios are used for the estimation of the semileptonic $t\bar{t}$ signal and the dileptonic $t\bar{t}$ background.

Table 5.2: Branching ratios for the semileptonic and dileptonic final states of $t\bar{t}$ [6].

$t\bar{t}$ decay	e+jets	μ+jets	ee	$\mu\mu$
$t\bar{t} \rightarrow$ WbWb	0.1721	0.17137	0.06627	0.06607

Tables 5.3, 5.4 are cut flow tables for e+4 jets and μ+4 jets. These tables show how event selection efficiency changes at each cut. The ε^{total} in Tables 5.3, 5.4 are product of all correction factors and weights of reweighting processes. ε^{total} can be written as follows:

- In Table 5.3, $\varepsilon^{total} = (\kappa_{electron\ ID} \times \kappa_{electron\ likelihood} \times Trigger\ probability \times b\ fragmentation\ weight \times Luminosity\ reweighting\ weight \times BeamWeight)$
- In Table, 5.4 $\varepsilon^{total} = \kappa_{\mu\ ID} \times \kappa_{\mu\ track} \times \kappa_{iso\ corr} \times \kappa_{\Delta R\ corr} \times Trigger\ probability \times b\ fragmentation\ weight \times Luminosity\ reweighting\ weight \times BeamWeight)$

Table 5.5 summarizes the preselection efficiencies and two or more b-tagging probabilities. To estimate the expected number of $t\bar{t}$ events, the branching ratios in Table 5.2 are chosen according to the final state and they are multiplied to the efficiencies summarized in Table 5.5.

Table 5.3: Summary of the $t\bar{t} \rightarrow$ e+jets event preselection efficiencies before b-tagging for four jets. Only statistical uncertainties are included.

Selection or κ	Events left	Exclusive selection efficiency[%]	Cumulative selection efficiency[%]
Particle selector	3774.47		
Data quality	3637.61	96.37 ± 0.18	96.37 ± 0.18
Vertex selection	3564.18	97.98 ± 0.19	94.43 ± 0.18
Loose Electron	1626.01	45.62 ± 0.11	43.08 ± 0.10
2nd electron veto	1625.65	99.98 ± 0.29	43.07 ± 0.10
Muon veto	1625.30	99.98 ± 0.29	43.06 ± 0.10
$\not\!\!E_T > 20$ GeV	1445.41	88.93 ± 0.26	38.29 ± 0.10
Tight Electron	1221.13	84.48 ± 0.27	32.35 ± 0.09
Triangle selection	1147.92	94.00 ± 0.31	30.41 ± 0.08
Leading jet > 40 GeV	1127.65	98.23 ± 0.34	29.88 ± 0.08
# good jets =4	342.16	30.34 ± 0.15	9.07 ± 0.04
ε^{total}		79.90	7.24 ± 0.04

The medium operating point of the NN b-tagging algorithm is chosen to tag b-quark jets, which requires NN output ≥ 0.65. The measured $t\bar{t}$ cross section $\sigma_{t\bar{t}} = 8.13$ pb [47] is used for estimating the expected number of the $t\bar{t}$ events.

Based on the preselection, background estimation and b-tagging introduced in the previous sections, the predicted numbers of background events are calculated and Tables 5.6 to 5.9 show both the predicted number of background and the observed number of data in e+jets and μ+jets for the cases of before b-tagging and after ≥ 2 b-tags. The uncertainty of multijet background takes the uncertainties of ϵ_{sig} and ϵ_{qcd} into account. The uncertainties for the $t\bar{t}$ signal and the other physics backgrounds are statistical uncertainties. In the tables, the first column tells about the background processes. The two final states of the $t\bar{t}$, lepton+jets and dilepton, are denoted as ttlj and ttll in the column. The main physics background W+jets are split into 4 processes according to their jet flavor content such as Wbb, Wcc, Wc and Wlp. The lp stands for light parton. The Z+jets background is also considered as separate subprocesses according to the Z boson decay modes and their jet flavor content. These subprocesses are represented as Z($\rightarrow$ ee)bb, Z($\rightarrow$ ee)cc, Z($\rightarrow$ ee)lp, Z($\rightarrow \mu\mu$)bb, Z($\rightarrow \mu\mu$)cc, Z($\rightarrow \mu\mu$)lp, Z($\rightarrow \tau\tau$)bb, Z($\rightarrow \tau\tau$)cc and Z($\rightarrow \tau\tau$)lp. The diboson processes are written as WW, WZ and ZZ

Table 5.4: Summary of the $t\bar{t} \to \mu$+jets event preselection efficiencies before b-tagging for four jets. Only statistical uncertainties are included.

Selection or κ	Events left	Exclusive selection efficiency[%]	Cumulative selection efficiency[%]
Particle selector	3759.40		
Data quality	3621.20	96.32 ± 0.18	96.32 ± 0.18
Vertex selection	3549.97	98.03 ± 0.19	94.43 ± 0.18
Loose Muon	1506.57	42.43 ± 0.11	40.07 ± 0.10
2nd muon veto	1506.39	99.99 ± 0.30	40.07 ± 0.10
Electron veto	1505.51	99.94 ± 0.30	40.05 ± 0.10
$\not\!\!E_T > 25$ GeV	1288.47	85.58 ± 0.26	34.27 ± 0.09
Tight Muon	1167.08	90.58 ± 0.30	31.04 ± 0.08
Triangle selection	1085.08	92.97 ± 0.32	28.86 ± 0.08
$W_{mT} < 250$	1074.62	99.04 ± 0.35	28.58 ± 0.08
Leading jet > 40 GeV	1056.79	98.34 ± 0.35	28.11 ± 0.08
$\not\!\!E_T < 250$ GeV	1055.89	99.91 ± 0.35	28.09 ± 0.08
# good jets = 4	344.75	32.65 ± 0.16	9.17 ± 0.04
ε^{total}		54.06	4.96 ± 0.03

Table 5.5: The preselection efficiencies and b-tagging probabilities. Only statistical uncertainties are given.

$t\bar{t}$ decay mode	Channel	Jet multiplicity	Preselection	≥ 2 tags
$t\bar{t} \to lj$	e+jets	= 4	0.0736 ± 0.0006	0.2527 ± 0.0034
	μ+jets	= 4	0.0503 ± 0.0004	0.2505 ± 0.0044
$t\bar{t} \to ll$	e+jet	= 4	0.0067 ± 0.0001	0.2687 ± 0.0098
	μ+jets	= 4	0.0040 ± 0.0001	0.3000 ± 0.0125

and the s-channel and t-channel for single top are denoted as tb and tqb, repectively.

Table 5.9 shows that μ+4 jets channel doesn't have a good agreement between data and Monte Carlo prediction after requiring 2 or more b-tags. Appendix E and F in the reference [47] mention detailed studies and discussions about this discrepancy.

5.5 The Comparison of Data and Monte Carlo Composition

To check whether the $t\bar{t}$ signal and background model the actual DØ data accurately, we make plots for the comparison of data and Monte Carlo. These plots are called "Control Plots" in DØ. By investigating control plots for main kinematic variables such as lepton p_T,

Table 5.6: Event yield for e+jets before b-tagging. The measured cross section $\sigma_{t\bar{t}} = 8.13$ pb is applied.

e+jets				
Contribution	1 jet	2 jets	3 jets	4 jets
Data	61199.00 ± 247.38	20423.00 ± 142.91	4118.00 ± 64.17	859.00 ± 29.31
Multijet	3156.07 ± 1547.25	1807.22 ± 318.31	451.80 ± 74.72	84.78 ± 14.95
WW	510.91 ± 6.93	560.06 ± 7.34	103.50 ± 3.21	15.29 ± 1.26
WZ	77.80 ± 1.70	98.74 ± 1.95	19.96 ± 0.86	2.81 ± 0.36
Wbb	956.18 ± 10.03	687.70 ± 8.52	153.75 ± 3.31	19.27 ± 0.86
Wc	3378.72 ± 36.26	1147.15 ± 15.05	166.45 ± 4.82	14.76 ± 0.90
Wcc	2221.83 ± 20.01	1443.20 ± 15.59	347.73 ± 6.65	41.86 ± 1.74
Wlp	48866.75 ± 127.80	13153.38 ± 45.55	1955.62 ± 15.63	191.15 ± 2.75
ZZ	6.80 ± 0.32	7.14 ± 0.37	2.72 ± 0.25	0.28 ± 0.06
Z($\rightarrow$ ee)bb	43.33 ± 1.34	40.86 ± 1.39	12.81 ± 0.80	2.48 ± 0.38
Z($\rightarrow \tau\tau$)bb	10.54 ± 0.66	9.46 ± 0.69	2.88 ± 0.34	0.52 ± 0.13
Z($\rightarrow$ ee)cc	82.30 ± 2.66	70.35 ± 2.45	23.07 ± 1.42	5.02 ± 0.76
Z($\rightarrow \tau\tau$)cc	26.99 ± 1.49	19.85 ± 1.16	6.73 ± 0.74	1.14 ± 0.30
Z($\rightarrow$ ee)lp	1209.44 ± 24.11	567.85 ± 13.96	114.12 ± 5.44	13.54 ± 1.67
Z($\rightarrow \tau\tau$)lp	441.68 ± 13.82	175.24 ± 7.40	39.22 ± 3.51	3.67 ± 0.76
tb	21.83 ± 0.31	46.04 ± 0.46	10.99 ± 0.23	1.71 ± 0.09
tqb	49.59 ± 0.60	71.65 ± 0.74	20.95 ± 0.43	3.82 ± 0.18
ttlj	38.35 ± 0.95	268.85 ± 2.62	602.13 ± 3.92	441.30 ± 3.32
ttll	94.27 ± 0.75	248.17 ± 1.24	83.58 ± 0.68	15.61 ± 0.28
Total	61193.38 ± 1553.38	20422.90 ± 322.90	4118.00 ± 77.32	859.00 ± 15.90

Table 5.7: Event yield for μ+jets before b-tagging. The measured cross section $\sigma_{t\bar{t}} = 8.13$ pb is applied.

μ+jets				
Contribution	1 jet	2 jets	3 jets	4 jets
Data	46374.00 ± 215.35	15290.00 ± 123.65	2904.00 ± 53.89	684.00 ± 26.15
Multijet	391.72 ± 660.63	149.64 ± 122.06	62.59 ± 27.90	10.32 ± 6.61
WW	363.66 ± 5.01	416.53 ± 5.43	77.00 ± 2.40	11.13 ± 0.92
WZ	61.03 ± 1.24	84.07 ± 1.52	15.92 ± 0.68	2.12 ± 0.27
Wbb	689.80 ± 7.33	551.14 ± 6.88	123.94 ± 2.60	26.62 ± 1.08
Wc	2369.54 ± 26.17	845.09 ± 11.21	124.44 ± 3.62	15.88 ± 0.98
Wcc	1621.98 ± 15.03	1176.73 ± 12.86	279.26 ± 5.20	55.73 ± 2.36
Wlp	37488.70 ± 98.24	10615.49 ± 36.52	1581.16 ± 11.94	228.38 ± 3.32
ZZ	7.15 ± 0.29	11.19 ± 0.39	2.33 ± 0.17	0.31 ± 0.06
Z($\rightarrow \mu\mu$)bb	67.66 ± 1.47	48.06 ± 1.34	11.05 ± 0.67	1.39 ± 0.20
Z($\rightarrow \tau\tau$)bb	6.09 ± 0.48	5.76 ± 0.45	2.04 ± 0.26	0.42 ± 0.15
Z($\rightarrow \mu\mu$)cc	158.16 ± 3.17	102.63 ± 2.56	21.36 ± 1.12	3.08 ± 0.47
Z($\rightarrow \tau\tau$)cc	13.27 ± 0.81	11.38 ± 0.76	4.02 ± 0.49	0.62 ± 0.23
Z($\rightarrow \mu\mu$)lp	2780.22 ± 30.14	777.56 ± 12.04	124.69 ± 4.22	11.68 ± 1.30
Z($\rightarrow \tau\tau$)lp	235.01 ± 8.70	105.84 ± 5.06	19.94 ± 2.10	2.43 ± 0.50
tb	17.66 ± 0.24	40.24 ± 0.37	11.14 ± 0.20	1.81 ± 0.08
tqb	32.12 ± 0.40	45.60 ± 0.49	12.26 ± 0.27	2.48 ± 0.12
ttlj	19.60 ± 0.56	154.67 ± 1.65	379.54 ± 2.62	300.34 ± 2.30
ttll	50.24 ± 0.46	148.49 ± 0.81	51.34 ± 0.46	9.25 ± 0.17
Total	46373.62 ± 669.38	15290.11 ± 129.56	2904.01 ± 31.71	684.00 ± 8.42

Table 5.8: Event yield for e+jets after requiring 2 or more medium b-tagged jets. The measured cross section $\sigma_{t\bar{t}} = 8.13$ pb is applied.

e+jets				
Contribution	1 jet	2 jets	3 jets	4 jets
Data	0.00 ± 0.00	184.00 ± 13.56	154.00 ± 12.41	99.00 ± 9.95
Multijet	0.00 ± 0.00	3.61 ± 2.27	4.18 ± 2.03	0.77 ± 1.30
WW	0.00 ± 0.00	0.63 ± 0.24	0.16 ± 0.15	0.00 ± 0.00
WZ	0.00 ± 0.00	3.99 ± 0.37	0.63 ± 0.13	0.04 ± 0.03
Wbb	0.00 ± 0.00	57.65 ± 2.44	13.27 ± 1.01	2.34 ± 0.31
Wc	0.00 ± 0.00	1.73 ± 0.49	0.71 ± 0.36	0.15 ± 0.12
Wcc	0.00 ± 0.00	7.13 ± 0.89	3.22 ± 0.56	0.60 ± 0.20
Wlp	0.00 ± 0.00	2.87 ± 1.05	2.14 ± 0.95	0.19 ± 0.11
ZZ	0.00 ± 0.00	0.31 ± 0.07	0.13 ± 0.06	0.06 ± 0.03
Z($\rightarrow$ ee)bb	0.00 ± 0.00	2.71 ± 0.35	0.95 ± 0.19	0.22 ± 0.10
Z($\rightarrow \tau\tau$)bb	0.00 ± 0.00	0.84 ± 0.20	0.46 ± 0.13	0.00 ± 0.00
Z($\rightarrow$ ee)cc	0.00 ± 0.00	0.07 ± 0.05	0.20 ± 0.10	0.03 ± 0.02
Z($\rightarrow \tau\tau$)cc	0.00 ± 0.00	0.13 ± 0.08	0.26 ± 0.17	0.10 ± 0.10
Z($\rightarrow$ ee)lp	0.00 ± 0.00	0.00 ± 0.00	0.00 ± 0.00	0.00 ± 0.00
Z($\rightarrow \tau\tau$)lp	0.00 ± 0.00	1.09 ± 1.07	0.03 ± 0.02	0.00 ± 0.00
tb	0.00 ± 0.00	9.82 ± 0.18	2.43 ± 0.09	0.34 ± 0.03
tqb	0.00 ± 0.00	2.22 ± 0.12	2.60 ± 0.14	0.74 ± 0.07
ttlj	0.00 ± 0.00	17.96 ± 0.57	103.14 ± 1.39	111.64 ± 1.41
ttll	0.00 ± 0.00	51.43 ± 0.47	21.43 ± 0.31	4.21 ± 0.13
Total	0.00 ± 0.00	164.21 ± 3.92	155.95 ± 2.95	121.43 ± 1.97

Table 5.9: Event yield for μ+jets after requiring 2 or more medium b-tagged jets. The measured cross section $\sigma_{t\bar{t}} = 8.13$ pb is applied.

μ+jets				
Contribution	1 jet	2 jets	3 jets	4 jets
Data	0.00 ± 0.00	109.00 ± 10.44	114.00 ± 10.68	98.00 ± 9.90
Multijet	0.00 ± 0.00	0.97 ± 1.48	0.00 ± 1.38	0.00 ± 1.17
WW	0.00 ± 0.00	0.39 ± 0.16	0.51 ± 0.23	0.12 ± 0.06
WZ	0.00 ± 0.00	3.24 ± 0.32	0.65 ± 0.13	0.13 ± 0.05
Wbb	0.00 ± 0.00	45.53 ± 2.05	10.84 ± 0.78	3.32 ± 0.42
Wc	0.00 ± 0.00	1.47 ± 0.52	0.18 ± 0.09	0.05 ± 0.04
Wcc	0.00 ± 0.00	7.25 ± 1.07	2.09 ± 0.46	1.59 ± 0.45
Wlp	0.00 ± 0.00	3.16 ± 0.88	1.11 ± 0.35	0.18 ± 0.10
ZZ	0.00 ± 0.00	0.58 ± 0.08	0.13 ± 0.04	0.02 ± 0.02
Z($\to \mu\mu$)bb	0.00 ± 0.00	3.84 ± 0.33	1.20 ± 0.21	0.25 ± 0.10
Z($\to \tau\tau$)bb	0.00 ± 0.00	0.33 ± 0.08	0.42 ± 0.10	0.06 ± 0.02
Z($\to \mu\mu$)cc	0.00 ± 0.00	0.56 ± 0.17	0.08 ± 0.04	0.04 ± 0.04
Z($\to \tau\tau$)cc	0.00 ± 0.00	0.18 ± 0.12	0.07 ± 0.07	0.00 ± 0.00
Z($\to \mu\mu$)lp	0.00 ± 0.00	0.30 ± 0.25	0.00 ± 0.00	0.37 ± 0.37
Z($\to \tau\tau$)lp	0.00 ± 0.00	0.18 ± 0.18	0.00 ± 0.00	0.00 ± 0.00
tb	0.00 ± 0.00	7.92 ± 0.13	2.33 ± 0.07	0.39 ± 0.03
tqb	0.00 ± 0.00	1.24 ± 0.07	1.47 ± 0.08	0.53 ± 0.05
ttlj	0.00 ± 0.00	9.75 ± 0.36	65.18 ± 0.95	74.93 ± 0.98
ttll	0.00 ± 0.00	30.70 ± 0.31	13.67 ± 0.22	2.77 ± 0.09
Total	0.00 ± 0.00	117.59 ± 3.04	99.93 ± 1.98	84.75 ± 1.70

jets p_T, $\not\!\!E_T$ and W transverse momentum and physics observables for CP violation analysis, we can know how well the $t\bar{t}$ signal and backgrounds composition estimated by the method in chapter 5 describes the attributes of the actual DØ data. Figures 5.3 to 5.17, show control plots for physics observables with before b-tagging and $\geq$ 2 b-tags that we would like to analyze. The other distributions for kinematic variables can be found in Appendix A. We can not find any significant discrepancy between the data and the Monte Carlo composition for physics observables and main kinematic variables. After requiring two or more b-tags, we can see that the background are significantly reduced and the $t\bar{t}$ signal is dominant. We measure asymmetries for CP violation analysis based on these data and Monte Carlo agreement and using the samples which include dominant $t\bar{t}$ signal obtained by the requirement of two or more b-tagged jets.

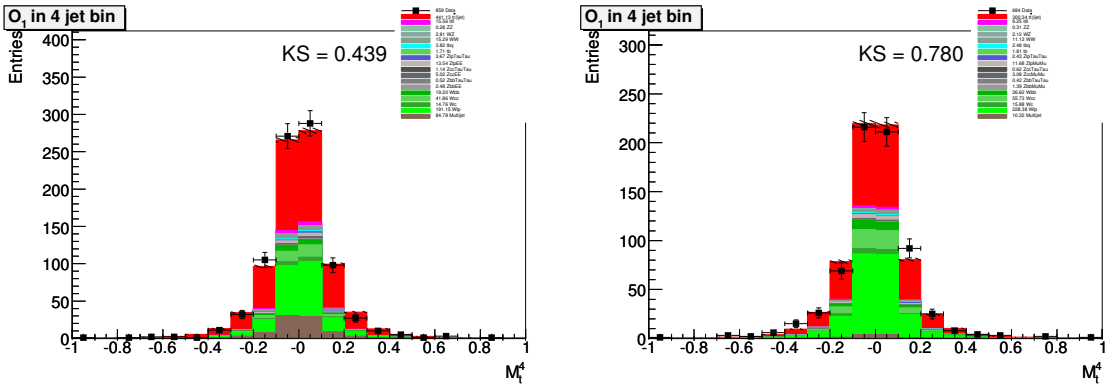

Figure 5.3: The comparison of Data and MC for O_1 with before b-tagging in e+4 jets channel (left) and μ+4 jets channel (right). The red contributions are $t\bar{t}$ events.

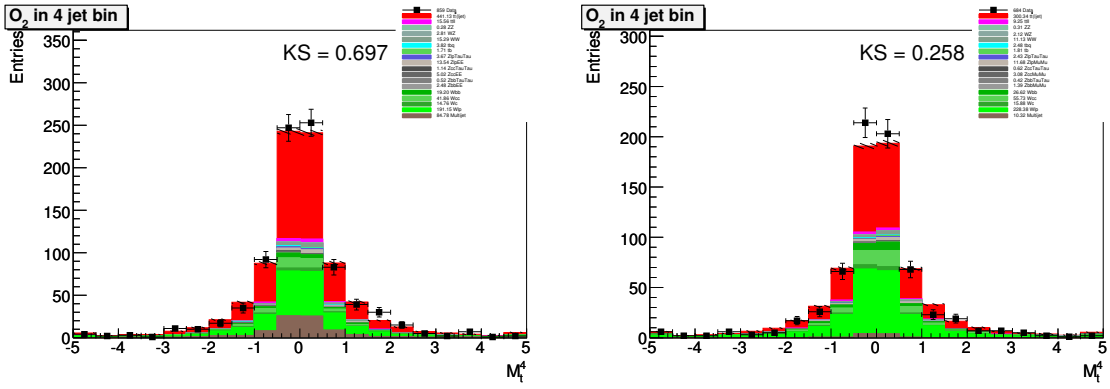

Figure 5.4: The comparison of Data and MC for O_2 with before b-tagging in e+4 jets channel (left) and μ+4 jets channel (right). The red contributions are $t\bar{t}$ events.

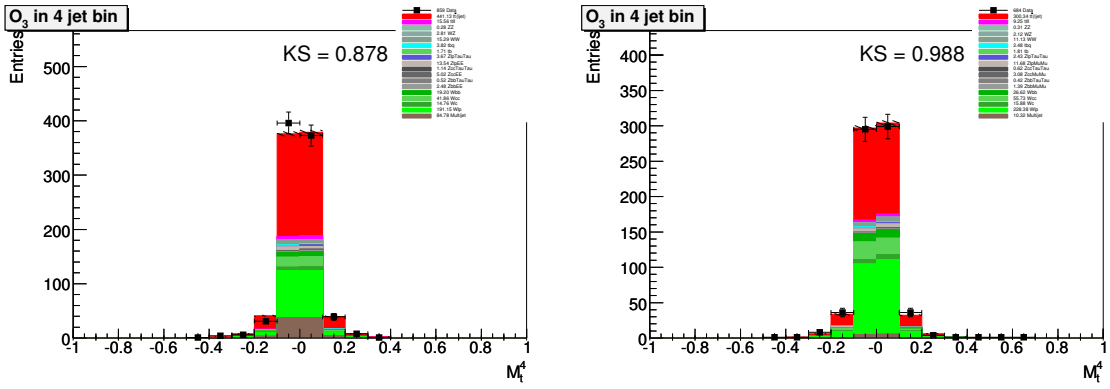

Figure 5.5: The comparison of Data and MC for O_3 with before b-tagging in e+4 jets channel (left) and μ+4 jets channel (right). The red contributions are $t\bar{t}$ events.

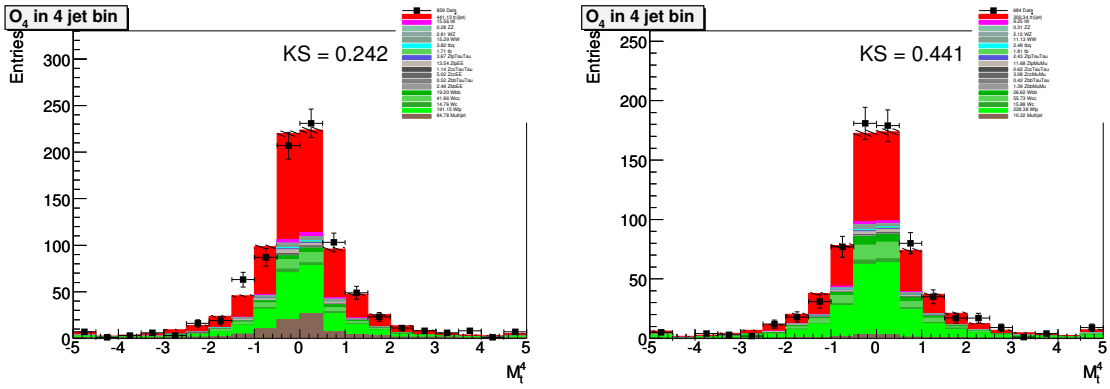

Figure 5.6: The comparison of Data and MC for O_4 with before b-tagging in e+4 jets channel (left) and μ+4 jets channel (right). The red contributions are $t\bar{t}$ events.

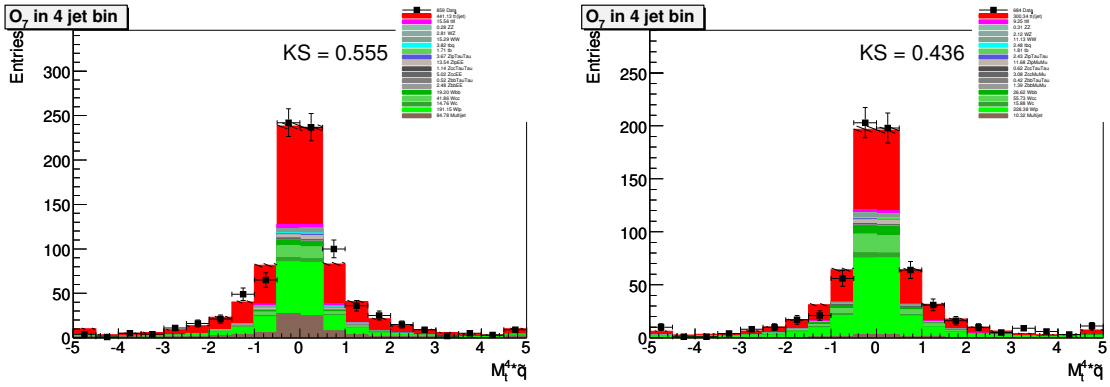

Figure 5.7: The comparison of Data and MC for O_7 with before b-tagging in e+4 jets channel (left) and μ+4 jets channel (right). The red contributions are $t\bar{t}$ events.

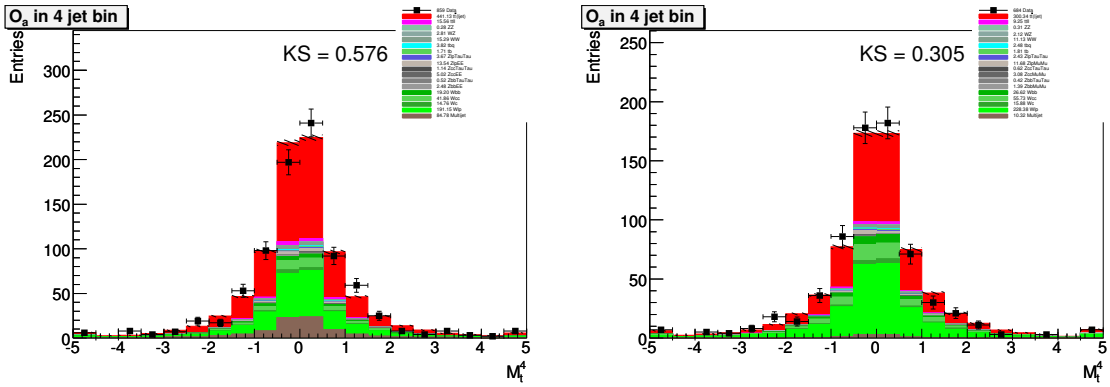

Figure 5.8: The comparison of Data and MC for O_a with before b-tagging in e+4 jets channel (left) and μ+4 jets channel (right). The red contributions are $t\bar{t}$ events.

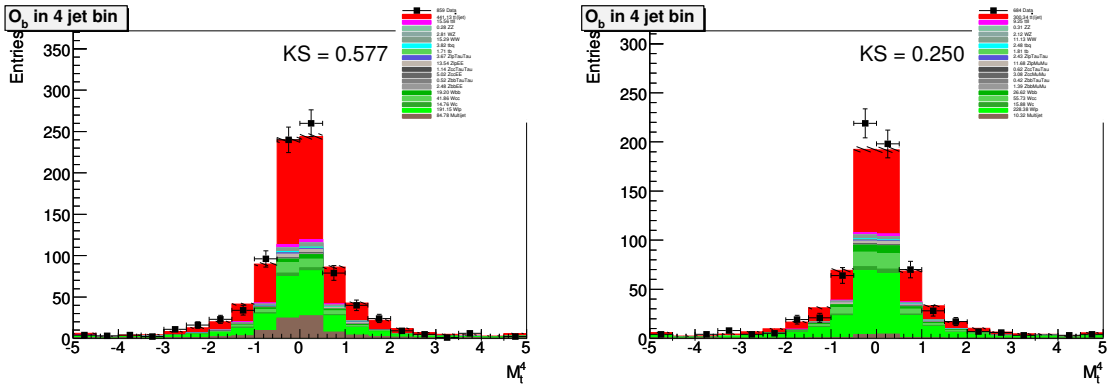

Figure 5.9: The comparison of Data and MC for O_b with before b-tagging in e+4 ets channel (left) and μ+j4 ets channel (right). The red contributions are $t\bar{t}$ events.

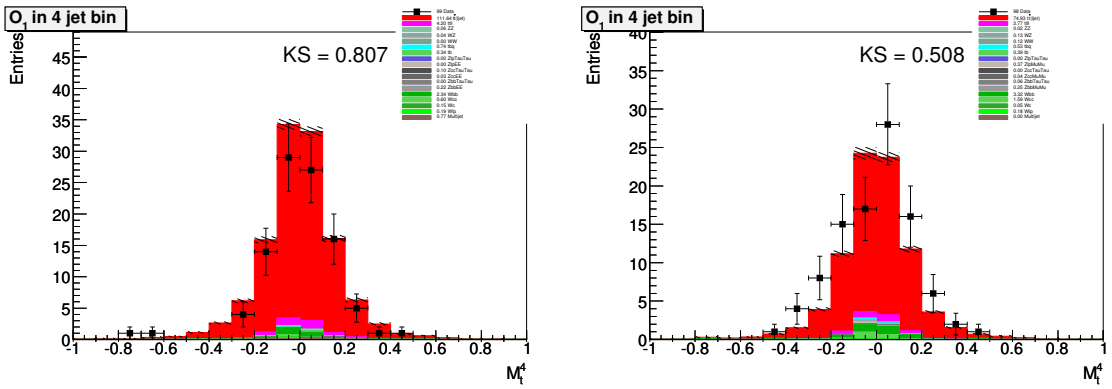

Figure 5.10: The comparison of Data and MC for O_1 with 2 b-tags in e+4 jets channel (left) and μ+4 jets channel (right). The two-b-tagged selection makes completely $t\bar{t}$ dominant in the sample.

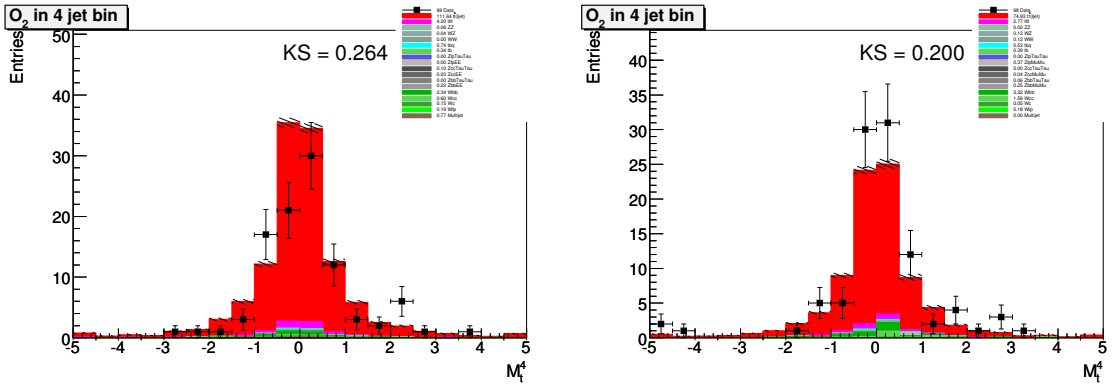

Figure 5.11: The comparison of Data and MC for O_2 with 2 b-tags in e+4 jets channel (left) and μ+4 jets channel (right). The two-b-tagged selection makes completely $t\bar{t}$ dominant in the sample.

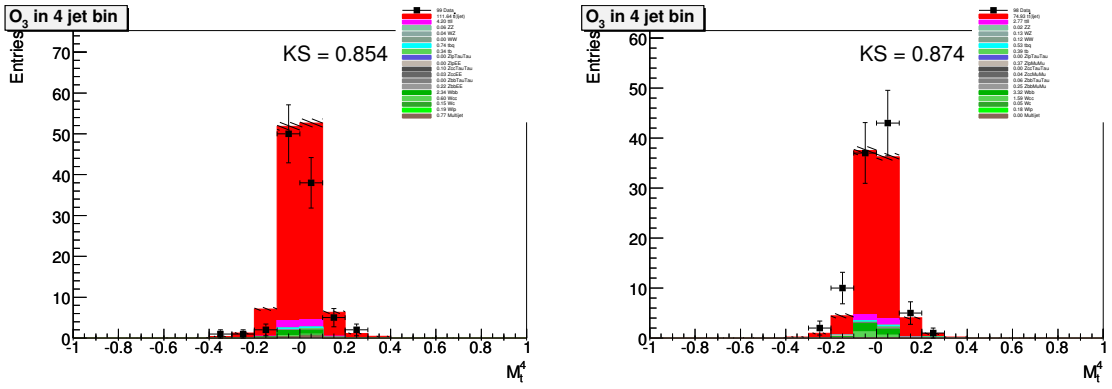

Figure 5.12: The comparison of Data and MC for O_3 with 2 b-tags in e+4 jets channel (left) and μ+4 jets channel (right). The two-b-tagged selection makes completely $t\bar{t}$ dominant in the sample.

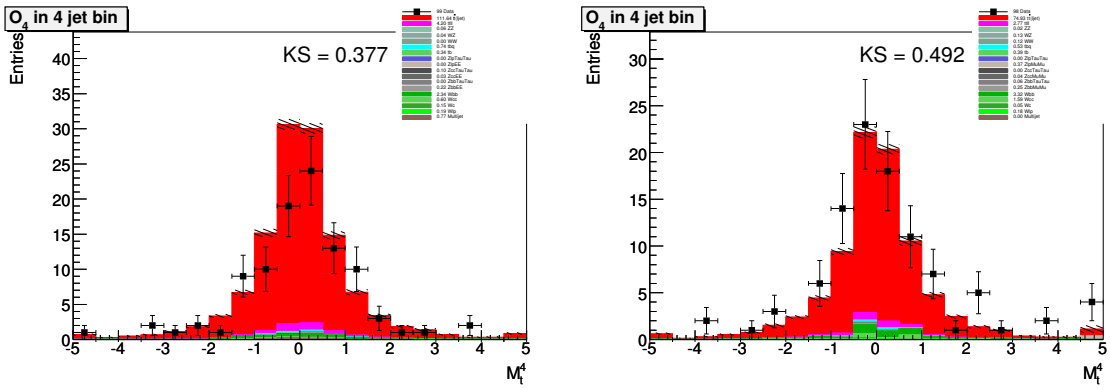

Figure 5.13: The comparison of Data and MC for O_4 with 2 b-tags in e+4 jets channel (left) and μ+4 jets channel (right). The two-b-tagged selection makes completely $t\bar{t}$ dominant in the sample.

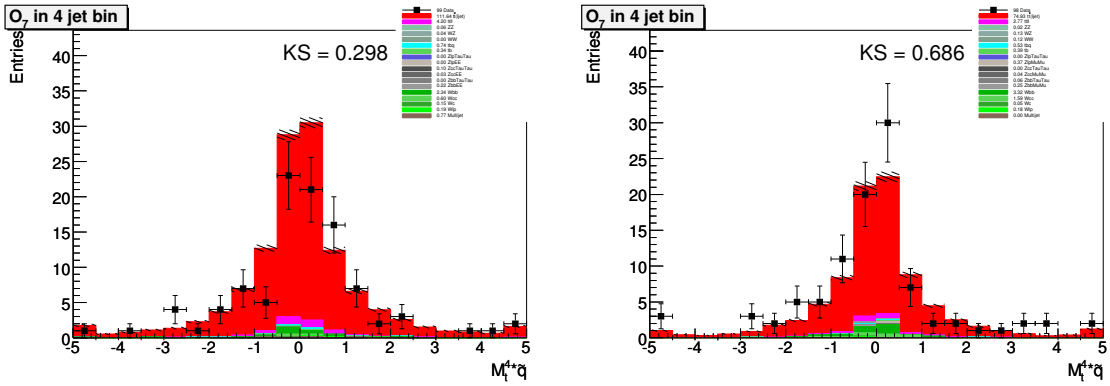

Figure 5.14: The comparison of Data and MC for O_7 with 2 b-tags in e+4 jets channel (left) and μ+4 jets channel (right). The two-b-tagged selection makes completely $t\bar{t}$ dominant in the sample.

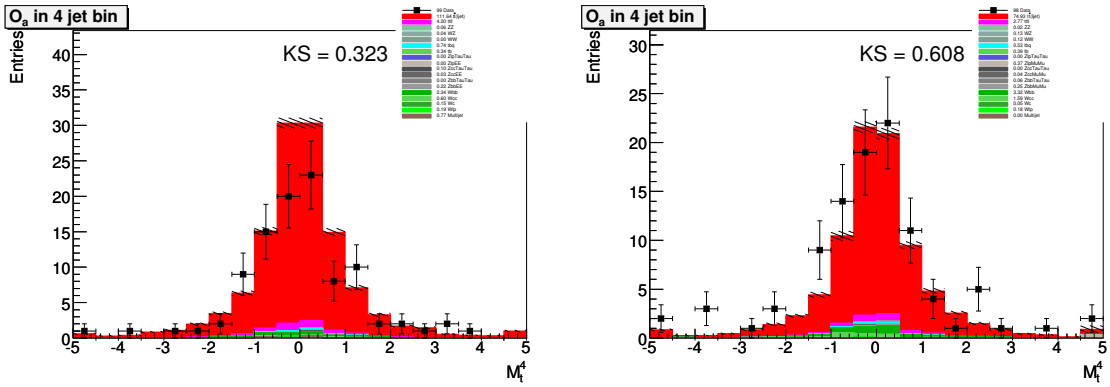

Figure 5.15: The comparison of Data and MC for O_a with 2 b-tags in e+4 jets channel (left) and μ+4 jets channel (right). The two-b-tagged selection makes completely $t\bar{t}$ dominant in the sample.

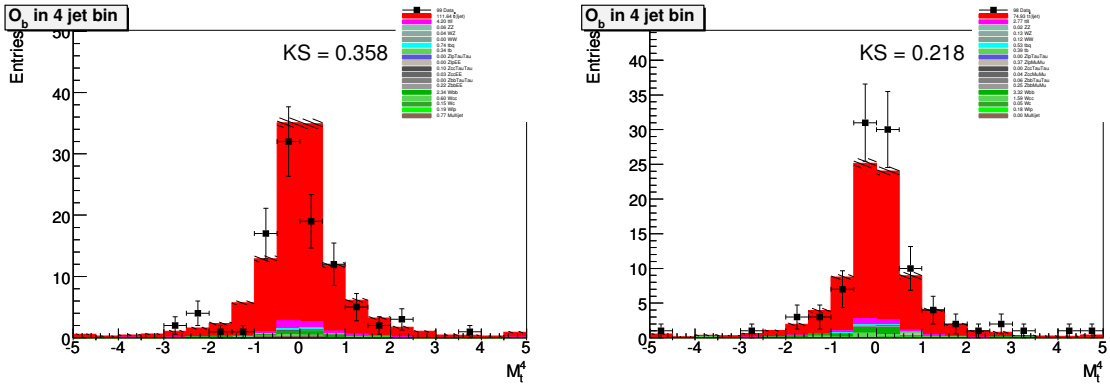

Figure 5.16: The comparison of Data and MC for O_b with 2 b-tags in e+4 ets channel (left) and μ+j4 ets channel (right). The two-b-tagged selection makes completely $t\bar{t}$ dominant in the sample.

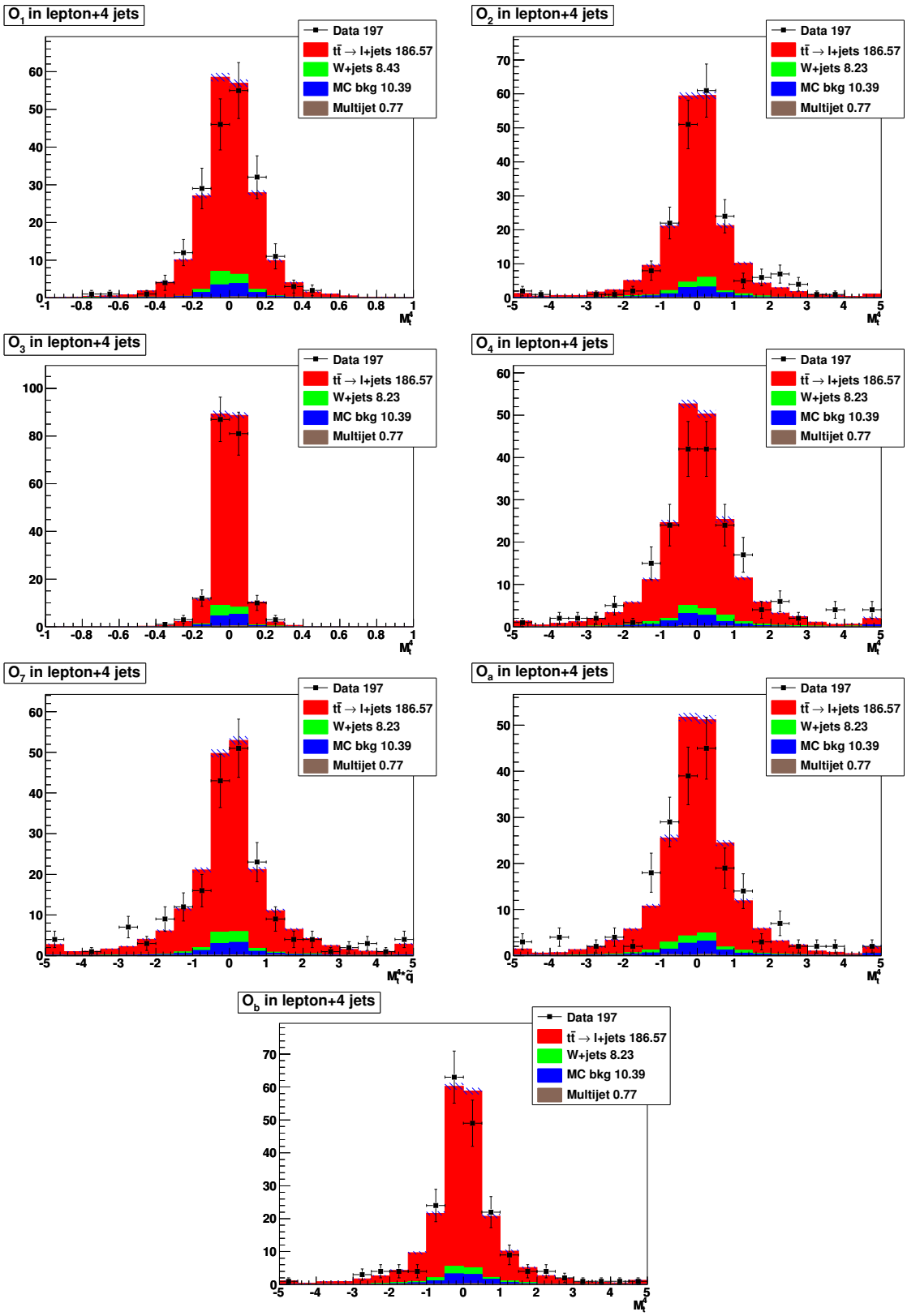

Figure 5.17: The comparison of Data and MC for all physics observables with 2 b-tags in lepton+4 jets channel. The two-b-tagged selection makes completely $t\bar{t}$ dominant in the sample.

CHAPTER 6. The Measurement of Asymmetry

6.1 The Measurement of Transverse Momentum

The physics observables described as Eq. 1.41 and 1.42 are the Levi-Civita tensor contracted with four vectors of reconstructed t and $\bar{t}$ quarks, b and $\bar{b}$ quark jets, light quark jet coming from hadronically decaying W boson, and lepton. These four vectors are reconstructed with transverse momentum and angular information of objects. Transverse momentum measurement of jets and lepton for the eight directions by DØ detector should not be significantly different so an not to give large bias to asymmetry measurement. The eight directions are referred to $(x, y, z), (-x, y, z), (-x, -y, z), (x, y, -z), (x, -y, z), (-x, -y, z), (-x, -y, -z)$ and $(x, -y, -z)$. These eight directions can be converted to ($\eta_{det} > 0$, $0 < \phi < \pi/2$), ($\eta_{det} > 0$, $\pi/2 < \phi < \pi$), ($\eta_{det} > 0$, $\pi < \phi < 3\pi/2$), ($\eta_{det} > 0$, $3\pi/2 < \phi < 2\pi$), ($\eta_{det} < 0$, $0 < \phi < \pi/2$), ($\eta_{det} < 0$, $\pi/2 < \phi < \pi$), ($\eta_{det} < 0$, $\pi < \phi < 3\pi/2$) and ($\eta_{det} < 0$, $3\pi/2 < \phi < 2\pi$). Using data and the $t\bar{t} \rightarrow l + jets$ Monte Carlo samples, the transverse momentum distributions for the eight directions are compared. Event selection criteria for the preselection described in section 5.1 is applied to both data and Monte Carlo samples. But the leading jet $p_T > 40$ GeV/c and the exactly 4 jets selection are not applied for more statistics. For Monte Carlo sample, the preselection efficiency is applied. All distributions are normalized to 1. Figure 6.1 shows jet p_T and electron p_T distributions for the eight directions for data and Monte Carlo in e+jets channel and Figure 6.2 are the comparison plots of the jet p_T and muon p_T in μ+jets channel. Both data and Monte Carlo don't have any large bias for measuring jet and lepton transverse momentum. Thus, the measurement of jet and lepton transverse momentum by the eight different segments of DØ detector can be considered that it does not contribute potential bias to the asymmetry measurement.

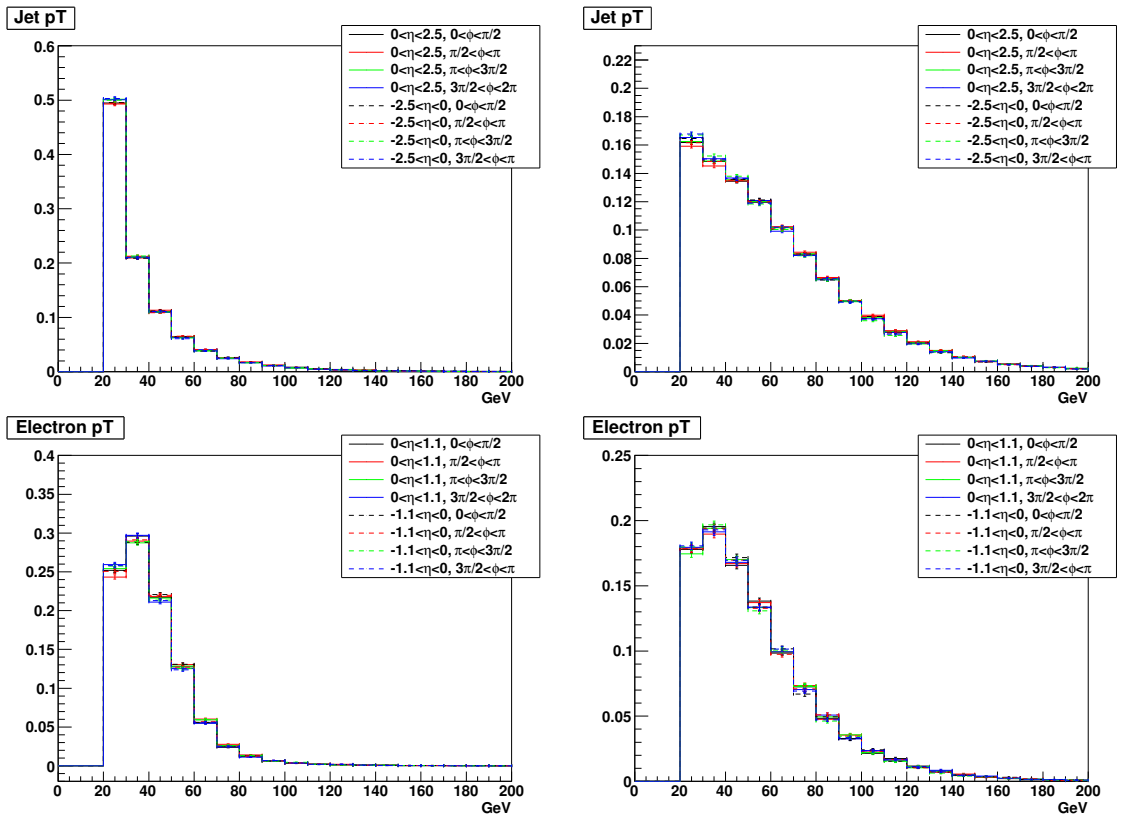

Figure 6.1: The transverse momentum distributions of jets in data (upper left) and Monte Carlo (upper right) and the transverse momentum distributions of electron in data (lower left) and Monte Carlo (lower right) for e+jets channel.

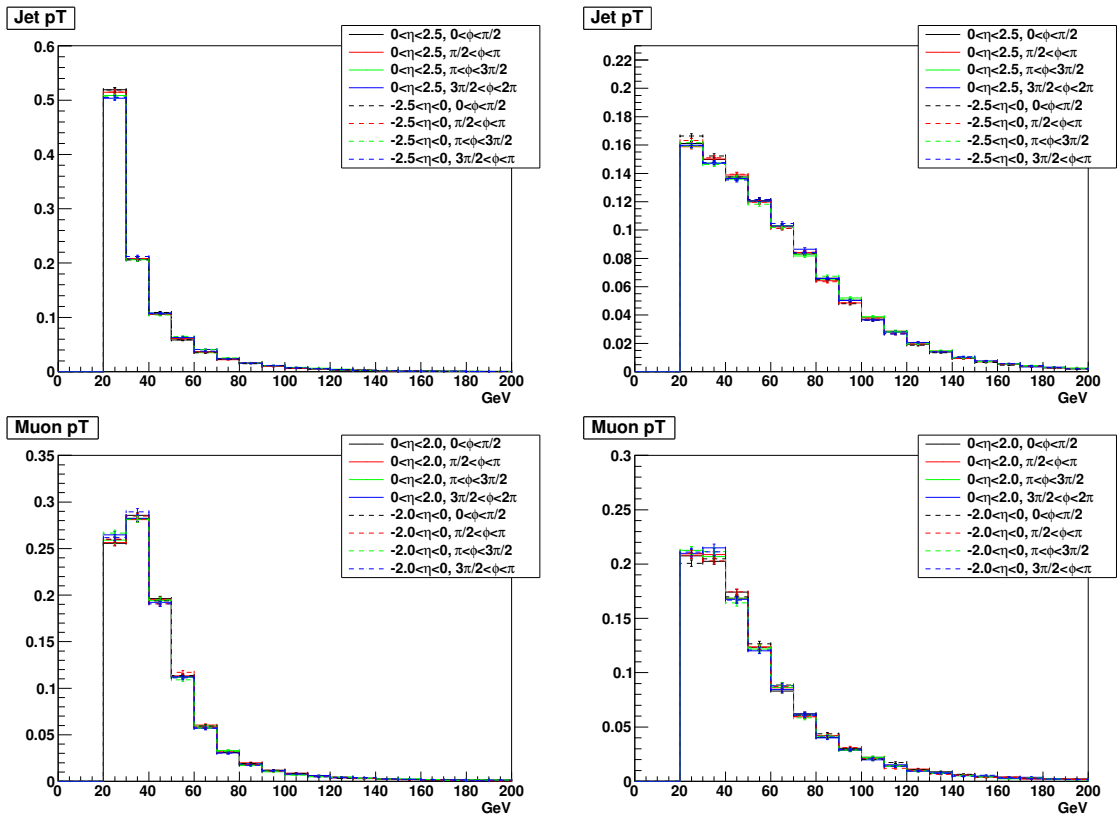

Figure 6.2: The transverse momentum distributions of jets in data (upper left) and Monte Carlo (upper right) and the transverse momentum distributions of muon in data (lower left) and Monte Carlo (lower right) for μ+jets channel.

6.2 Asymmetry Prediction

In chapter 1, the integrated counting asymmetry, Eq. 1.43, is constructed to measure CP-odd violating asymmetry. Using Eq. 1.43, asymmetries are measured with $t\bar{t} \to$ lepton+jets Monte Carlo truth information and DØ Monte Carlo which includes detector simulation, digitization and reconstruction. These asymmetry predictions by Monte Carlo truth information and DØ Monte Carlo are calculated with Standard Model (SM) ALPGEN+PYTHIA Monte Carlo sample. For Monte Carlo truth information, the final state particles such as b-quarks, light quarks, electron or muon and their neutrinos are found and they are confirmed to come from top quarks or W bosons by requiring parent or grand parent particles. Figures 6.3 and 6.4 drawn with Monte Carlo truth information are distributions of physics observables for $t\bar{t} \to W^+bW^-\bar{b} \to q\bar{q}'be^-\bar{\nu}_{e^-}\bar{b} + e^+\nu_{e^+}bq\bar{q}'\bar{b}$ and $t\bar{t} \to W^+bW^-\bar{b} \to q\bar{q}'b\mu^-\bar{\nu}_{\mu^-}\bar{b} + \mu^+\nu_{\mu^+}bq\bar{q}'\bar{b}$, respectively. For DØ Monte Carlo, events are selected with the event selection criteria introduced in section 5.1, event corrections are applied, the preselection efficiency and the b-tag probability are multiplied to the sample. Figures 6.5 and 6.6 show distributions of physics observables for e+4 jets and μ+4 jets channels drawn with DØ Monte Carlo samples. Based on Figures 6.3, 6.4, 6.5 and 6.6, the asymmetry for each physics observable is calculated. Calculated asymmetries are shown in Tables 6.1 and 6.2. ALPGEN generator predicts all CP-odd asymmetries are 0 and also asymmetries predicted with DØ Monte Carlo prediction are consistent with 0. The DØ Monte Carlo prediction implies the no bias is produced by the DØ detector, event selection, event corrections and b-tagging.

Table 6.1: Asymmetry prediction with Monte Carlo truth information and reconstructed Monte Carlo event information for e+jets.

	Monte Carlo truth information	DØ Monte Carlo information
O_1	$+0.0004 \pm 0.0021$	-0.0084 ± 0.0126
O_2	$+0.0016 \pm 0.0021$	$+0.0001 \pm 0.0126$
O_3	$+0.0005 \pm 0.0021$	-0.0033 ± 0.0126
O_4	-0.0024 ± 0.0021	-0.0074 ± 0.0126
O_7	$+0.0010 \pm 0.0021$	$+0.0186 \pm 0.0126$
O_a	-0.0019 ± 0.0021	$+0.0049 \pm 0.0126$
O_b	$+0.0033 \pm 0.0021$	$+0.0010 \pm 0.0126$

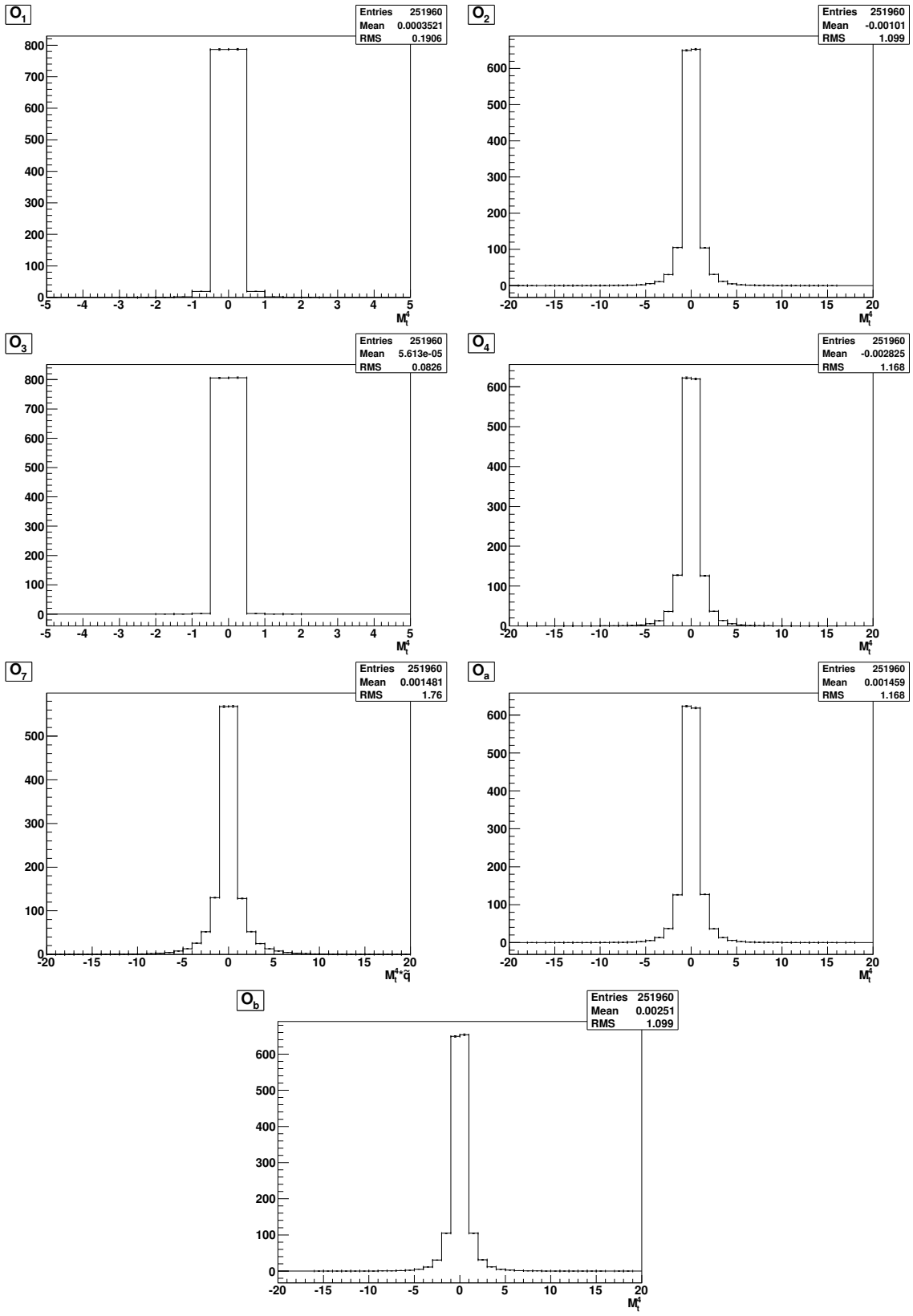

Figure 6.3: The distributions of physics observables for $t\bar{t} \rightarrow W^+bW^-\bar{b} \rightarrow q\bar{q}'be^-\bar{\nu}_{e^-}\bar{b} + e^+\nu_{e^+}bq\bar{q}'\bar{b}$ derived with Monte Carlo truth information.

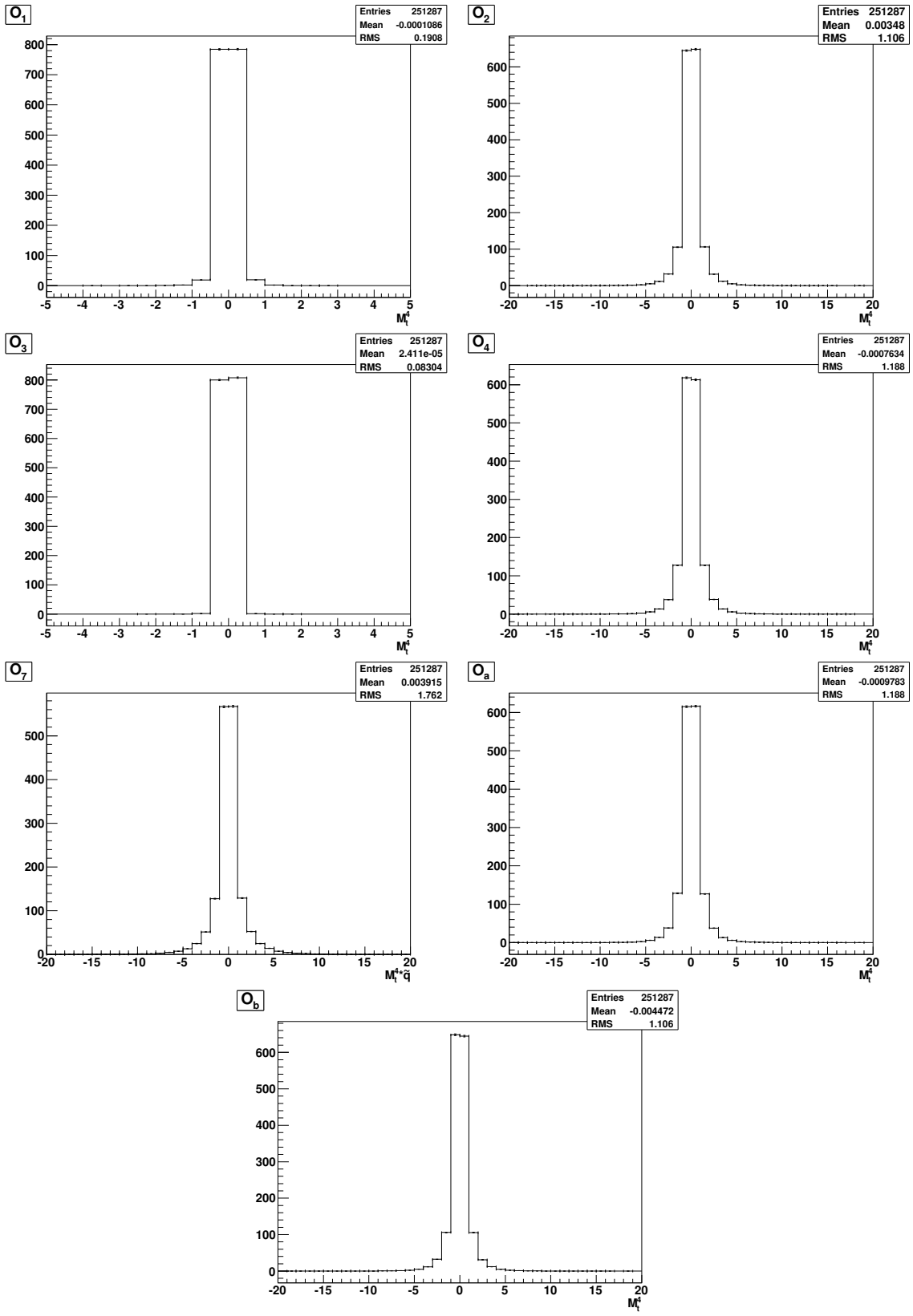

Figure 6.4: The distributions of physics observables for $t\bar{t} \rightarrow W^+bW^-\bar{b} \rightarrow q\bar{q}'b\mu^-\bar{\nu}_{\mu^-}\bar{b} + \mu^+\nu_{\mu^+}bq\bar{q}'\bar{b}$ derived with Monte Carlo truth information.

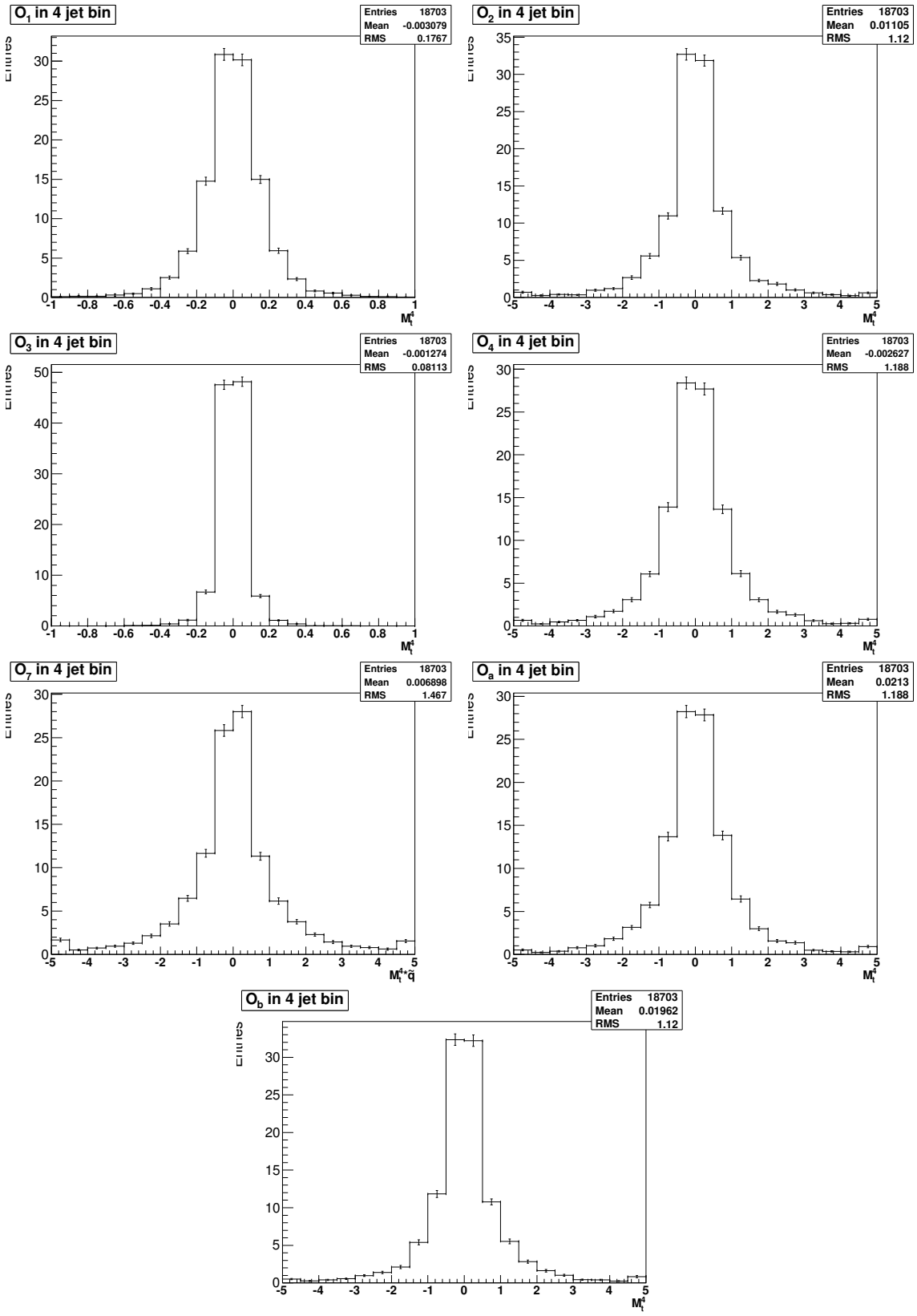

Figure 6.5: The distributions of physics observables for e+4 jets. Distributions are normalized using $\sigma_{t\bar{t}} = 8.13$ pb.

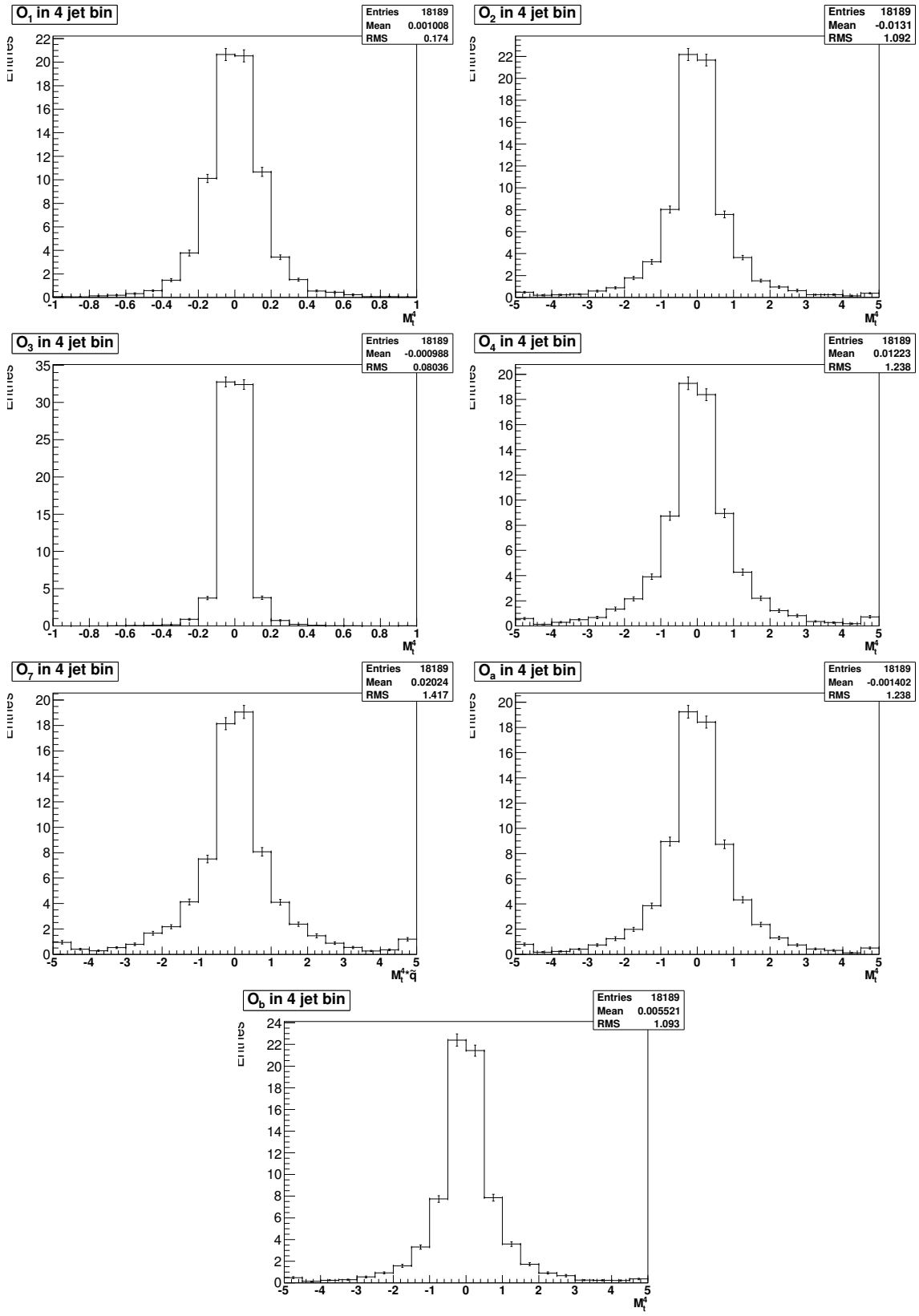

Figure 6.6: The distributions of physics observables for μ+4 jets. Distributions are normalized using $\sigma_{t\bar{t}} = 8.13$ pb.

Table 6.2: Asymmetry prediction with Monte Carlo truth information and reconstructed Monte Carlo event information for μ+jets.

	Monte Carlo truth information	DØ Monte Carlo information
O_1	$+0.0003 \pm 0.0021$	$+0.0027 \pm 0.0131$
O_2	$+0.0028 \pm 0.0021$	-0.0116 ± 0.0131
O_3	$+0.0045 \pm 0.0021$	-0.0061 ± 0.0131
O_4	-0.0026 ± 0.0021	-0.0031 ± 0.0131
O_7	$+0.0025 \pm 0.0021$	$+0.0235 \pm 0.0131$
O_a	-0.0006 ± 0.0021	-0.0049 ± 0.0131
O_b	-0.0034 ± 0.0021	-0.0055 ± 0.0131

6.3 Asymmetry Extraction

Asymmetry is extracted using a maximum likelihood fit. The likelihood function is defined as:

$$L(\sigma_{t\bar{t}}, A_{O_i}) = [\prod_i \mathcal{P}(N_i^{obs}, N_i^{pred})] \cdot \mathcal{P}(N_{l-t}^{obs}, N_{l-t}^{pred}) \tag{6.1}$$

where $\sigma_{t\bar{t}}$ is the fitted $t\bar{t}$ cross section. $\mathcal{P}(N_i^{obs}, N_i^{pred})$ represents the Poisson probability density function that we find N_i^{obs} observed events when the the predicted events N_i^{pred} is given. In Eq. 6.1, i runs over the positive and negative regions of O_i. Thus, N_i^{obs} is the number of selected data in the positive or negative regions of O_i and N_i^{pred} is the predicted number of events in the positive or negative regions of O_i. N_i^{pred} is a function of two fitting parameters, $\sigma_{t\bar{t}}$ and A_{O_i}:

$$\begin{aligned} N_i^{pred} &= N_t^{t\bar{t}} \frac{1+A}{2} f_i^{O_i>0}(1-C) + N_t^{t\bar{t}} \frac{1-A}{2} f_i^{O_i<0}(1-C) + N_t^W f_i^W (1-C) \\ &+ N_i^{MC} f_i^{MC}(1-C) + (N_t^{multijets} + C(N_t^{t\bar{t}} + N_t^W + N_i^{MC})) f_i^{multijet} \end{aligned} \tag{6.2}$$

$$C = \frac{1-\epsilon_{sig}}{\epsilon_{sig}} \frac{\epsilon_{qcd}}{1-\epsilon_{qcd}} \tag{6.3}$$

where A_{O_i} is the fitted asymmetry and f_i is the event fraction for each positive and negative region of O_i in each background template. First term represents the number of the $t\bar{t}$ signal for the positive region and the second term is the number of the $t\bar{t}$ signal for the negative

region. Thus, when N_i^{pred} predicts the number of events for the positive region, $f_i^{O_i>0} = 1$ and $f_i^{O_i<0} = 0$. On the contrary, when N_i^{pred} predicts the number of events for the negative region, $f_i^{O_i>0} = 0$ and $f_i^{O_i<0} = 1$. Also, C plays a role as a factor that scales the $t\bar{t}$ signal and physics backgrounds to the tight multijet sample and enables us to estimate the contamination of the multijet template by the $t\bar{t}$ signal and the other physics background. In Eq. 6.2, $N_t^{t\bar{t}}$ is the function of the $t\bar{t}$ cross section and can be written as Eq. 6.4. Thus, we can extract the asymmetry and the $t\bar{t}$ cross section simultaneously.

$$N_t^{t\bar{t}} = \epsilon^{presel} \cdot P^{b-tag} \cdot Br \cdot \sigma_{t\bar{t}} \cdot \mathcal{L} \tag{6.4}$$

We use the preselection efficiencies and b-tag probabilities described in Table 5.5. In Eq. 6.1, the second term is a Poisson constraint consisting of the observed number of events in the loose - tight data sample and the predicted number of events for loose - tight sample. The contamination by the signal and other physics backgrounds is taken into account to the prediction.

$$N_{l-t}^{pred} = \frac{1-\epsilon_{signal}}{\epsilon_{signal}}(N_t^{t\bar{t}} + N_t^W + N_t^{MC}) + \frac{1-\epsilon_{QCD}}{\epsilon_{QCD}} N_t^{multijet} \tag{6.5}$$

The predicted number for loose - tight can be derived using matrix method introduced in section 5.2.1. First, if we express N_l and N_t in terms of $N_l^{t\bar{t}}, N_l^{W+jets}, N_l^{MC}$ and $N_l^{multijet}$.

$$N_l = N_l^{t\bar{t}} + N_l^{W+jets} + N_l^{MC} + N_l^{multijet} \tag{6.6}$$

$$N_t = \epsilon_{sig} N_l^{t\bar{t}} + \epsilon_{sig} N_l^{W+jets} + \epsilon_{sig} N_l^{MC} + \epsilon_{qcd} N_l^{multijet}, \tag{6.7}$$

then the individual components can be written as:

$$N_t^{t\bar{t}} = \epsilon_{sig} N_l^{t\bar{t}},\ N_t^{W+jets} = \epsilon_{sig} N_l^{W+jets},\ N_t^{MC} = \epsilon_{sig} N_l^{MC},\ N_t^{multijet} = \epsilon_{qcd} N_l^{multijet} \tag{6.8}$$

By subtracting Eq. 6.7 from Eq. 6.6 and using relations of the individual components in Eq. 6.8, the predicted numbers of events for loose - tight can be obtained as Eq. 6.5. To extract asymmetry, the negative log likelihood function is minimized:

$$-\log\, L(\sigma_{t\bar{t}}, A_{O_i}) \simeq \sum_i (-N_i^{obs}\, \log\, N_i^{pred} + N_i^{pred}) - N_{l-t}^{obs}\, \log\, N_{l-t}^{pred} + N_{l-t}^{pred} \tag{6.9}$$

This maximum likelihood fit with fitting parameters, asymmetry and $t\bar{t}$ cross section, finds a $t\bar{t}$ cross section (or the number of events in the $t\bar{t}$ signal) and an asymmetry simultaneously which gives the best Poisson probability.

6.3.1 Asymmetry and Cross Section

We perform the maximum likelihood fit for e+4 jets and μ+4 jets samples selected with $\geq$2 b-tags. The asymmetry and cross section results include only statistical uncertainties in Table 6.3 and 6.4. Table 6.3 shows the measured asymmetries for all physics observables. The measured $t\bar{t}$ cross section results are shown in Table 6.4. These cross section results are

Table 6.3: The measured asymmetries for all physics observables for e+jets, μ+jets and lepton+jets channels. The uncertainties are statistical only.

	e+jets	μ+jets	lepton+jets
O_1	$0.007^{+0.115}_{-0.115}$ (stat.)	$0.097^{+0.111}_{-0.112}$ (stat.)	$0.053^{+0.081}_{-0.081}$ (stat.)
O_2	$0.128^{+0.113}_{-0.115}$ (stat.)	$0.090^{+0.111}_{-0.112}$ (stat.)	$0.106^{+0.080}_{-0.081}$ (stat.)
O_3	$-0.117^{+0.115}_{-0.114}$ (stat.)	$0.015^{+0.112}_{-0.112}$ (stat.)	$-0.049^{+0.081}_{-0.080}$ (stat.)
O_4	$0.098^{+0.114}_{-0.115}$ (stat.)	$-0.006^{+0.112}_{-0.112}$ (stat.)	$0.046^{+0.081}_{-0.081}$ (stat.)
O_7	$0.079^{+0.114}_{-0.115}$ (stat.)	$0.001^{+0.112}_{-0.112}$ (stat.)	$0.039^{+0.081}_{-0.081}$ (stat.)
O_a	$-0.010^{+0.115}_{-0.115}$ (stat.)	$-0.040^{+0.112}_{-0.112}$ (stat.)	$-0.025^{+0.081}_{-0.081}$ (stat.)
O_b	$-0.182^{+0.115}_{-0.113}$ (stat.)	$0.073^{+0.111}_{-0.112}$ (stat.)	$-0.053^{+0.081}_{-0.080}$ (stat.)

consistent with those of the cross section measurement in [47], which measured the $t\bar{t}$ cross section using three jet and four or more jet events with 1 b-tag and $\geq$ 2 b-tags.

Table 6.4: The measured cross section results for e+jets, μ+jets and lepton+jets. The uncertainties are statistical only.

	e+jets [pb]	μ+jets [pb]	lepton+jets [pb]
$\geq$2 b-tagged events	$6.51^{+0.69}_{-0.65}$ (stat.)	$9.42^{+1.06}_{-0.99}$ (stat.)	$7.59^{+0.58}_{-0.55}$ (stat.)

6.4 The Dilution of Asymmetry

In Eq. 1.41, O_3, O_4 and O_b include Q_l (lepton charge) term and O_2, O_4, O_7, O_a and O_b have $(p_b - p_{\bar{b}})$ or $(p_b + p_{\bar{b}})$ terms. These charge, $(p_b - p_{\bar{b}})$ and $(p_b + p_{\bar{b}})$ terms may lead these variables to have random sign and dilute asymmetry. In this section, asymmetry dilution by these terms is investigated.

6.4.1 Charge Misidentification

The lepton charge term may lead O_3, O_4 and O_b to have random sign due to a charge misidentification which is caused by the limited ability of tracking detectors. High momentum track of a lepton can be almost a straight line under a magnetic field and the charge of a lepton can be misidentified due to the curvature uncertainty. To derive the charge misidentification probabilities for electron and muon, we used the data samples which contain two high p_T electrons or muons and whose integrated luminosities are 4281.66 pb^{-1}, and $Z \rightarrow ee$ and $Z \rightarrow \mu\mu$ Monte Carlo samples. Lepton selection criteria are exactly same as those introduced in section 5.1 except events which contains jet or jets is rejected and two electrons or muons are required in a event. To keep good $Z \rightarrow ee$ and $Z \rightarrow \mu\mu$ events, Z mass window 70 GeV/c^2 – 110 GeV/c^2 cut is applied to both selected data and Monte Carlo events. Figure 6.7 shows invariant mass distributions reconstructed with two electrons in data and Monte Carlo and Figure 6.8 are invariant mass distributions reconstructed with two muons in data and Monte Carlo. As Figure 6.7 and 6.8 show, the Z mass peaks are well reconstructed and these leptons can be considered to come from the Z boson decay with good confidence.

Let us set f_1 and f_2 as probabilities that charges of two elections or muons are misidentified. The product of two charges can be established as Eq. 6.10 [62].

$$q_1 q_2 \;=\; f_1 f_2 \times (-1) + (1-f_1) f_2 \times (+1) + (1-f_2) f_1 \times (+1) + (1-f_1)(1-f_2) \times (-1) \quad (6.10)$$

Eq. 6.10 can be reduced to Eq. 6.11.

$$q_1 q_2 \;=\; (1-2f_1)(1-2f_2) \quad (6.11)$$

If charges of both electron and positron or muon and antimuon are misidentified with an equal probability, i.e. $f_1 = f_2 = f$, Eq. 6.11 becomes

$$q_1 q_2 \;=\; -(1-2f)^2$$

or

$$4f^2 - 4f + (1 + q_1 q_2) \;=\; 0 \quad (6.12)$$

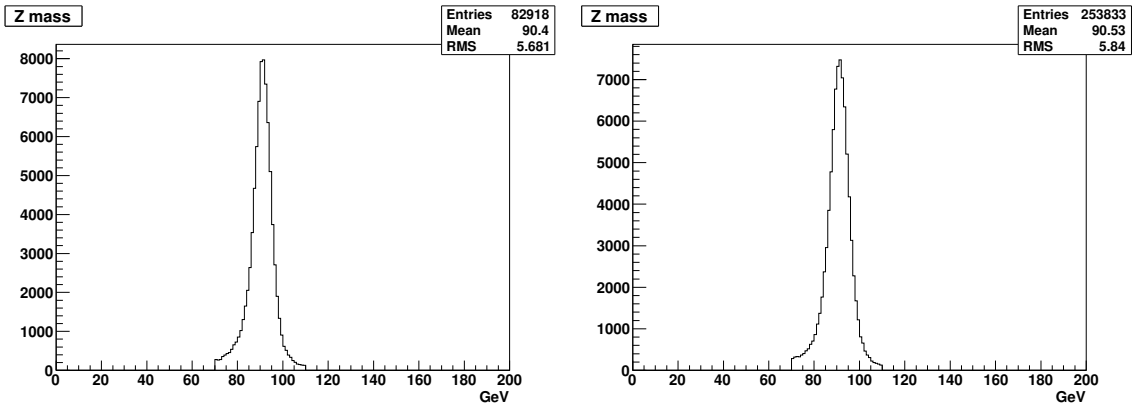

Figure 6.7: Z→ee mass distributions for data (left) and MC (right).

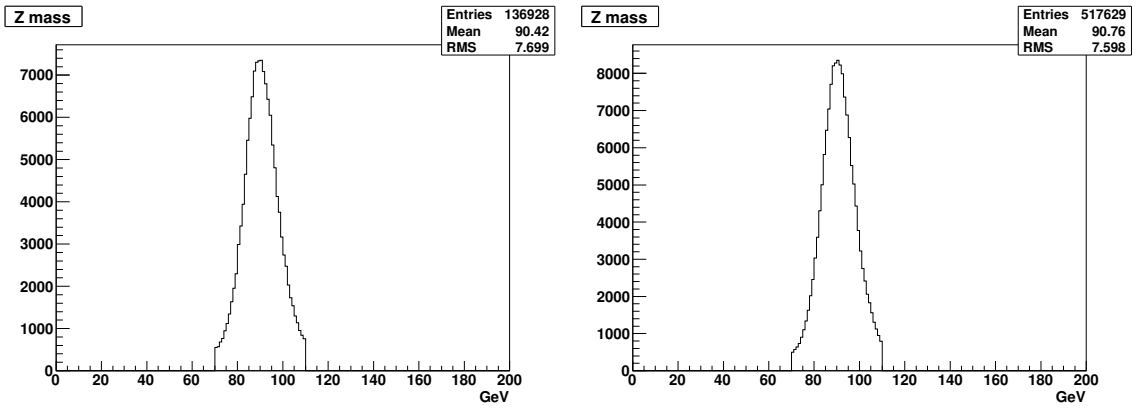

Figure 6.8: Z→ $\mu\mu$ mass distributions for data (left) and MC (right).

By solving Eq 6.13, we can get Eq. 6.13.

$$f = \frac{1 \pm \sqrt{|q_1 q_2|}}{2} \tag{6.13}$$

When the product of $q_1 q_2$ is negative, we take "-" sign and "+" sign is taken when the product of $q_1 q_2$ is positive. Figures 6.9 and 6.10 are distributions of the product of $q_1 q_2$ for $Z \to ee$ and $Z \to \mu\mu$ in data and Monte Carlo samples, respectively.

Using Eq. 6.13 and the distributions in Figures 6.9 and 6.10, the charge misidentification probabilities are derived for data and Monte Carlo and shown in Table 6.5 and 6.6. Data and Monte Carlo have different charge misidentification probabilities. The derived charge misidentification probabilities are consistent with those described in the measurement of the $t\bar{t}$ production cross section in dilepton final state analysis [64].

Table 6.5: Electron charge misidentification probability (in %).

	Data (%)	MC (%)
-1.1 $< \eta_{det} <$ 1.1	0.276	0.071

Table 6.6: Muon charge misidentification probability (in %).

	Data (%)	MC (%)
-2.0 $< \eta_{det} <$ 2.0	0.011	0.005

According to the charge misidentification probabilities, the number of charge-misidentified events is evaluated for both data and Monte Carlo and the number of events is changed for both data and Monte Carlo to see how asymmetry is shifted. Two worst cases are assumed:

1. when charges of events in the positive region of O_i are misidentified but those in the negative region are identified correctly, these events should move to the negative region, where $i = 3, 4, b$. This case is denoted as the subscript "$_{+\to-}$" in Table 6.7, 6.8 and 6.9.

2. when charges of events in the negative region of O_i are misidentified but those in the positive region are identified correctly, these events should move to the positive region, where $i = 3, 4, b$. This case is denoted as the subscript "$_{-\to+}$" in Table 6.7, 6.8 and 6.9

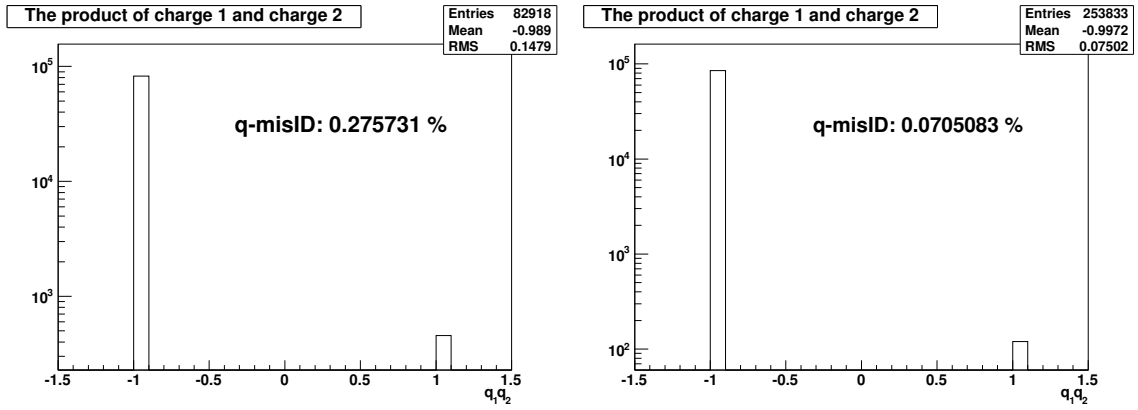

Figure 6.9: The products of charges of two electrons in Z→ee channel for data (left) and MC (right)

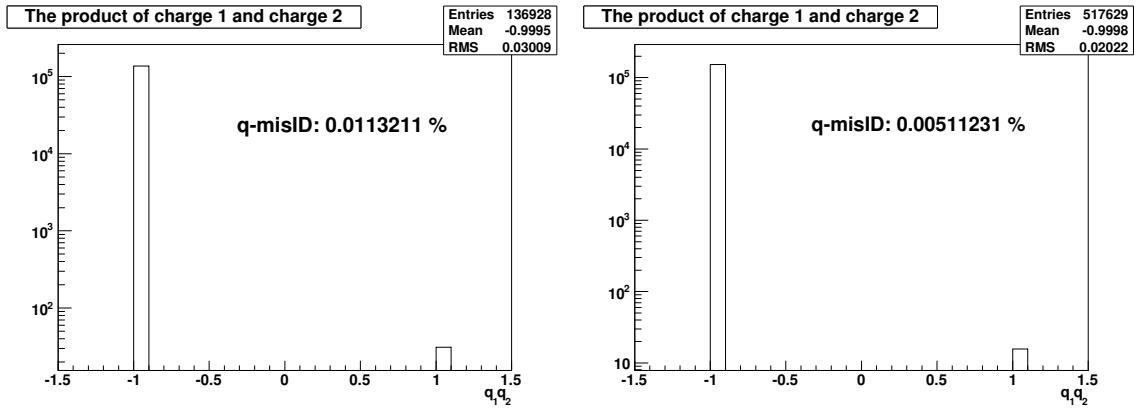

Figure 6.10: The products of charges of two muons in Z→ $\mu\mu$ channel for data (left) and MC (right)

After changing the number of events for both data, the $t\bar{t}$ signal and all backgrounds for each case, the maximum likelihood fit is performed and asymmetry for each O_i, where $i = 3, 4, b$ is extracted. The asymmetry shifts by charge misidentification for e+jets, μ+jets and lepton+jets channels are shown in Table 6.7, 6.8 and 6.9. The $\sigma_{+\to-}$ is evaluated by subtracting $A_{central}$ from $A_{+\to-}$ ($A_{+\to-} - A_{central}$) and subtracting $A_{central}$ from $A_{-\to+}$ ($A_{-\to+} - A_{central}$) gives asymmetry shift $\sigma_{-\to+}$.

Table 6.7: Asymmetry shifts by charge misidentification in e+jets channel.

	$A_{central}$	$A_{+\to-}$	$A_{-\to+}$	$\sigma_{+\to-}$	$\sigma_{-\to+}$
O_3	-0.117	-0.119	-0.114	-0.002	0.003
O_4	0.098	0.095	0.100	-0.003	0.002
O_b	-0.182	-0.184	-0.179	-0.002	0.003

Table 6.8: Asymmetry shifts by charge misidentification in μ+jets channel.

	$A_{central}$	$A_{+\to-}$	$A_{-\to+}$	$\sigma_{+\to-}$	$\sigma_{-\to+}$
O_3	0.015	0.014	0.015	-0.001	0.000
O_4	-0.006	-0.006	-0.005	0.000	0.001
O_b	0.073	0.073	0.074	0.000	0.001

Table 6.9: Asymmetry shifts by charge misidentification in lepton+jets channel.

	$A_{central}$	$A_{+\to-}$	$A_{-\to+}$	$\sigma_{+\to-}$	$\sigma_{-\to+}$
O_3	-0.049	-0.050	-0.048	-0.001	0.001
O_4	0.046	0.044	0.047	-0.002	0.001
O_b	-0.053	-0.054	-0.051	-0.001	0.002

According to Table 6.7, 6.8 and 6.9, the shift by charge misidentification is 0.3% at most. The asymmetry shifts by charge misidentification are considered as a factor in asymmetry dilution.

6.4.2 A Different Calorimeter Response to $b/\bar{b}$ Quark Jets

The sign of physics observables O_i which include $(p_b - p_{\bar{b}})$ or $(p_b + p_{\bar{b}})$ terms can be assigned randomly due to a different calorimeter response to b and $\bar{b}$ quark jets. First off, the transverse momentum distributions of b and $\bar{b}$ are checked in the $t\bar{t}$ signal Monte Carlo sample since flavors of jets can be found by matching reconstructed jets with parton level information in Monte Carlo events. To check a different calorimeter response, b and $\bar{b}$ quark jets are found by matching a reconstructed jet to b or $\bar{b}$ quark in the selected $t\bar{t}$ Monte Carlo sample. This selected $t\bar{t}$ Monte Carlo sample is a set of events which pass event selection criteria described in section 5.1 but leading jet $p_T > 40$ GeV/c cut is not required for more statistics. Figure 6.11 shows the comparison of the transverse momentum distributions of b and $\bar{b}$ quark jets in e+4 jets and μ+4 jets samples. In Figure 6.11, lower left and right plots are drawn by dividing the transverse momentum distribution of b quark jet by that of $\bar{b}$ quark jet. As the lower left and right plots show, the ratios of the transverse momentum distributions of b and $\bar{b}$ quark jets for e+4 jets and μ+4 jets channels are almost flat and about 1. In addition, mean values for the distributions of b and $\bar{b}$ quark jets in e+jets channel are $p_T^{b-quark\ jet} = 65.62 \pm 0.14$ GeV/c and $p_T^{\bar{b}-quark\ jet} = 65.69 \pm 0.15$ GeV/c, respectively, and those in μ+jets channel are $p_T^{b-quark\ jet} = 66.11 \pm 0.15$ GeV/c and $p_T^{\bar{b}-quark\ jet} = 65.75 \pm 0.15$ GeV/c, respectively. These demonstrate there is no difference between calorimeter responses for b and $\bar{b}$ quark jets in Monte Carlo simulation at least.

But in the analysis that performed a measurement of the mass difference between top and antitop quarks [65], a different calorimeter response for b and $\bar{b}$ quark jets was studied using data. The main idea is that the different calorimeter responses of b and $\bar{b}$ quark jets resulted from a different content of K^+ and K^- mesons whose inelastic nuclear cross sections are different. To estimate the different calorimeter response of b and $\bar{b}$ quark jets in data, $b\bar{b}$ QCD events are selected with cuts which require $p_T^{jet} > 15$ GeV/c, $p_T^{jet1} + p_T^{jet2} > 60$ GeV/c, $\Delta\phi(jet1, jet2) > 2.5$, and exactly two b-tags. A soft muon is required to be inside a jet cone ($\Delta R < 0.5$) for one of two b-tagged jets. This jet associated with a soft muon is referred to as the tag jet and the other jet is referred to as the probe jet. By identifying the charge of

the muon, the tag jet can be determined as either b or $\bar{b}$ quark-like jets. The difference of the transverse momentum between the tag and probe jets is defined as $\Delta p_T \equiv p_T^{tag} - p_T^{probe}$. Figure 6.12 shows the distributions of $< p_T >^-$ and $< p_T >^+$, where '-', '+' signs in the superscripts stand for the tag jet which has the negatively charged and the positively charged muons inside the jet cone, respectively. From the distributions, the mean values $< p_T >^- = -10.77 \pm 0.08$ GeV and $< p_T >^+ = -10.60 \pm 0.08$ GeV are found. The different calorimeter response for b and $\bar{b}$ quark jets can be estimated as:

$$\Delta\mathcal{R} = < p_T >^+ - < p_T >^- = 0.17 \pm 0.12 \text{ GeV/c} \tag{6.14}$$

If we find the fraction of different calorimeter response to the mean of distribution derived with average transverse momentum of two jets,

$$f = \frac{\Delta\mathcal{R}}{< \frac{1}{2} \cdot (p_T^{tag} + p_T^{probe}) >} = 0.0042 \tag{6.15}$$

From Eq. 6.15, we modify the momenta of b and $\bar{b}$ quark jets in Monte Carlo samples by multiplying by $1 - 1/2 \cdot f = 0.9979$ and $1 + 1/2 \cdot f = 1.0021$, respectively. Also four vector for b and $\bar{b}$ quark jets are modified using these factors. Then, asymmetries for O_i, where $i = 2, 4, 7, a, b$, are measured with and without the modification of $b/\bar{b}$ quark jet energy. The asymmetry shift σ is found by the difference between asymmetry extracted with modified $b/\bar{b}$ quark jet energy and that without the modification (σ =A (modified $b/\bar{b}$ jet energy) − $A_{central}$) for each O_i in e+jet, μ+jets and lepton+jets channels.

Table 6.10: Asymmetry variation by the modification of $b/\bar{b}$ jet energy scale for e+jets channel.

	$A_{central}$	A (modified $b/\bar{b}$ jet energy)	σ
O_2	0.128	0.128	0.000
O_4	0.098	0.098	0.000
O_7	0.079	0.079	0.000
O_a	-0.010	-0.010	0.000
O_b	-0.182	-0.182	0.000

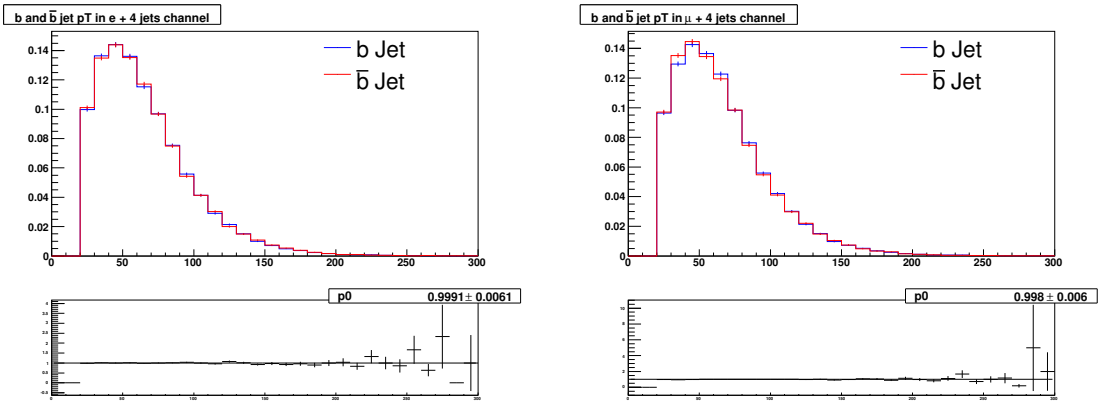

Figure 6.11: The transverse momentum distributions of b and $\bar{b}$ jets for e+jets channel (left) and μ+jets channel (right) in MC.

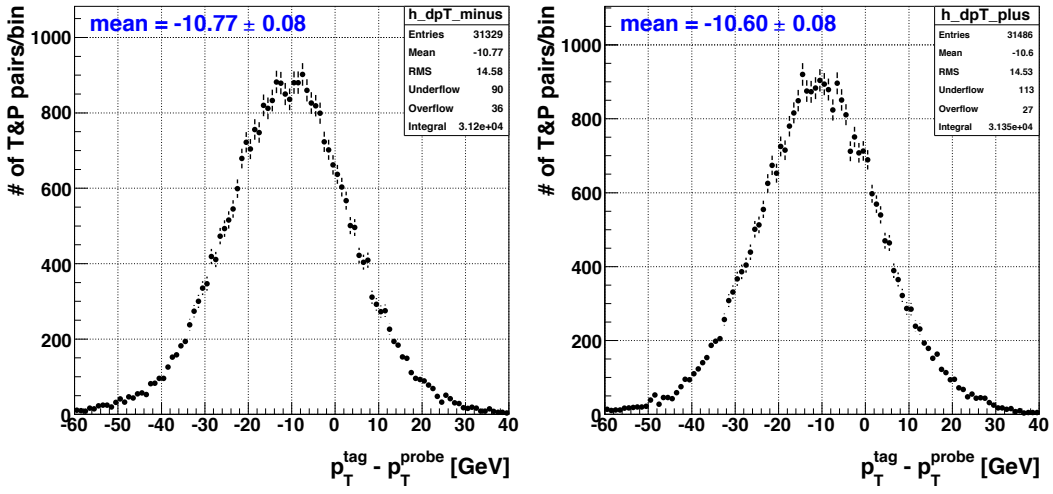

Figure 6.12: The distribution for the difference of the transverse momenta between the tag and probe jets ($\Delta p_T \equiv p_T^{tag} - p_T^{probe}$). The distributions of Δp_T derived with the tag jet associate with negatively and positively charged muons are the left and right plots, respectively [65].

Table 6.11: Asymmetry variation by the modification of $b/\bar{b}$ jet energy scale for μ+jets channel.

	$A_{central}$	A (modified $b/\bar{b}$ jet energy)	σ
O_2	0.090	0.090	0.000
O_4	-0.006	-0.006	0.000
O_7	0.001	0.001	0.000
O_a	-0.040	-0.040	0.000
O_b	0.073	0.073	0.000

Table 6.12: Asymmetry variation by the modification of $b/\bar{b}$ jet energy scale for lepton+jets channel.

	$A_{central}$	A (modified $b/\bar{b}$ jet energy)	σ
O_2	0.106	0.106	0.000
O_4	0.046	0.046	0.000
O_7	0.039	0.039	0.000
O_a	-0.025	-0.025	0.000
O_b	-0.053	-0.053	0.000

Table 6.10, 6.11, 6.12 show asymmetry shifts by the modification of $b/\bar{b}$ jet energy. From the scale factors 0.9979 and 1.0021, the difference of calorimeter responses for $b/\bar{b}$ quark jets is very small and asymmetry variation is insensitive to this modification. All asymmetries for O_2, O_4, O_7, O_a and O_b are not changed by the relative jet energy modification for b and $\bar{b}$ quark jets and it is demonstrated by Table 6.10, 6.11, 6.12.

6.4.3 Measurement Resolution

Physics observables, O_2, O_4, O_7, O_a and O_b, have possibility that kinematic mismeasurement gives random sign to these observables due to $(p_b - p_{\bar{b}})$ or $(p_b + p_{\bar{b}})$. So, we shift the energy of b or $\bar{b}$ quark jet which is more energetic between b and $\bar{b}$ quark jets to estimate how much asymmetry varies by kinematic mismeasurement. The momentum and energy of b or $\bar{b}$ quark jet are varied by 1-σ up and down using the form for the jet p_T resolution, Eq. 6.16, and four vector for b or $\bar{b}$ quark jet is adjusted accordingly. The p_T resolution for jets by DØ calorimeter performance is written as [66]:

$$\frac{\sigma(p_T)}{p_T} = \sqrt{\frac{N^2}{p_T^2} + \frac{S^2}{p_T} + C^2} \tag{6.16}$$

and parameters, C, S and N, have different values in accordance with detector eta of jet. Parameters for the jet p_T resolution are shown in Table 6.13.

Table 6.13: Parameters for the jet p_T resolution [66].

	C	S	N
$\|\eta\| \leq 0.8$	0.062	1.144	3.550
$0.8 < \|\eta\| \leq 1.6$	0.110	0.814	6.322
$1.6 < \|\eta\| \leq 2.4$	0.0	1.302	2.920
$2.4 < \|\eta\| \leq 3.6$	0.063	1.108	6.075

To estimate the asymmetry dilution by kinematic measurement, the $t\bar{t}$ signal Mone Carlo sample is used and required to pass all event selection criteria and weights for all corrections, preselection efficiencies and b-tag probabilities are applied to both e+jets and μ+jets channels. But distributions are not normalized to the measured $t\bar{t}$ cross section. Since the normalization to the measured $t\bar{t}$ cross section is just to multiply by a scale factor and doesn't change shape of distribution, this normalization doesn't affect the result. If the middle plots from Figures 6.13 to 6.22 are compared to plots in Figures 6.5 and 6.6 which are normalized to the measured $t\bar{t}$ cross section, there are no shape differences between them. Thus, weighted events are used for this study. Figures 6.13 to 6.22 show the variations of O_2, O_4, O_7, O_a ,O_b by jet energy up, down and without jet energy shift in e+jets and μ+jets channels and how distributions of these physics observables vary. Based on these distributions, we investigate how the sign of each event is changed by the variation of b or $\bar{b}$ jet energy. Events in Monte Carlo sample have duplicated run number and event number, so we used eta and phi information of two b and $\bar{b}$ quark jets to assign unique event ID. First off, using the information of run number, event number, eta and phi of two b quark jets, we confirmed these information can be used as unique event ID. For each O_i distribution, where $i = 2, 4, 7, a, b$, events are distributed in the positive and negative regions around 0. What we are interested in are:

1. how many events in the positive region move to the negative region.

2. how many events in the negative region move to the positive region.

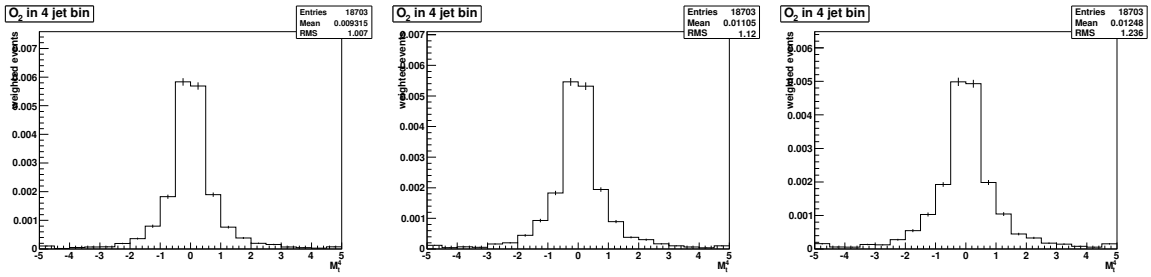

Figure 6.13: The distributions of O_2 by varying b or $\bar{b}$ quark jet energy down (left) and up(right). The middle distribution of O_2 is drawn without variation of b or $\bar{b}$ quark jet energy in e+jets channel.

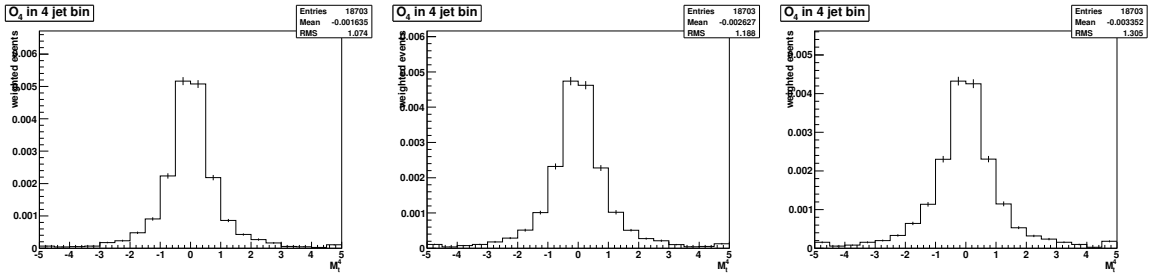

Figure 6.14: The distributions of O_4 by varying b or $\bar{b}$ quark jet energy down (left) and up(right). The middle distribution of O_4 is drawn without variation of b or $\bar{b}$ quark jet energy in e+jets channel

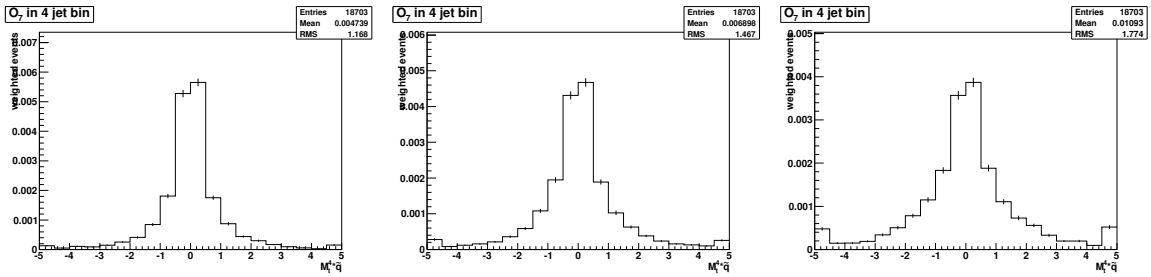

Figure 6.15: The distributions of O_7 by varying b or $\bar{b}$ quark jet energy down (left) and up(right). The middle distribution of O_7 is drawn without variation of b or $\bar{b}$ quark jet energy in e+jets channel

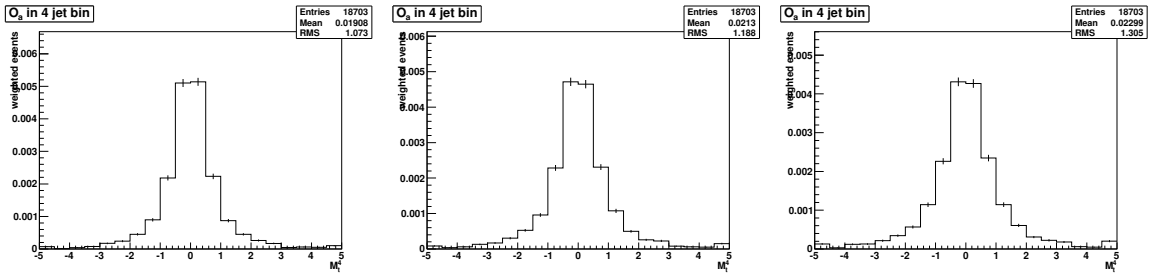

Figure 6.16: The distributions of O_a by varying b or $\bar{b}$ quark jet energy down (left) and up(right). The middle distribution of O_a is drawn without variation of b or $\bar{b}$ quark jet energy in e+jets channel

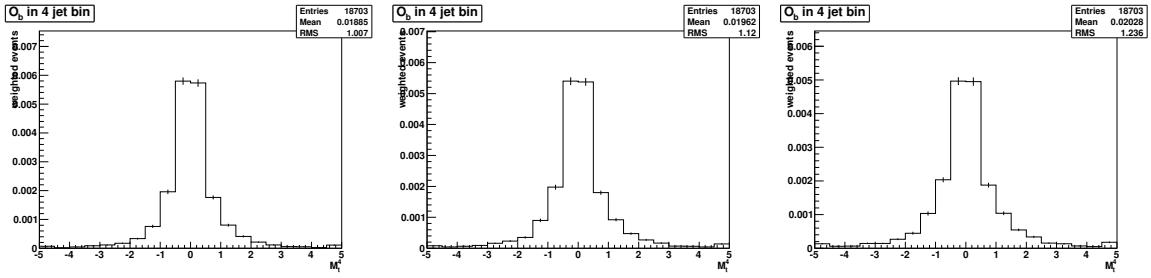

Figure 6.17: The distributions of O_b by varying b or $\bar{b}$ quark jet energy down (left) and up(right). The middle distribution of O_b is drawn without variation of b or $\bar{b}$ quark jet energy in e+jets channel

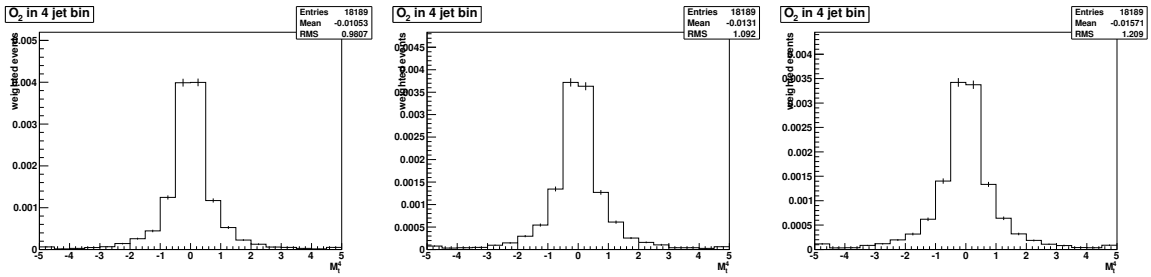

Figure 6.18: The distributions of O_2 by varying b or $\bar{b}$ quark jet energy down (left) and up(right). The middle distribution of O_2 is drawn without variation of b or $\bar{b}$ quark jet energy in μ+jets channel.

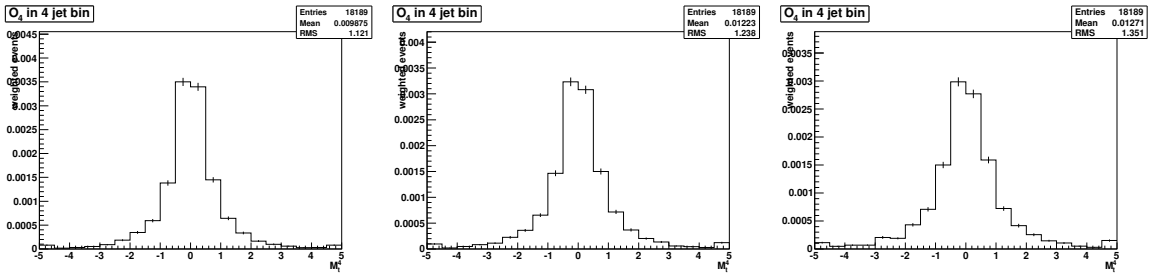

Figure 6.19: The distributions of O_4 by varying b or $\bar{b}$ quark jet energy down (left) and up(right). The middle distribution of O_4 is drawn without variation of b or $\bar{b}$ quark jet energy in μ+jets channel.

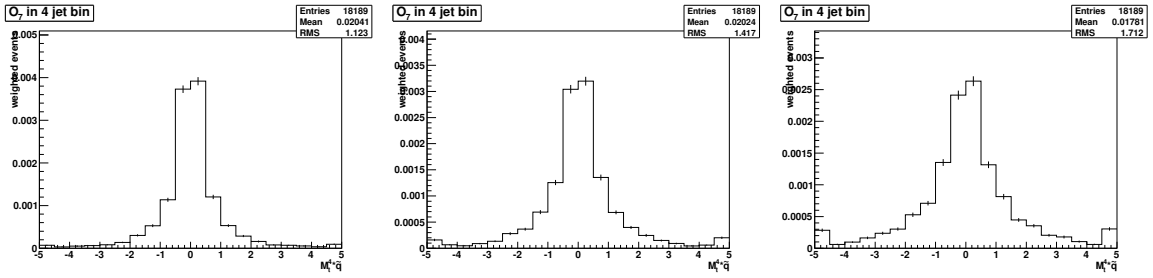

Figure 6.20: The distributions of O_7 by varying b or $\bar{b}$ quark jet energy down (left) and up(right). The middle distribution of O_7 is drawn without variation of b or $\bar{b}$ quark jet energy in μ+jets channel.

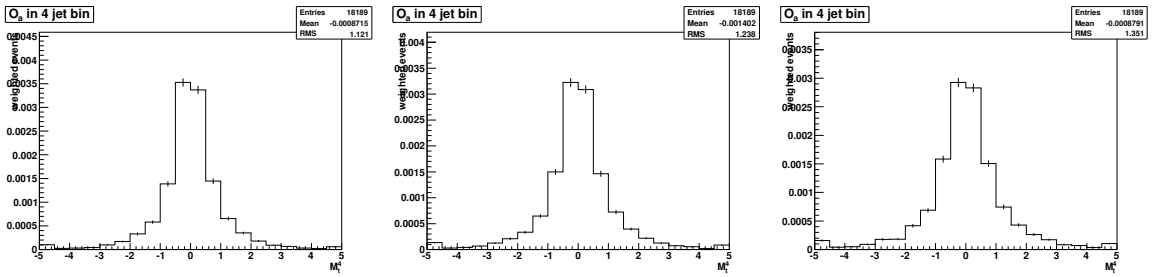

Figure 6.21: The distributions of O_a by varying b or $\bar{b}$ quark jet energy down (left) and up(right). The middle distribution of O_a is drawn without variation of b or $\bar{b}$ quark jet energy in μ+jets channel.

These two cases dilute asymmetry. Thus, events in the positive and negative regions are considered separately. Figures 6.23 to 6.32 show distributions of O_i fluctuation of all individual events by the variation of b or $\bar{b}$ quark energy. O_i of each event is calculated for no variation of b or $\bar{b}$ quark jet energy and also calculated for b or $\bar{b}$ quark jet energy up and down. Four cases can be considered after the variation of jet energy:

1. Positive O_i remains in the positive region.
2. Positive O_i moves to the negative region.
3. Negative O_i remains in the negative region.
4. Negative O_i moves to the positive region.

Also, each case in the above is considered for each jet energy up and down. The difference between O_i for varied b or $\bar{b}$ quark jet energy and O_i for no variation is calculated for the four cases. It can be represented with the form,

$$\Delta O_i \quad = O_i^{\Delta E} - O_i \tag{6.17}$$

$$\text{where} \quad \Delta E = E_b \pm \sigma_{E_b} \text{ and } i = 2, 4, 7, a, b. \tag{6.18}$$

From Figures 6.23 to 6.32, the left plots are distributions for the combination of case 1 and 2 and the right plots are those for case 3 and 4.

Table 6.14: The RMS fluctuations of positive and negative O_i for e+jets channel, where $i = 2, 4, 7, a, b$.

	Positive O_i	Negative O_i
O_2	$\pm$ 0.1811	$\pm$ 0.1804
O_4	$\pm$ 0.1892	$\pm$ 0.1720
O_7	$\pm$ 0.4677	$\pm$ 0.4671
O_a	$\pm$ 0.1909	$\pm$ 0.1699
O_b	$\pm$ 0.1854	$\pm$ 0.1759

From Figures 6.23 to 6.32, the RMS fluctuation of the nominal O_i can be found for its original sign is positive and negative, separately. Table 6.14 and 6.15 show the RMS fluctuation of each positive and negative O_i in e+jets and μ+jets channels, where $i = 2, 4, 7, a, b$. The case

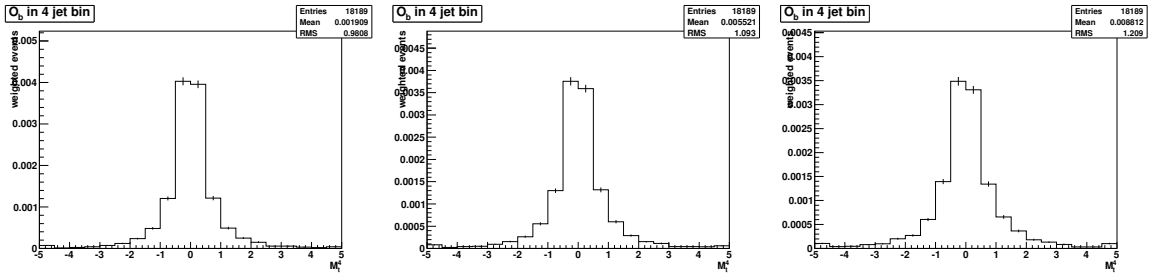

Figure 6.22: The distributions of O_b by varying b or $\bar{b}$ quark jet energy down (left) and up(right). The middle distribution of O_b is drawn without variation of b or $\bar{b}$ quark jet energy in μ+jets channel.

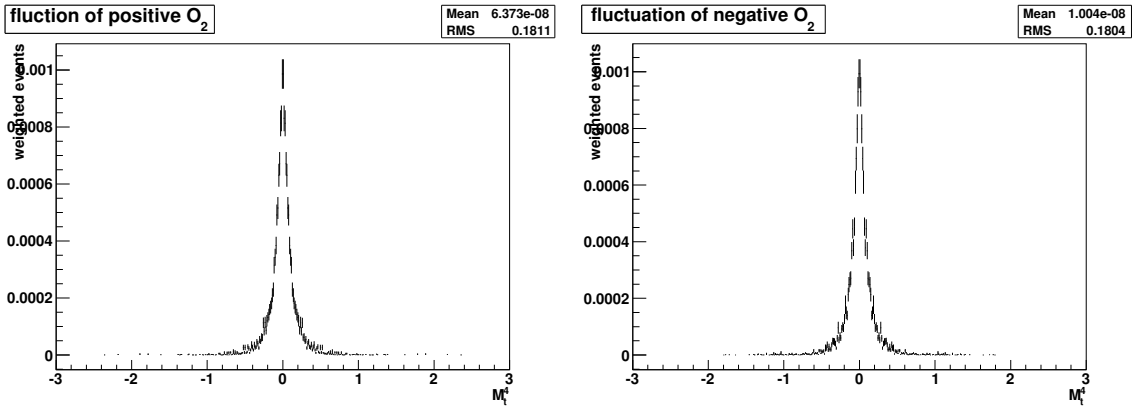

Figure 6.23: The fluctuation of positive O_2 (left) and negative O_2 (right) for e+jets channel.

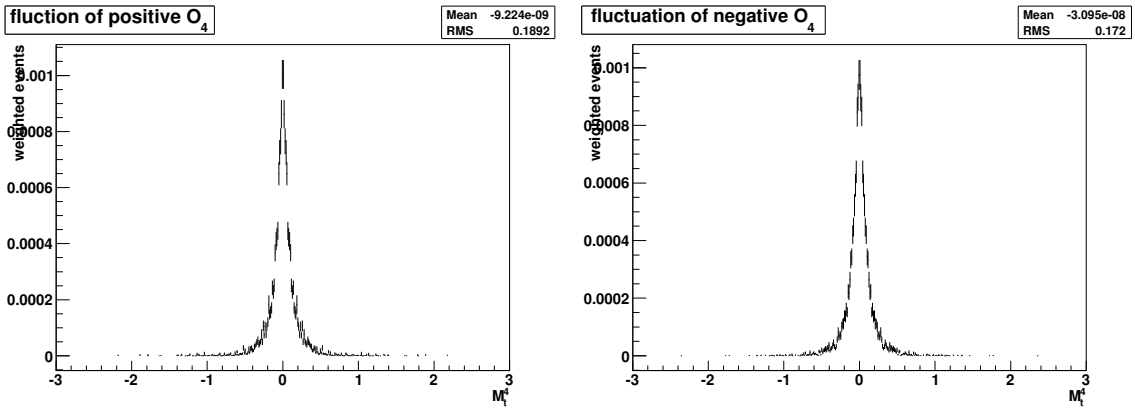

Figure 6.24: The fluctuation of positive O_4 (left) and negative O_4 (right) for e+jets channel.

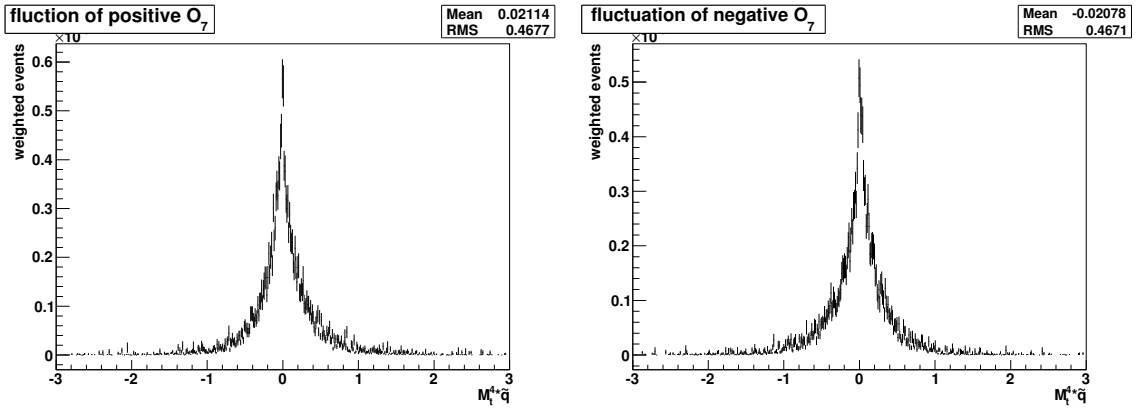

Figure 6.25: The fluctuation of positive O_7 (left) and negative O_7 (right) for e+jets channel.

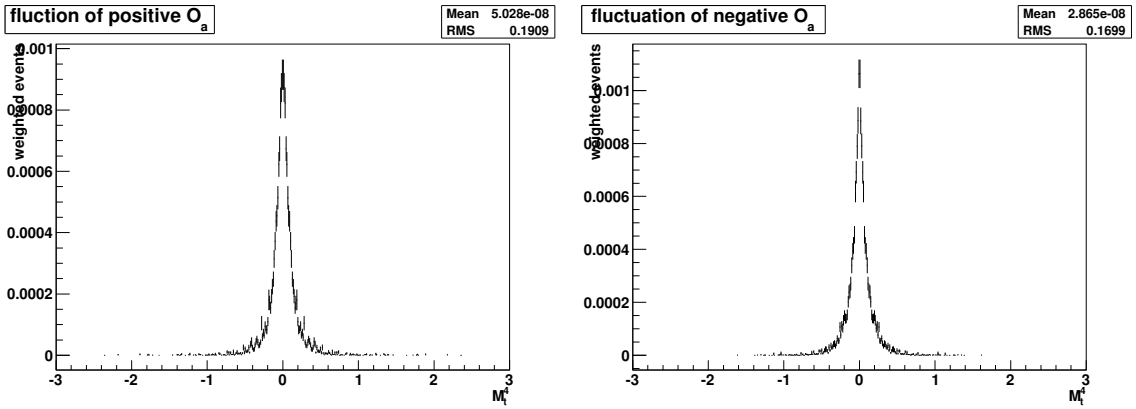

Figure 6.26: The fluctuation of positive O_a (left) and negative O_a (right) for e+jets channel.

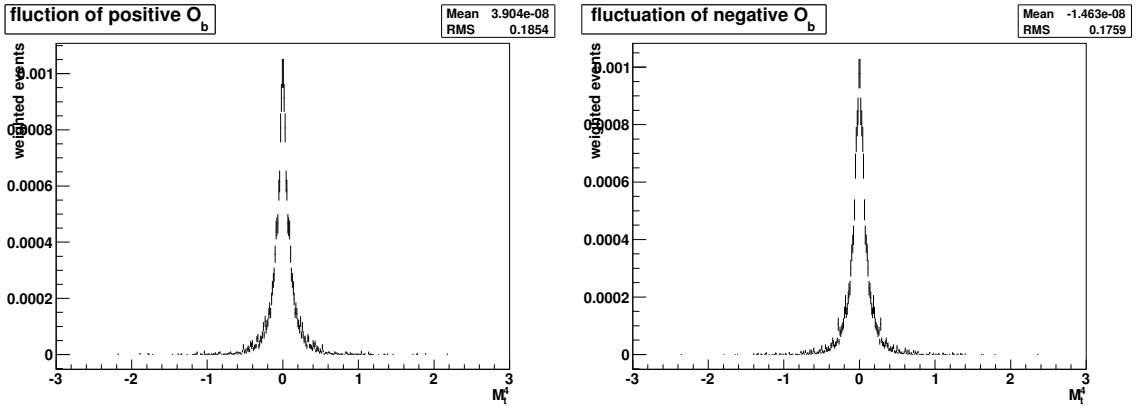

Figure 6.27: The fluctuation of positive O_b (left) and negative O_b (right) for e+jets channel.

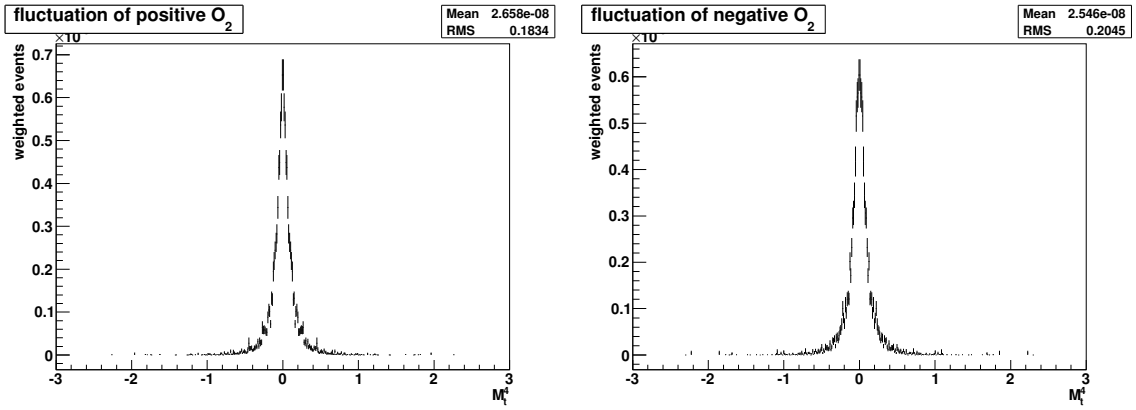

Figure 6.28: The fluctuation of positive O_2 (left) and negative O_2 (right) for μ+jets channel.

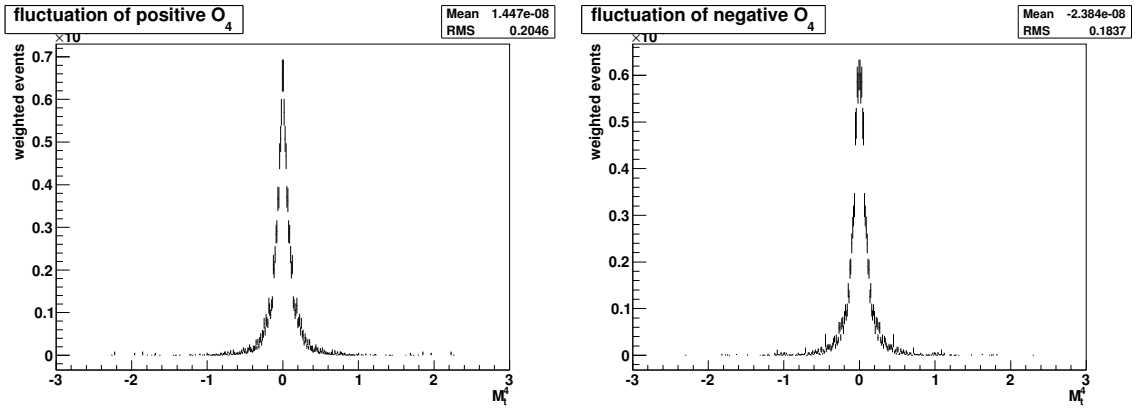

Figure 6.29: The fluctuation of positive O_4 (left) and negative O_4 (right) for μ+jets channel.

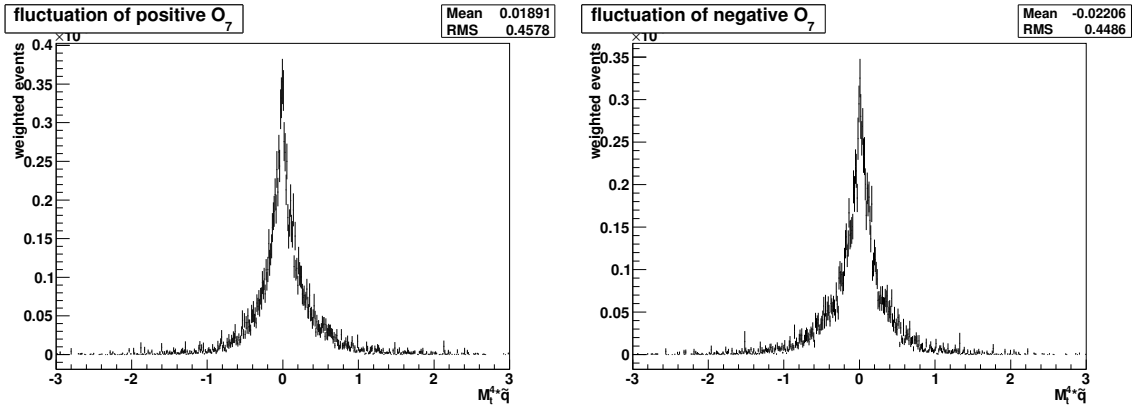

Figure 6.30: The fluctuation of positive O_7 (left) and negative O_7 (right) for μ+jets channel.

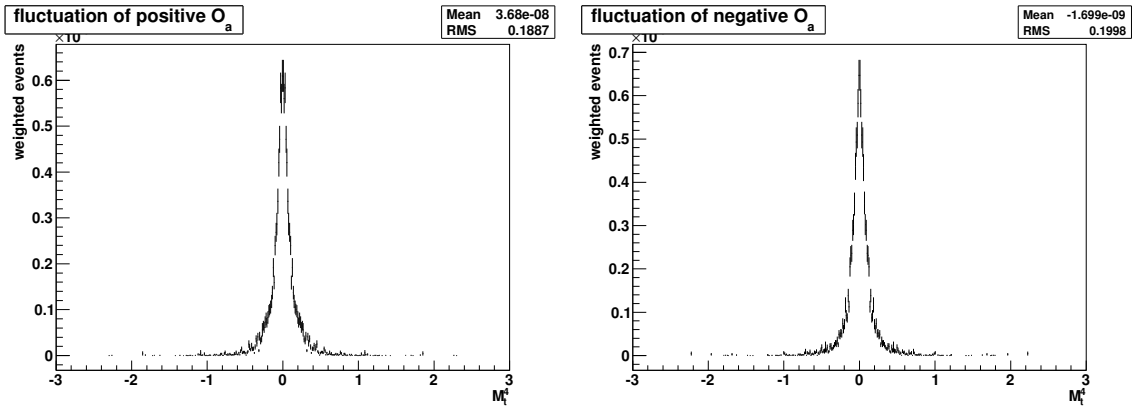

Figure 6.31: The fluctuation of positive O_a (left) and negative O_a (right) for μ+jets channel.

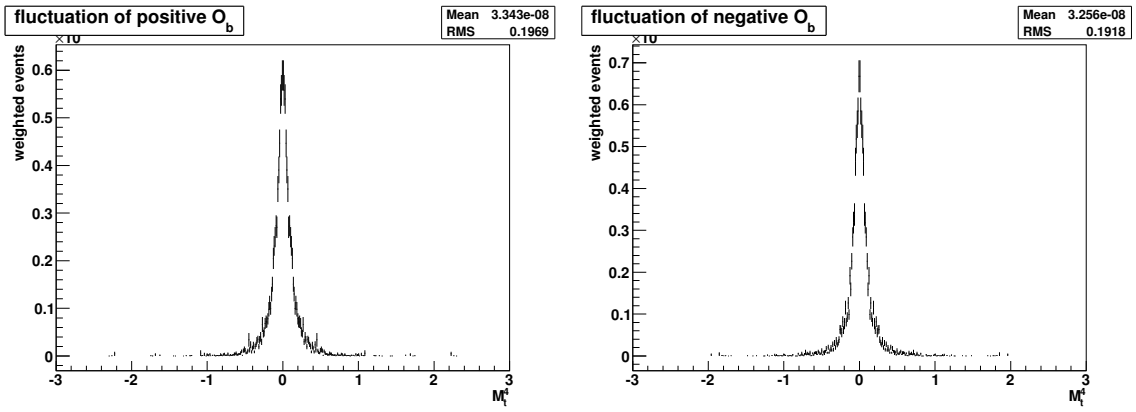

Figure 6.32: The fluctuation of positive O_b (left) and negative O_b (right) for μ+jets channel.

Table 6.15: The RMS fluctuations of positive and negative O_i for μ+jets channels, where $i = 2, 4, 7, a, b$.

	Positive O_i	Negative O_i
O_2	$\pm$ 0.1834	$\pm$ 0.2045
O_4	$\pm$ 0.2046	$\pm$ 0.1837
O_7	$\pm$ 0.4578	$\pm$ 0.4486
O_a	$\pm$ 0.1887	$\pm$ 0.1998
O_b	$\pm$ 0.1969	$\pm$ 0.1918

2 and 4 change asymmetry and the number of weighted events for these two cases are found. We calculate the probabilities that positive O_i changes to the negative sign and negative O_i changes to the positive sign (Tables 6.16, 6.17, 6.18 and 6.19) and find the changes of asymmetries by applying the probabilities to the extracted asymmetries.

In Tables 6.16, 6.17, 6.18 and 6.19, the second column contains the number of weighted events that O_i in the positive (negative) region moves to the negative (positive) region by the variation of b or $\bar{b}$ quark jet energy and the numbers in the third column are the total number of weighted events in the positive (negative) region when no variation of b or $\bar{b}$ quark jet energy is applied. The fourth column has the probability that the sign of positive (negative) O_i is changed to the negative (positive) sign by the variation of b or $\bar{b}$ quark jet energy in e+jets and μ+jets channels.

Table 6.16: The probabilities that the sign of positive O_i is changed to the negative sign by the variation of b or $\bar{b}$ quark jet energy in e+jets channel.

	$O_i^+ \rightarrow O_i^-$	Total number of O_i^+	Probability
O_2	0.000338	0.009318	0.0363
O_4	0.000280	0.009248	0.0303
O_7	0.000220	0.009490	0.0232
O_a	0.000254	0.009363	0.0271
O_b	0.000355	0.009326	0.0381

Since these fluctuations are related to the energy resolution of calorimeter, the measured energies of b and $\bar{b}$ quark jets for not only data but also Monte Carlo are ambiguous within the energy resolution of calorimeter. Thus, events near 0, mainly within the RMS uncertainties

Table 6.17: The probabilities that the sign of negative O_i is changed to the positive sign by the variation of b or $\bar{b}$ quark jet energy in e+jets channel.

	$O_i^- \to O_i^+$	Total number of O_i^-	Probability
O_2	0.000332	0.009316	0.0356
O_4	0.000247	0.009386	0.0263
O_7	0.000246	0.009144	0.0269
O_a	0.000273	0.009271	0.0294
O_b	0.000316	0.009308	0.0339

Table 6.18: The probabilities that the sign of positive O_i is changed to the negative sign by the variation of b or $\bar{b}$ quark jet energy in μ+jets channel.

	$O_i^+ \to O_i^-$	Total number of O_i^+	Probability
O_2	0.000217	0.006207	0.0349
O_4	0.000154	0.006261	0.0246
O_7	0.000168	0.006427	0.0261
O_a	0.000155	0.006249	0.0248
O_b	0.000231	0.006246	0.0370

shown in Tables 6.14 and 6.15, have random signs for physics observables O_2, O_4, O_7, O_a ,O_b. With the probabilities in Tables 6.16, 6.17, 6.18 and 6.19 derived with the $t\bar{t}$ signal Monte Carlo sample that are dominant in 2 b-tags samples, the number of events is changed for both data and Monte Carlo and asymmetries are extracted using the changed number of events.

Tables 6.20, 6.21 and 6.22 show the variations of asymmetries by kinematic mismeasurement for e+jet, μ+jets and lepton+jets. In Tables 6.20, 6.21 and 6.22, the second column shows the nominal values when any variations are not applied, asymmetries extracted with the probability that the positive and negative O_i change to opposite sign are denoted as $A_{O_i^+ \to O_i^-}$ in the

Table 6.19: The probabilities that the sign of negative O_i is changed to the positive sign by the variation of b or $\bar{b}$ quark jet energy in μ+jets channel.

	$O_i^- \to O_i^+$	Total number of O_i^-	Probability
O_2	0.000261	0.006353	0.0411
O_4	0.000174	0.006299	0.0276
O_7	0.000172	0.006133	0.0280
O_a	0.000173	0.006311	0.0274
O_b	0.000248	0.006314	0.0393

Table 6.20: Asymmetry variation by the probability that the positive and negative O_i change to opposite sign in e+jets channel.

	$A_{central}$	$A_{O_i^+ \to O_i^-}$	$A_{O_i^- \to O_i^+}$	$\sigma_{O_i^+ \to O_i^-}$	$\sigma_{O_i^- \to O_i^+}$
O_2	0.128	0.087	0.159	-0.041	0.031
O_4	0.098	0.065	0.122	-0.033	0.024
O_7	0.079	0.054	0.103	-0.025	0.024
O_a	-0.010	-0.036	0.020	-0.026	0.030
O_b	-0.182	-0.213	-0.142	-0.031	0.040

Table 6.21: Asymmetry variation by the probability that the positive and negative O_i change to opposite sign in μ+jets channel.

	$A_{central}$	$A_{O_i^+ \to O_i^-}$	$A_{O_i^- \to O_i^+}$	$\sigma_{O_i^+ \to O_i^-}$	$\sigma_{O_i^- \to O_i^+}$
O_2	0.090	0.052	0.128	-0.038	0.038
O_4	-0.006	-0.030	0.022	-0.024	0.028
O_7	0.001	-0.026	0.029	-0.027	0.028
O_a	-0.040	-0.064	-0.012	-0.024	0.028
O_b	0.073	0.034	0.110	-0.039	0.037

third column and $A_{O_i^- \to O_i^+}$ in the fourth column, respectively. The fifth and sixth columns include the quantities of shifted asymmetries, which are calculated by subtracting $A_{central}$ from $A_{O_i^+ \to O_i^-}$ and $A_{O_i^- \to O_i^+}$, respectively. The ambiguous signs of O_2, O_4, O_7, O_a ,O_b by the calorimeter performance result in the shift of asymmetry by 0.041 at maximum. The energy resolution of calorimeter plays a very important role to determine sign of physics observables O_2, O_4, O_7, O_a ,O_b and measure more accurate asymmetry. These asymmetry variations are taken into account as a factor of asymmetry dilution.

Table 6.22: Asymmetry variation by the probability that the positive and negative O_i change to opposite sign in lepton+jets channel.

	$A_{central}$	$A_{O_i^+ \to O_i^-}$	$A_{O_i^- \to O_i^+}$	$\sigma_{O_i^+ \to O_i^-}$	$\sigma_{O_i^- \to O_i^+}$
O_2	0.106	0.067	0.141	-0.039	0.035
O_4	0.046	0.017	0.071	-0.029	0.025
O_7	0.039	0.014	0.066	-0.025	0.027
O_a	-0.025	-0.050	0.004	-0.025	0.029
O_b	-0.053	-0.088	-0.015	-0.035	0.038

6.4.4 Summary for The Dilution of Asymmetry

In section 6.4.1, 6.4.2 and 6.4.3, several important sources which result in ambiguous asymmetry measurement are investigated. All of these uncertainties in asymmetry measurement are related to the performance of DØ detector directly. Tables 6.23, 6.24 and 6.25 summarize all of these uncertainties and show quadratic sum of all uncertainties resulted from the dilution factors. In Tables 6.23, 6.24 and 6.25, "x" indicates there is no uncertainty corresponding to the dilution factor.

Table 6.23: Summary of uncertainties resulting from the dilution factors in e+jets channel.

	$A_{central}$	$\sigma_{charge\ mis-ID}$	$\sigma_{response\ of\ b/\bar{b}\ jets}$	$\sigma_{measurement\ resolution}$	σ_{sum}
O_2	0.128	x	0.000	$^{+0.031}_{-0.041}$	$^{+0.031}_{-0.041}$
O_3	-0.117	$^{+0.003}_{-0.002}$	x	x	$^{+0.003}_{-0.002}$
O_4	0.098	$^{+0.002}_{-0.003}$	0.000	$^{+0.024}_{-0.033}$	$^{+0.024}_{-0.033}$
O_7	0.079	x	0.000	$^{+0.024}_{-0.025}$	$^{+0.024}_{-0.025}$
O_a	-0.010	x	0.000	$^{+0.030}_{-0.026}$	$^{+0.030}_{-0.026}$
O_b	-0.182	$^{+0.003}_{-0.002}$	0.000	$^{+0.040}_{-0.031}$	$^{+0.040}_{-0.031}$

Table 6.24: Summary of uncertainties resulting from the dilution factors in μ+jets channel.

	$A_{central}$	$\sigma_{charge\ mis-ID}$	$\sigma_{response\ of\ b/\bar{b}\ jets}$	$\sigma_{measurement\ resolution}$	σ_{sum}
O_2	0.090	x	0.000	$^{+0.038}_{-0.038}$	$^{+0.038}_{-0.038}$
O_3	0.015	-0.001	x	x	-0.001
O_4	-0.006	+0.001	0.000	$^{+0.028}_{-0.024}$	$^{+0.028}_{-0.024}$
O_7	0.001	x	0.000	$^{+0.028}_{-0.027}$	$^{+0.028}_{-0.027}$
O_a	-0.040	x	0.000	$^{+0.028}_{-0.024}$	$^{+0.028}_{-0.024}$
O_b	0.073	+0.001	0.000	$^{+0.037}_{-0.039}$	$^{+0.037}_{-0.039}$

Table 6.25: Summary of uncertainties resulting from the dilution factors in lepton+jets channel.

	$A_{central}$	$\sigma_{charge\ mis-ID}$	$\sigma_{response\ of\ b/\bar{b}\ jets}$	$\sigma_{measurement\ resolution}$	σ_{sum}
O_2	0.106	x	0.000	$^{+0.035}_{-0.039}$	$^{+0.035}_{-0.039}$
O_3	-0.049	$^{+0.001}_{-0.001}$	x	x	$^{+0.001}_{-0.001}$
O_4	0.046	$^{+0.001}_{-0.002}$	0.000	$^{+0.025}_{-0.029}$	$^{+0.025}_{-0.029}$
O_7	0.039	x	0.000	$^{+0.027}_{-0.025}$	$^{+0.027}_{-0.025}$
O_a	-0.025	x	0.000	$^{+0.029}_{-0.025}$	$^{+0.029}_{-0.025}$
O_b	-0.053	$^{+0.002}_{-0.001}$	0.000	$^{+0.038}_{-0.035}$	$^{+0.038}_{-0.035}$

6.5 Systematic Uncertainty

Uncertainties described in section 6.4 are related to DØ detector performance. Also, there exist the systematic uncertainties caused by different sources. These various systematic uncertainty sources come from corrections to compensate differences between data and Monte Carlo and can affect the preselection efficiencies and the b-tagging probabilities. The integrated luminosity measurement in DØ has 6.1% uncertainty [67] and it is taken into account as one of systematic uncertainties in the asymmetry measurement.

6.5.1 Uncertainties on The Preselection Efficiency

The systematic uncertainties introduced in this section affect the preselection efficiency.

Data quality event flags Applying data quality loses efficiency and 0.5% is estimated as its systematic uncertainty [68].

Luminosity profile difference in data and Monte Carlo To compensate the difference between data and MC luminosity profile, reweighting the MC luminosity profile is applied to match a luminosity profile in data. The uncertainty comes from luminosity reweighting. The uncertainty 0.1% is assigned [64].

The distribution of vertex z position difference between data and MC The distribution of vertex z position in simulated events is different from that in real data. The uncertainty is measured to be 0.6% between data and MC [64, 69].

Primary vertex scale factor The efficiency of primary vertex selection between data and MC is different in lepton+jets channel. A scale factor 1.0 is used and the relative uncertainty 1.5% is estimated for this scale factor in [70].

Z p_T reweighting The Z p_T in Monte Carlo is rewighted to match that in data. The uncertainty incurred by this reweighting and the constant values quoted in [64] are taken to account as the systematic uncertainties.

Electron ID scale factor An electron in Monte Carlo has different efficiency to pass the electron identification cuts from data. A scale factor to account for this difference is applied and this scale factor has a systematic uncertainty of 3.8%, which is quadratic sum of the uncertainty coming from the evaluation of the background in $Z \to ee$ samaple (3.1%), the uncertainty for a variation of luminosity profile depending on electron selection criteria (0.5%), the dependence on the distance to the closest jet (0.6%), 0.5% arising by the jet multiplicity and the uncertainty caused by the different p_T spectrum (2%). These uncertainties are provided by EM ID group.

Muon ID and track scale factor The certification note [71] Muon ID group estimate the systematic uncertainties of 1.2% and1.6% for tracking and muon identification, respectively.

Muon isolation scale factor The uncertainty for the muon isolation scale factor is estimated to be 1.3% [71].

Lepton momentum scale For electron, the mismodeling of the material in the EM calorimeter leads the electron energy scale of the standard Monte Carlo samples to be significantly shifted with respect to the true value. To account for the different electron energy scale between data and MC, the electron energy is smeared using a scale function which is function of the reconstructed electron energy in the MC samples:$f(E_{reco}) = p_0 + p_1 ln(E_{reco}) + p_2[ln(E_{reco})]^2$. The difference between this electron energy scale and the standard one is taken into account as the systematic uncertainty. For muon, the muon momentum scale differs in data and MC since the mean value of $J/\psi \to \mu\mu$ and $Z \to \mu\mu$ invariant masses are not same in data and MC. To account for this difference, muon momentum scale functions are derived and applied to muon momentum in MC. The largest difference between the central muon momentum measurement and the measured muon momentum after applying momentum scale functions are taken into account as the systematic uncertainty [72]. This estimation is conducted on a $t\bar{t}$ sample in Run IIb (4281.66 pb^{-1}) yields. 0.4% or less (relying on the jet multiplicity) for the electron

momentum and 0.02% or less for the muon momentum scale are estimated for an effect on the selection efficiency. These uncertainties are applied to the signal and background samples.

Electron and muon trigger efficiencies The trigger efficiency is shifted by one standard deviation up and down and then the a weight of an events is recalculated for the uncertainty of the electron trigger. For the single muon trigger, a constant systematic uncertainty 5% is assigned.

Parton distribution function The momentum distribution of partons in hadrons is described by a parton distribution function. The DØ standard MC samples are generated with the parton distribution function CTEQ6L1. The systematic uncertainty considered by the parton distribution function is estimated by reweighting the parton momentum fraction x_1 and x_2 of events from CTEQ6L1 to CTEQ6.1M and its twenty uncertainty PDF sets. The uncertainty is calculated by the quadratic sum of the relative differences between the measured asymmetry after reweighting to CTEQ6.1M and the measured asymmetries corresponding to the twenty PDF uncertainty sets [72].

b-fragmentation reweighting The default b-fragmentation function from PYTHIA is reweighted to match a function which is consistent with the measurement in the e^+e^- experiments. The systematic uncertainty is found by the relative difference between the default fragmentation function and the fragmentation functions tuned to LEP and SLD experiments [54].

Uncertainties MC cross sections A uncertainty for single top cross section by the NLO calculation is 12.6% [73] and the uncertainty for the diboson cross section is 7%. The uncertainty for the Z+jets sample is taken from the reference [64].

Uncertainty on the branching ratios for $t\bar{t} \to lj$ and $t\bar{t} \to ll$ The uncertainties on the branching ratios for $t\bar{t} \to lj$ and $t\bar{t} \to ll$ are 0.8% and 1.7%, respectively. These uncertainties are applied to semileptonic and dileptonic $t\bar{t}$ processes.

Limited Monte Carlo statistics This uncertainty comes from limited Monte Carlo statistics. The statistical uncertainties are determined with the preselection efficiency and $b-$tagging probability of event for the signal and Monte Carlo backgrounds and are used to estimate this systematic uncertainty.

Uncertainty of the measured $t\bar{t}$ cross section In this analysis, the measured $t\bar{t}$ cross section $8.13^{+1.02}_{-0.90}$ (stat.+sys.) is used to estimated the $t\bar{t}$ signal contribution. The uncertainty of the measured $t\bar{t}$ cross section is one source of systematic uncertainties and this is taken into account.

Signal modeling The higher order effects and a different hadronization modeling simulated by MCNLO result in different preselection and $b-$tagging efficiency. The relative asymmetry difference between ALPGEN and MC@NLO simulations is calculated and is taken to be the systematic uncertainty [72].

Color reconnection Strong color correlation between outgoing parton from the hard scattering and the underlying event can be interpreted as a sign of color reconnections. To estimate this systematic uncertatiny, PYTHIA Tune Apro and Tune ACRpro are used. The latter contains the explicit implementation of color reconnection model. These two tunes give the most extreme deviation that is generated by the color reconnection models. The relative differences between these two tunes and the default PYTHIA showering is taken into account [72].

ISR/FSR The the effect from the initial and final state radiation (ISR/FSR) is estimated with a $t\bar{t}$ PYTHIA samples generated with CTEQ5L and ISR/FSR variation. The samples including with ISR/FSR variation are also generated with CTEQ5L. The relative asymmetry differences calculated with these samples are the systematic uncertainty by the ISR/FSR variation [72].

Top mass The $t\bar{t}$ signals used in this analysis were generated with top quark mass 172.5 GeV/c^2. Using the $t\bar{t}$ signals generated with top quark masses 170 GeV/c^2 and 175 GeV/c^2, the asymmetry shift by the variation of top quark mass is investigated.

6.5.2 Uncertainties on The $b-$tagging Probability

b-,c- and light quark jet tag Scale Factors The uncertainties associated with b-,c- and light jet tag scale factors are evaluated by raising and lowering the corresponding scale factor by one standard deviation up and down [74].

Jet taggability parameterization The uncertainty coming from the taggability parameterization is obtained by shifting the taggability scale factors by one standard deviation up and down [63].

b quark jet energy scale There exists the difference between the JES for b-hadrons and the nominal inclusive JES (Jet Energy Scale). The JES for b-hadrons are estimated to be 1.8% smaller than the nominal JES. This uncertainty is obtained by shifting down the nominal JES of all b jets by 1.8% [75].

TRF for Summer10 data set Data set used in this analysis is called "Summer09 extended (4281.66 pb^{-1})" data set and TRF derived for Summer09 extended data set is used in this analysis. But the $t\bar{t}$ cross section measurement in lepton+jets channel using b-tagging method analysis conducted with Summer09 data set is approved with the certified TRF derived using Summer10 data set (5596.55 pb^{-1}). The difference between asymmetries measured with two TRFs is taken into account as a systematic uncertainty.

6.5.3 Uncertainties on Multijet Background

Matrix Method which estimates the yield of multijet background has uncertainty coming from the uncertainties on ε_{qcd} and ε_{sig}. The uncertainties for ε_{qcd} and ε_{sig} are introduced in section 5.2.1. In addition, the uncertainty arisen by the limited statistics of "loose-tight" data sample is taken into account as a systematic uncertainty.

6.5.4 Uncertainties for W+jets and Z+jets scale factors

The heavy flavor scale factors for Zcc and Zbb are 1.67 and 1.52 and an uncertainty of 20% for these scaled factors are assumed [76]. Also, a heavy flavor scale factor for Wc events is

applied with the value of 1.27 and the uncertainty 12% and 1.47 are applied to Wcc and Wbb events with the uncertainty 15%. Reference [77] describes the method to determine the heavy flavor scale factors for Wcc and Wbb in detail.

6.5.5 Uncertainties Related to Jet

Jet Energy Scale uncertainty The systematic uncertainty caused by the jet energy scale (JES) uncertainty is evaluated by the variation of the JES correction by 1σ up and down [60].

$$\sigma = \sqrt{\sigma^2_{stat.,data} + \sigma^2_{sys.,data} + \sigma^2_{stat.,MC} + \sigma^2_{sys.,MC}} \tag{6.19}$$

Jet energy resolution The jet energy in Monte Carlo is smeared using the jet energy resolution of data. This jet energy smearing is varied by one standard deviation up and down.

Jet reconstrucntion Identification efficiency In data and Monte Carlo, calorimeter clusters which don't satisfy the standard jet requirement are removed. Monte Carlo has slightly higher efficiency for jet identification than data. To account for this difference, the scale factor parameterized in p_T and η is used to remove Monte Carlo jets. By varying this scale factor by one standard deviation down, the number of jets removed is changed to estimated the systematic uncertainty. This uncertainty is symmetrized.

Vertex confirmation In Run IIb, vertex confirmed jets which have at least two tracks associated with a related primary vertex is used. To account for the different rate of vertex confirmed jets between data and Monte Carlo, a scale factor is applied to Monte Carlo. This scale factor has uncertainty and this uncertainty is applied.

6.5.6 Summary of Systematic Uncertainties

We varied each independent systematic uncertainty source by one standard deviation up and down and propagate the variation. Then, the asymmetry extraction is performed for each independent systematic uncertainty source varied by one standard deviation up and down.

Table 6.26 $\sim$ 6.46 show how asymmetry is varied by each systematic uncertainty source for each physics observable O_i, where i =1, 2, 3, 4, 7, a, b.

Table 6.26: Summary of systematic uncertainties for O_1 in e+jets.

Summary of systematic uncertainties on asymmetry measurement		
A_{O1} : 0.007	+0.115 (stat.)	-0.115 (stat.)
Source	$+\sigma$	$-\sigma$
Luminosity	0.000	0.000
Luminosity reweight	0.000	0.000
Data quality	0.000	0.000
PVz reweight	0.000	0.000
PV scale factor	0.000	0.000
Electron ID scale factor	0.000	0.000
Electron momentum scale	0.000	0.000
Electron trigger efficiency	0.001	-0.002
Zp_T Reweighting	0.000	0.000
Z heavy scale factor	0.001	-0.001
W heavy scale factor	0.001	-0.001
$t\bar{t}$ measured cross section	0.002	-0.003
$t\bar{t}$ branching fractions	0.000	0.000
Top mass	0.000	-0.001
MC background cross section	0.000	0.000
Signal modeling	0.011	-0.007
PDF	0.002	-0.002
ISR/FSR variation	0.003	0.000
Color reconnection	0.003	0.000
b fragmentation	0.000	0.000
b tag TRF	0.000	0.000
light tag TRF	0.000	0.000
TRF for Summer10 data set	0.000	0.000
Taggability scale factor	0.000	0.000
Jet energy resolution	0.000	-0.006
Jet energy scale	0.000	-0.005
Sample-dependent JES	0.002	0.000
b-jet energy scale	0.000	-0.001
Jet reconstruction and identification	0.000	0.000
Vetexconfirmation	0.000	0.000
Limited Monte Carlo statistics	0.000	0.000
Statistics in Loose - Tight	0.000	0.000
ε_{qcd}	0.002	-0.002
ε_{sig}	0.001	0.000
Total systematic	0.013	-0.012

Table 6.27: Summary of systematic uncertainties for O_2 in e+jets.

Summary of systematic uncertainties on asymmetry measurement		
A_{O2} : 0.128	+0.113 (stat.)	-0.115 (stat.)
Source	$+\sigma$	$-\sigma$
Luminosity	0.001	-0.001
Luminosity reweight	0.000	0.000
Data quality	0.000	0.000
PVz reweight	0.000	0.000
PV scale factor	0.000	0.000
Electron ID scale factor	0.001	-0.001
Electron momentum scale	0.000	0.000
Electron trigger efficiency	0.000	-0.002
Zp_T Reweighting	0.000	0.000
Z heavy scale factor	0.000	0.000
W heavy scale factor	0.001	-0.001
$t\bar{t}$ measured cross section	0.001	-0.001
$t\bar{t}$ branching fractions	0.000	0.000
Top mass	0.000	-0.001
MC background cross section	0.000	0.000
Signal modeling	0.010	0.000
PDF	0.005	-0.007
ISR/FSR variation	0.000	-0.014
Color reconnection	0.001	0.000
b fragmentation	0.000	-0.002
b tag TRF	0.002	-0.002
light tag TRF	0.000	-0.001
TRF for Summer10 data set	0.000	-0.001
Taggability scale factor	0.000	0.000
Jet energy resolution	0.000	-0.006
Jet energy scale	0.000	-0.006
Sample-dependent JES	0.000	-0.001
b-jet energy scale	0.001	0.000
Jet reconstruction and identification	0.001	-0.001
Vetexconfirmation	0.002	0.000
Limited Monte Carlo statistics	0.003	-0.002
Statistics in Loose - Tight	0.001	-0.001
ε_{qcd}	0.001	-0.001
ε_{sig}	0.001	0.000
Total systematic	0.012	-0.019

Table 6.28: Summary of systematic uncertainties for O_3 in e+jets.

Summary of systematic uncertainties on asymmetry measurement		
A_{O3} : -0.117	+0.115 (stat.)	-0.114 (stat.)
Source	$+\sigma$	$-\sigma$
Luminosity	0.001	-0.001
Luminosity reweight	0.000	0.000
Data quality	0.000	0.000
PVz reweight	0.000	0.000
PV scale factor	0.000	0.000
Electron ID scale factor	0.001	-0.001
Electron momentum scale	0.000	0.000
Electron trigger efficiency	0.001	-0.001
Zp_T Reweighting	0.000	0.000
Z heavy scale factor	0.001	-0.001
W heavy scale factor	0.000	0.000
$t\bar{t}$ measured cross section	0.001	-0.001
$t\bar{t}$ branching fractions	0.000	0.000
Top mass	0.000	0.000
MC background cross section	0.000	0.000
Signal modeling	0.000	-0.008
PDF	0.009	-0.009
ISR/FSR variation	0.010	-0.006
Color reconnection	0.005	0.000
b fragmentation	0.000	0.000
b tag TRF	0.001	-0.001
light tag TRF	0.001	-0.001
TRF for Summer10 data set	0.001	0.000
Taggability scale factor	0.001	0.000
Jet energy resolution	0.003	-0.004
Jet energy scale	0.002	0.000
Sample-dependent JES	0.002	0.000
b-jet energy scale	0.000	-0.001
Jet reconstruction and identification	0.001	-0.001
Vetexconfirmation	0.000	0.000
Limited Monte Carlo statistics	0.003	-0.003
Statistics in Loose - Tight	0.001	-0.001
ε_{qcd}	0.002	-0.003
ε_{sig}	0.004	0.000
Total systematic	0.016	-0.015

Table 6.29: Summary of systematic uncertainties for O_4 in e+jets.

Summary of systematic uncertainties on asymmetry measurement		
A_{O4} : 0.098	+0.114 (stat.)	-0.115 (stat.)
Source	$+\sigma$	$-\sigma$
Luminosity	0.000	0.000
Luminosity reweight	0.000	0.000
Data quality	0.000	0.000
PVz reweight	0.000	0.000
PV scale factor	0.000	0.000
Electron ID scale factor	0.000	0.000
Electron momentum scale	0.000	0.000
Electron trigger efficiency	0.000	-0.001
Zp_T Reweighting	0.000	0.000
Z heavy scale factor	0.000	0.000
W heavy scale factor	0.000	0.000
$t\bar{t}$ measured cross section	0.001	-0.001
$t\bar{t}$ branching fractions	0.000	0.000
Top mass	0.000	0.000
MC background cross section	0.000	0.000
Signal modeling	0.007	-0.002
PDF	0.009	-0.009
ISR/FSR variation	0.018	0.000
Color reconnection	0.000	-0.004
b fragmentation	0.000	-0.001
b tag TRF	0.001	-0.001
light tag TRF	0.000	-0.001
TRF for Summer10 data set	0.000	0.000
Taggability scale factor	0.000	-0.001
Jet energy resolution	0.005	0.000
Jet energy scale	0.004	0.000
Sample-dependent JES	0.000	-0.002
b-jet energy scale	0.000	0.000
Jet reconstruction and identification	0.000	0.000
Vetexconfirmation	0.000	-0.002
Limited Monte Carlo statistics	0.000	0.000
Statistics in Loose - Tight	0.000	0.000
ε_{qcd}	0.000	0.000
ε_{sig}	0.000	-0.001
Total systematic	0.022	-0.011

Table 6.30: Summary of systematic uncertainties for O_7 in e+jets.

Summary of systematic uncertainties on asymmetry measurement		
A_{O7} : 0.079	+0.114 (stat.)	-0.115 (stat.)
Source	$+\sigma$	$-\sigma$
Luminosity	0.001	-0.001
Luminosity reweight	0.000	0.000
Data quality	0.000	0.000
PVz reweight	0.000	0.000
PV scale factor	0.000	0.000
Electron ID scale factor	0.000	0.000
Electron momentum scale	0.000	0.000
Electron trigger efficiency	0.001	-0.004
Zp_T Reweighting	0.000	0.000
Z heavy scale factor	0.000	0.000
W heavy scale factor	0.001	-0.001
$t\bar{t}$ measured cross section	0.001	-0.001
$t\bar{t}$ branching fractions	0.000	0.000
Top mass	0.000	0.000
MC background cross section	0.000	0.000
Signal modeling	0.007	0.000
PDF	0.009	-0.010
ISR/FSR variation	0.000	-0.009
Color reconnection	0.000	-0.002
b fragmentation	0.000	-0.001
b tag TRF	0.001	-0.001
light tag TRF	0.000	-0.000
TRF for Summer10 data set	0.000	-0.001
Taggability scale factor	0.000	0.000
Jet energy resolution	0.001	-0.005
Jet energy scale	0.000	-0.008
Sample-dependent JES	0.002	0.000
b-jet energy scale	0.000	-0.002
Jet reconstruction and identification	0.004	-0.004
Vetexconfirmation	0.000	-0.001
Limited Monte Carlo statistics	0.001	-0.001
Statistics in Loose - Tight	0.000	-0.000
ε_{qcd}	0.001	-0.001
ε_{sig}	0.003	0.000
Total systematic	0.013	-0.018

Table 6.31: Summary of systematic uncertainties for O_a in e+jets.

Summary of systematic uncertainties on asymmetry measurement		
A_{Oa} : -0.010	+0.115 (stat.)	-0.115 (stat.)
Source	$+\sigma$	$-\sigma$
Luminosity	0.000	0.000
Luminosity reweight	0.000	0.000
Data quality	0.000	0.000
PVz reweight	0.000	0.000
PV scale factor	0.000	0.000
Electron ID scale factor	0.000	0.000
Electron momentum scale	0.000	0.000
Electron trigger efficiency	0.002	0.000
Zp_T Reweighting	0.000	0.000
Z heavy scale factor	0.000	0.000
W heavy scale factor	0.000	0.000
$t\bar{t}$ measured cross section	0.000	0.000
$t\bar{t}$ branching fractions	0.000	0.000
Top mass	0.000	0.000
MC background cross section	0.000	0.000
Signal modeling	0.000	-0.005
PDF	0.010	-0.010
ISR/FSR variation	0.009	-0.008
Color reconnection	0.004	0.000
b fragmentation	0.000	0.000
b tag TRF	0.001	0.000
light tag TRF	0.000	0.000
TRF for Summer10 data set	0.001	0.000
Taggability scale factor	0.000	0.000
Jet energy resolution	0.003	0.000
Jet energy scale	0.002	-0.001
Sample-dependent JES	0.001	0.000
b-jet energy scale	0.000	0.000
Jet reconstruction and identification	0.001	-0.001
Vetexconfirmation	0.001	0.000
Limited Monte Carlo statistics	0.000	0.000
Statistics in Loose - Tight	0.000	0.000
ε_{qcd}	0.000	0.000
ε_{sig}	0.000	-0.003
Total systematic	0.015	-0.014

Table 6.32: Summary of systematic uncertainties for O_b in e+jets.

Summary of systematic uncertainties on asymmetry measurement		
A_{Ob} : -0.182	+0.115 (stat.)	-0.113 (stat.)
Source	$+\sigma$	$-\sigma$
Luminosity	0.001	-0.001
Luminosity reweight	0.000	0.000
Data quality	0.000	0.000
PVz reweight	0.000	0.000
PV scale factor	0.000	0.000
Electron ID scale factor	0.001	-0.001
Electron momentum scale	0.000	0.000
Electron trigger efficiency	0.000	-0.008
Zp_T Reweighting	0.000	0.000
Z heavy scale factor	0.000	0.000
W heavy scale factor	0.001	-0.001
$t\bar{t}$ measured cross section	0.001	-0.001
$t\bar{t}$ branching fractions	0.000	0.000
Top mass	0.000	0.000
MC background cross section	0.000	0.000
Signal modeling	0.000	-0.008
PDF	0.011	-0.011
ISR/FSR variation	0.014	0.000
Color reconnection	0.002	-0.003
b fragmentation	0.000	0.000
b tag TRF	0.001	-0.002
light tag TRF	0.001	-0.001
TRF for Summer10 data set	0.000	-0.001
Taggability scale factor	0.001	0.000
Jet energy resolution	0.000	-0.006
Jet energy scale	0.000	-0.005
Sample-dependent JES	0.000	0.000
b-jet energy scale	0.000	-0.008
Jet reconstruction and identification	0.008	-0.008
Vetexconfirmation	0.000	-0.007
Limited Monte Carlo statistics	0.003	-0.003
Statistics in Loose - Tight	0.001	-0.001
ε_{qcd}	0.002	-0.002
ε_{sig}	0.003	0.000
Total systematic	0.020	-0.023

Table 6.33: Summary of systematic uncertainties for O_1 in μ+jets.

Summary of systematic uncertainties on asymmetry measurement		
A_{O1} : 0.097	+0.111 (stat.)	-0.112 (stat.)
Source	$+\sigma$	$-\sigma$
Luminosity	0.001	-0.001
Luminosity reweight	0.000	0.000
Data quality	0.000	0.000
PVz reweight	0.000	0.000
PV scale factor	0.000	0.000
Muon ID scale factor	0.000	0.000
Muon tracking scale factor	0.000	0.000
Muon isolation scale factor	0.000	0.000
Muon momentum scale	0.000	0.000
Muon trigger efficiency	0.001	-0.001
Zp_T Reweighting	0.000	0.000
Z heavy scale factor	0.000	0.000
W heavy scale factor	0.001	-0.001
$t\bar{t}$ measured cross section	0.001	-0.001
$t\bar{t}$ branching fractions	0.000	0.000
Top mass	0.000	0.000
MC background cross section	0.000	0.000
Signal modeling	0.005	-0.001
PDF	0.011	-0.010
ISR/FSR variation	0.004	-0.004
Color reconnection	0.002	-0.002
b fragmentation	0.001	0.000
b tag TRF	0.001	-0.001
light tag TRF	0.001	-0.001
TRF for Summer10 data set	0.000	0.000
Taggability scale factor	0.001	0.000
Jet energy resolution	0.000	-0.005
Jet energy scale	0.003	0.000
Sample-dependent JES	0.001	0.000
b-jet energy scale	0.000	-0.001
Jet reconstruction and identification	0.005	-0.005
Vetexconfirmation	0.001	0.000
Limited Monte Carlo statistics	0.007	-0.007
Statistics in Loose - Tight	0.000	0.000
ε_{qcd}	0.000	0.000
ε_{sig}	0.000	0.000
Total systematic	0.016	-0.015

Table 6.34: Summary of systematic uncertainties for O_2 in μ+jets.

Summary of systematic uncertainties on asymmetry measurement		
A_{O2} : 0.090	+0.111 (stat.)	-0.112 (stat.)
Source	$+\sigma$	$-\sigma$
Luminosity	0.001	-0.001
Luminosity reweight	0.000	0.000
Data quality	0.000	0.000
PVz reweight	0.000	0.000
PV scale factor	0.000	0.000
Muon ID scale factor	0.000	0.000
Muon tracking scale factor	0.000	0.000
Muon isolation scale factor	0.000	0.000
Muon momentum scale	0.000	0.000
Muon trigger efficiency	0.001	-0.001
Zp_T Reweighting	0.000	0.000
Z heavy scale factor	0.000	0.000
W heavy scale factor	0.002	-0.001
$t\bar{t}$ measured cross section	0.002	-0.002
$t\bar{t}$ branching fractions	0.000	0.000
Top mass	0.000	0.000
MC background cross section	0.000	0.000
Signal modeling	0.002	-0.009
PDF	0.011	-0.011
ISR/FSR variation	0.000	-0.001
Color reconnection	0.001	-0.005
b fragmentation	0.000	0.000
b tag TRF	0.001	-0.001
light tag TRF	0.000	0.000
TRF for Summer10 data set	0.002	0.000
Taggability scale factor	0.000	-0.001
Jet energy resolution	0.005	-0.001
Jet energy scale	0.006	0.000
Sample-dependent JES	0.000	-0.002
b-jet energy scale	0.003	0.000
Jet reconstruction and identification	0.003	-0.003
Vetexconfirmation	0.001	0.000
Limited Monte Carlo statistics	0.006	-0.007
Statistics in Loose - Tight	0.000	-0.000
ε_{qcd}	0.000	0.000
ε_{sig}	0.000	0.000
Total systematic	0.016	-0.017

Table 6.35: Summary of systematic uncertainties for O_3 in μ+jets.

Summary of systematic uncertainties on asymmetry measurement		
A_{O3} : 0.015	+0.112 (stat.)	-0.112 (stat.)
Source	$+\sigma$	$-\sigma$
Luminosity	0.001	-0.001
Luminosity reweight	0.000	0.000
Data quality	0.000	0.000
PVz reweight	0.000	0.000
PV scale factor	0.000	0.000
Muon ID scale factor	0.000	0.000
Muon tracking scale factor	0.000	0.000
Muon isolation scale factor	0.000	0.000
Muon momentum scale	0.000	0.000
Muon trigger efficiency	0.001	-0.001
Zp_T Reweighting	0.000	0.000
Z heavy scale factor	0.000	0.000
W heavy scale factor	0.001	-0.002
$t\bar{t}$ measured cross section	0.001	-0.002
$t\bar{t}$ branching fractions	0.000	0.000
Top mass	0.000	0.000
MC background cross section	0.000	0.000
Signal modeling	0.008	-0.004
PDF	0.012	-0.012
ISR/FSR variation	0.008	0.000
Color reconnection	0.003	0.000
b fragmentation	0.002	0.000
b tag TRF	0.001	-0.001
light tag TRF	0.001	-0.001
TRF for Summer10 data set	0.000	0.000
Taggability scale factor	0.001	0.000
Jet energy resolution	0.001	0.000
Jet energy scale	0.003	0.000
Sample-dependent JES	0.001	0.000
b-jet energy scale	0.000	-0.001
Jet reconstruction and identification	0.005	-0.005
Vetexconfirmation	0.000	-0.002
Limited Monte Carlo statistics	0.007	-0.006
Statistics in Loose - Tight	0.000	0.000
ε_{qcd}	0.000	0.000
ε_{sig}	0.001	0.000
Total systematic	0.019	-0.015

Table 6.36: Summary of systematic uncertainties for O_4 in μ+jets.

Summary of systematic uncertainties on asymmetry measurement		
A_{O4} : -0.006	+0.112 (stat.)	-0.112 (stat.)
Source	$+\sigma$	$-\sigma$
Luminosity	0.000	0.000
Luminosity reweight	0.000	0.000
Data quality	0.000	0.000
PVz reweight	0.000	0.000
PV scale factor	0.000	0.000
Muon ID scale factor	0.000	0.000
Muon tracking scale factor	0.000	0.000
Muon isolation scale factor	0.000	0.000
Muon momentum scale	0.000	0.000
Muon trigger efficiency	0.000	0.000
Zp_T Reweighting	0.000	0.000
Z heavy scale factor	0.000	0.000
W heavy scale factor	0.000	0.000
$t\bar{t}$ measured cross section	0.001	-0.001
$t\bar{t}$ branching fractions	0.000	0.000
Top mass	0.000	0.000
MC background cross section	0.000	0.000
Signal modeling	0.000	-0.003
PDF	0.012	-0.013
ISR/FSR variation	0.002	0.000
Color reconnection	0.000	-0.002
b fragmentation	0.000	0.000
b tag TRF	0.000	0.000
light tag TRF	0.001	-0.001
TRF for Summer10 data set	0.000	0.000
Taggability scale factor	0.000	-0.001
Jet energy resolution	0.000	-0.002
Jet energy scale	0.000	-0.005
Sample-dependent JES	0.000	0.000
b-jet energy scale	0.003	0.000
Jet reconstruction and identification	0.006	0.006
Vetexconfirmation	0.000	-0.001
Limited Monte Carlo statistics	0.004	-0.004
Statistics in Loose - Tight	0.000	0.000
ε_{qcd}	0.000	0.000
ε_{sig}	0.000	0.000
Total systematic	0.015	-0.016

Table 6.37: Summary of systematic uncertainties for O_7 in μ+jets.

Summary of systematic uncertainties on asymmetry measurement		
A_{O7} : 0.001	+0.112 (stat.)	-0.112 (stat.)
Source	$+\sigma$	$-\sigma$
Luminosity	0.000	0.000
Luminosity reweight	0.000	0.000
Data quality	0.000	0.000
PVz reweight	0.000	0.000
PV scale factor	0.000	0.000
Muon ID scale factor	0.000	0.000
Muon tracking scale factor	0.000	0.000
Muon isolation scale factor	0.000	0.000
Muon momentum scale	0.000	0.000
Muon trigger efficiency	0.000	0.000
Zp_T Reweighting	0.000	0.000
Z heavy scale factor	0.000	0.000
W heavy scale factor	0.000	0.000
$t\bar{t}$ measured cross section	0.000	0.000
$t\bar{t}$ branching fractions	0.000	0.000
Top mass	0.000	0.000
MC background cross section	0.000	0.000
Signal modeling	0.001	-0.005
PDF	0.013	-0.013
ISR/FSR variation	0.000	-0.007
Color reconnection	0.000	-0.002
b fragmentation	0.000	-0.000
b tag TRF	0.000	0.000
light tag TRF	0.002	-0.002
TRF for Summer10 data set	0.002	0.000
Taggability scale factor	0.000	0.000
Jet energy resolution	0.002	0.000
Jet energy scale	0.000	-0.003
Sample-dependent JES	0.000	-0.002
b-jet energy scale	0.000	0.000
Jet reconstruction and identification	0.003	-0.003
Vetexconfirmation	0.004	0.000
Limited Monte Carlo statistics	0.002	-0.003
Statistics in Loose - Tight	0.000	0.000
ε_{qcd}	0.000	0.000
ε_{sig}	0.000	0.000
Total systematic	0.015	-0.017

Table 6.38: Summary of systematic uncertainties for O_a in μ+jets.

Summary of systematic uncertainties on asymmetry measurement		
A_{Oa} : -0.040	+0.112 (stat.)	-0.112 (stat.)
Source	$+\sigma$	$-\sigma$
Luminosity	0.000	0.000
Luminosity reweight	0.000	0.000
Data quality	0.000	0.000
PVz reweight	0.000	0.000
PV scale factor	0.000	0.000
Muon ID scale factor	0.000	0.000
Muon tracking scale factor	0.000	0.000
Muon isolation scale factor	0.000	0.000
Muon momentum scale	0.000	0.000
Muon trigger efficiency	0.000	0.000
Zp_T Reweighting	0.000	0.000
Z heavy scale factor	0.000	0.000
W heavy scale factor	0.000	0.000
$t\bar{t}$ measured cross section	0.001	-0.001
$t\bar{t}$ branching fractions	0.000	0.000
Top mass	0.000	0.000
MC background cross section	0.000	0.000
Signal modeling	0.003	-0.002
PDF	0.013	-0.013
ISR/FSR variation	0.002	-0.005
Color reconnection	0.002	0.000
b fragmentation	0.002	0.000
b tag TRF	0.000	0.000
light tag TRF	0.003	-0.003
TRF for Summer10 data set	0.000	-0.001
Taggability scale factor	0.001	0.000
Jet energy resolution	0.002	-0.003
Jet energy scale	0.000	-0.008
Sample-dependent JES	0.000	0.000
b-jet energy scale	0.000	-0.004
Jet reconstruction and identification	0.004	-0.004
Vetexconfirmation	0.000	-0.003
Limited Monte Carlo statistics	0.002	-0.002
Statistics in Loose - Tight	0.000	0.000
ε_{qcd}	0.000	0.000
ε_{sig}	0.000	0.000
Total systematic	0.015	-0.018

Table 6.39: Summary of systematic uncertainties for O_b in μ+jets.

Summary of systematic uncertainties on asymmetry measurement		
A_{Ob} : 0.073	+0.111 (stat.)	-0.112 (stat.)
Source	$+\sigma$	$-\sigma$
Luminosity	0.001	-0.001
Luminosity reweight	0.000	0.000
Data quality	0.000	0.000
PVz reweight	0.000	0.000
PV scale factor	0.000	0.000
Muon ID scale factor	0.000	0.000
Muon tracking scale factor	0.000	0.000
Muon isolation scale factor	0.000	0.000
Muon momentum scale	0.000	0.000
Muon trigger efficiency	0.001	-0.001
Zp_T Reweighting	0.000	0.000
Z heavy scale factor	0.000	0.000
W heavy scale factor	0.001	-0.001
$t\bar{t}$ measured cross section	0.001	-0.001
$t\bar{t}$ branching fractions	0.000	0.000
Top mass	0.000	0.000
MC background cross section	0.000	0.000
Signal modeling	0.007	-0.007
PDF	0.013	-0.013
ISR/FSR variation	0.000	-0.007
Color reconnection	0.000	-0.005
b fragmentation	0.000	0.000
b tag TRF	0.001	-0.001
light tag TRF	0.002	-0.002
TRF for Summer10 data set	0.000	0.000
Taggability scale factor	0.000	0.000
Jet energy resolution	0.001	-0.003
Jet energy scale	0.002	-0.001
Sample-dependent JES	0.000	-0.001
b-jet energy scale	0.000	0.000
Jet reconstruction and identification	0.006	-0.006
Vetexconfirmation	0.002	0.000
Limited Monte Carlo statistics	0.002	-0.002
Statistics in Loose - Tight	0.000	0.000
ε_{qcd}	0.000	0.000
ε_{sig}	0.000	0.000
Total systematic	0.017	-0.019

Table 6.40: Summary of systematic uncertainties for O_1 in lepton+jets.

Summary of systematic uncertainties on asymmetry measurement		
A_{O1} : 0.053	+0.081 (stat.)	-0.081 (stat.)
Source	$+\sigma$	$-\sigma$
Luminosity	0.001	-0.001
Luminosity reweight	0.000	0.000
Data quality	0.000	0.000
PVz reweight	0.000	0.000
PV scale factor	0.000	0.000
Electron ID scale factor	0.000	0.000
Electron momentum scale	0.000	0.000
Electron trigger efficiency	0.001	-0.002
Muon ID scale factor	0.000	0.000
Muon tracking scale factor	0.000	0.000
Muon isolation scale factor	0.000	0.000
Muon momentum scale	0.000	0.000
Muon trigger efficiency	0.001	-0.001
Zp_T Reweighting	0.000	0.000
Z heavy scale factor	0.000	0.000
W heavy scale factor	0.001	0.001
$t\bar{t}$ measured cross section	0.001	-0.002
$t\bar{t}$ branching fractions	0.000	0.000
Top mass	0.000	0.000
MC background cross section	0.000	0.000
Signal modeling	0.007	-0.003
PDF	0.013	-0.013
ISR/FSR variation	0.004	-0.002
Color reconnection	0.002	0.000
b fragmentation	0.000	0.000
b tag TRF	0.000	0.000
light tag TRF	0.000	0.000
TRF for Summer10 data set	0.000	0.000
Taggability scale factor	0.001	0.000
Jet energy resolution	0.000	-0.005
Jet energy scale	0.000	0.000
Sample-dependent JES	0.001	0.000
b-jet energy scale	0.000	-0.001
Jet reconstruction and identification	0.002	-0.002
Vetexconfirmation	0.001	0.000
Limited Monte Carlo statistics	0.004	-0.004
Statistics in Loose - Tight	0.000	0.000
ε_{qcd}	0.001	-0.001
ε_{sig}	0.003	0.000
Total systematic	0.017	-0.015

Table 6.41: Summary of systematic uncertainties for O_2 in lepton+jets.

Summary of systematic uncertainties on asymmetry measurement		
A_{O2} : 0.106	+0.080 (stat.)	-0.081 (stat.)
Source	$+\sigma$	$-\sigma$
Luminosity	0.000	0.000
Luminosity reweight	0.000	0.000
Data quality	0.000	0.000
PVz reweight	0.000	0.000
PV scale factor	0.000	0.000
Electron ID scale factor	0.001	-0.001
Electron momentum scale	0.000	0.000
Electron trigger efficiency	0.000	-0.002
Muon ID scale factor	0.000	0.000
Muon tracking scale factor	0.000	0.000
Muon isolation scale factor	0.000	0.000
Muon momentum scale	0.000	0.000
Muon trigger efficiency	0.001	-0.001
Zp_T Reweighting	0.000	0.000
Z heavy scale factor	0.000	0.000
W heavy scale factor	0.000	0.000
$t\bar{t}$ measured cross section	0.001	-0.001
$t\bar{t}$ branching fractions	0.000	0.000
Top mass	0.000	0.000
MC background cross section	0.000	0.000
Signal modeling	0.002	-0.001
PDF	0.013	-0.014
ISR/FSR variation	0.000	-0.007
Color reconnection	0.002	-0.002
b fragmentation	0.000	-0.001
b tag TRF	0.001	-0.001
light tag TRF	0.000	0.000
TRF for Summer10 data set	0.002	0.000
Taggability scale factor	0.000	0.000
Jet energy resolution	0.001	-0.003
Jet energy scale	0.002	0.000
Sample-dependent JES	0.000	-0.002
b-jet energy scale	0.002	0.000
Jet reconstruction and identification	0.001	-0.001
Vetexconfirmation	0.001	0.000
Limited Monte Carlo statistics	0.003	-0.003
Statistics in Loose - Tight	0.000	0.000
ε_{qcd}	0.000	0.000
ε_{sig}	0.001	0.000
Total systematic	0.014	-0.017

Table 6.42: Summary of systematic uncertainties for O_3 in lepton+jets.

Summary of systematic uncertainties on asymmetry measurement		
A_{O3} : -0.049	+0.081 (stat.)	-0.080 (stat.)
Source	$+\sigma$	$-\sigma$
Luminosity	0.000	0.000
Luminosity reweight	0.000	0.000
Data quality	0.000	0.000
PVz reweight	0.000	0.000
PV scale factor	0.000	0.000
Electron ID scale factor	0.001	-0.001
Electron momentum scale	0.000	0.000
Electron trigger efficiency	0.001	-0.001
Muon ID scale factor	0.000	0.000
Muon tracking scale factor	0.000	0.000
Muon isolation scale factor	0.000	0.000
Muon momentum scale	0.000	0.000
Muon trigger efficiency	0.001	-0.001
Zp_T Reweighting	0.000	0.000
Z heavy scale factor	0.000	0.000
W heavy scale factor	0.001	-0.001
$t\bar{t}$ measured cross section	0.001	-0.001
$t\bar{t}$ branching fractions	0.000	0.000
Top mass	0.000	0.000
MC background cross section	0.000	0.000
Signal modeling	0.004	-0.005
PDF	0.014	-0.014
ISR/FSR variation	0.008	0.000
Color reconnection	0.003	0.000
b fragmentation	0.001	0.000
b tag TRF	0.000	0.000
light tag TRF	0.000	0.000
TRF for Summer10 data set	0.000	0.000
Taggability scale factor	0.001	0.000
Jet energy resolution	0.002	-0.001
Jet energy scale	0.003	0.000
Sample-dependent JES	0.002	0.000
b-jet energy scale	0.000	-0.001
Jet reconstruction and identification	0.003	-0.003
Vetexconfirmation	0.000	-0.001
Limited Monte Carlo statistics	0.002	-0.002
Statistics in Loose - Tight	0.000	0.000
ε_{qcd}	0.001	-0.001
ε_{sig}	0.006	0.000
Total systematic	0.019	-0.016

Table 6.43: Summary of systematic uncertainties for O_4 in lepton+jets.

Summary of systematic uncertainties on asymmetry measurement		
A_{O4} : 0.046	+0.081 (stat.)	-0.081 (stat.)
Source	$+\sigma$	$-\sigma$
Luminosity	0.000	0.000
Luminosity reweight	0.000	0.000
Data quality	0.000	0.000
PVz reweight	0.000	0.000
PV scale factor	0.000	0.000
Electron ID scale factor	0.000	0.000
Electron momentum scale	0.000	0.000
Electron trigger efficiency	0.000	-0.001
Muon ID scale factor	0.000	0.000
Muon tracking scale factor	0.000	0.000
Muon isolation scale factor	0.000	0.000
Muon momentum scale	0.000	0.000
Muon trigger efficiency	0.000	0.000
Zp_T Reweighting	0.000	0.000
Z heavy scale factor	0.000	0.000
W heavy scale factor	0.000	0.000
$t\bar{t}$ measured cross section	0.001	-0.001
$t\bar{t}$ branching fractions	0.000	0.000
Top mass	0.000	0.000
MC background cross section	0.000	0.000
Signal modeling	0.002	-0.002
PDF	0.014	-0.014
ISR/FSR variation	0.008	0.000
Color reconnection	0.000	-0.003
b fragmentation	0.000	0.000
b tag TRF	0.001	-0.001
light tag TRF	0.000	0.000
TRF for Summer10 data set	0.000	0.000
Taggability scale factor	0.000	-0.001
Jet energy resolution	0.001	0.000
Jet energy scale	0.001	-0.003
Sample-dependent JES	0.000	-0.001
b-jet energy scale	0.002	0.000
Jet reconstruction and identification	0.004	-0.004
Vetexconfirmation	0.000	-0.001
Limited Monte Carlo statistics	0.002	-0.002
Statistics in Loose - Tight	0.000	0.000
ε_{qcd}	0.000	0.000
ε_{sig}	0.002	0.000
Total systematic	0.017	-0.016

Table 6.44: Summary of systematic uncertainties for O_7 in lepton+jets.

Summary of systematic uncertainties on asymmetry measurement		
A_{O7} : 0.039	+0.081 (stat.)	-0.081 (stat.)
Source	$+\sigma$	$-\sigma$
Luminosity	0.000	0.000
Luminosity reweight	0.000	0.000
Data quality	0.000	0.000
PVz reweight	0.000	0.000
PV scale factor	0.000	0.000
Electron ID scale factor	0.000	0.000
Electron momentum scale	0.000	0.000
Electron trigger efficiency	0.001	-0.004
Muon ID scale factor	0.000	0.000
Muon tracking scale factor	0.000	0.000
Muon isolation scale factor	0.000	0.000
Muon momentum scale	0.000	0.000
Muon trigger efficiency	0.000	0.000
Zp_T Reweighting	0.000	0.000
Z heavy scale factor	0.000	0.000
W heavy scale factor	0.001	-0.001
$t\bar{t}$ measured cross section	0.001	-0.001
$t\bar{t}$ branching fractions	0.000	0.000
Top mass	0.000	0.000
MC background cross section	0.000	0.000
Signal modeling	0.004	0.000
PDF	0.015	-0.015
ISR/FSR variation	0.000	-0.008
Color reconnection	0.000	-0.002
b fragmentation	0.000	-0.001
b tag TRF	0.000	0.000
light tag TRF	0.002	-0.002
TRF for Summer10 data set	0.002	0.000
Taggability scale factor	0.000	0.000
Jet energy resolution	0.002	-0.002
Jet energy scale	0.000	-0.003
Sample-dependent JES	0.000	0.000
b-jet energy scale	0.000	-0.001
Jet reconstruction and identification	0.004	-0.004
Vetexconfirmation	0.002	0.000
Limited Monte Carlo statistics	0.000	0.000
Statistics in Loose - Tight	0.000	-0.000
ε_{qcd}	0.001	-0.001
ε_{sig}	0.003	0.000
Total systematic	0.017	-0.019

Table 6.45: Summary of systematic uncertainties for O_a in lepton+jets.

Summary of systematic uncertainties on asymmetry measurement		
A_{Oa} : -0.025	+0.081 (stat.)	-0.081 (stat.)
Source	$+\sigma$	$-\sigma$
Luminosity	0.000	0.000
Luminosity reweight	0.000	0.000
Data quality	0.000	0.000
PVz reweight	0.000	0.000
PV scale factor	0.000	0.000
Electron ID scale factor	0.000	0.000
Electron momentum scale	0.000	0.000
Electron trigger efficiency	0.002	0.000
Muon ID scale factor	0.000	0.000
Muon tracking scale factor	0.000	0.000
Muon isolation scale factor	0.000	0.000
Muon momentum scale	0.000	0.000
Muon trigger efficiency	0.000	0.000
Zp_T Reweighting	0.000	0.000
Z heavy scale factor	0.000	0.000
W heavy scale factor	0.000	0.000
$t\bar{t}$ measured cross section	0.001	-0.001
$t\bar{t}$ branching fractions	0.000	0.000
Top mass	0.000	0.000
MC background cross section	0.000	0.000
Signal modeling	0.002	-0.004
PDF	0.015	-0.015
ISR/FSR variation	0.001	-0.002
Color reconnection	0.003	0.000
b fragmentation	0.001	0.000
b tag TRF	0.000	0.000
light tag TRF	0.002	-0.002
TRF for Summer10 data set	0.001	0.000
Taggability scale factor	0.000	0.000
Jet energy resolution	0.003	-0.001
Jet energy scale	0.000	-0.004
Sample-dependent JES	0.000	0.000
b-jet energy scale	0.000	-0.002
Jet reconstruction and identification	0.003	-0.003
Vetexconfirmation	0.000	-0.002
Limited Monte Carlo statistics	0.001	-0.001
Statistics in Loose - Tight	0.000	0.000
ε_{qcd}	0.000	0.000
ε_{sig}	0.000	-0.001
Total systematic	0.016	-0.017

Table 6.46: Summary of systematic uncertainties for O_b in lepton+jets.

Summary of systematic uncertainties on asymmetry measurement		
A_{Ob} : -0.053	+0.081 (stat.)	-0.080 (stat.)
Source	$+\sigma$	$-\sigma$
Luminosity	0.000	0.000
Luminosity reweight	0.000	0.000
Data quality	0.000	0.000
PVz reweight	0.000	0.000
PV scale factor	0.000	0.000
Electron ID scale factor	0.001	-0.001
Electron momentum scale	0.000	0.000
Electron trigger efficiency	0.000	-0.008
Muon ID scale factor	0.000	0.000
Muon tracking scale factor	0.000	0.000
Muon isolation scale factor	0.000	0.000
Muon momentum scale	0.000	0.000
Muon trigger efficiency	0.001	-0.001
Zp_T Reweighting	0.000	0.000
Z heavy scale factor	0.000	0.000
W heavy scale factor	0.000	0.000
$t\bar{t}$ measured cross section	0.000	0.000
$t\bar{t}$ branching fractions	0.000	0.000
Top mass	0.000	0.000
MC background cross section	0.000	0.000
Signal modeling	0.000	-0.005
PDF	0.015	-0.015
ISR/FSR variation	0.004	-0.005
Color reconnection	0.000	-0.005
b fragmentation	0.000	0.000
b tag TRF	0.000	0.000
light tag TRF	0.001	-0.001
TRF for Summer10 data set	0.000	-0.001
Taggability scale factor	0.000	0.000
Jet energy resolution	0.000	-0.004
Jet energy scale	0.000	-0.001
Sample-dependent JES	0.000	-0.001
b-jet energy scale	0.000	-0.004
Jet reconstruction and identification	0.006	-0.006
Vetexconfirmation	0.000	-0.001
Limited Monte Carlo statistics	0.004	-0.004
Statistics in Loose - Tight	0.000	0.000
ε_{qcd}	0.000	0.000
ε_{sig}	0.002	0.000
Total systematic	0.017	-0.021

6.6 Asymmetry Results

To test CP violation in $t\bar{t}$ events decaying to lepton+jets in the DØ experiment, physics observables are established in Reference [16]. With these physics observables, CP violating asymmetries, asymmetry dilution, and systematic uncertainties are measured with two or more b-tagged events in e+jets, μ+jets and lepton+jets. The final results for e+jets, μ+jets and lepton+jets are presented in Table 6.47, 6.48 and 6.49, respectively. In these tables, "x" indicates there is no corresponding uncertainty.

Table 6.47: The final results of CP violating asymmetry measurements in e+jets channel.

	$A_{central}$	$\sigma_{stat.}$	$\sigma_{dilution}$	$\sigma_{sys.}$	$\sigma_{stat.+dilution+sys.}$
O_1	+0.007	$^{+0.115}_{-0.115}$	x	$^{+0.013}_{-0.012}$	$^{+0.116}_{-0.116}$
O_2	+0.128	$^{+0.113}_{-0.115}$	$^{+0.031}_{-0.041}$	$^{+0.012}_{-0.019}$	$^{+0.118}_{-0.124}$
O_3	-0.117	$^{+0.115}_{-0.114}$	$^{+0.003}_{-0.002}$	$^{+0.016}_{-0.015}$	$^{+0.116}_{-0.115}$
O_4	+0.098	$^{+0.114}_{-0.115}$	$^{+0.024}_{-0.033}$	$^{+0.022}_{-0.011}$	$^{+0.119}_{-0.120}$
O_7	+0.079	$^{+0.114}_{-0.115}$	$^{+0.024}_{-0.025}$	$^{+0.013}_{-0.018}$	$^{+0.117}_{-0.119}$
O_a	-0.010	$^{+0.115}_{-0.115}$	$^{+0.030}_{-0.026}$	$^{+0.015}_{-0.014}$	$^{+0.120}_{-0.119}$
O_b	-0.182	$^{+0.115}_{-0.113}$	$^{+0.040}_{-0.031}$	$^{+0.020}_{-0.023}$	$^{+0.123}_{-0.119}$

Table 6.48: The final results of CP violating asymmetry measurements in μ+jets channel.

	$A_{central}$	$\sigma_{stat.}$	$\sigma_{dilution}$	$\sigma_{sys.}$	$\sigma_{stat.+dilution+sys.}$
O_1	+0.097	$^{+0.111}_{-0.112}$	x	$^{+0.016}_{-0.015}$	$^{+0.112}_{-0.113}$
O_2	+0.090	$^{+0.111}_{-0.112}$	$^{+0.038}_{-0.038}$	$^{+0.016}_{-0.017}$	$^{+0.118}_{-0.119}$
O_3	+0.015	$^{+0.112}_{-0.112}$	$^{0.000}_{-0.001}$	$^{+0.019}_{-0.015}$	$^{+0.114}_{-0.113}$
O_4	-0.006	$^{+0.112}_{-0.112}$	$^{+0.028}_{-0.024}$	$^{+0.015}_{-0.016}$	$^{+0.116}_{-0.116}$
O_7	+0.001	$^{+0.112}_{-0.112}$	$^{+0.028}_{-0.027}$	$^{+0.015}_{-0.017}$	$^{+0.116}_{-0.116}$
O_a	-0.040	$^{+0.112}_{-0.112}$	$^{+0.028}_{-0.024}$	$^{+0.015}_{-0.018}$	$^{+0.116}_{-0.116}$
O_b	+0.073	$^{+0.111}_{-0.112}$	$^{+0.037}_{-0.039}$	$^{+0.017}_{-0.019}$	$^{+0.118}_{-0.120}$

Table 6.49: The final results of CP violating asymmetry measurements in lepton+jets channel.

	$A_{central}$	$\sigma_{stat.}$	$\sigma_{dilution}$	$\sigma_{sys.}$	$\sigma_{stat.+dilution+sys.}$
O_1	+0.053	$^{+0.081}_{-0.081}$	x	$^{+0.017}_{-0.015}$	$^{+0.083}_{-0.082}$
O_2	+0.106	$^{+0.080}_{-0.081}$	$^{+0.035}_{-0.039}$	$^{+0.014}_{-0.017}$	$^{+0.088}_{-0.091}$
O_3	-0.049	$^{+0.081}_{-0.080}$	$^{+0.001}_{-0.001}$	$^{+0.019}_{-0.016}$	$^{+0.083}_{-0.082}$
O_4	+0.046	$^{+0.081}_{-0.081}$	$^{+0.025}_{-0.029}$	$^{+0.017}_{-0.016}$	$^{+0.086}_{-0.088}$
O_7	+0.039	$^{+0.081}_{-0.081}$	$^{+0.027}_{-0.025}$	$^{+0.017}_{-0.019}$	$^{+0.087}_{-0.087}$
O_a	-0.025	$^{+0.081}_{-0.081}$	$^{+0.029}_{-0.025}$	$^{+0.016}_{-0.017}$	$^{+0.088}_{-0.086}$
O_b	-0.053	$^{+0.081}_{-0.080}$	$^{+0.038}_{-0.035}$	$^{+0.017}_{-0.021}$	$^{+0.091}_{-0.090}$

Table 6.49 shows the final results for e+jets and μ+jets channels combined. In this table, the asymmetry of O_2 is the most significant excursion:

$$l + \text{jets}: \quad O_2 \;=\; 0.106\ ^{+0.088}_{-0.091}\ (\text{stat.} + \text{dilution} + \text{sys.})$$

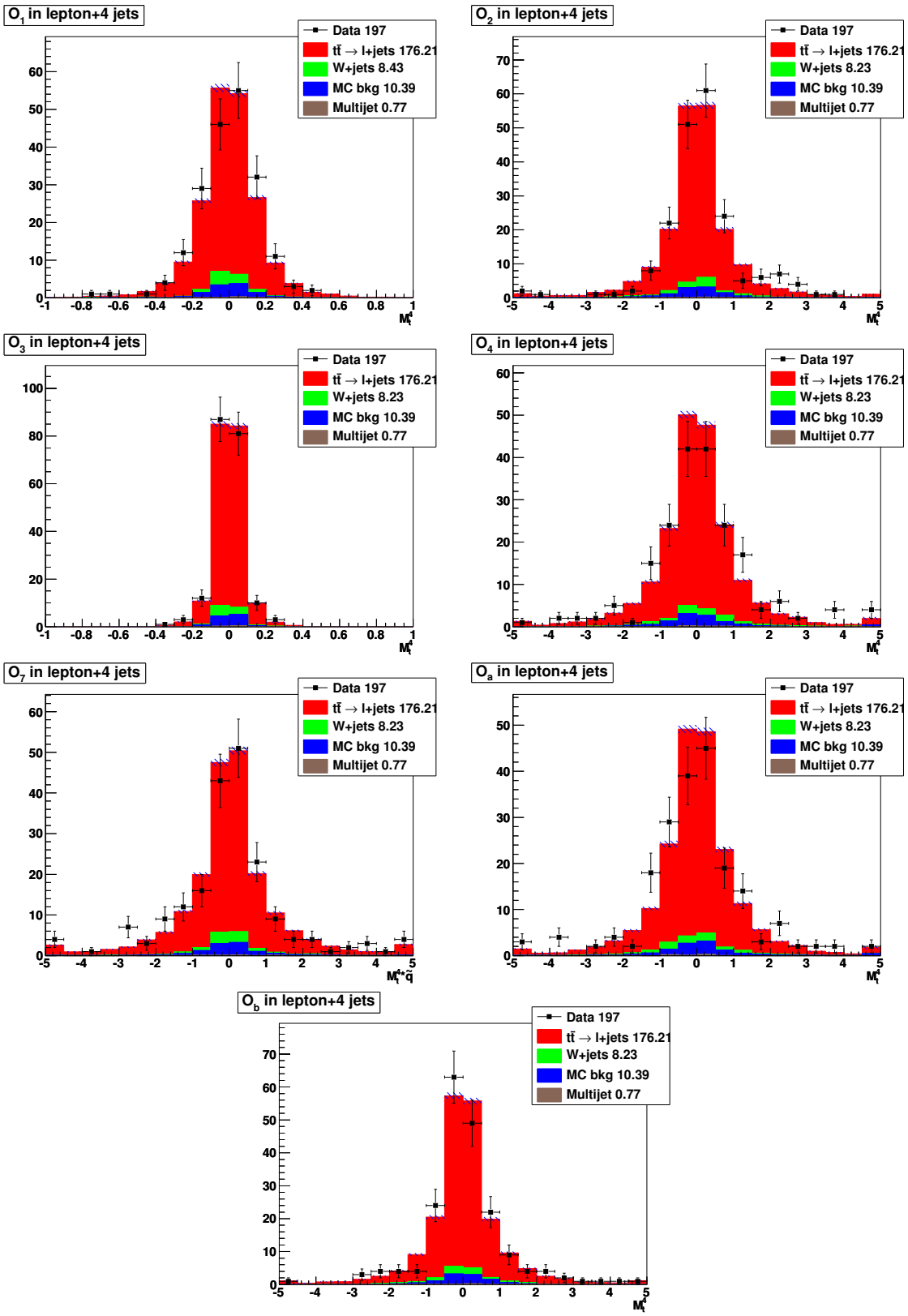

Figure 6.33: The distributions of all physics observables with 2 b-tags and the fitted number of $t\bar{t}$ in lepton+jets.

CHAPTER 7. Conclusion

The CP violating asymmetries for the $t\bar{t}$ pair production are measured in the lepton+jets channel for 4281.66 pb^{-1} of data at $\sqrt{s} = 1.96$ TeV. The b-tagging algorithm is used to reduce background contributions significantly. The CP violating asymmetry results that combine e+jets and μ+jets are:

$$
\begin{aligned}
l + \text{jets}: \quad \mathrm{O}_1 &= +0.053\ ^{+0.083}_{-0.083}\ (\text{stat.} + \text{dilution} + \text{sys.}) \\
\mathrm{O}_2 &= +0.106\ ^{+0.088}_{-0.091}\ (\text{stat.} + \text{dilution} + \text{sys.}) \\
\mathrm{O}_3 &= -0.049\ ^{+0.083}_{-0.082}\ (\text{stat.} + \text{dilution} + \text{sys.}) \\
\mathrm{O}_4 &= +0.046\ ^{+0.086}_{-0.088}\ (\text{stat.} + \text{dilution} + \text{sys.}) \\
\mathrm{O}_7 &= +0.039\ ^{+0.087}_{-0.086}\ (\text{stat.} + \text{dilution} + \text{sys.})
\end{aligned}
$$

The asymmetry results to measure CP conserving contamination in the CP-odd signal are:

$$
\begin{aligned}
l + \text{jets}: \quad \mathrm{O}_a &= -0.025\ ^{+0.088}_{-0.086}\ (\text{stat.} + \text{dilution} + \text{sys.}) \\
\mathrm{O}_b &= -0.053\ ^{+0.091}_{-0.090}\ (\text{stat.} + \text{dilution} + \text{sys.})
\end{aligned}
$$

If the measurement uncertainties derived with statistical, dilution and systematic are considered, the measured asymmetries for all physics observables except O_2 are consistent with the Standard Model prediction. Also, O_a and O_b are consistent with the Standard Model prediction. But O_2 gives the largest asymmetry when the measurement uncertainty is taken into account. We could find about 1.2σ statistical sensitivity at the Tevatron with 4281.66 pb^{-1}.

In Table 6.49, the fractions of uncertainties for statistical, dilution and systematics are about 80%, 17% and 3% in the physics observable O_2. The statistical uncertainty is predominant in this analysis. The fractions of uncertainties can be interpreted as:

1. The contributions of the systematic uncertainties are very small compared to the statistical uncertainty. The systematic uncertainties considered in this analysis show how asymmetries vary by changing the contributions of backgrounds. Therefore, if backgrounds are efficiently removed for this analysis, the systematic uncertainties becomes very small and don't affect the uncertainties of the asymmetry measurements.

2. The factors for asymmetry dilution studied in this analysis are related to DØ detector performance. Uncertainties from these dilution factors can be considered as irreducible factors. Especially, the energy resolution of DØ hadronic calorimeter gives the biggest uncertainty to O_2, O_4, O_7, O_a and O_b among the dilution factors. Thus, a hadronic calorimeter which has a better energy resolution is needed, or more statistical sensitivity, to measure a more accurate asymmetry.

3. This analysis is affected by the statistical uncertainty predominantly. To find CP violation and anomalous top-quark coupling, the statistical uncertainty should be reduced significantly. Thus, more data are needed.

If we assume that the asymmetry of O_2 is maintained at 10.6% at 12 fb^{-1} and the b-tagging probability is the same, the statistical uncertainty will be decreased by a factor of two. Under this assumption, if we consider the dilution and systematic uncertainty, it will not be easy to find a 3σ statistical sensitivity at the Tevatron. The LHC already started accumulating data. In the future, I hope that my friends at the LHC will find CP violation in $t\bar{t}$ production with high statistics.

APPENDIX A. Control Plots

A.1 Control Plots for e+4 jets before b-tagging

This chapter shows control plots for several kinematic variables drawn with before b-tag and ≥ 2 b-tags in e+4 jets and μ+ 4 jets. The definitions of the kinematic variables are described below. To estimate the $t\bar{t}$ signal, we used the measured cross section $\sigma_{t\bar{t}} = 8.13$ pb.

- x_1, x_2: momentum fractions (Bjorken x).
- $(x_1 + x_2) \times p$: x_1, x_2 are momentum fractions and p is proton or anti-proton momentum.
- H_T: sum of the transverse momenta of all jets.
- H_T^{all}: sum of the transverse energy of all objets in the final state.
- p_T^W: the transverse momentum of the W boson.
- Centrality: H_T/H, H is the scalar sum of all jet energies.
- Sphericity: $S = \frac{3}{2}(\lambda_2 + \lambda_3)$, $\lambda_1 \geq \lambda_2 \geq \lambda_3$ are the three eigenvalues of a normalized tensor $S^{\alpha\beta} = \frac{\sum_i p_i^\alpha p_i^\beta}{\sum_i |\mathbf{p}_i|^2}$, where $\alpha, \beta = 1, 2, 3$ are the x, y and z components and $\mathbf{p}_i$ is the momentum of particle i in the event. $\lambda_1 + \lambda_2 + \lambda_3 = 1$. $S \approx 0$ is 2-jet event (back-to-back) and $S \approx 1$ corresponds to isotropic event. [78].
- Aplanarity: $A = \frac{3}{2}\lambda_3$, λ_3 is the smallest eigenvalue of the normalized momentum tensor $S^{\alpha\beta}$. A is the value between 0 and $\frac{1}{2}$. $A \approx 0$ is a planar event and $A \approx \frac{1}{2}$ is an isotropic event.
- Planarity: $P = \lambda_2 - \lambda_3$. $P \approx 1$ is a back-to-back jet-like structure event while $P \approx 0$ is high multiplicity isotropic event structure.

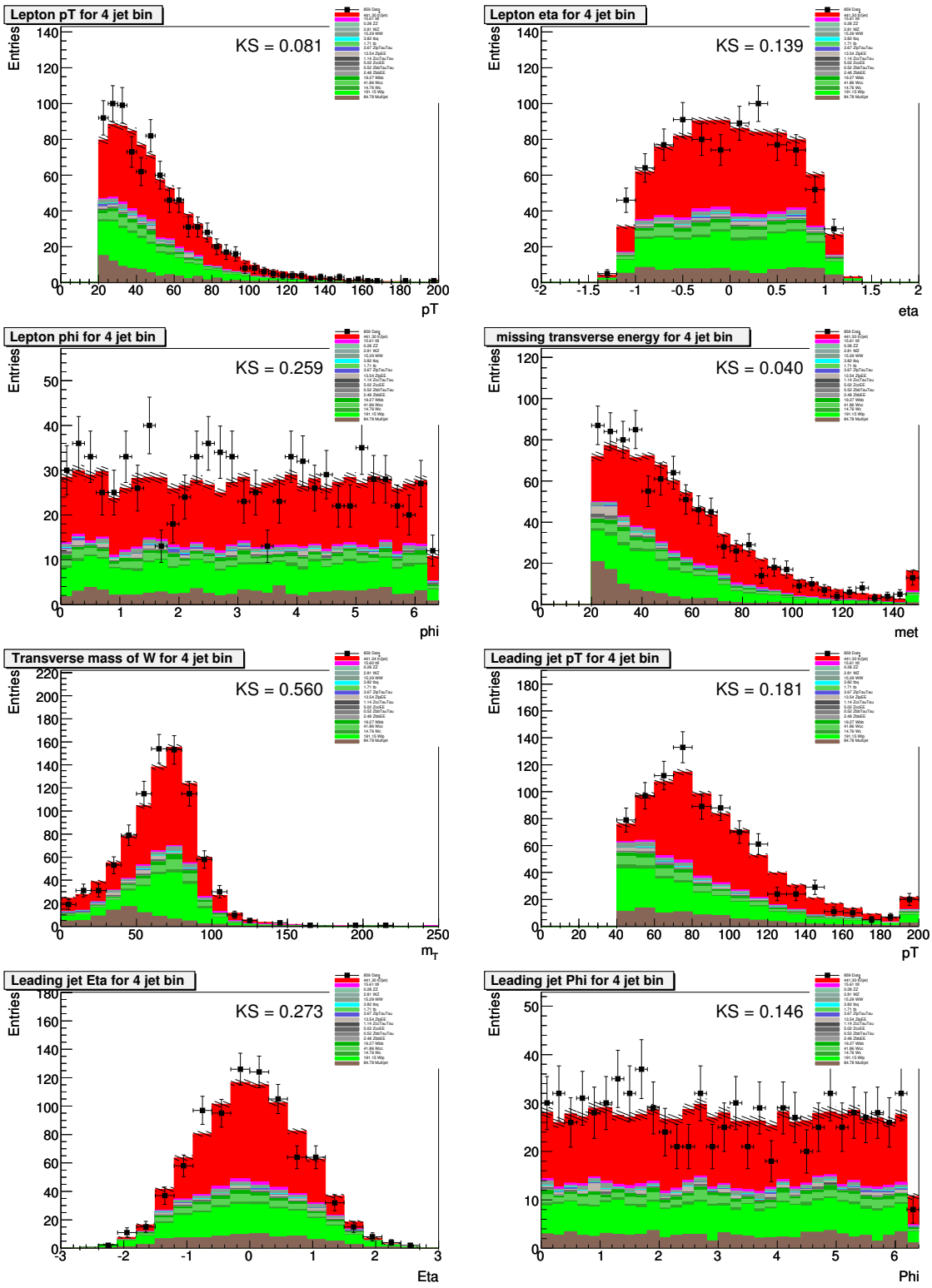

Figure A.1: The comparison of Data and Monte Carlo before b-tagging in e+jets channel.

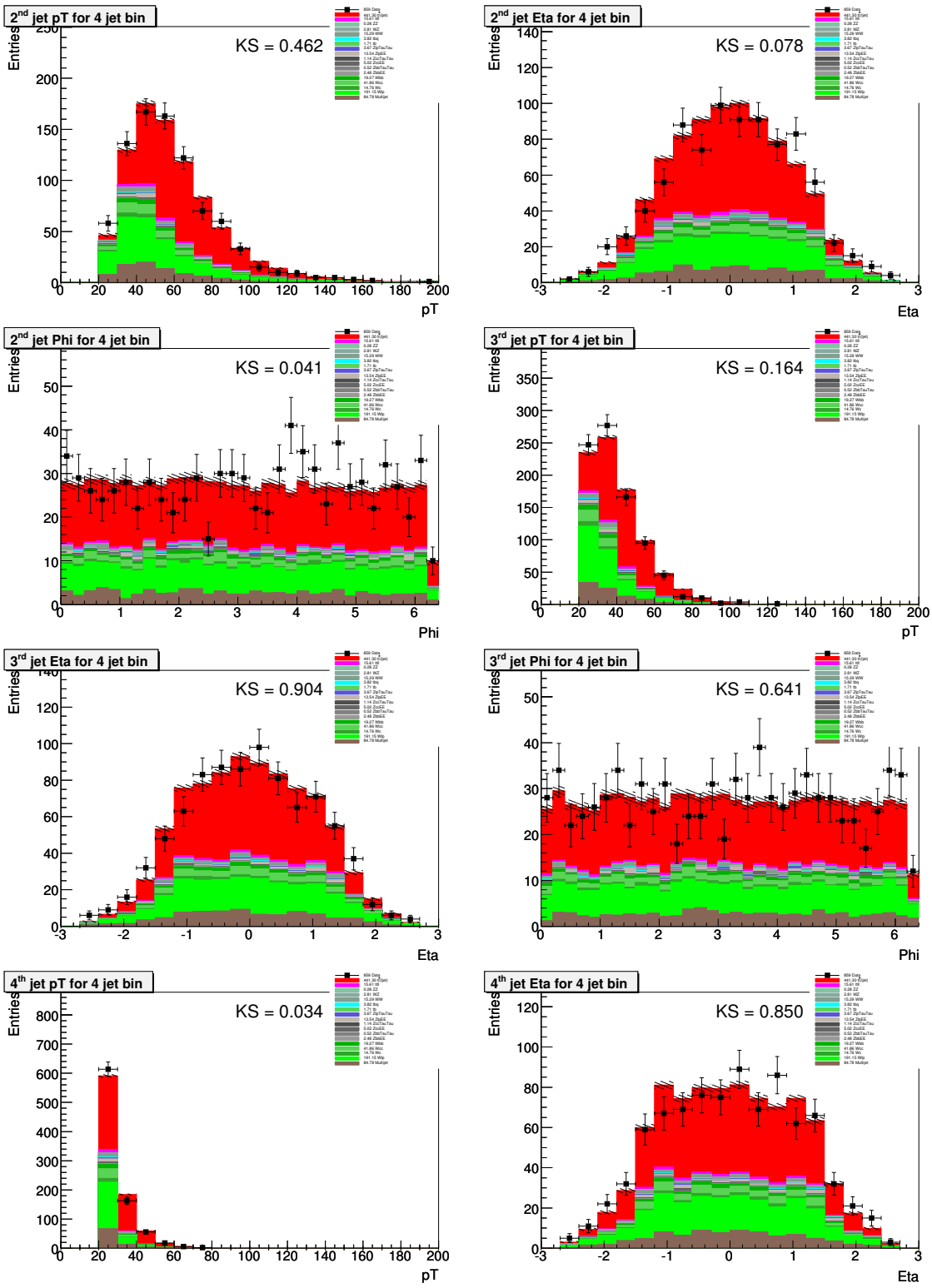

Figure A.2: The comparison of Data and Monte Carlo before b-tagging in e+jets channel.

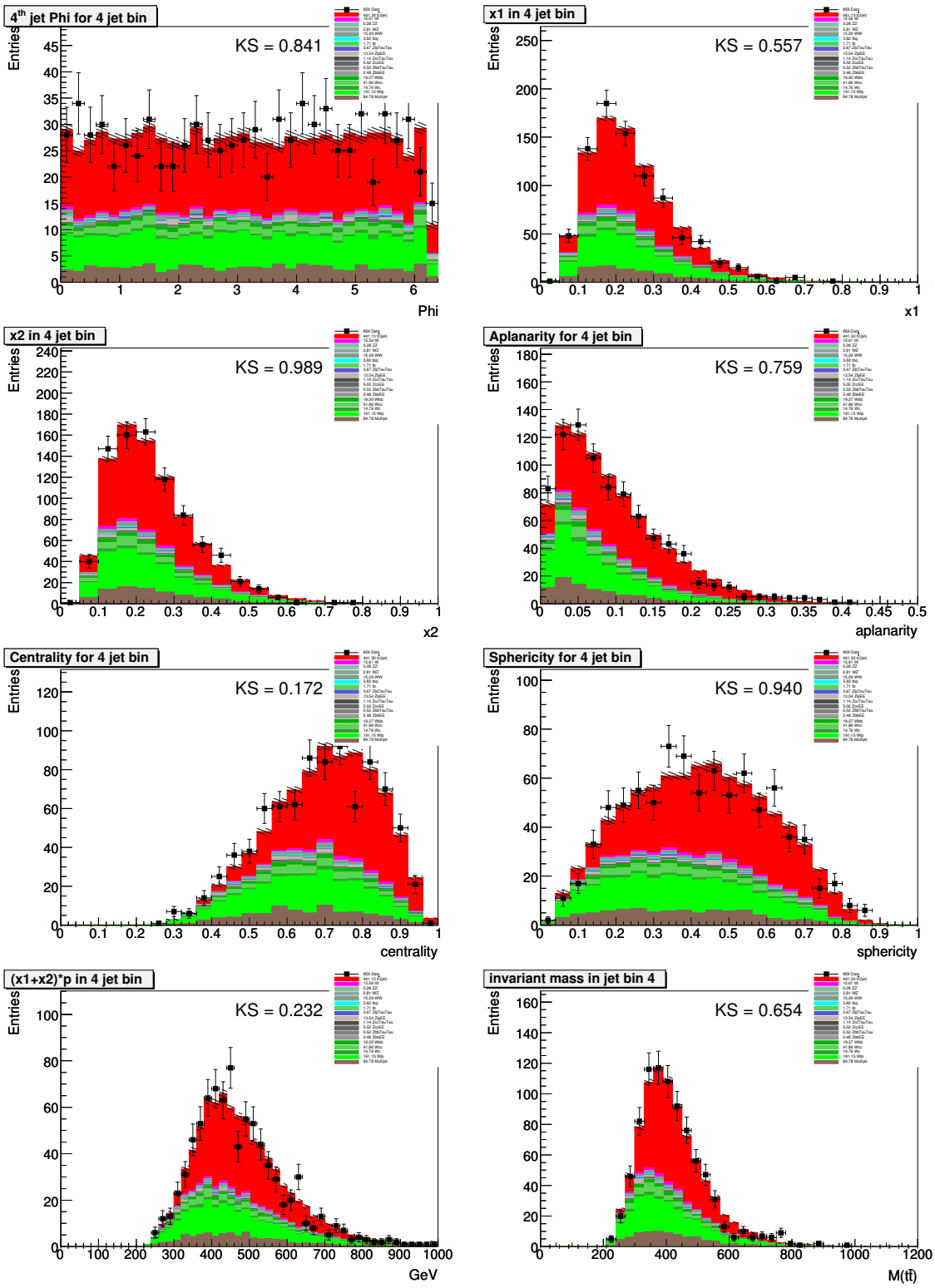

Figure A.3: The comparison of Data and Monte Carlo before b-tagging in e+jets channel.

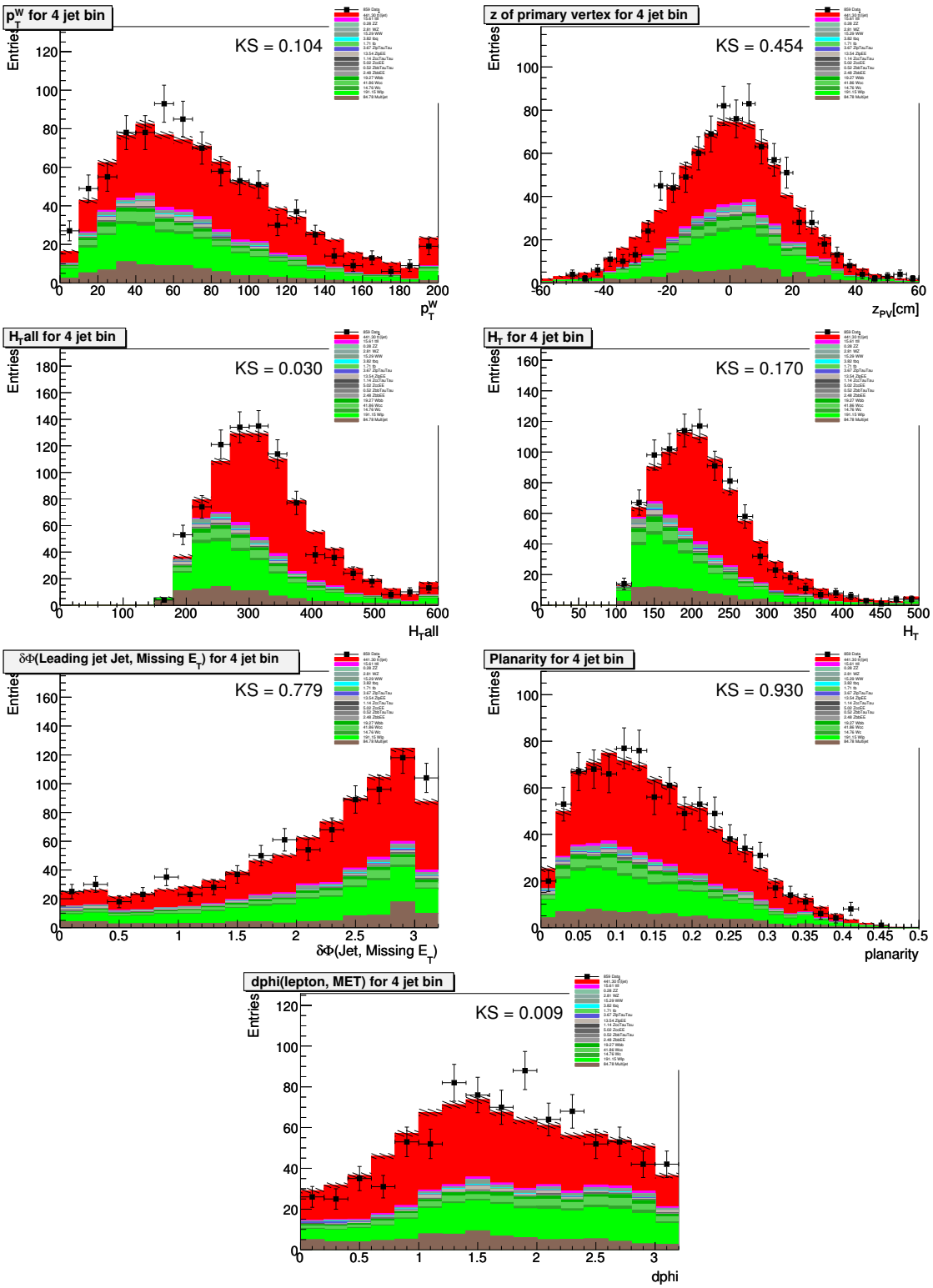

Figure A.4: The comparison of Data and Monte Carlo before b-tagging in e+jets channel.

A.2 Control Plots for μ+4 jets before b-tagging

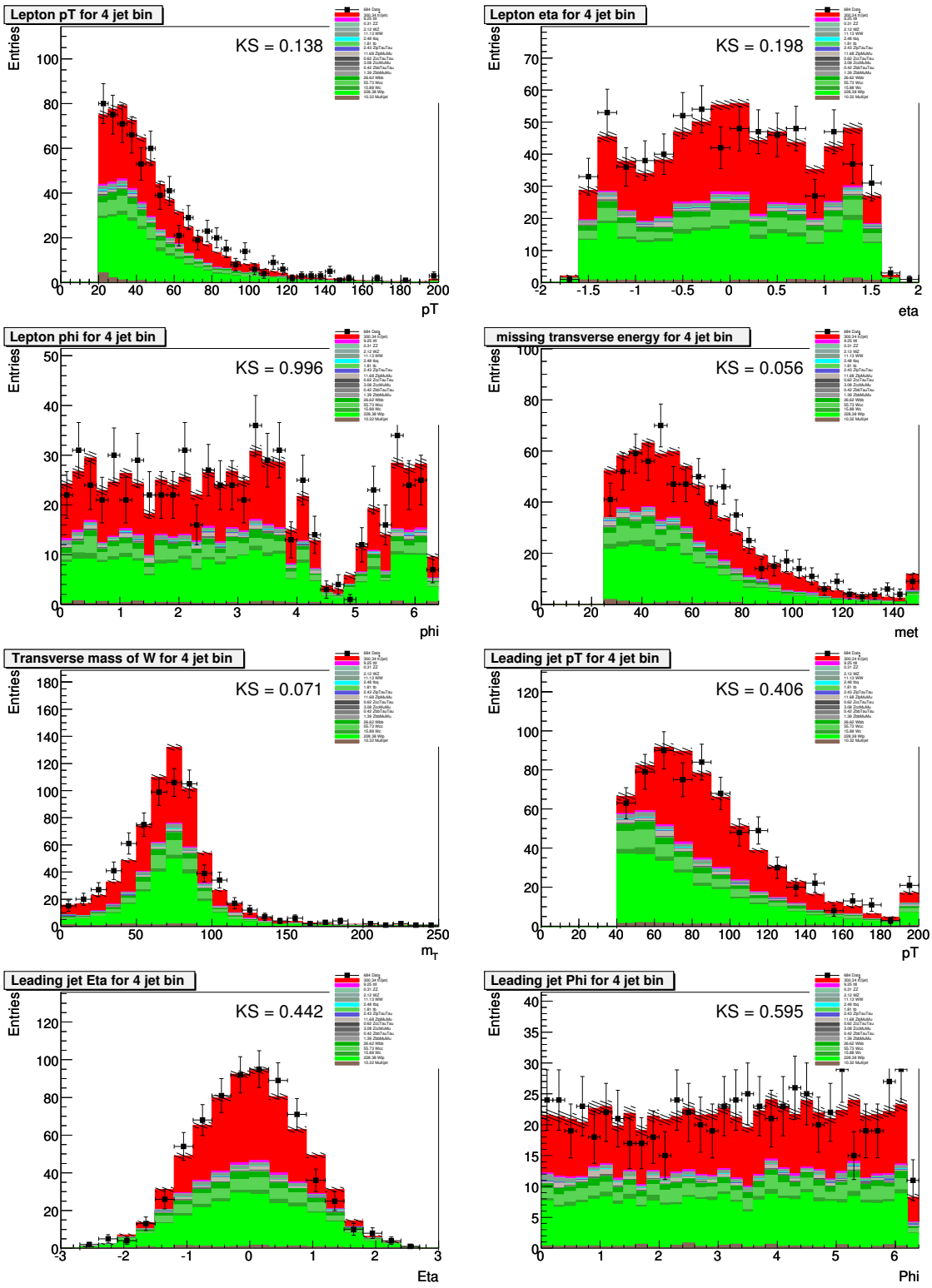

Figure A.5: The comparison of Data and Monte Carlo before b-tagging in μ+jets channel.

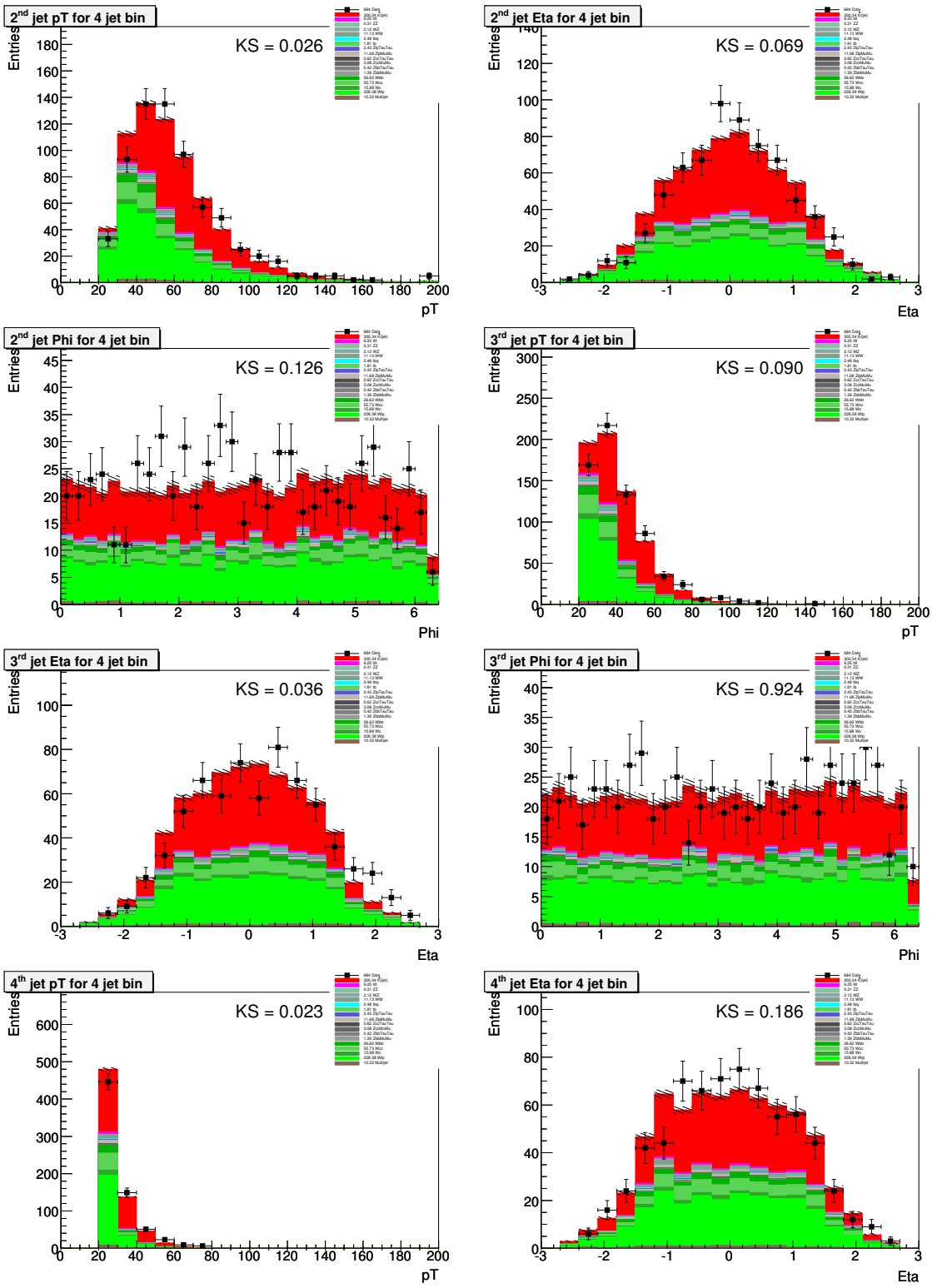

Figure A.6: The comparison of Data and Monte Carlo before b-tagging in μ+jets channel.

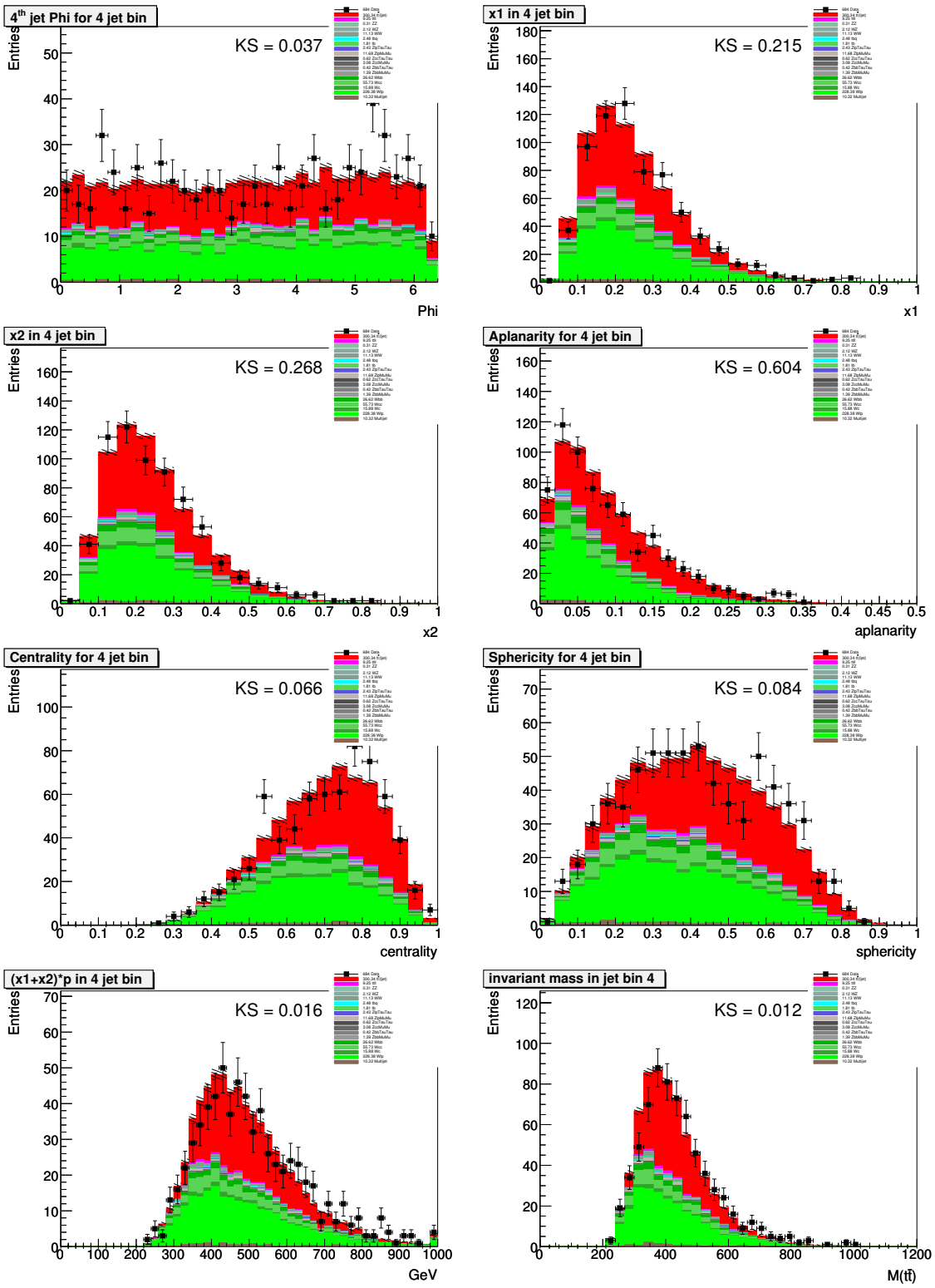

Figure A.7: The comparison of Data and Monte Carlo before b-tagging in μ+jets channel.

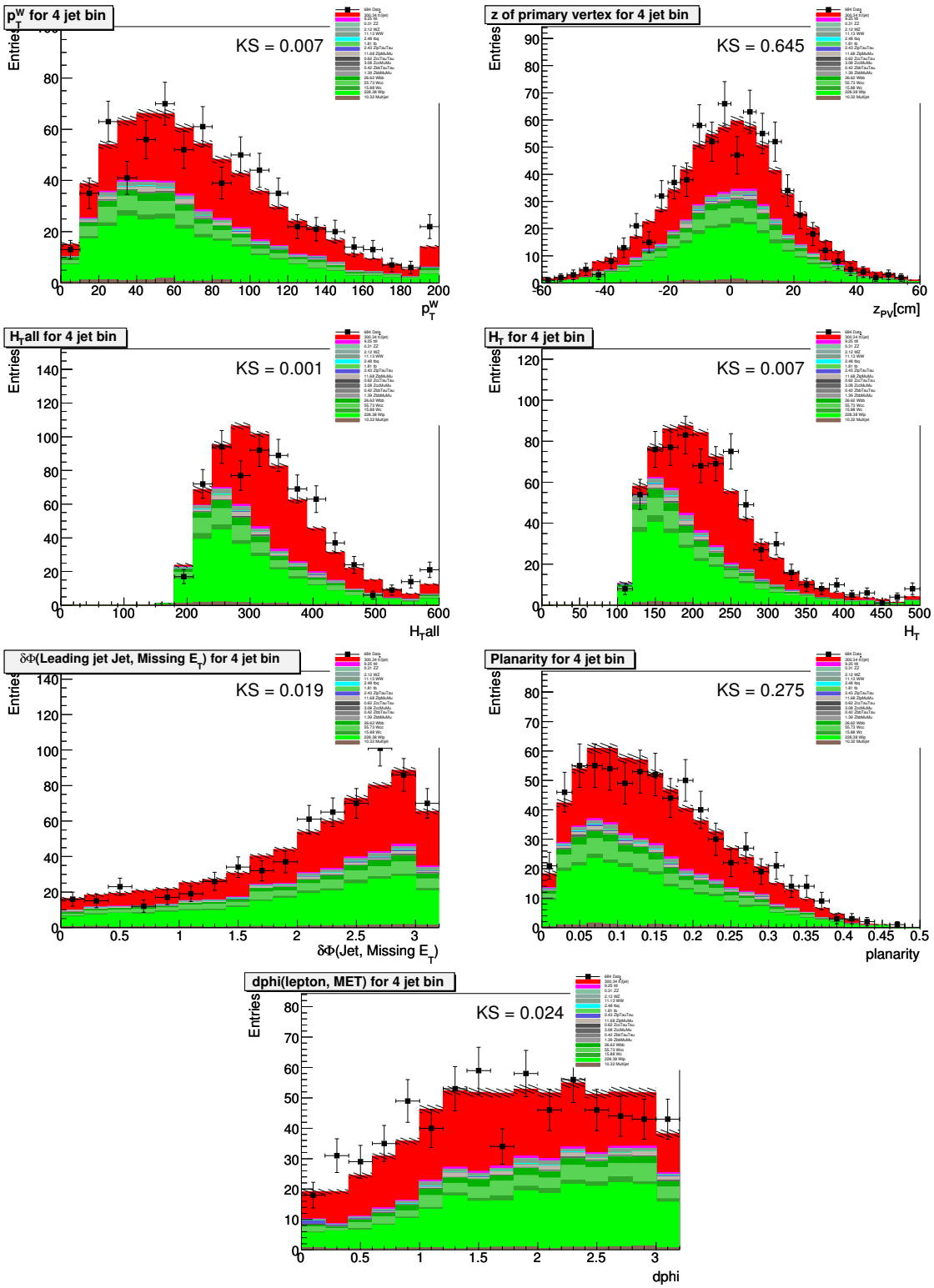

Figure A.8: The comparison of Data and Monte Carlo before b-tagging in μ+jets channel.

A.3 Control Plots for e+4 jets with $\geq$ 2 b-tags

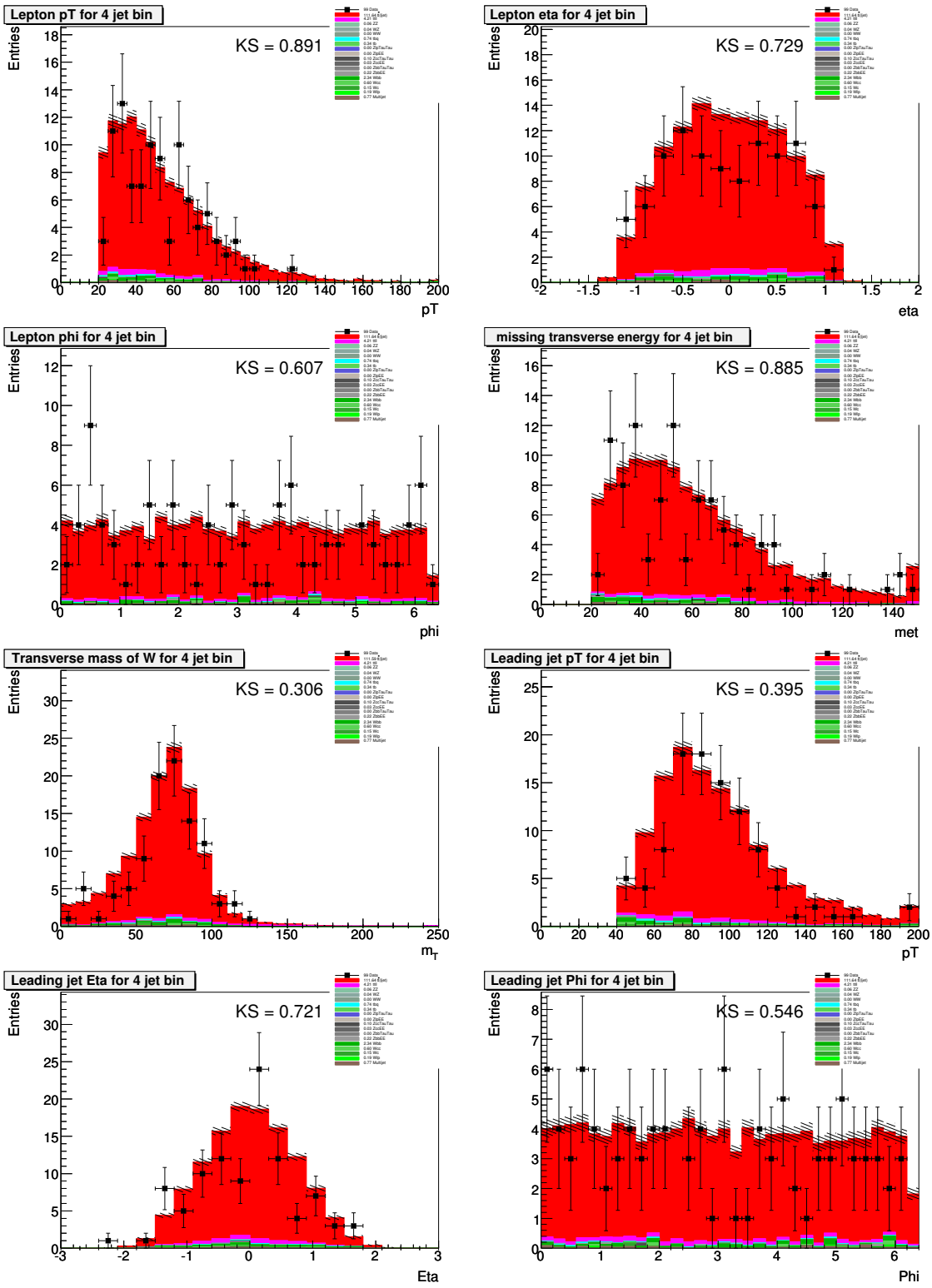

Figure A.9: The comparison of Data and Monte Carlo with ≥ 2 b-tags in e+jets channel.

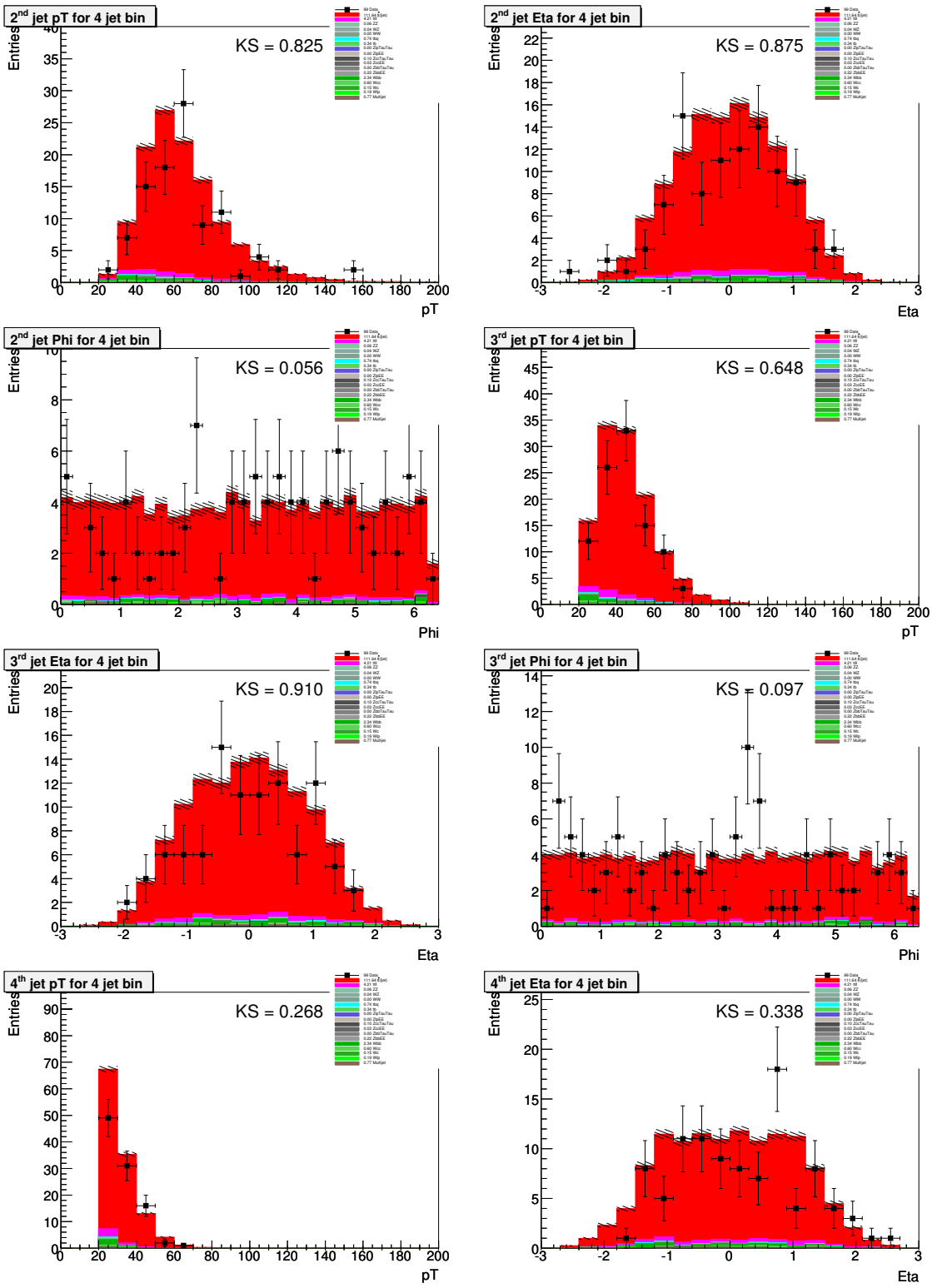

Figure A.10: The comparison of Data and Monte Carlo with ≥ 2 b-tags in e+jets channel.

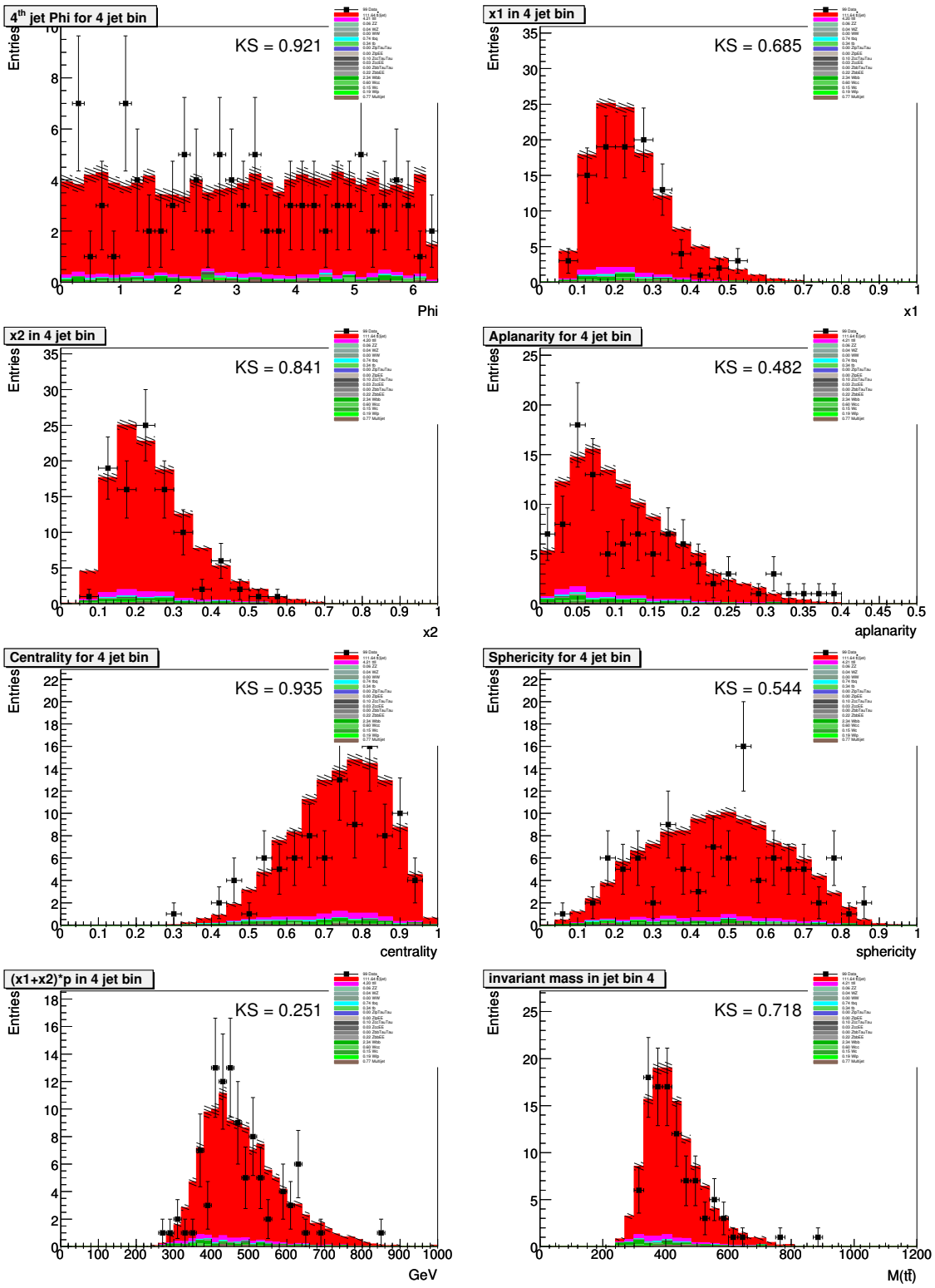

Figure A.11: The comparison of Data and Monte Carlo with ≥ 2 b-tags in e+jets channel.

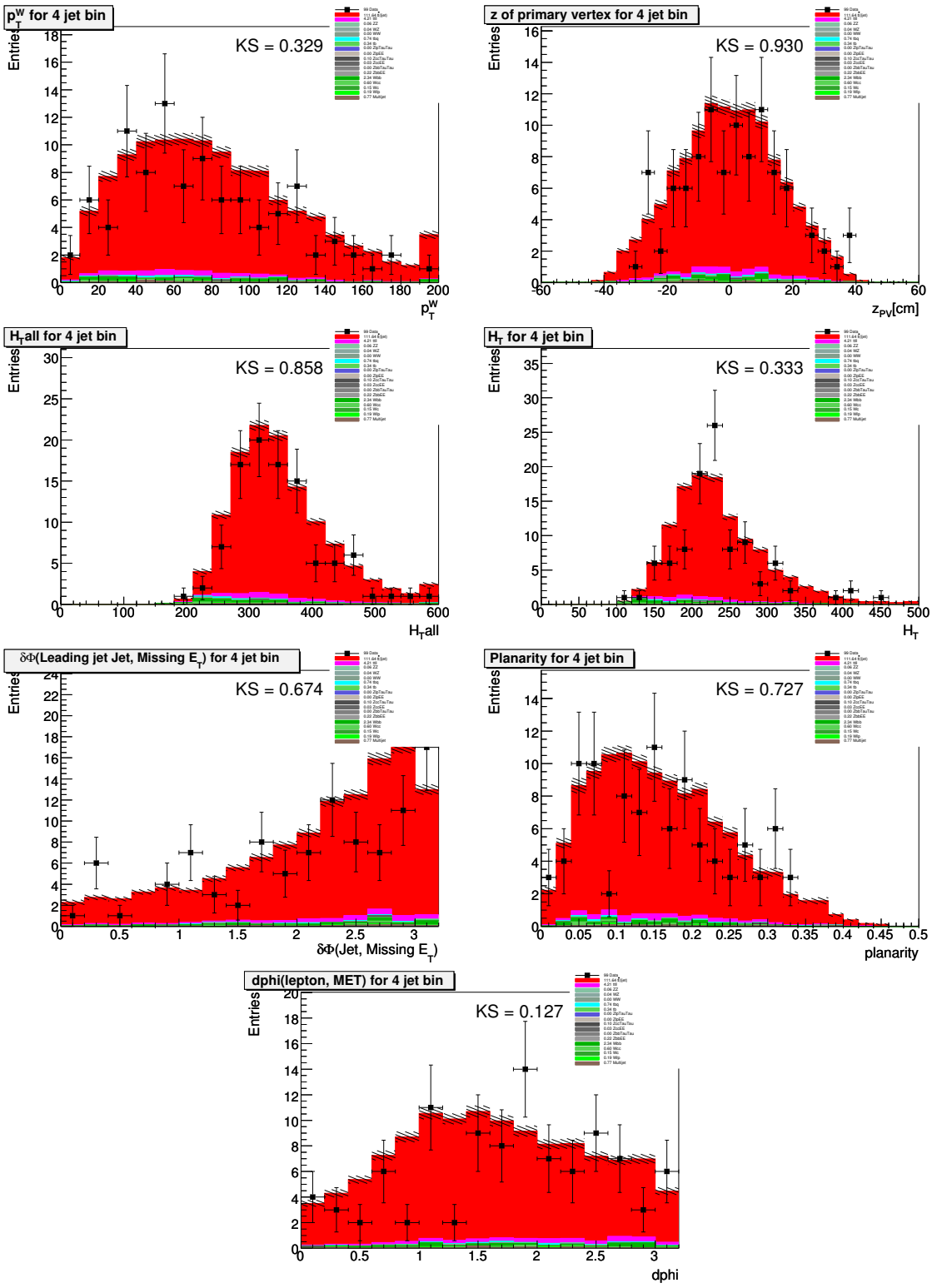

Figure A.12: The comparison of Data and Monte Carlo with ≥ 2 b-tags in e+jets channel.

A.4 Control Plots for μ+4 jets with $\geq$ 2 b-tags

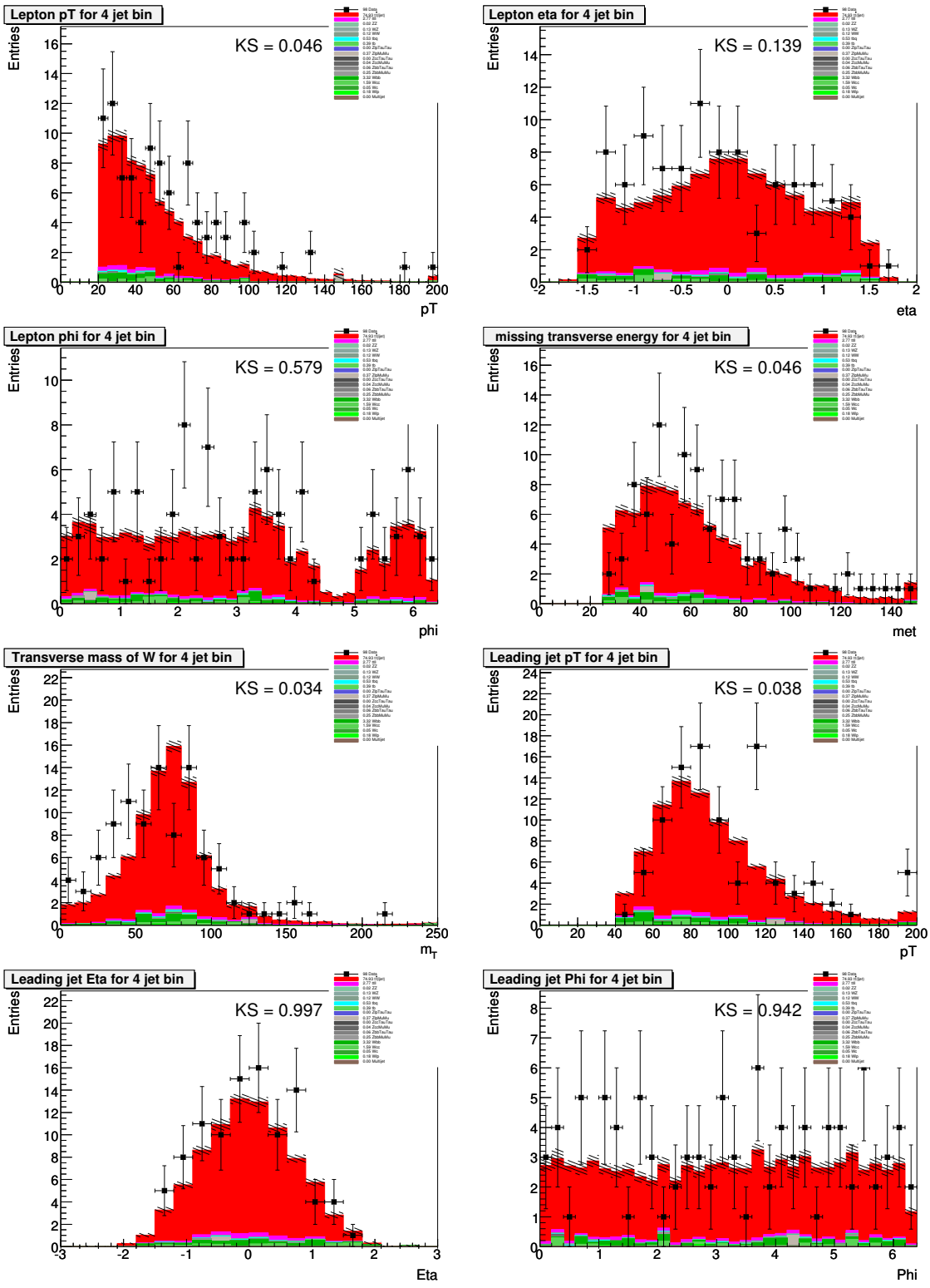

Figure A.13: The comparison of Data and Monte Carlo with ≥ 2 b-tags in μ+jets channel.

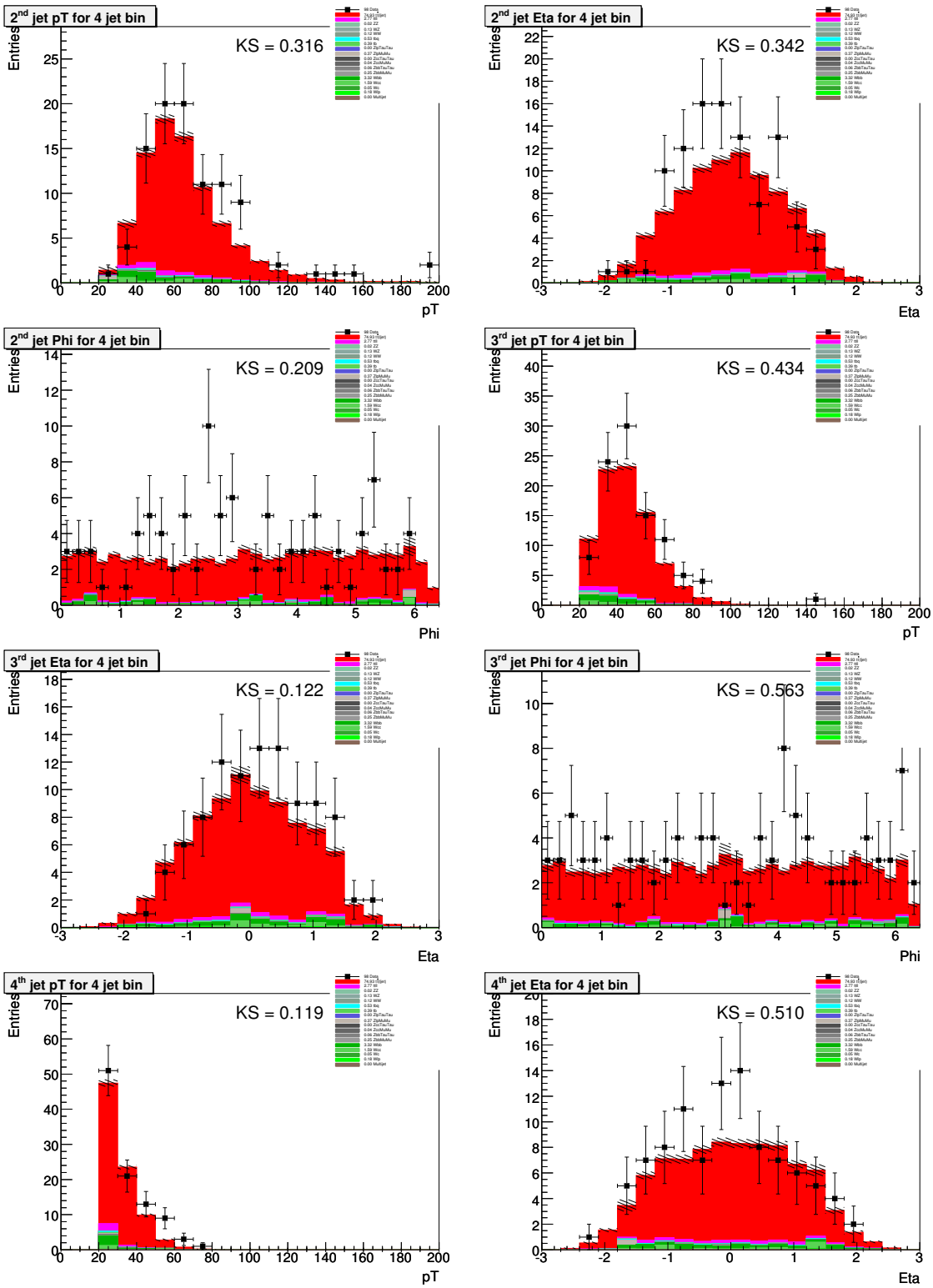

Figure A.14: The comparison of Data and Monte Carlo with ≥ 2 b-tags in μ+jets channel.

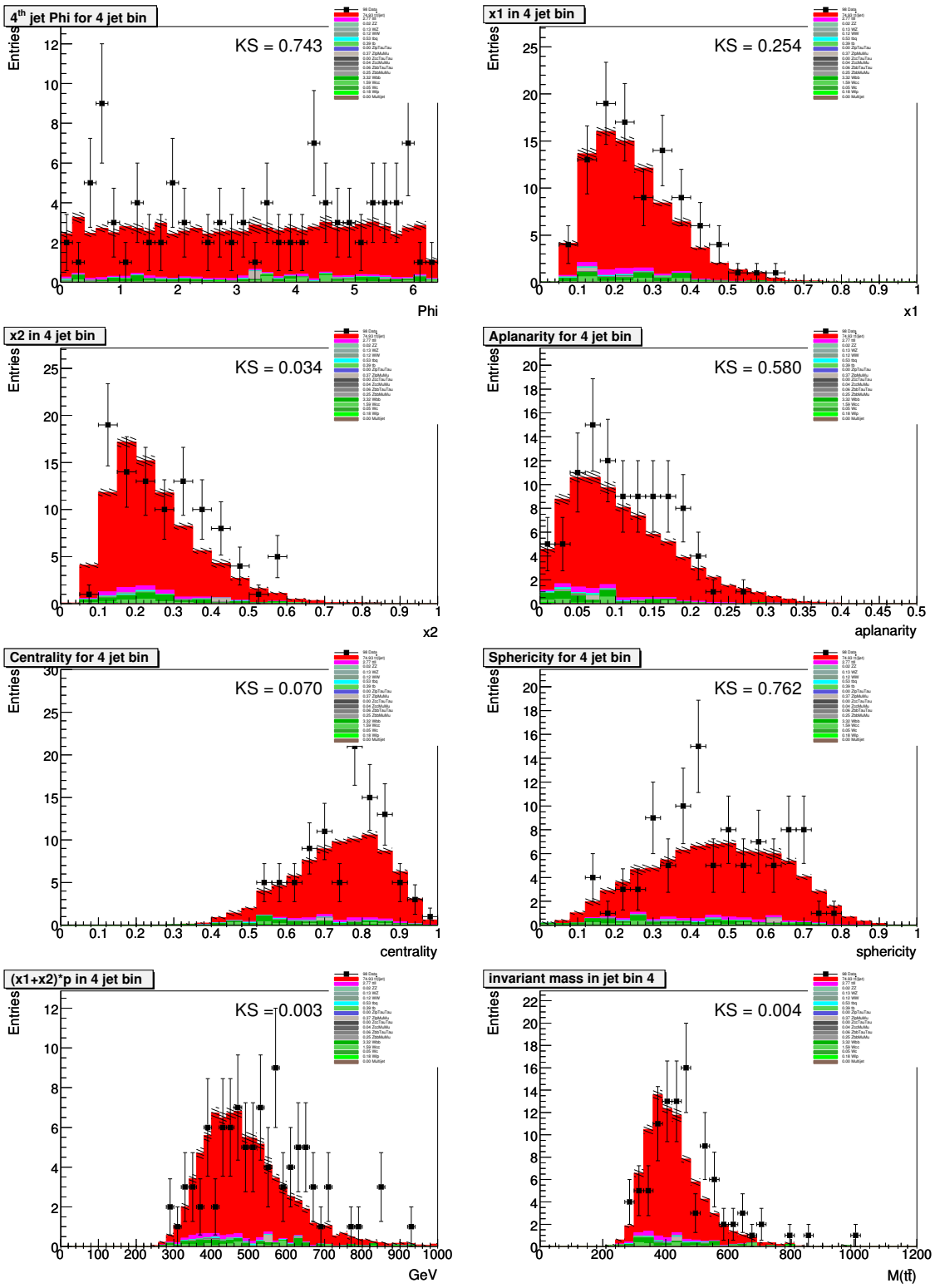

Figure A.15: The comparison of Data and Monte Carlo with ≥ 2 b-tags in μ+jets channel.

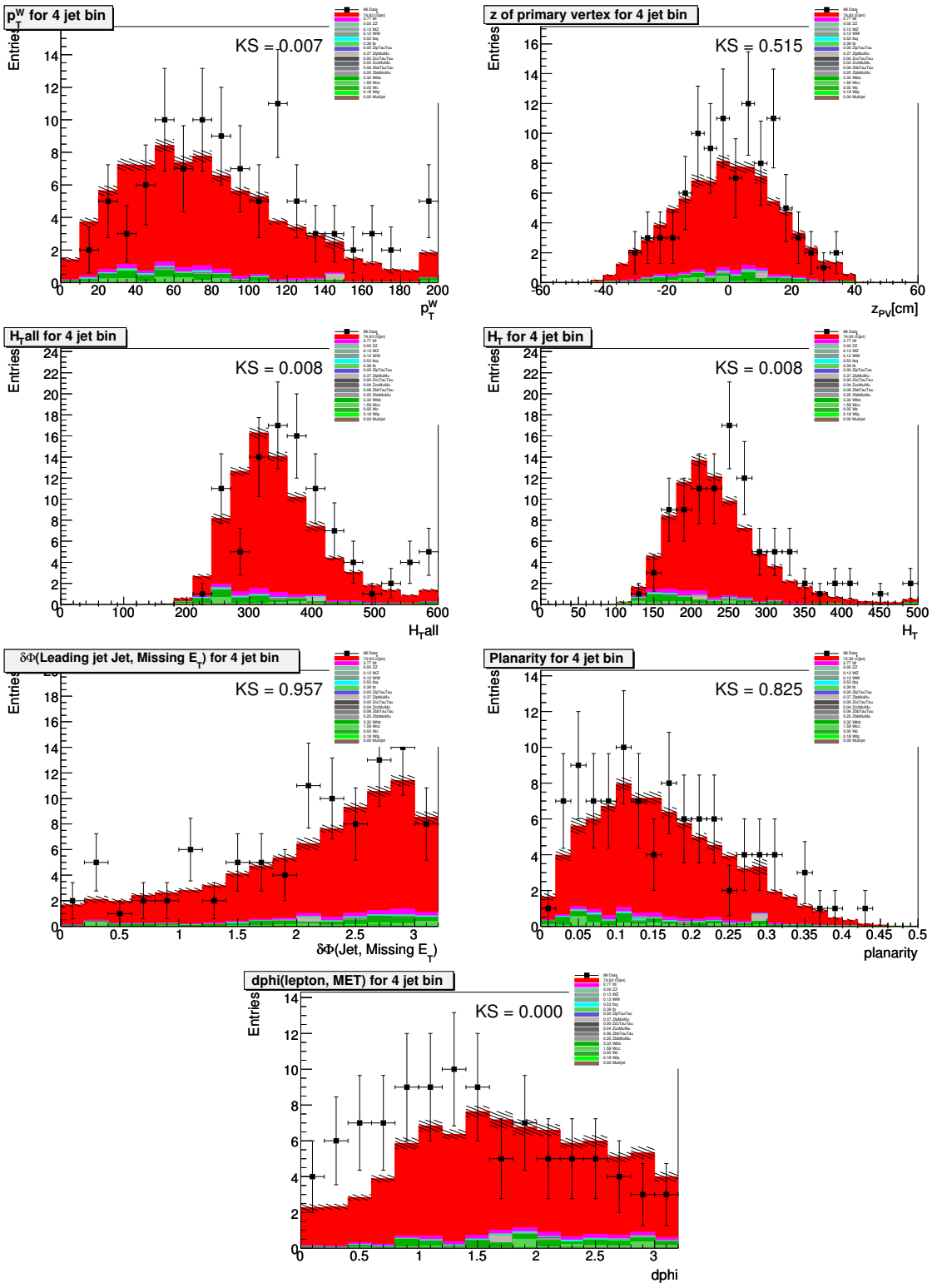

Figure A.16: The comparison of Data and Monte Carlo with ≥ 2 b-tags in μ+jets channel.

APPENDIX B. Reflection at the Boundary of an Absorbing Medium

The following describes an addition to the GEANT4 code to properly treat reflection in optical Cerenkov calorimeters.

Let a plane wave be incident on the boundary of a medium having a complex index of refraction

$$\mathcal{N} = n + i\kappa$$

And let's denote the angle of incidence by θ and the angle of refraction by ϕ. Now we express the law of refraction in terms of the complex index of refraction in a purely formal way as

$$\mathcal{N} = \frac{\sin\theta}{\sin\phi}$$

Here the angle ϕ is a complex number. It turns out that ϕ is very useful in simplifying the equations related to reflection and refraction by an absorbing medium. From the above definition of ϕ, we have

$$\cos\phi = \sqrt{1 - \frac{\sin^2\theta}{\mathcal{N}^2}}$$

If we derive the coefficient of reflection using the boundary conditions giving the continuity of the tangential components of the electric and magnetic fields for TE polarization[1] and TM polarization[2].

$$r_{TE} = \frac{\cos\theta - \mathcal{N}\cos\phi}{\cos\theta + \mathcal{N}\cos\phi} \qquad (TE\ polarization)$$

$$r_{TM} = \frac{\mathcal{N}\cos\theta - \cos\phi}{\mathcal{N}\cos\theta + \cos\phi} \qquad (TM\ polarization)$$

Now we can get the reflectance for TE and TM polarization.

$$R_{TE} = |r_{TE}|^2 \qquad (TE\ polarization)$$

[1] Transverse Electric, the electric field vector of incident wave is perpendicular to the plane of incidence

[2] Transverse Magnetic, the magnetic field vector of the incident wave is perpendicular to the plane of incidence

$$R_{TM} = |r_{TM}|^2 \qquad (TM\ polarization)$$

The above two cases are only for purely TE and TM polarized optical photon [79].

In GEANT4, if we don't set polarization for optical photon, the optical photon has random polarization. In other words, an optical photon can have both a TE polarization component and a TM polarization component. So, by the definition of the reflectance[3], we can derive the reflectance of a randomly polarized optical photon. Let $\vec{E_0}$ be the electric field vector of incident wave and $\vec{E'}$ be the electric field vector of reflected wave for a randomly polarized optical photon. Also, the electric field vector of incident wave is perpendicular and parallel to the plane of incidence for TE and TM polarization, respectively. The electric field vector is $\vec{E_\perp}$ and $\vec{E_\parallel}$ for TE and TM polarization respectively. If we write $\vec{E_0}$ and $\vec{E'}$ in terms of $\vec{E_\perp}$ and $\vec{E_\parallel}$

$$\vec{E_0} = \vec{E_\perp} + \vec{E_\parallel}$$

$$\vec{E'} = |r_{TE}|\vec{E_\perp} + |r_{TM}|\vec{E_\parallel},$$

we can get the reflectance for a randomly polarized optical photon at the boundary of an absorbing medium.

$$R = |r|^2 = \frac{|\vec{E'}|^2}{|\vec{E_0}|^2} = \frac{|r_{TE}|^2 E_\perp^2 + |r_{TM}|^2 E_\parallel^2}{E_\perp^2 + E_\parallel^2}$$

This implementation was added to the optical boundary process since GEANT 4.9.1 and is being used for GEANT4 simulation.
http://geant4.web.cern.ch/geant4/UserDocumentation/UsersGuides/ForApplicationDeveloper/BackupVersions/V9.3/html/AllResources/TrackingAndPhysics/physicsProcessOptical.src/GetReflectivity.pdf

[3]The *reflectance* is defined as the fraction of the incident light energy that is reflected

APPENDIX C. Photon Identification for Run II Data

C.1 Introduction

ANN (Artificial Neural Networks) performs the selection of the high p_T, isolated photons efficiently and selected photons have played a important role for analyses which use photon such as the $h \to \gamma\gamma$ analysis [80]. The study to optimize photon selection and measuring scale factors to account for the difference of photon selection efficiency between data and MC, are conducted. This appendix is written based on Reference [90].

C.2 Data and MC Samples

The 2EMhighpt and 2MUhighpt dataset skimmed by the Common Sample Group are used and the SAM definitions are:

- CSG_CAF_2EMhighpt_PASS2_p21.10.00
- CSG_CAF_2EMhighpt_PASS4_p21.10.00_p20.12.00
- CSG_CAF_2EMhighpt_PASS4_p21.10.00_p20.12.01
- CSG_CAF_2EMhighpt_PASS4_p21.10.00_p20.12.02
- CSG_CAF_2EMhighpt_PASS4_p21.10.00_p20.12.04
- CSG_CAF_2EMhighpt_PASS4_p21.12.00_p20.12.05_allfix
- CSG_CAF_2MUhighpt_PASS2_p21.10.00
- CSG_CAF_2MUhighpt_PASS4_p21.10.00_p20.12.00

- CSG_CAF_2MUhighpt_PASS4_p21.10.00_p20.12.01
- CSG_CAF_2MUhighpt_PASS4_p21.10.00_p20.12.02
- CSG_CAF_2MUhighpt_PASS4_p21.10.00_p20.12.04
- CSG_CAF_2MUhighpt_PASS4_p21.12.00_p20.12.05_allfix

This study uses the QCD di-photon, emjet [81], Zee and $Z \rightarrow \mu\mu+\gamma$ MC samples. Table C.1 shows the request IDs for MC samples.

Table C.1: Request IDs for this study are listed. PYTHIA [46] generates all events for these samples [90].

MC sample	Request IDs
QCD $\gamma\gamma$(m=15-50GeV)	99614-18
QCD $\gamma\gamma$(m=50-130GeV)	90252-53,99619-21
QCD $\gamma\gamma$(m=130-250GeV)	90254,99622-25
$Z \rightarrow \mu\mu + \gamma$	88454-55
EMjet (pThat=10-20GeV)	93773,93782,93788,93798-99,94115-17
EMjet (pThat=20-30GeV)	93174,93187,93196
EMjet (pThat=30-40GeV)	93016
EMjet (pThat=40-60GeV)	93015
EMjet (pThat=60-80GeV)	93014
EMjet (pThat=80-120GeV)	93013
Z/$\gamma*$ →ee (m=15-60GeV)	86887-91,86898-902
Z/$\gamma*$ →ee (m=60-130GeV)	86882-6,86893-7,94342-51
Z/$\gamma*$ →ee (m=130-250GeV)	104837-41

C.3 Event Selection

The primary vertex is required to be within the SMT fiducial regions: $|z_{PV}| < 60$ cm. Variables for photon selection are introduced in [82] and using those variables, each photon candidate are required to satisfy:

- in CC ($-1.1 < \eta_{det} < 1.1$) or EC ($1.5 < |\eta_{det}| < 2.5$) η fiducial region
- E_T (transverse energy) > 10 GeV

- id=±11 or 10
- isolation< 0.2
- EM fraction> 0.9

The electron candidates are selected in $Z \to ee$ MC and data with the tag-and-probe method described in sction C.8. This method is applied to data in order to find $Z \to l^+l^- + \gamma$ candidates, where $l = e, \mu$. Detail event selection method is described in [84]. Photon candidates are found using these selection criteria and Figures C.1 - C.4 show distributions of variables which are used to select photon candidates, and their cut efficiencies as function of variables. The distributions of variables of γ, jet, $Z \to ee$ MC samples and $Z \to ee$ data are compared and it is confirmed that photon and jet have distinguishable features in the distributions of these variables.

C.4 Optimization for the Run IIb Data

C.4.1 Core Cuts

Table C.2 shows the previous (Run IIa data) selection criteria for photon candidate. But while data are accumulated through Run IIb operation, $W/Z\gamma$ events are expected to be found significantly. Thus, the necessity to select the low transverse energy of photon (10 GeV) for $W/Z\gamma$ analysis arises. The "core0" cut is designed for the analyses which use the low transverse energy of photon. In addition, Artificial Neural Network (ANN) for photon selection are trained and the output of ANN plays a role as one variable to select photon candidate [83]. Table C.3 shows the developed core definitions for photon selection.

The comparison of the old and new core cut performances are shown in Figures C.5 and C.6. The new core cuts keep the similar signal efficiency as the old core definitions while they reject more efficiently fake photons than the previous cuts. Figures C.7 - C.12 show the efficiencies as function of the transverse momentum, detector η and ϕ of photons for all individual core definitions. The scale factors are derived with $Z \to ee$ data and MC, and

Table C.2: The previous core definitions for the Run IIa data. The CC is referred to $-1.1 < \eta_{det} < 1.1$ and EC is definded as $1.5 < |\eta_{det}| < 2.5$. The eq1 = $7.3 \cdot \eta_{det}^2$ - $35.9 \cdot |\eta_{det}|$ + 45.7, and eq2 = $7.5 \cdot \eta_{det}^2$ - $36.0 \cdot |\eta_{det}|$ + 44.8 [90].

Variables	CCcore1	CCcore2	ECcore1	ECcore2
Isolation <	0.10	0.07	0.10	0.07
EMfrac >	0.95	0.95	0.95	0.95
Track isolation <	2.5	2.0	2.0	1.5
HMx8 <	-	-	-	10
Sigphi <	18	16	eq1	eq1
Sigz <	-	-	eq2	eq2

Table C.3: The developed core definitions for CC ($-1.1 < \eta_{det} < 1.1$) and EC ($1.5 < |\eta_{det}| < 2.5$) regions. The eq1 = $7.3 \cdot \eta_{det}^2$ - $35.9 \cdot |\eta_{det}|$ + 45.7, and eq2 = $7.5 \cdot \eta_{det}^2$ - $36.0 \cdot |\eta_{det}|$ + 44.8. These core definitions are applied to Run IIb data [90].

Variables	CCcore0	CCcore1	CCcore2	ECcore0	ECcore1	ECcore2
Isolation <	0.15	0.10	0.07	0.15	0.10	0.07
EMfrac >	0.90	0.95	0.97	0.90	0.95	0.97
Track isolation <	2.0	2.0	1.5	1.5	1.5	1.5
HMx8 <	-	-	-	-	30	30
Sigphi <	18	18	18	eq1	eq1	eq1
Sigz <	-	-	-	eq2	eq2	eq2
ANN5 >	0.1	0.1	0.3	-	-	-
ANN4 >	-	-	-	0.05	0.1	0.3

account for the different efficiencies between data and MC. The background subtraction is performed in $Z \to ee$ data and the background subtraction method is described in section C.8.

C.4.2 "No-Track" Matching

Photon doesn't leave hits to the tracking system, so if an EM object which passes core cut has a track associated with itself, this photon candidate can be rejected. Two things can cause that a photon candidate has a track: (1) A photon can be converted by the interaction with the material of the inner tracking system through pair production process. (2) A random track coming from underlying events can be overlaid to a photon candidate. This photon candidates can be removed using the tracking matching probability (P_{trk}). In addition, the track matching probability can reduce the rate selecting photon candidates faked by electrons. The "hits on

the road" method provides discrimination between photon and electron [85]. This hits on the road discriminant (D_{hor}) is only available for the CC (Central Calorimeter) region. To find optimized cuts, signal efficiency and fake rate are investigated by varying both P_{trk} and D_{hor} and Figures C.13 - C.18 show the results correspond to core definitions. Table C.4 shows the optimized P_{trk} and D_{hor} cut values for all individual core definitions. Section C.8.2 describes the efficiency that electron passes no-track match requirement, as function of p_T, η_{det} and ϕ_{det}.

Table C.4: The recommended cuts for the spatial track match probability (P_{trk}) and hits on the road discriminant (D_{hor}) corresponding to core definitions. The scale factors and their systematic uncertainties are estimated with $Z\gamma$ data and MC [90].

Variables	CCcore0	CCcore1	CCcore2	ECcore0	ECcore1	ECcore2
$P_{trk} <$	0.0	0.0	0.0	0.001	0.0	0.0
$D_{hor} >$	0.8	0.9	0.9	-	-	-
Scale factor	0.988 ± 0.015	1.009 ± 0.015	1.009 ± 0.015	0.999 ± 0.020	0.982 ± 0.020	0.982 ± 0.020

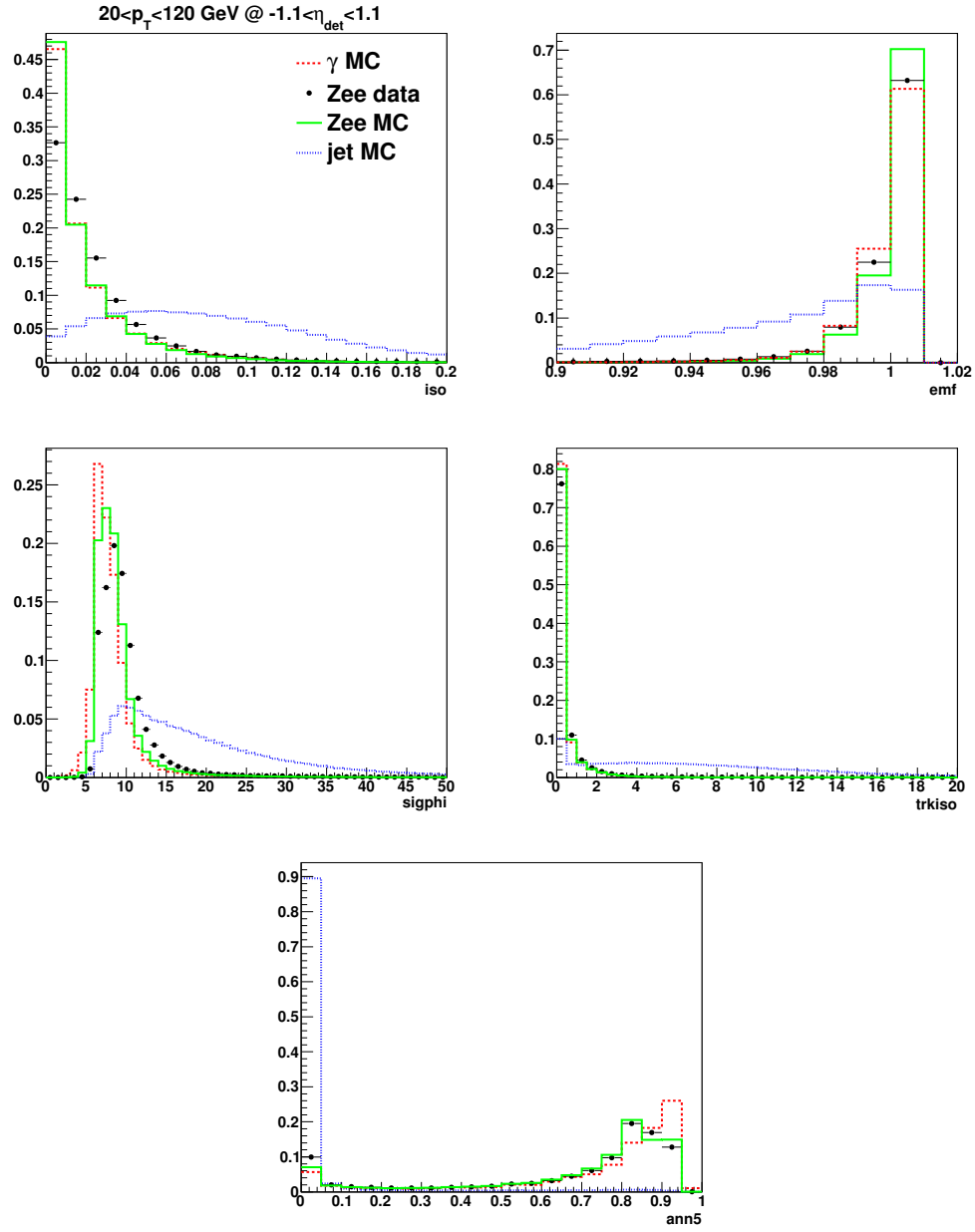

Figure C.1: The distributions of variables to identify photon in the CC ($-1.1 < \eta_{det} < 1.1$) region produced with γ, jet MC, and electron data and MC samples [90].

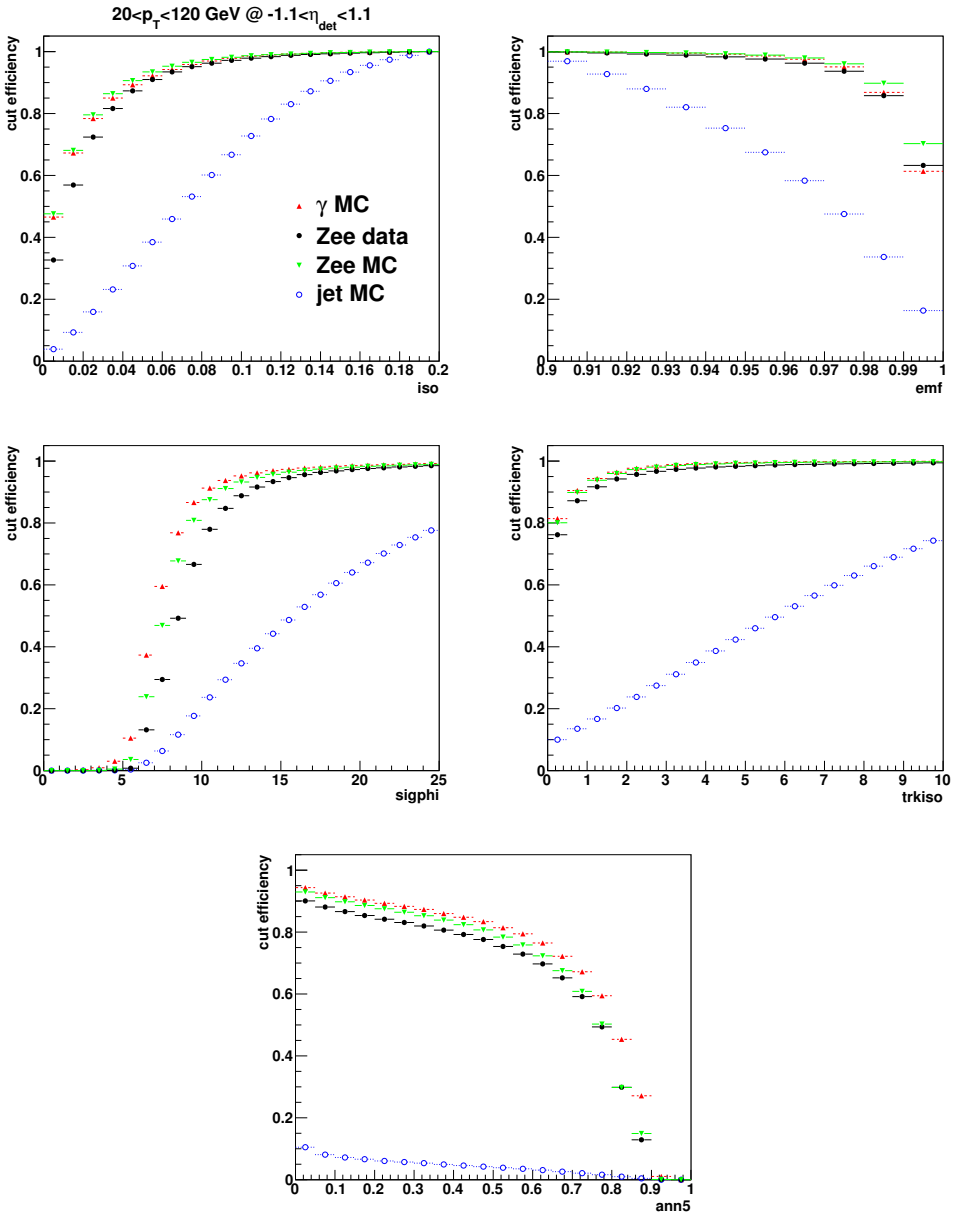

Figure C.2: The efficiency vs variables for photon identification for the CC ($-1.1 < \eta_{det} < 1.1$) region produced with γ, jet MC, and electron data and MC samples [90].

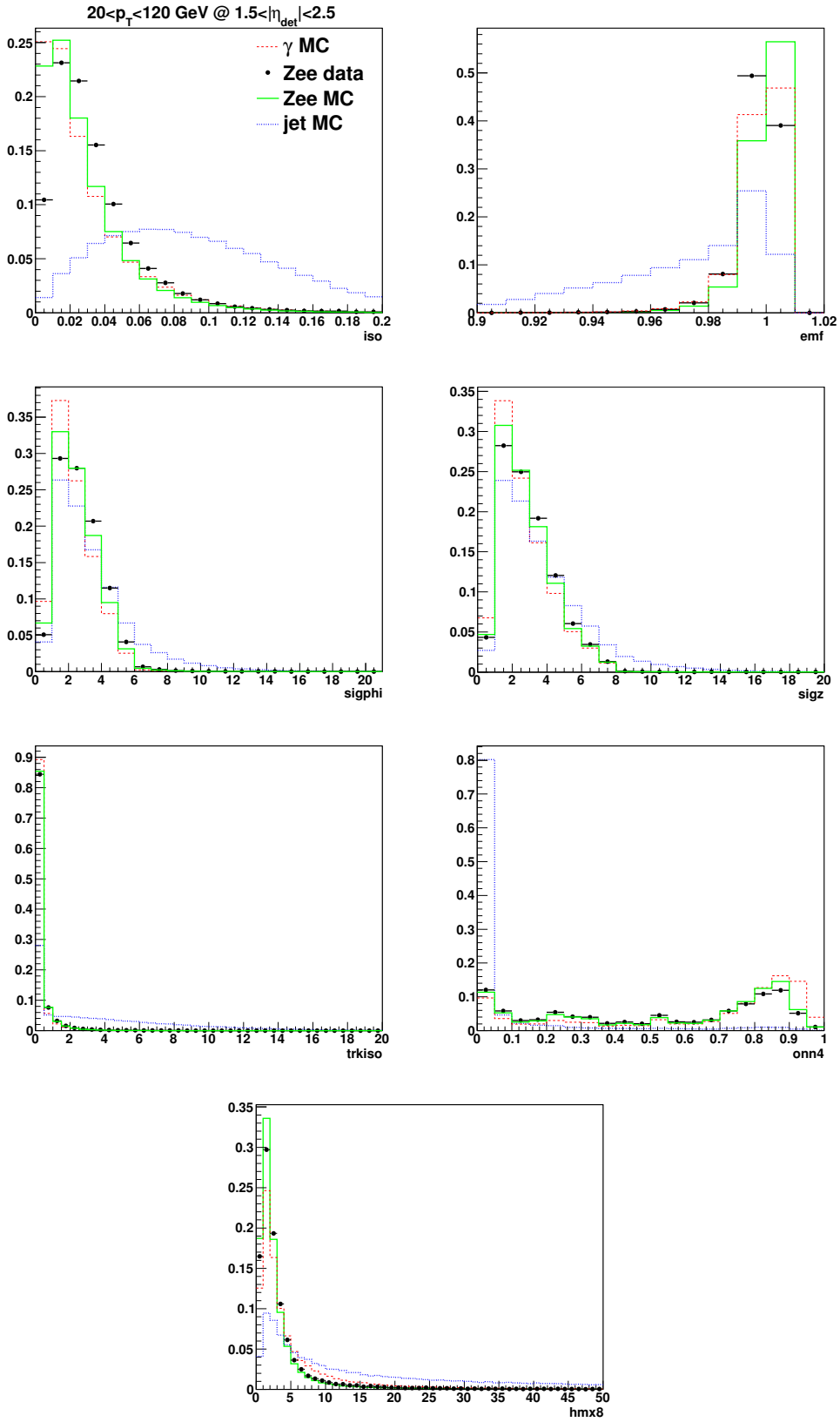

Figure C.3: The distributions of variables to identify photon in the EC ($1.5 < |\eta_{det}| < 2.5$) region produced with γ, jet MC, and electron data and MC samples [90].

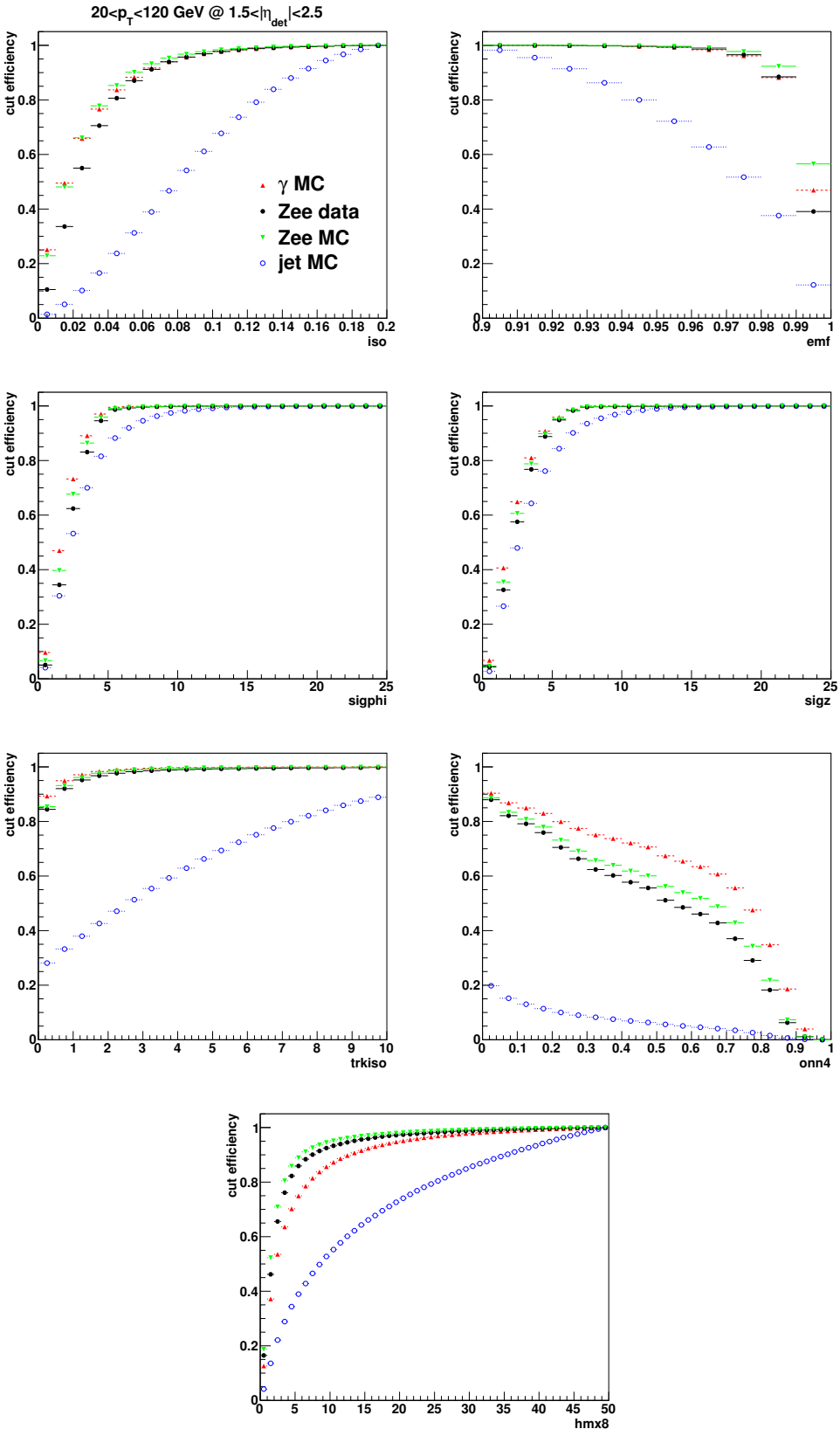

Figure C.4: The efficiency vs variables for photon identification for the EC ($1.5 < |\eta_{det}| < 2.5$) region produced with γ, jet MC, and electron data and MC samples [90].

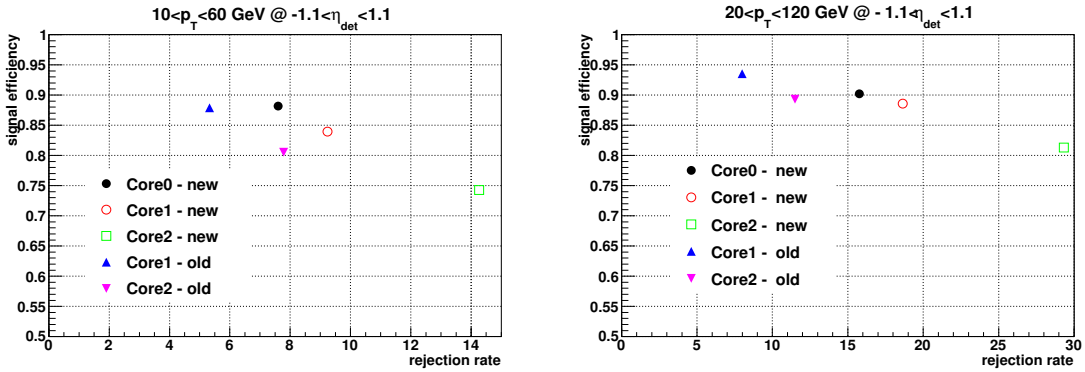

Figure C.5: The signal efficiency vs the rejection rate of core cuts in the CC region ($-1.1 < \eta_{det} < 1.1$) for $10 < p_T < 60$ GeV (left) and $20 < p_T < 120$ GeV (right) [90].

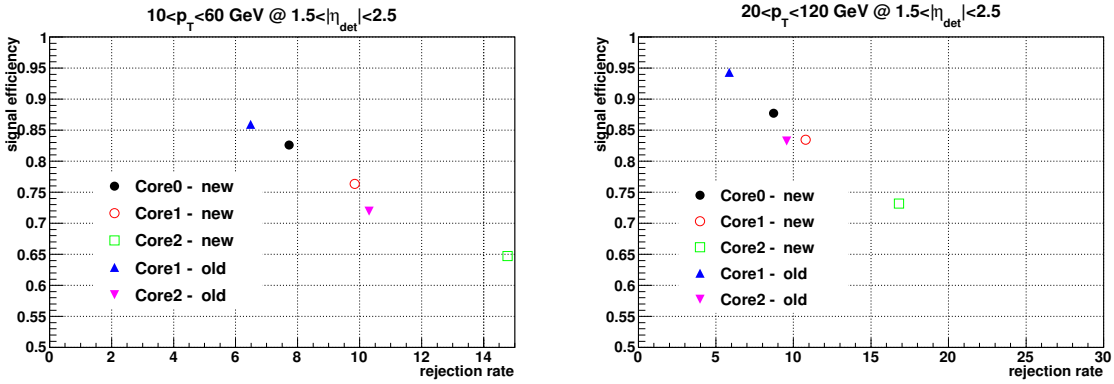

Figure C.6: The signal efficiency vs the rejection rate of core cuts in the EC region ($1.51 < |\eta_{det}| < 2.5$) for $10 < p_T < 60$ GeV (left) and $20 < p_T < 120$ GeV(right) [90].

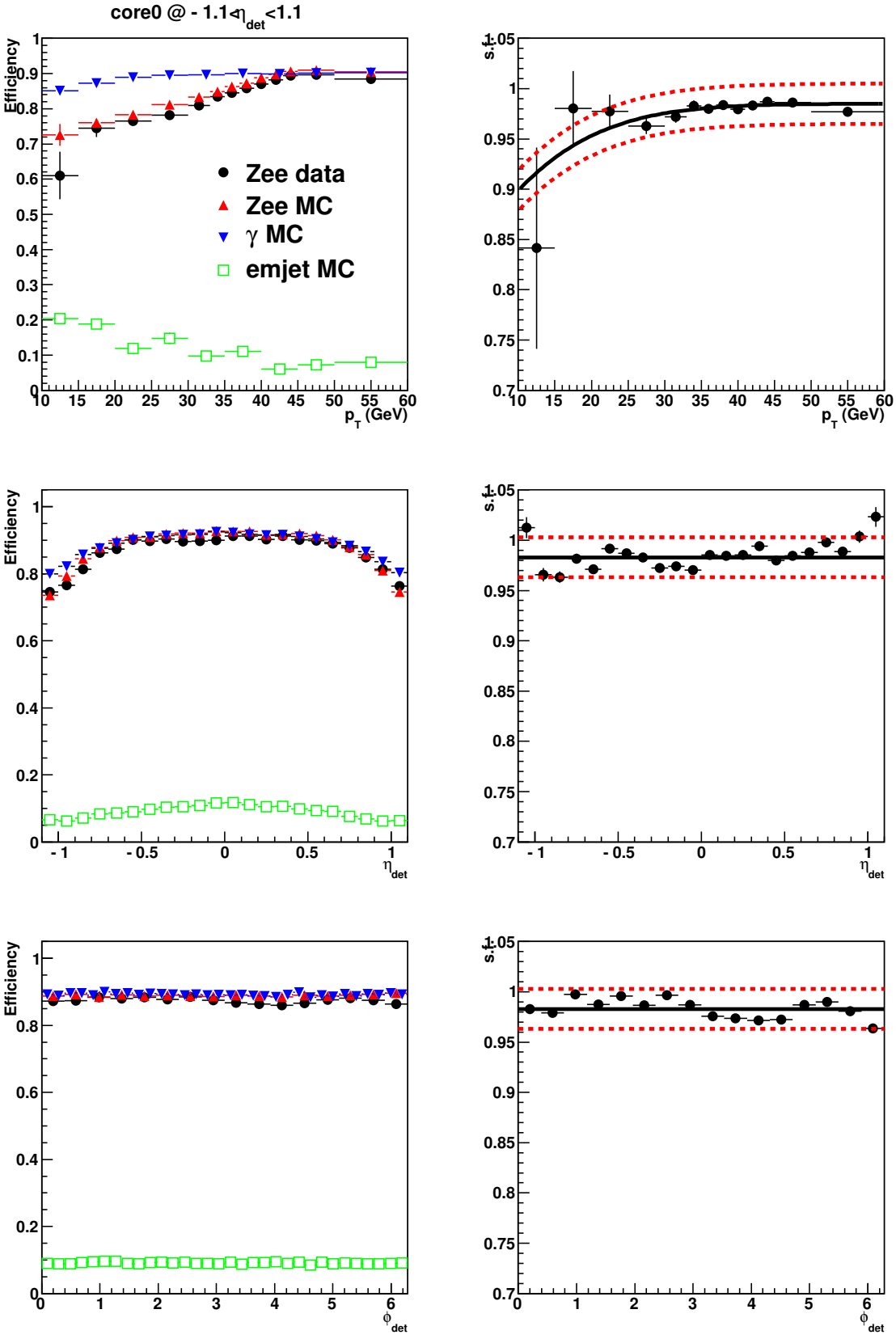

Figure C.7: The efficiency that the preselected EM clusters pass **CCcore0** requirements vs p_T, η_{det} and ϕ_{det} for Run IIb data and MC (left). The ratio of the efficiency derived with $Z \to ee$ data to that with MC (right). This ratio is scale factor that accounts for the different efficiency between data and MC [90].

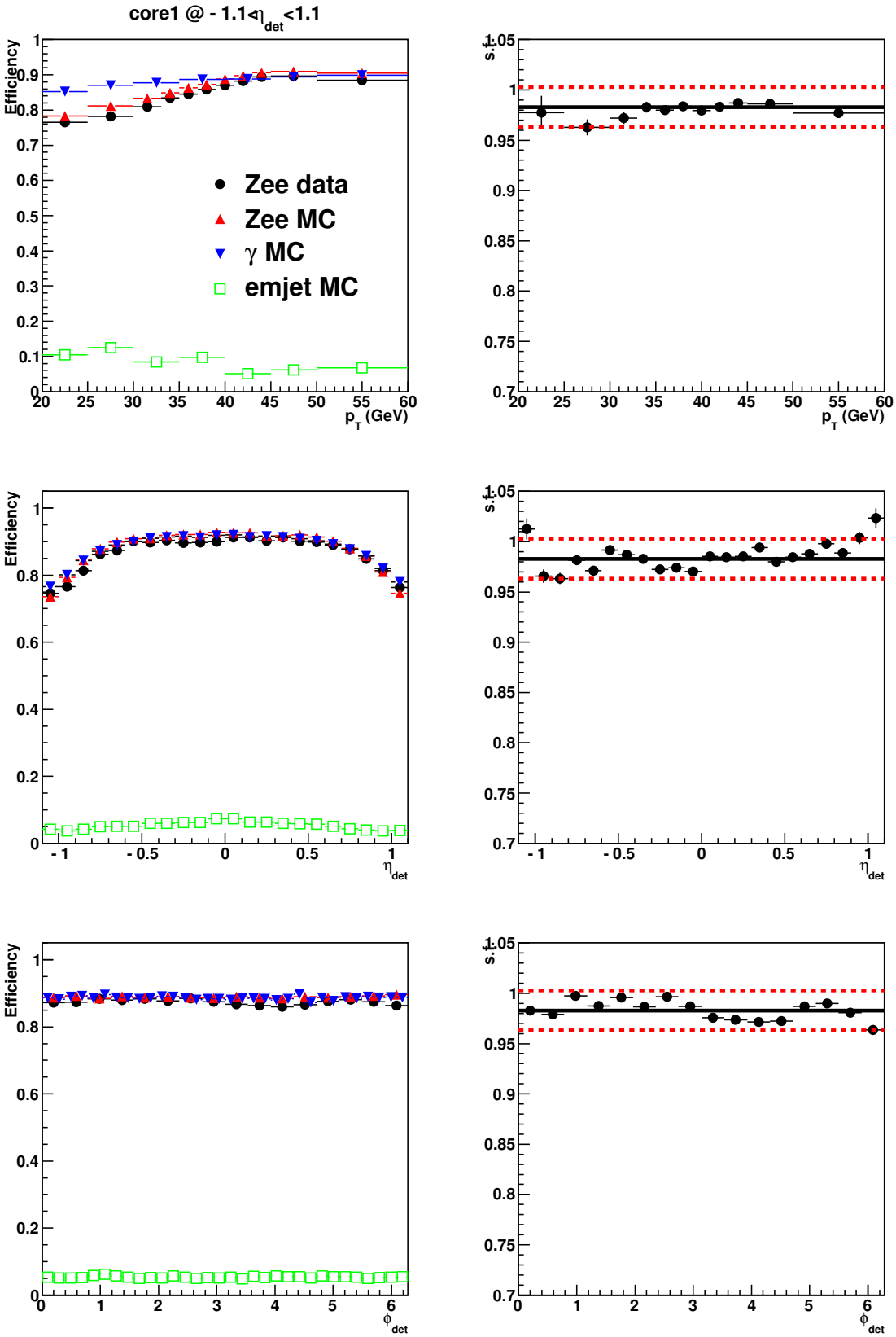

Figure C.8: The efficiency that the preselected EM clusters pass **CCcore1** requirements vs p_T, η_{det} and ϕ_{det} for Run IIb data and MC (left). The ratio of the efficiency derived with $Z \to ee$ data to that with MC (right). This ratio is scale factor that accounts for the different efficiency between data and MC [90].

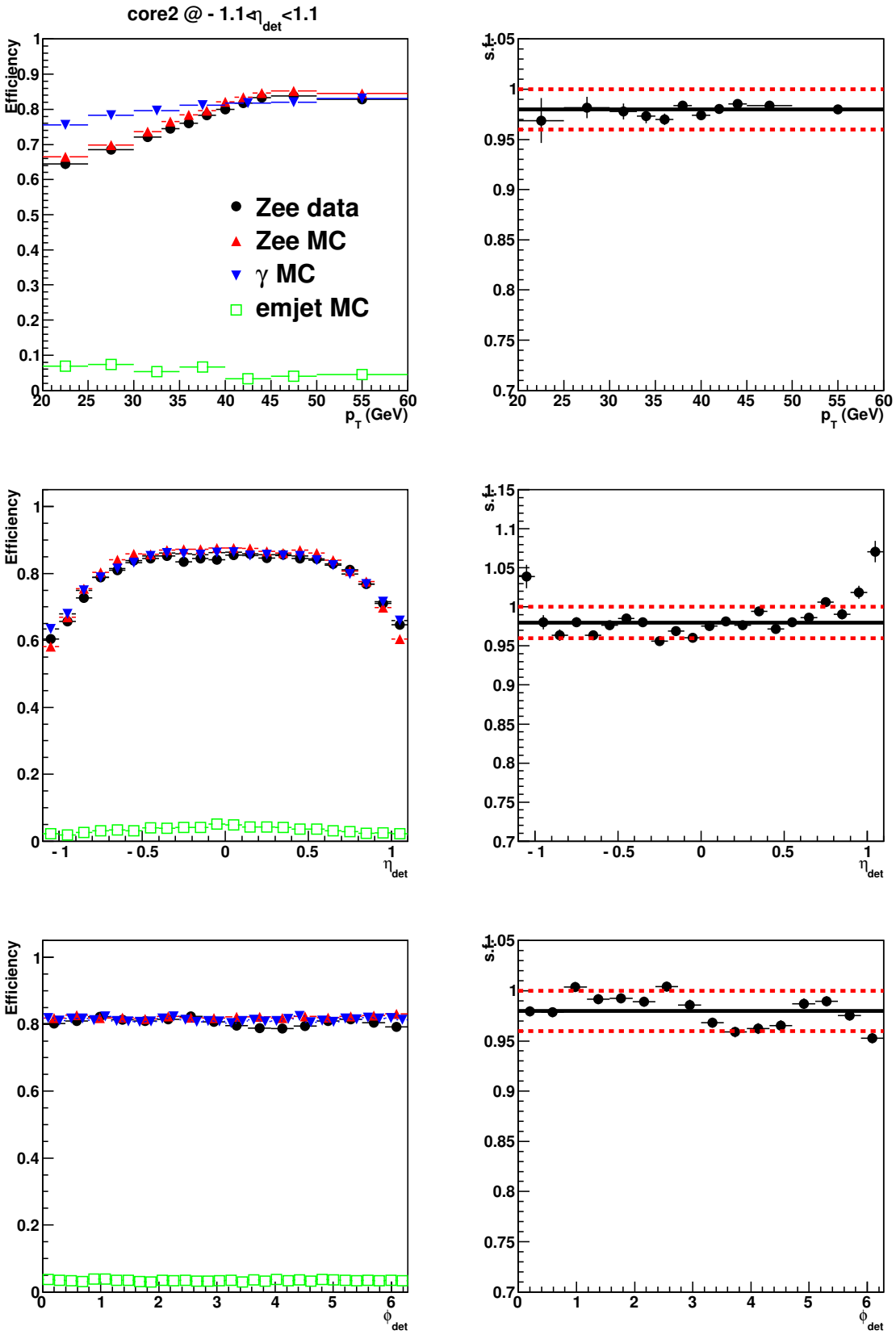

Figure C.9: The efficiency that the preselected EM clusters pass **CCcore2** requirements vs p_T, η_{det} and ϕ_{det} for Run IIb data and MC (left). The ratio of the efficiency derived with $Z \to ee$ data to that with MC (right). This ratio is scale factor that accounts for the different efficiency between data and MC [90].

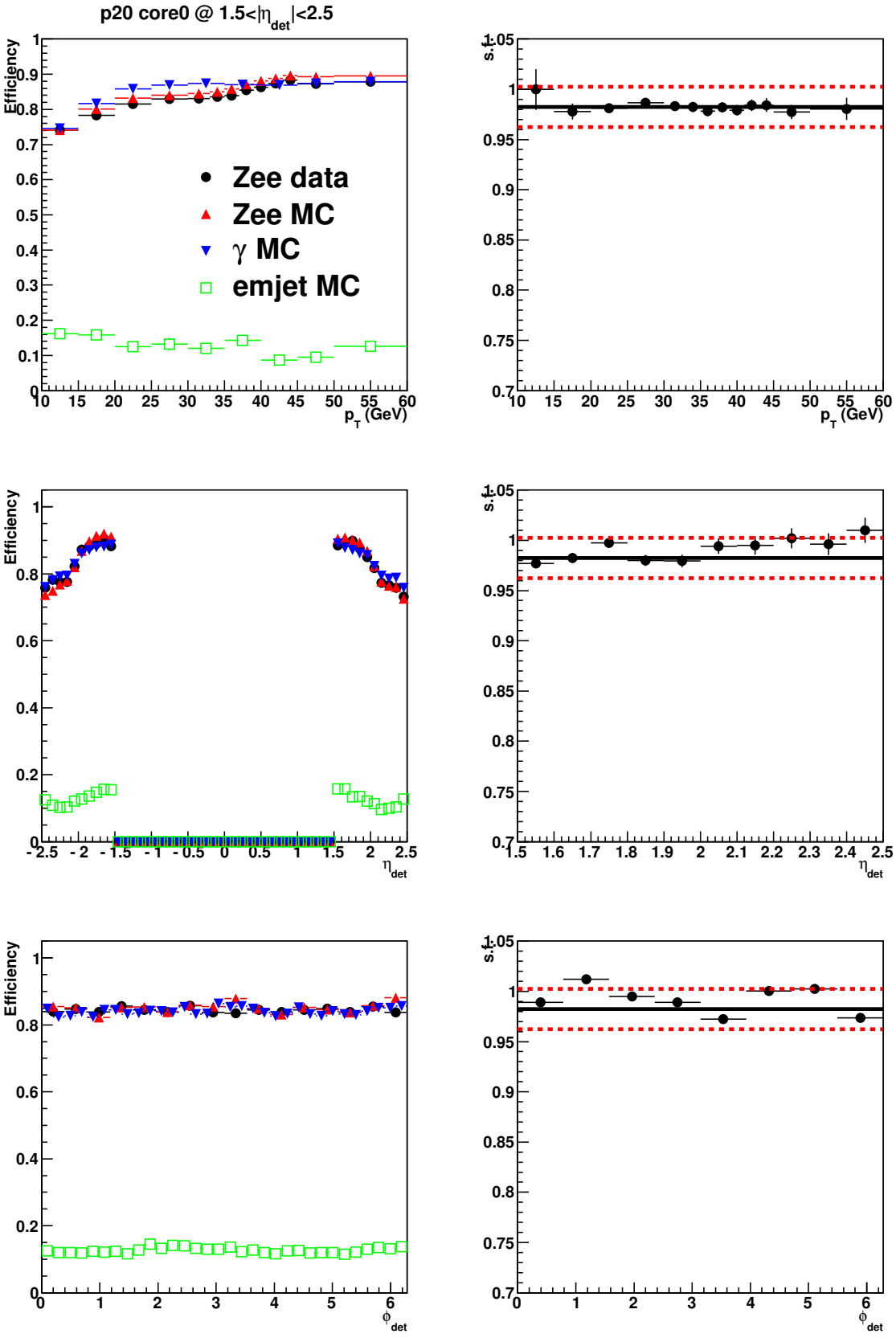

Figure C.10: The efficiency that the preselected EM clusters pass **ECcore0** requirements vs p_T, η_{det} and ϕ_{det} for Run IIb data and MC (left). The ratio of the efficiency derived with $Z \to ee$ data to that with MC (right). This ratio is scale factor that accounts for the different efficiency between data and MC [90].

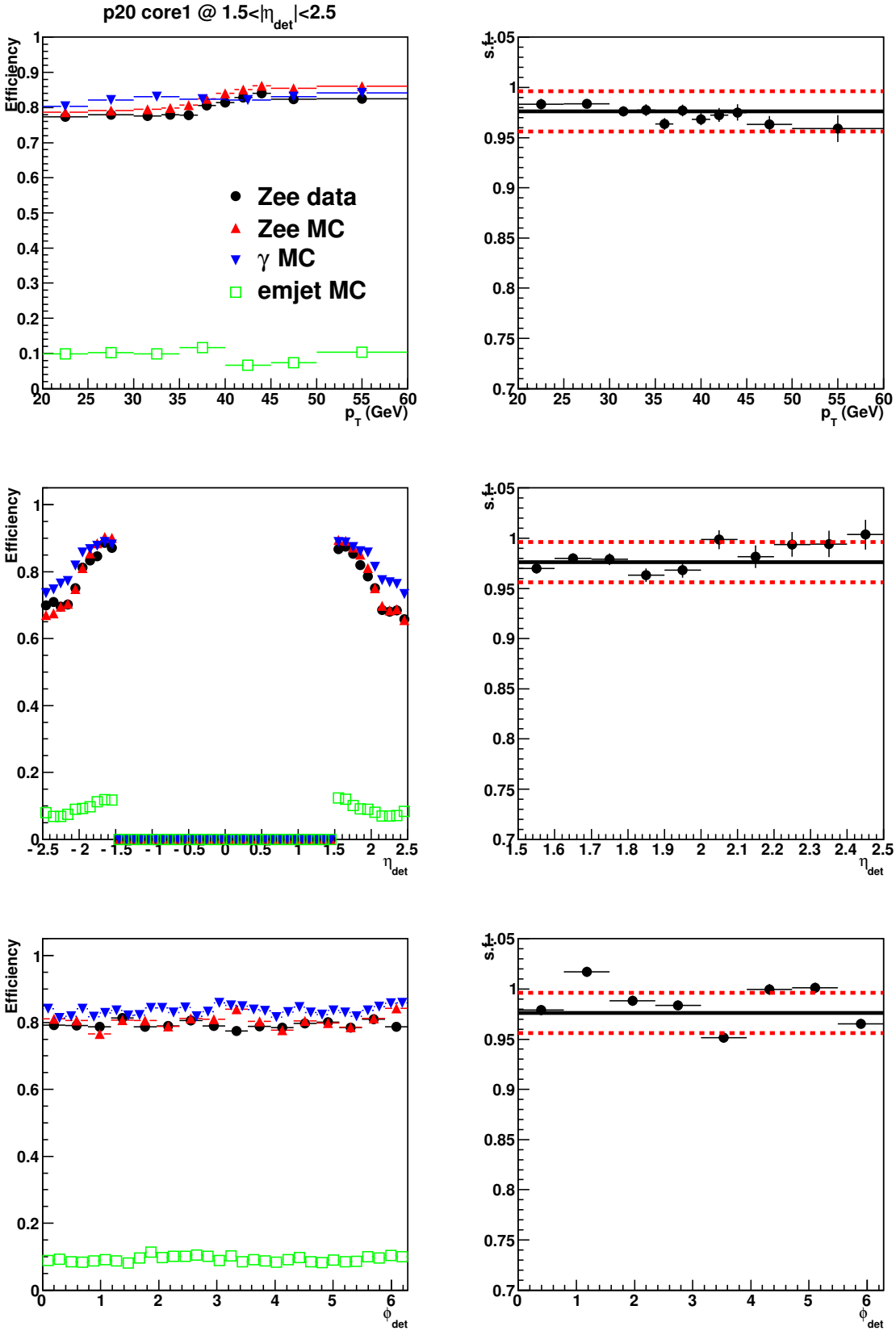

Figure C.11: The efficiency that the preselected EM clusters pass **ECcore1** requirements vs p_T, η_{det} and ϕ_{det} for Run IIb data and MC (left). The ratio of the efficiency derived with $Z \to ee$ data to that with MC (right). This ratio is scale factor that accounts for the different efficiency between data and MC [90].

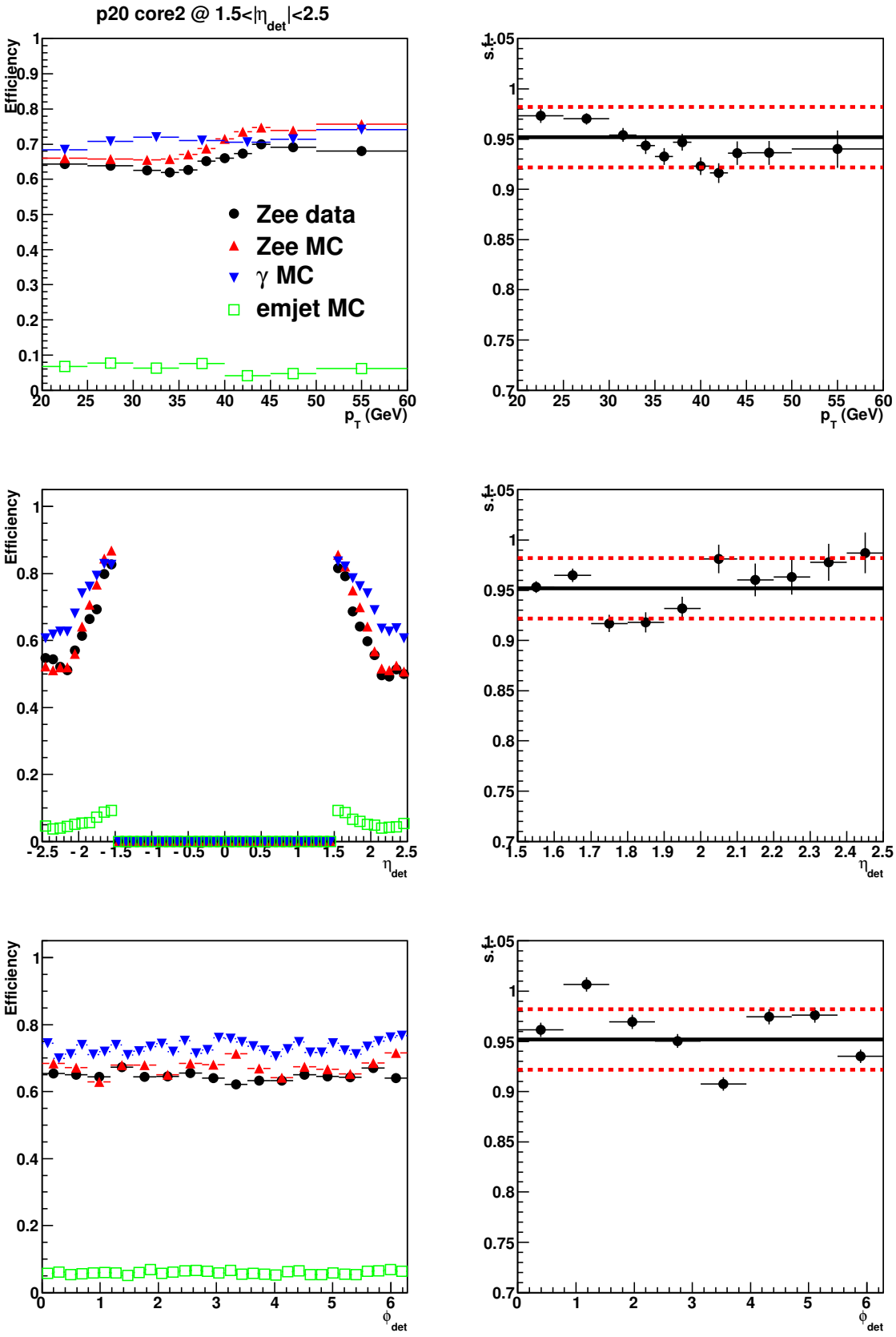

Figure C.12: The efficiency that the preselected EM clusters pass **ECcore2** requirements vs p_T, η_{det} and ϕ_{det} for Run IIb data and MC (left). The ratio of the efficiency derived with $Z \to ee$ data to that with MC (right). This ratio is scale factor that accounts for the different efficiency between data and MC [90].

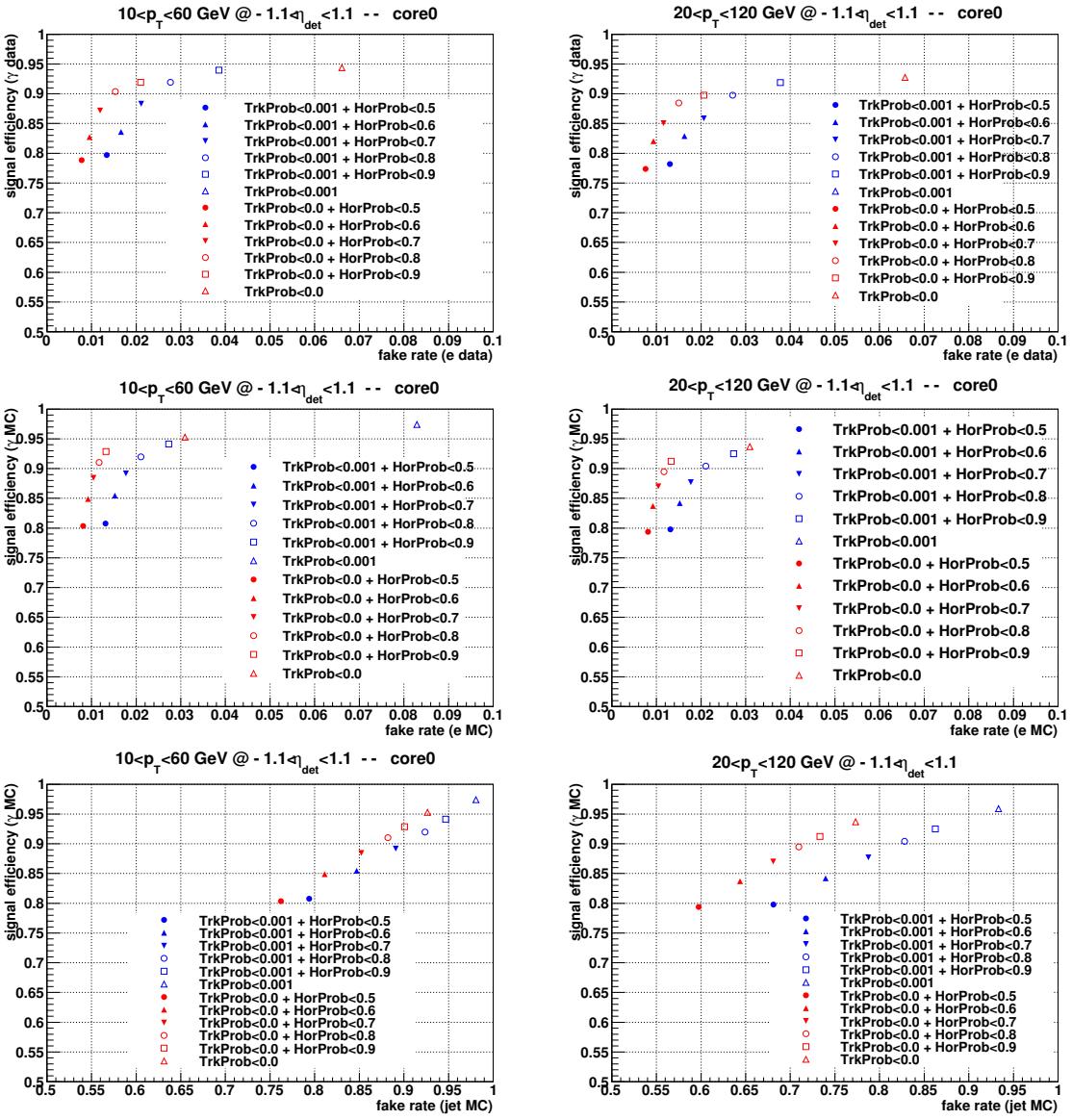

Figure C.13: The performance of "no-track" match. The efficiency that γ selected with CC-core0 cut in data or MC passes P_{trk} and D_{hor} requirement, is referred to signal efficiency, and the efficiency that electron or jet selected as photon by CCcore0 cut in data or MC passes P_{trk} and D_{hor} requirement, is referred to fake rate. Top left ($10< p_T <60$ GeV) and right ($20< p_T <120$ GeV) are γ vs electron efficiency plot in data. Mid left ($10< p_T <60$ GeV) and right ($20< p_T <120$ GeV) are γ vs electron efficiency plot in MC. Bottom left ($10< p_T <60$ GeV) and right ($20< p_T <120$ GeV) are γ vs jet efficiency plot in MC [90].

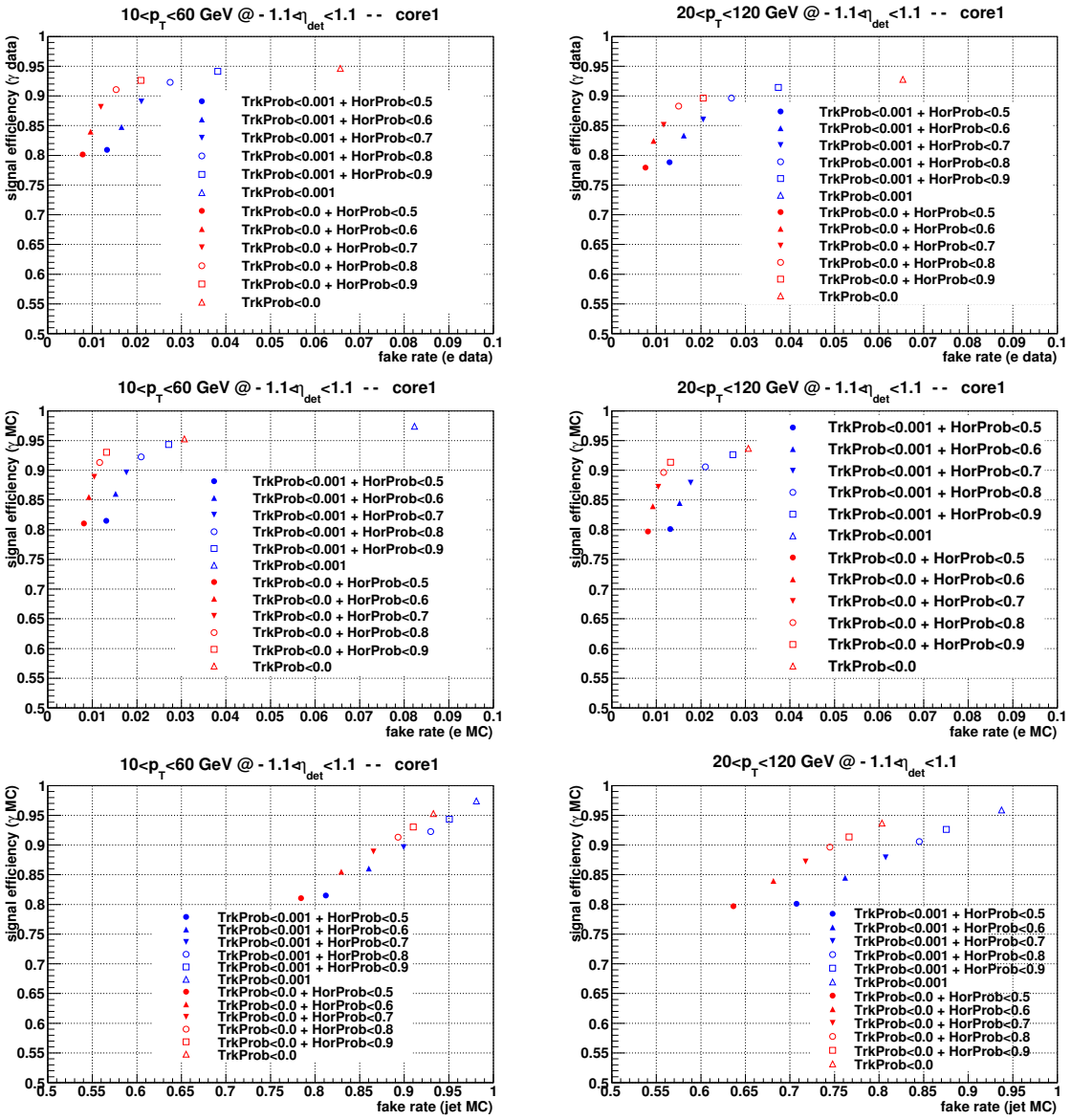

Figure C.14: The performance of "no-track" match. The efficiency that γ selected with CCcore1 cut in data or MC passes P_{trk} and D_{hor} requirement, is referred to signal efficiency, and the efficiency that electron or jet selected as photon by CCcore1 cut in data or MC passes P_{trk} and D_{hor} requirement, is referred to fake rate. Top left (10< p_T <60 GeV) and right (20< p_T <120 GeV) are γ vs electron efficiency plot in data. Mid left (10< p_T <60 GeV) and right (20< p_T <120 GeV) are γ vs electron efficiency plot in MC. Bottom left (10< p_T <60 GeV) and right (20< p_T <120 GeV) are γ vs jet efficiency plot in MC [90].

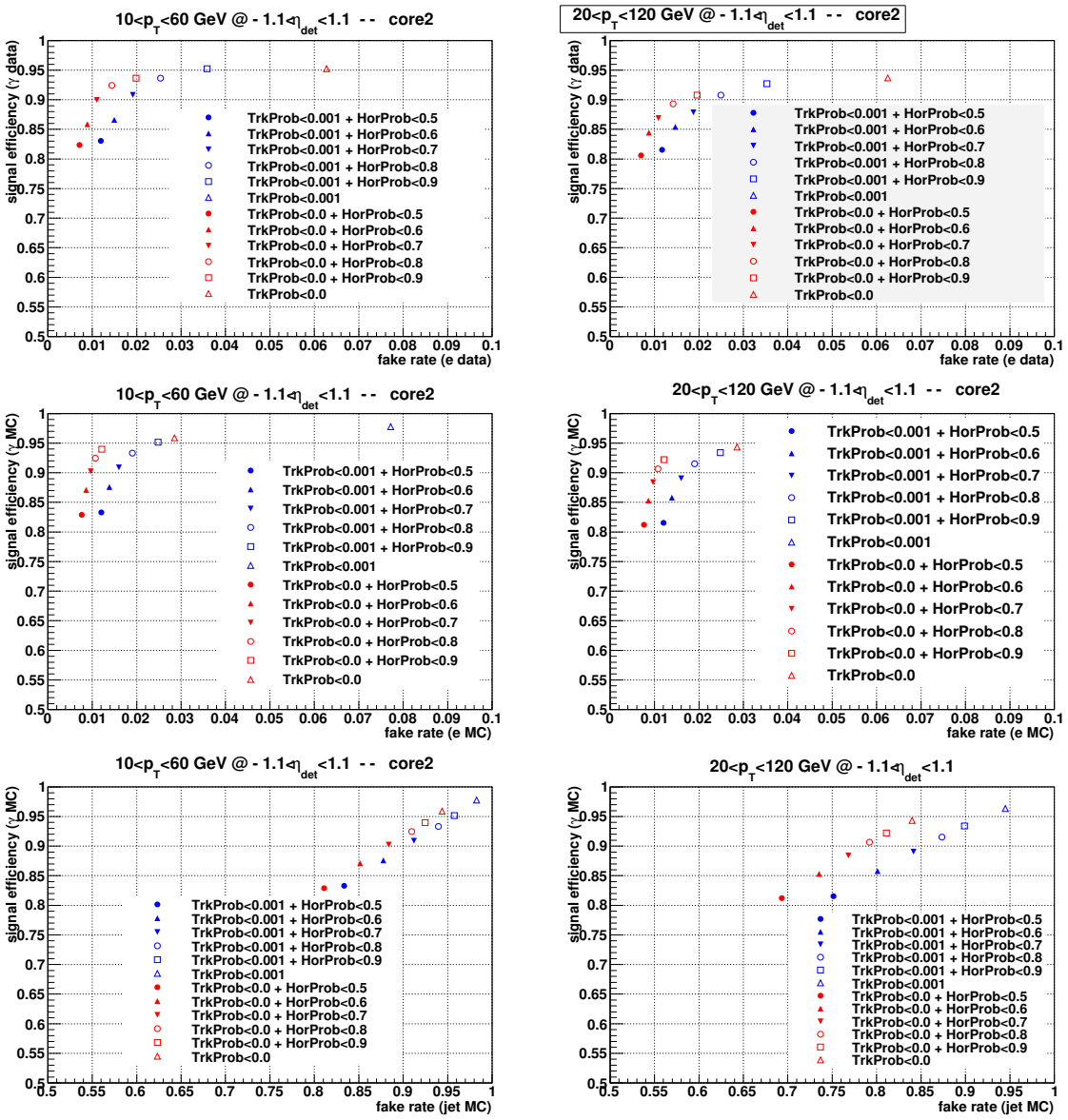

Figure C.15: The performance of "no-track" match. The efficiency that γ selected with CC-core2 cut in data or MC passes P_{trk} and D_{hor} requirement, is referred to signal efficiency, and the efficiency that electron or jet selected as photon by CCcore2 cut in data or MC passes P_{trk} and D_{hor} requirement, is referred to fake rate. Top left ($10< p_T <60$ GeV) and right ($20< p_T <120$ GeV) are γ vs electron efficiency plot in data. Mid left ($10< p_T <60$ GeV) and right ($20< p_T <120$ GeV) are γ vs electron efficiency plot in MC. Bottom left ($10< p_T <60$ GeV) and right ($20< p_T <120$ GeV) are γ vs jet efficiency plot in MC [90].

C.5 Optimization for the Run IIa Data

Photon selection efficiencies in the Run IIa data are rederived with the new photon definition as well as the ANN output. The 2EMhighpt and 2MUhighpt skimmed datasets provided by the Common Sample Group are used:

- CSG_CAF_2EMhighpt_PASS3_p18.14.00
- CSG_CAF_2MUhighpt_PASS3_p18.14.00

The QCD di-photon, emjet, $Z \to ee$ and $Z \to \mu\mu + \gamma$ MC samples are used for this Run IIa study. Table C.5 shows the corresponding SAM requests.

Table C.5: Request IDs used for the Run IIa study are listed. PYTHIA [46] generates all events for these samples.

MC sample	p17 ReqID
QCD $\gamma\gamma$(m=50-130GeV)	90212
QCD $\gamma\gamma$(m=130-250GeV)	90213
$Z \to \mu\mu + \gamma$	90534-5
EMjet (pThat=30-40GeV)	71332
EMjet (pThat=40-60GeV)	72212
EMjet (pThat=60-80GeV)	72213
EMjet (pThat=80-120GeV)	72214
Z/$\gamma*$ →ee (m=60-130GeV)	38770-84
Z/$\gamma*$ →ee (m=130-250GeV)	41249-50

The event selection described in section C.3 is applied to both data and MC. The distributions of variables used for photon selection are shown in Figures C.20 and C.21 . Table C.6 describes the new core definitions ant their requirements and Figure C.22 shows the developed performance of the new core definitions compared to the previous core definitions. Figures C.25 - C.30 show the efficiencies as function of the transverse momentum, detector η and ϕ of photons for all individual core definitions for Run IIa, and corresponding scale factors derived with $Z \to ee$ data and MC. The background subtraction is performed in $Z \to ee$ Run IIa data and the background subtraction method is described in section C.8.

Using photons passed core cuts in Table C.6, the "no-track" match requirement which is combination of the spatial track match probability and the "hits on the road" discriminant is

Table C.6: Run IIa core definitions for CC ($-1.1 < \eta_{det} < 1.1$) and EC ($1.5 < |\eta_{det}| < 2.5$) regions. The eq1 = $2.74 \cdot \eta_{det}^2$ - $16.3 \cdot |\eta_{det}|$ + 25.0, and eq2 = $5.96 \cdot \eta_{det}^2$ - $30.6 \cdot |\eta_{det}|$ + 40.7 [90].

Variables	CCcore0	CCcore1	CCcore2	ECcore0	ECcore1	ECcore2
Isolation <	0.15	0.10	0.07	0.15	0.10	0.07
EMfrac >	0.90	0.95	0.97	0.90	0.95	0.97
Track isolation <	2.0	2.0	1.5	1.5	1.5	1.5
HMx8 <	-	-	-	-	30	30
Sigphi <	14	14	14	eq1	eq1	eq1
Sigz <	-	-	-	eq2	eq2	eq2
ANN5 >	0.1	0.1	0.3	-	-	-
ANN4 >	-	-	-	0.05	0.1	0.3

Table C.7: The recommended cuts for the spatial track match probability (P_{trk}) and the hits on the road discriminant (D_{hor}) corresponding to core definitions in Run IIa. The scale factors and their systematic uncertainties are estimated with $Z\gamma$ data and MC [90].

Variables	CCcore0	CCcore1	CCcore2	ECcore0	ECcore1	ECcore2
P_{trk} <	0.0001	0.0001	0.0001	0.001	0.0001	0.0001
D_{hor} <	0.5	0.5	0.5	-	-	-
Scale factor	0.987±0.020	0.987±0.020	0.987±0.020	0.989±0.025	0.992±0.025	0.992±0.025

applied to select no-track matched photon and Figure C.23 shows the signal efficiency vs the fake rate distributions for the various P_{trk} and D_{hor} cut values. The optimized P_{trk} and D_{hor} cuts for all individual core cuts and scale factors for corresponding cases are described in Table C.7. Section C.8.2 describes the efficiency that electrons pass no-track match requirement, as function of p_T, η_{det} and ϕ_{det}.

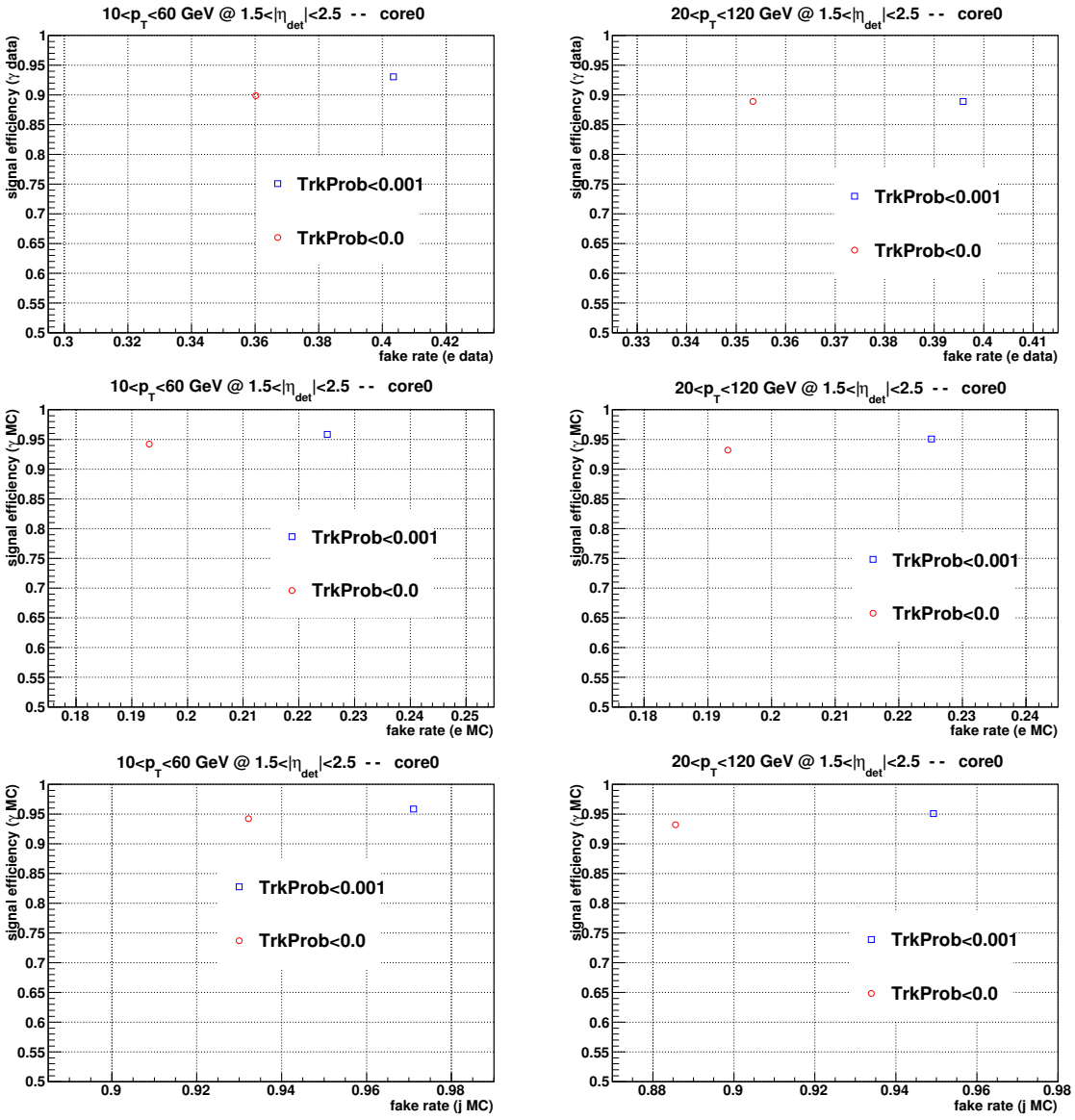

Figure C.16: The performance of "no-track" match. The efficiency that γ selected with ECcore0 cut in data or MC passes P_{trk} requirement, is referred to signal efficiency, and the efficiency that electron or jet selected as photon by ECcore0 cut in data or MC passes P_{trk} requirement, is referred to fake rate. Top left ($10< p_T <60$ GeV) and right ($20< p_T <120$ GeV) are γ vs electron efficiency plot in data. Mid left ($10< p_T <60$ GeV) and right ($20< p_T <120$ GeV) are γ vs electron efficiency plot in MC. Bottom left ($10< p_T <60$ GeV) and right ($20< p_T <120$ GeV) are γ vs jet efficiency plot in MC [90].

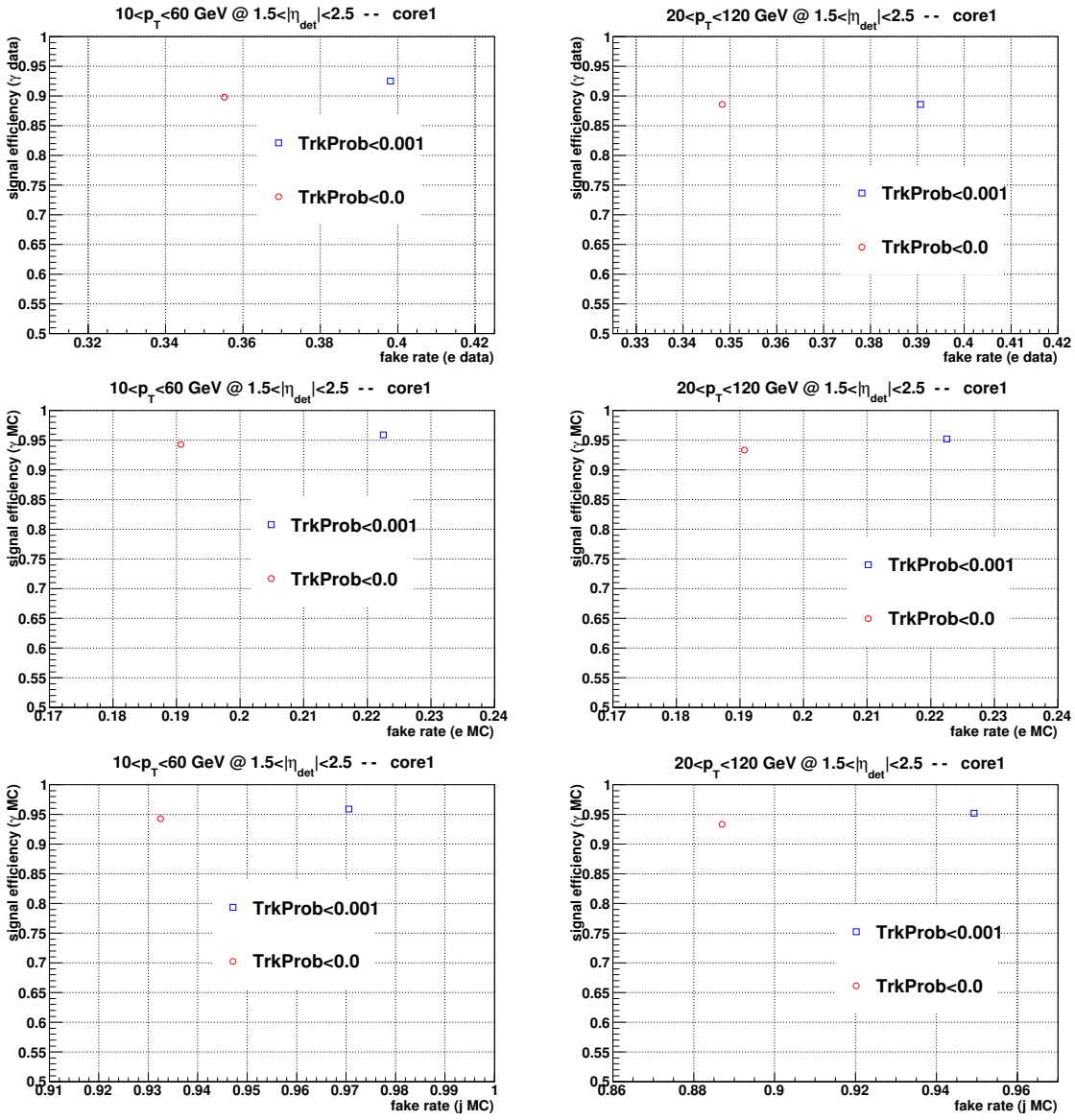

Figure C.17: The performance of "no-track" match. The efficiency that γ selected with ECcore1 cut in data or MC passes P_{trk} requirement, is referred to signal efficiency, and the efficiency that electron or jet selected as photon by ECcore1 cut in data or MC passes P_{trk} requirement, is referred to fake rate. Top left ($10< p_T <60$ GeV) and right ($20< p_T <120$ GeV) are γ vs electron efficiency plot in data. Mid left ($10< p_T <60$ GeV) and right ($20< p_T <120$ GeV) are γ vs electron efficiency plot in MC. Bottom left ($10< p_T <60$ GeV) and right ($20< p_T <120$ GeV) are γ vs jet efficiency plot in MC [90].

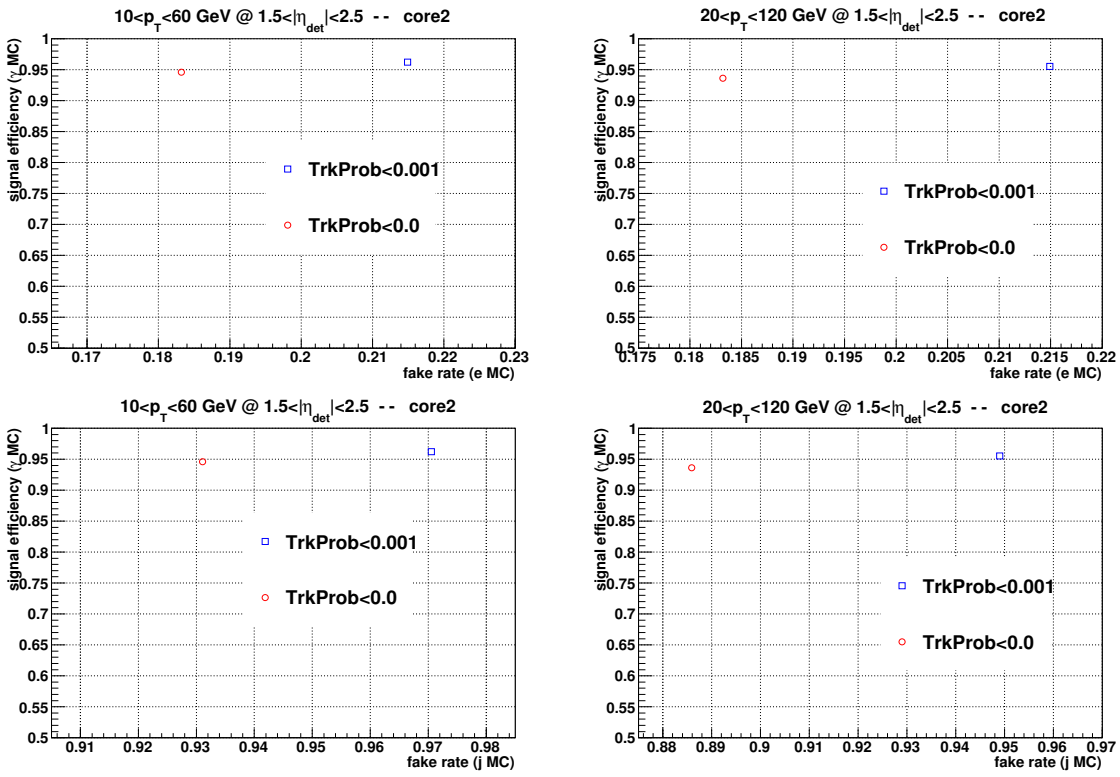

Figure C.18: The performance of "no-track" match. The efficiency that γ selected with ECcore2 cut in data or MC passes P_{trk} requirement, is referred to signal efficiency, and the efficiency that electron or jet selected as photon by ECcore2 cut in data or MC passes P_{trk} requirement, is referred to fake rate. Top left ($10< p_T <60$ GeV) and right ($20< p_T <120$ GeV) are γ vs electron efficiency plot in data. Mid left ($10< p_T <60$ GeV) and right ($20< p_T <120$ GeV) are γ vs electron efficiency plot in MC. Bottom left ($10< p_T <60$ GeV) and right ($20< p_T <120$ GeV) are γ vs jet efficiency plot in MC [90].

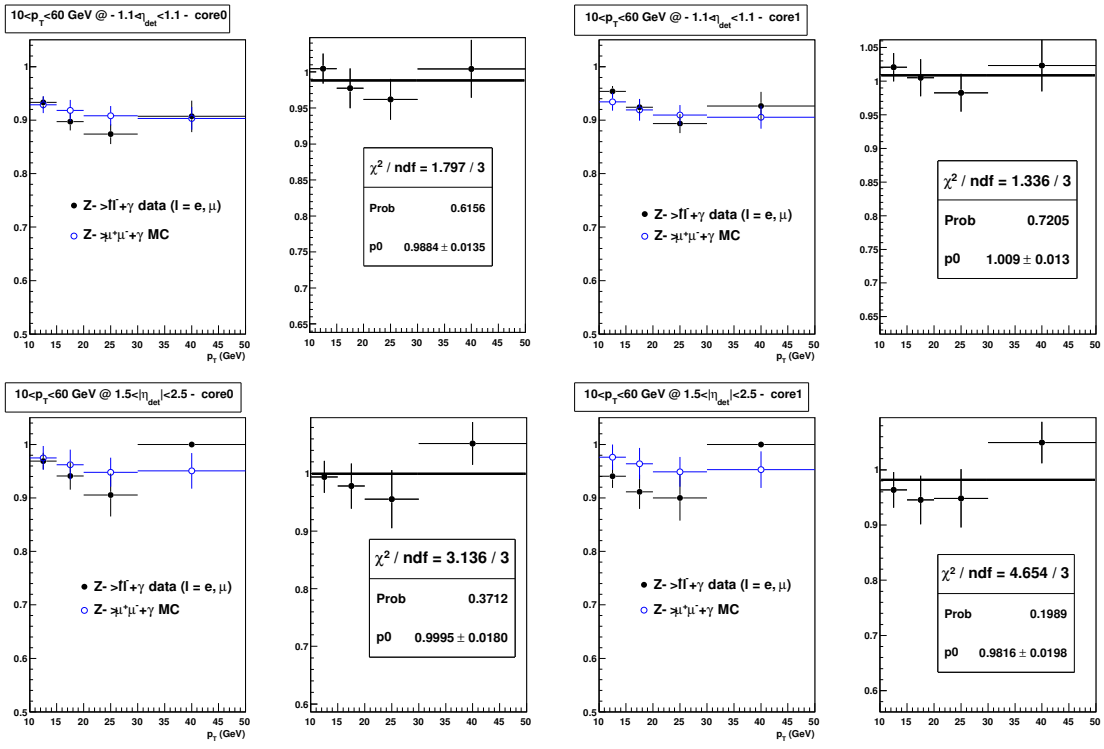

Figure C.19: The "no-track" matching efficiencies as function of photon p_T in $Z \to l^+l^- + \gamma$ data and $Z \to \mu^+\mu^- + \gamma$ MC for CCcore0 (top left), CCcore1 (top right), ECcore0 (bottom left), and ECcore1 (bottom right), and their scale factors vs p_T [90].

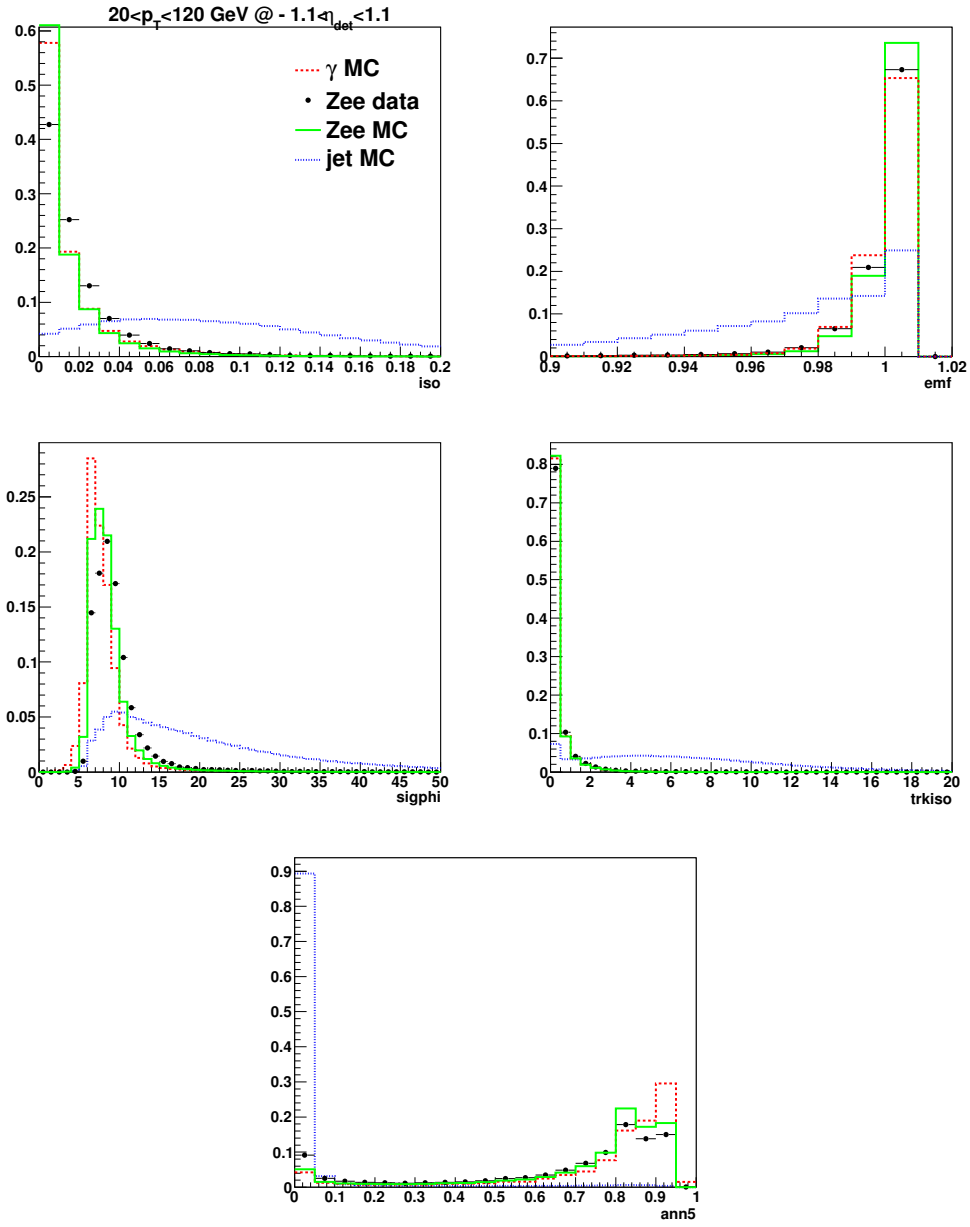

Figure C.20: The distributions of variables to identify photon in the CC ($-1.1 < \eta_{det} < 1.1$) region produced with γ, jet MC and electron data and MC samples for Run IIa [90].

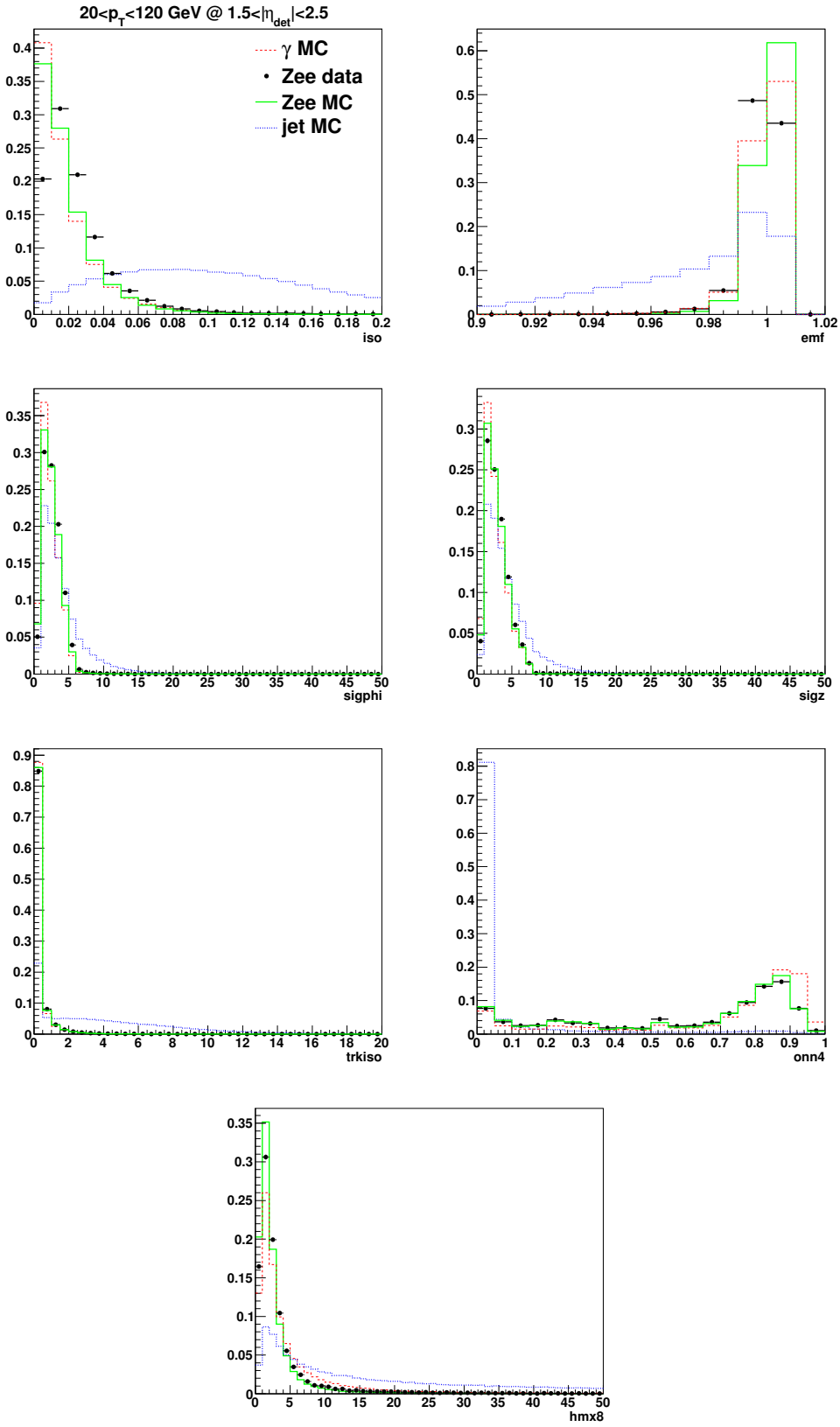

Figure C.21: The distributions of variables to identify photon in the EC ($1.5 < |\eta_{det}| < 2.5$) region produced with γ, jet MC and electron data and MC samples for Run IIa [90].

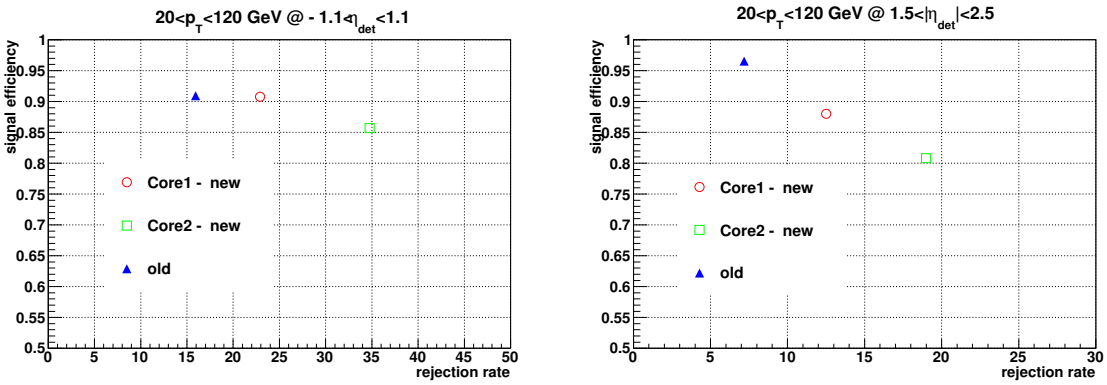

Figure C.22: The signal efficiency vs the rejection rate of core cuts in the CC ($-1.1 < \eta_{det} < 1.1$) region (left) and the EC ($1.51 < |\eta_{det}| < 2.5$) region (right) for $20 < p_T < 120$ GeV [90].

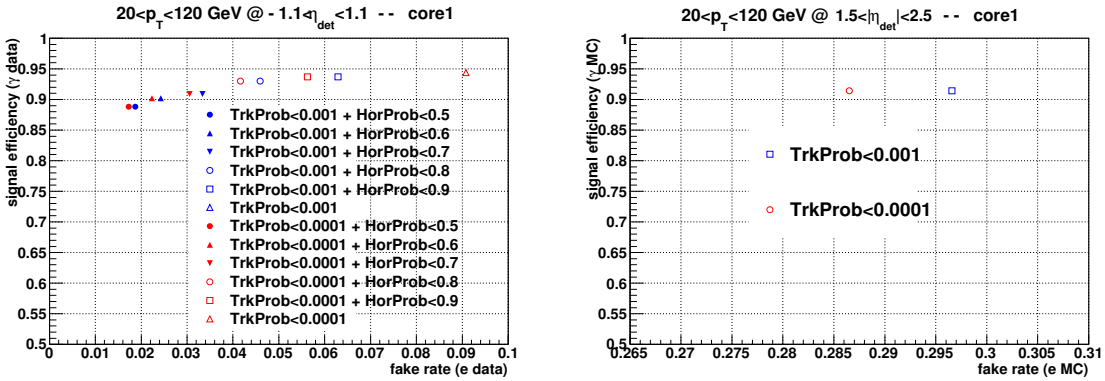

Figure C.23: The performance of "no-track" match for CC (left) and EC (right). The efficiency that γ selected with core cuts passes P_{trk} and D_{hor} requirement, is referred to signal efficiency, and the efficiency that electron or jet selected as photon by core cut passes P_{trk} and D_{hor} requirement, is referred to fake rate [90].

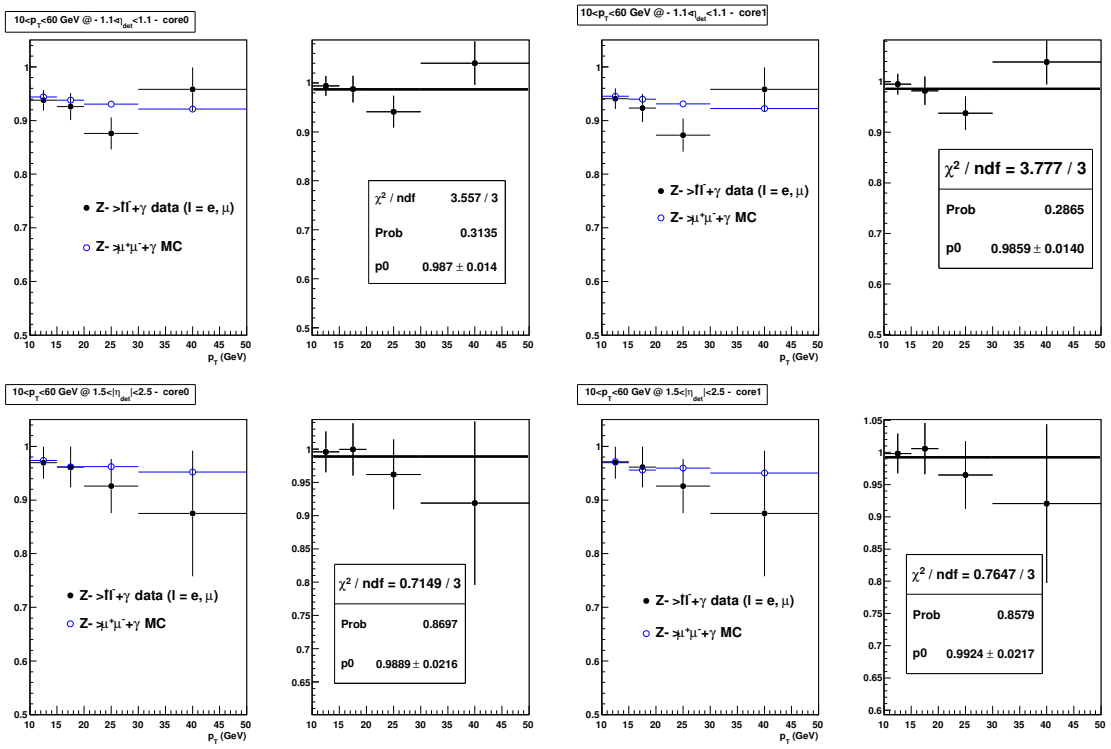

Figure C.24: The "no-track" matching efficiencies as function of photon p_T in $Z \to l^+l^- + \gamma$ data and $Z \to \mu^+\mu^- + \gamma$ MC for CCcore0 (top left), CCcore1 (top right), ECcore0 (bottom left), and ECcore1 (bottom right), and their scale factors vs p_T [90].

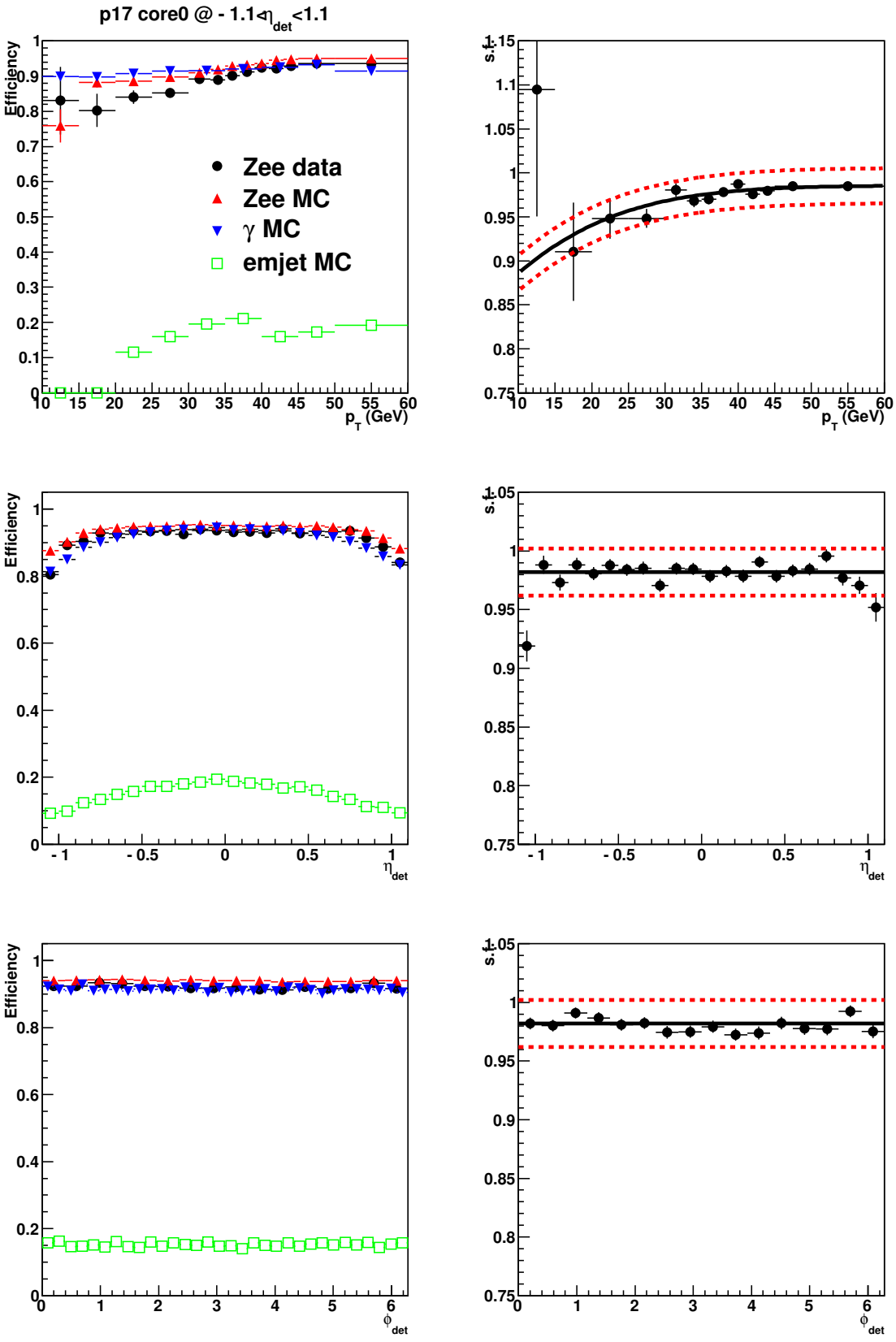

Figure C.25: The efficiency that the preselected EM clusters pass **CCcore0** requirements vs p_T, η_{det} and ϕ_{det} for Run IIb data and MC (left). The ratio of the efficiency derived with $Z \to ee$ data to that with MC (right). This ratio is scale factor that accounts for the different efficiency between data and MC [90].

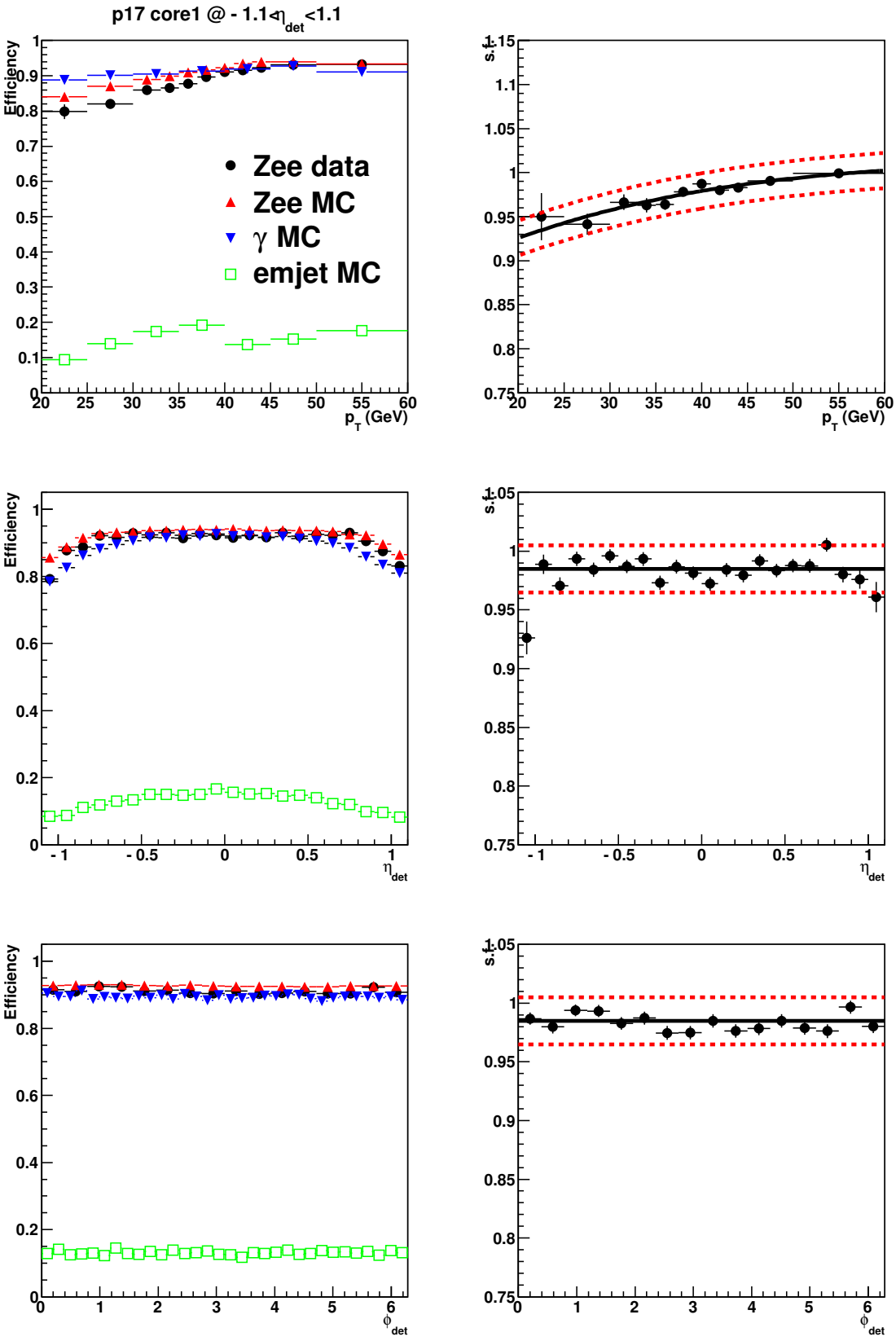

Figure C.26: The efficiency that the preselected EM clusters pass **CCcore1** requirements vs p_T, η_{det} and ϕ_{det} for Run IIb data and MC (left). The ratio of the efficiency derived with $Z \rightarrow ee$ data to that with MC (right). This ratio is scale factor that accounts for the different efficiency between data and MC [90].

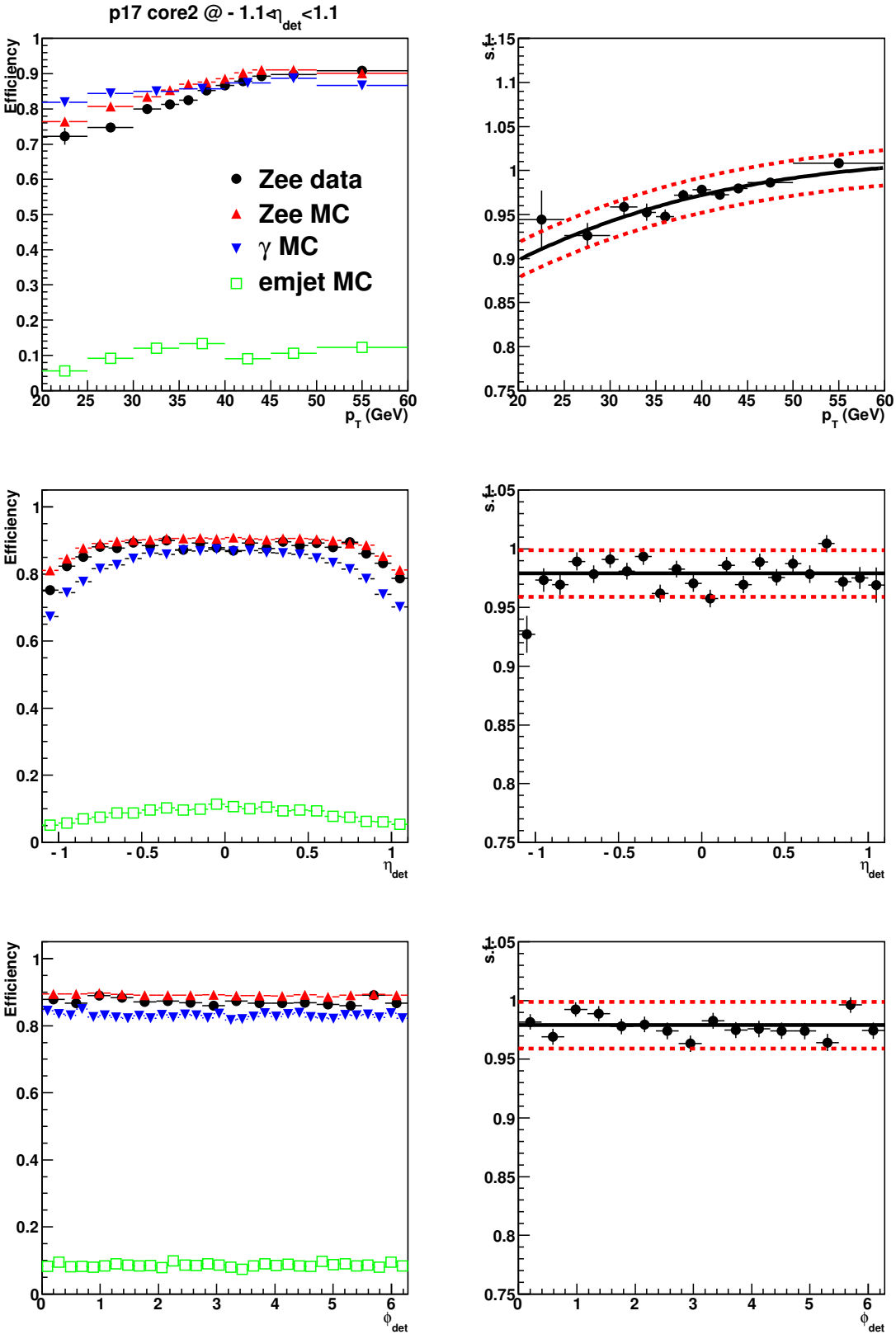

Figure C.27: The efficiency that the preselected EM clusters pass **CCcore2** requirements vs p_T, η_{det} and ϕ_{det} for Run IIb data and MC (left). The ratio of the efficiency derived with $Z \to ee$ data to that with MC (right). This ratio is scale factor that accounts for the different efficiency between data and MC [90].

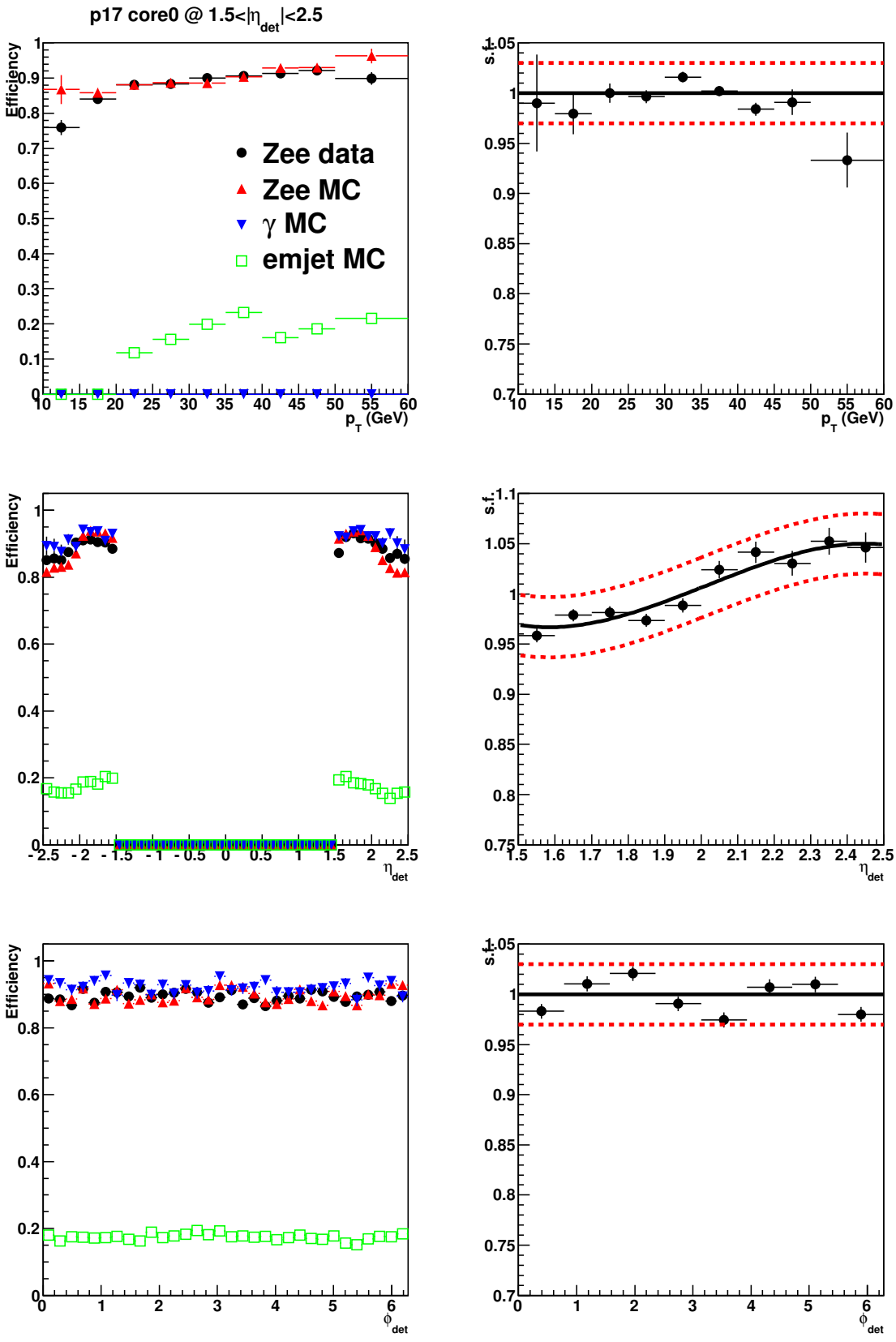

Figure C.28: The efficiency that the preselected EM clusters pass **ECcore0** requirements vs p_T, η_{det} and ϕ_{det} for Run IIb data and MC (left). The ratio of the efficiency derived with $Z \to ee$ data to that with MC (right). This ratio is scale factor that accounts for the different efficiency between data and MC [90].

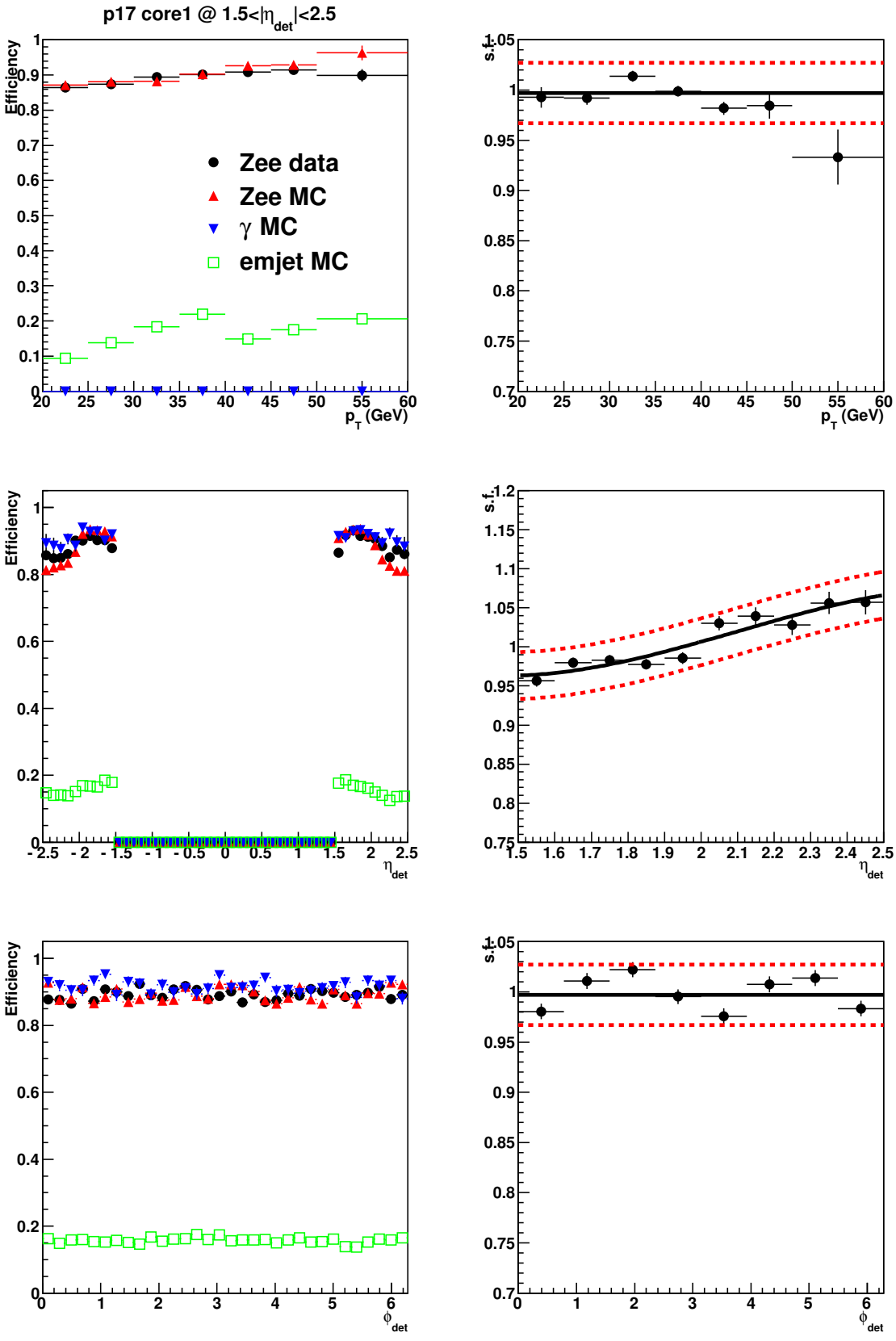

Figure C.29: The efficiency that the preselected EM clusters pass **ECcore1** requirements vs p_T, η_{det} and ϕ_{det} for Run IIb data and MC (left). The ratio of the efficiency derived with $Z \rightarrow ee$ data to that with MC (right). This ratio is scale factor that accounts for the different efficiency between data and MC [90].

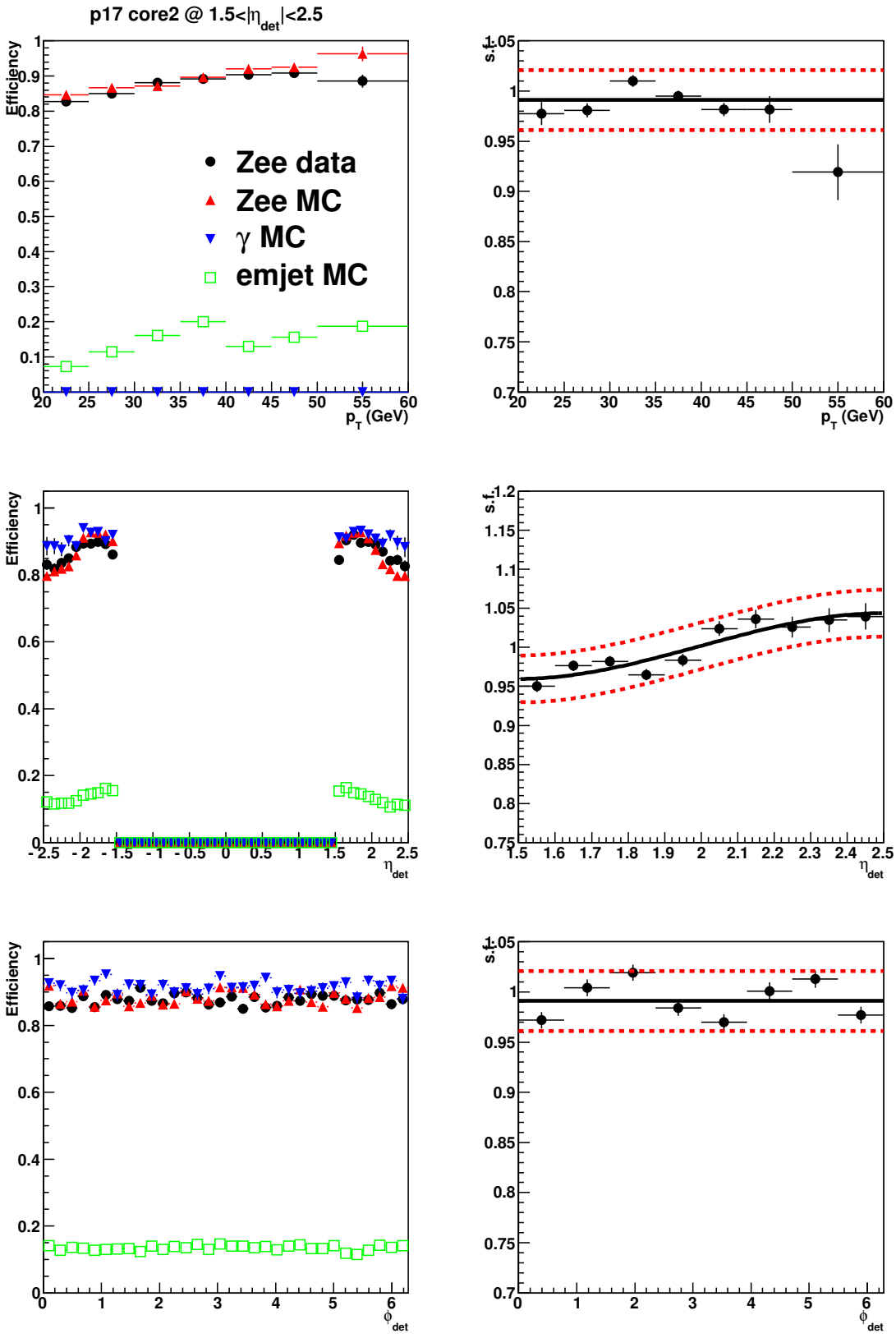

Figure C.30: The efficiency that the preselected EM clusters pass **ECcore2** requirements vs p_T, η_{det} and ϕ_{det} for Run IIb data and MC (left). The ratio of the efficiency derived with $Z \to ee$ data to that with MC (right). This ratio is scale factor that accounts for the different efficiency between data and MC [90].

C.6 Scale Factors and Systematic Uncertainties

Optimized photon selection and no-track matching cuts for Run IIb and Run IIa are shown in Tables C.3, C.4, C.6 and C.7, and their systematic uncertainties are shown in Table C.8. The main systematic uncertainty sources are:

- Uncertainty of cut efficiency based on the calorimeter and pre-shower variables. The one standard deviation of the fitted scale factor is taken into account. The one standard deviations of scale factors are shown in Figures C.7 - C.12 and C.25 - C.30.
- Uncertainty coming from the no-track match. The scale factors are estimated with $Z \to l^+l^-$ data and MC. The statical uncertainty of data is their main uncertainties, and this is considered as the systematic uncertainty. Figures C.19 and C.24.
- Since the scale factors are measured with $Z \to ee$ data and MC, there exists difference between γ and electron. The efficiency difference between γ and electron are taken into account and conservatively 1% is assigned.

Table C.8: Systematic uncertainties for p20 (p17) photon identification [90].

Systematic uncertainty	CCcore0 (%)	CCcore1 (%)	CCcore2 (%)	ECcore0 (%)	ECcore1 (%)	ECcore2 (%)
Core cuts	2.0	2.0	2.0	2.0	2.0	2.0
No-track match	1.5 (2.0)	1.5 (2.0)	1.5 (2.0)	2.0 (2.5)	2.0 (2.5)	2.0 (2.5)
Diff. eff. b/w e and γ	1.0	1.0	1.0	1.0	1.0	1.0
Total	2.7 (3.0)	2.7 (3.0)	2.7 (3.0)	3.0 (3.4)	3.0 (3.4)	3.0 (3.4)

The core1 and core2 cuts are suggested to used for photon $p_T > 20$ GeV and the core0 is designed for the low p_T of photon. In addition, the core2 cut selects high purity of photons and this cut is proper for the di-photon cross section measurement. Tables C.9 - C.11 show the final scale factors with systematic uncertainties corresponding to Run IIa or Run IIb data and core cuts.

C.7 Conclusion

The recommended cuts for the photon identification and their scale factors with systematic uncertainties for Run II data taken from April 2002 to June 2009 are described.

Table C.9: Scale factors and their systematic uncertainties for the Run IIb CCcore0 and Run IIa CCcore cuts [90].

p_T (GeV)	Run IIb CCcore0	Run IIa CCcore0	Run IIa CCcore1	Run IIa CCcore2
10 – 15	0.905 ± 0.100	0.891 ± 0.144	-	-
15 – 20	0.932 ± 0.037	0.918 ± 0.056	-	-
20 – 25	0.949 ± 0.027	0.937 ± 0.030	0.922 ± 0.030	0.899 ± 0.033
25 – 30	0.960 ± 0.027	0.950 ± 0.030	0.938 ± 0.030	0.920 ± 0.030
30 – 33	0.965 ± 0.027	0.958 ± 0.030	0.949 ± 0.030	0.935 ± 0.030
33 – 35	0.968 ± 0.027	0.961 ± 0.030	0.954 ± 0.030	0.943 ± 0.030
35 – 37	0.969 ± 0.027	0.964 ± 0.030	0.959 ± 0.030	0.949 ± 0.030
37 – 39	0.970 ± 0.027	0.965 ± 0.030	0.963 ± 0.030	0.954 ± 0.030
39 – 41	0.971 ± 0.027	0.967 ± 0.030	0.966 ± 0.030	0.959 ± 0.030
41 – 43	0.972 ± 0.027	0.968 ± 0.030	0.970 ± 0.030	0.964 ± 0.030
43 – 45	0.972 ± 0.027	0.969 ± 0.030	0.973 ± 0.030	0.968 ± 0.030
45 – 50	0.973 ± 0.027	0.970 ± 0.030	0.978 ± 0.030	0.975 ± 0.030
> 50	0.973 ± 0.027	0.972 ± 0.030	0.985 ± 0.030	0.985 ± 0.030

Table C.10: Scale factors and their systematic uncertainties for all Run IIb core cuts except CCcore0 [90].

Run IIb	CCcore1	CCcore2	ECcore0	ECcore1	ECcore2
Scale factor	0.992 ± 0.027	0.989 ± 0.027	0.975 ± 0.030	0.965 ± 0.030	0.935 ± 0.030

Table C.11: Scale factors and their systematic uncertainties for the Run IIa ECcore cuts [90].

η_{det}	ECcore0	ECcore1	ECcore2
1.5 – 1.6	0.957 ± 0.040	0.957 ± 0.044	0.953 ± 0.040
1.6 – 1.7	0.958 ± 0.040	0.962 ± 0.044	0.957 ± 0.040
1.7 – 1.8	0.964 ± 0.040	0.970 ± 0.044	0.965 ± 0.040
1.8 – 1.9	0.975 ± 0.040	0.980 ± 0.044	0.976 ± 0.040
1.9 – 2.0	0.988 ± 0.040	0.992 ± 0.044	0.988 ± 0.040
2.0 – 2.1	1.002 ± 0.040	1.005 ± 0.044	1.000 ± 0.040
2.1 – 2.2	1.016 ± 0.040	1.018 ± 0.044	1.012 ± 0.040
2.2 – 2.3	1.028 ± 0.040	1.031 ± 0.044	1.023 ± 0.040
2.3 – 2.4	1.036 ± 0.040	1.043 ± 0.044	1.031 ± 0.040
2.4 – 2.5	1.039 ± 0.040	1.054 ± 0.044	1.035 ± 0.040

C.8 Background Subtraction

At the Tevatron, there is not pure photon data enough to measure efficiencies and scale factors with small uncertainty. Therefore, $Z \rightarrow ee$ data and MC selected with the tag-and-probe method are used to measure scale factors for various photon selection cuts since electrons have similar performance to photons on the core cuts. The tag electron is required to pass:

- emfrac > 0.97
- isolation < 0.07
- track iso < 2 GeV
- H-matrix7 < 12
- ANN7 > 0.6
- likelihood8 > 0.8

To select a probe electron , the invariant mass of tag and probe electrons should satisfy the Z mass window cut ($82 < M_{ee} < 100$ GeV), and the probe electron must pass the event selection described in section C.3. There can be QCD contribution in the low p_T region, and result can be biased by the QCD contribution, therefore background estimation is conducted using "Template fitting", and "Side-band fitting" for the purpose of cross check.

C.8.0.1 Template Fitting

To estimate and subtract the QCD contribution, the fitting on the invariant mass spectrum of the di-electron is conducted by minimizing the difference between the templates of expected events and the data template. The templates of expected events consist of the Pythia $Z \rightarrow ee$ simulation and the multijet background which is estimated by reverting the H-matrx7 (> 25) requirement in the QCD data. Figures C.31 - C.34 show the template fitting results for Run IIa and Run IIb in different p_T regions. In the captions, CC-CC is refers that two electrons are found in same Central Calorimeter region, and CC-EC means that one electron is identified in the Central Calorimeter region and the other electron is found in the End Calorimeter region.

C.8.1 Side-band Fitting

The purpose of QCD background estimation by the side-band fitting is to cross check the result by the template fitting. Assuming that the events below the invariant mass of the di-electron 60 GeV ($M_{ee} < 60$ GeV) and above 120 GeV ($M_{ee} > 120$ GeV) are from the QCD background contribution predominantly, the side-band fitting is done in the invariant mass of the di-electron spectrum. Using the exponential function $\exp(p0 + p1 * M_{ee} + p2 * M_{ee}^2)$, the outside of signal region is fitted and the shape of background contribution in the signal region is interpolated by the exponential function, where the signal region is referred to $60 < M_{ee} < 110$ GeV. The side-band fitting results are shown in Figures C.35 - C.42, and the efficiency scale factors derived with the subtraction of QCD background by the side-band fitting are shown in Tables C.12 and C.13.

Table C.12: Scale factors and their statistical uncertainties for the CCcore cuts in Run IIb data [90].

η_{det}	CCcore0	CCcore1	CCcore2
10 GeV $< p_T <$ 15 GeV	0.686 ± 0.060	0.660 ± 0.070	0.659 ± 0.083
15 GeV $< p_T <$ 20 GeV	1.061 ± 0.028	1.064 ± 0.035	1.085 ± 0.048
20 GeV $< p_T <$ 25 GeV	0.956 ± 0.012	0.928 ± 0.014	0.906 ± 0.018
25 GeV $< p_T <$ 30 GeV	0.964 ± 0.007	0.960 ± 0.007	0.951 ± 0.009

Table C.13: Scale factors and their statistical uncertainties for the ECcore cuts in Run IIb data [90].

η_{det}	ECcore0	ECcore1	ECcore2
10 GeV $< p_T <$ 15 GeV	0.995 ± 0.021	0.995 ± 0.024	0.996 ± 0.032
15 GeV $< p_T <$ 20 GeV	0.977 ± 0.010	0.975 ± 0.011	0.943 ± 0.016
20 GeV $< p_T <$ 25 GeV	0.993 ± 0.005	0.993 ± 0.006	0.986 ± 0.009
25 GeV $< p_T <$ 30 GeV	0.984 ± 0.004	0.979 ± 0.005	0.959 ± 0.007

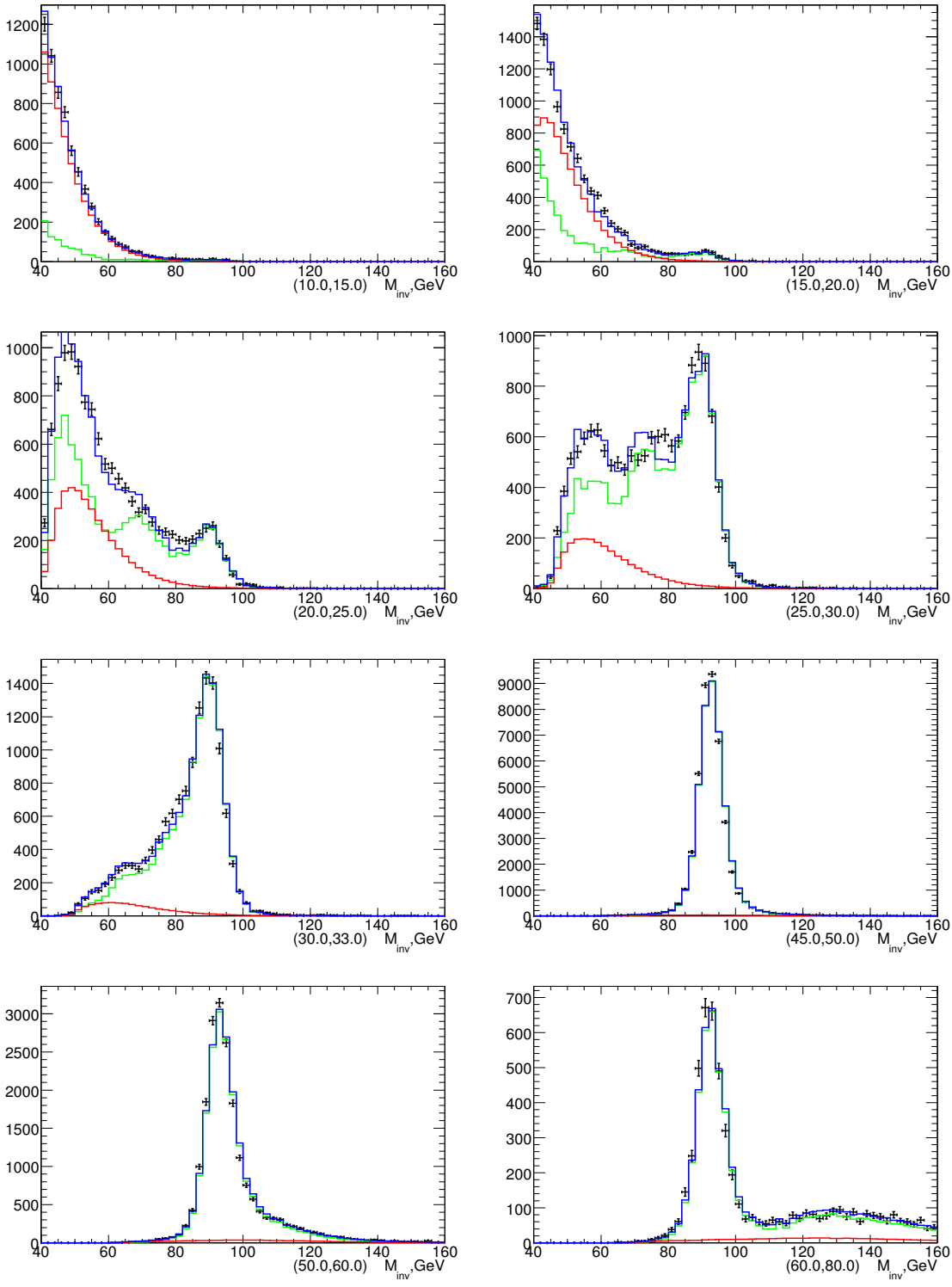

Figure C.31: The template fitting on the Z mass spectrum for the various p_T regions of CC-CC probe electrons in Run IIb data and MC [90].

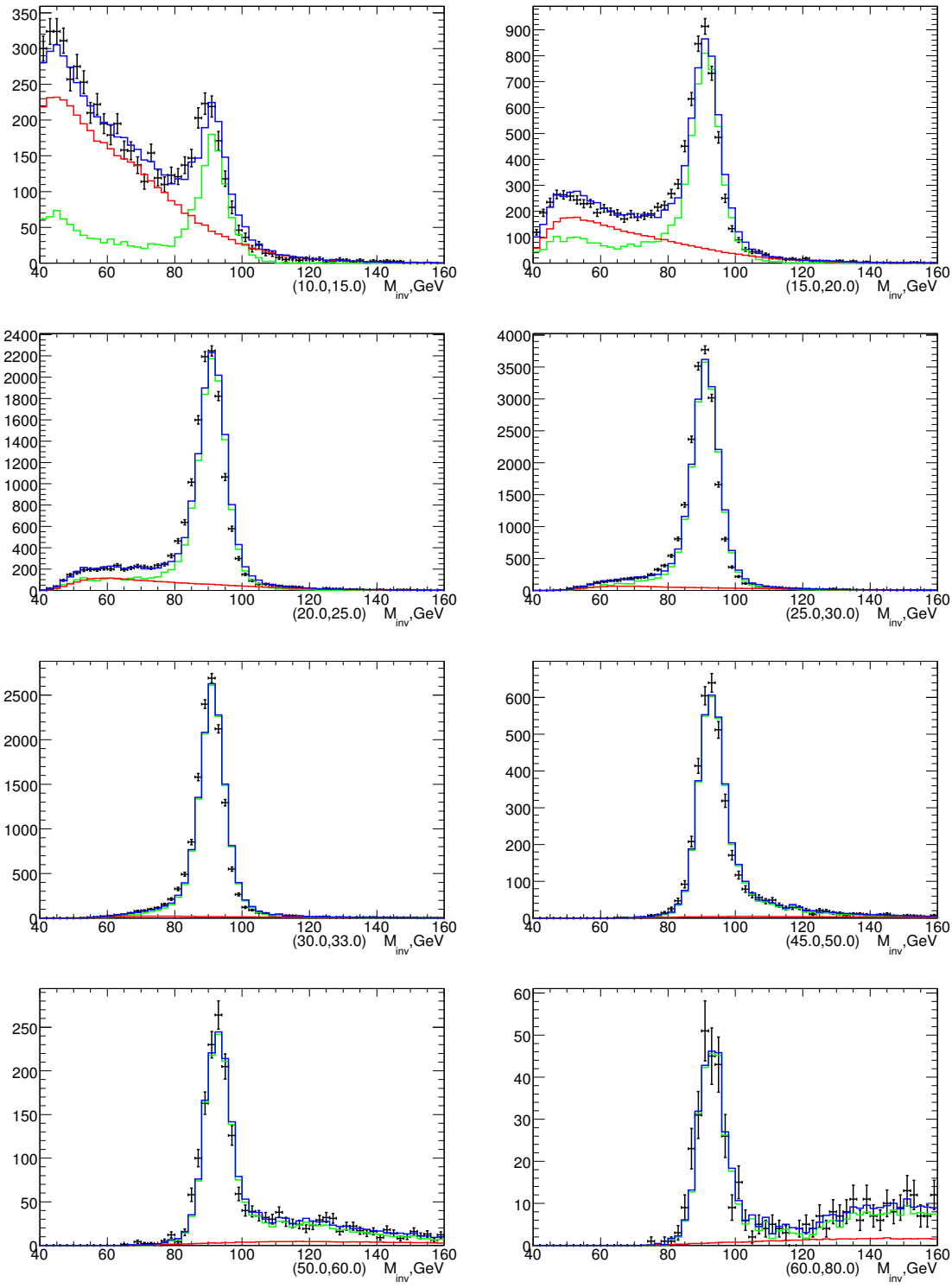

Figure C.32: The template fitting on the Z mass spectrum for the various p_T regions of CC-EC probe electrons in Run IIb data and MC [90].

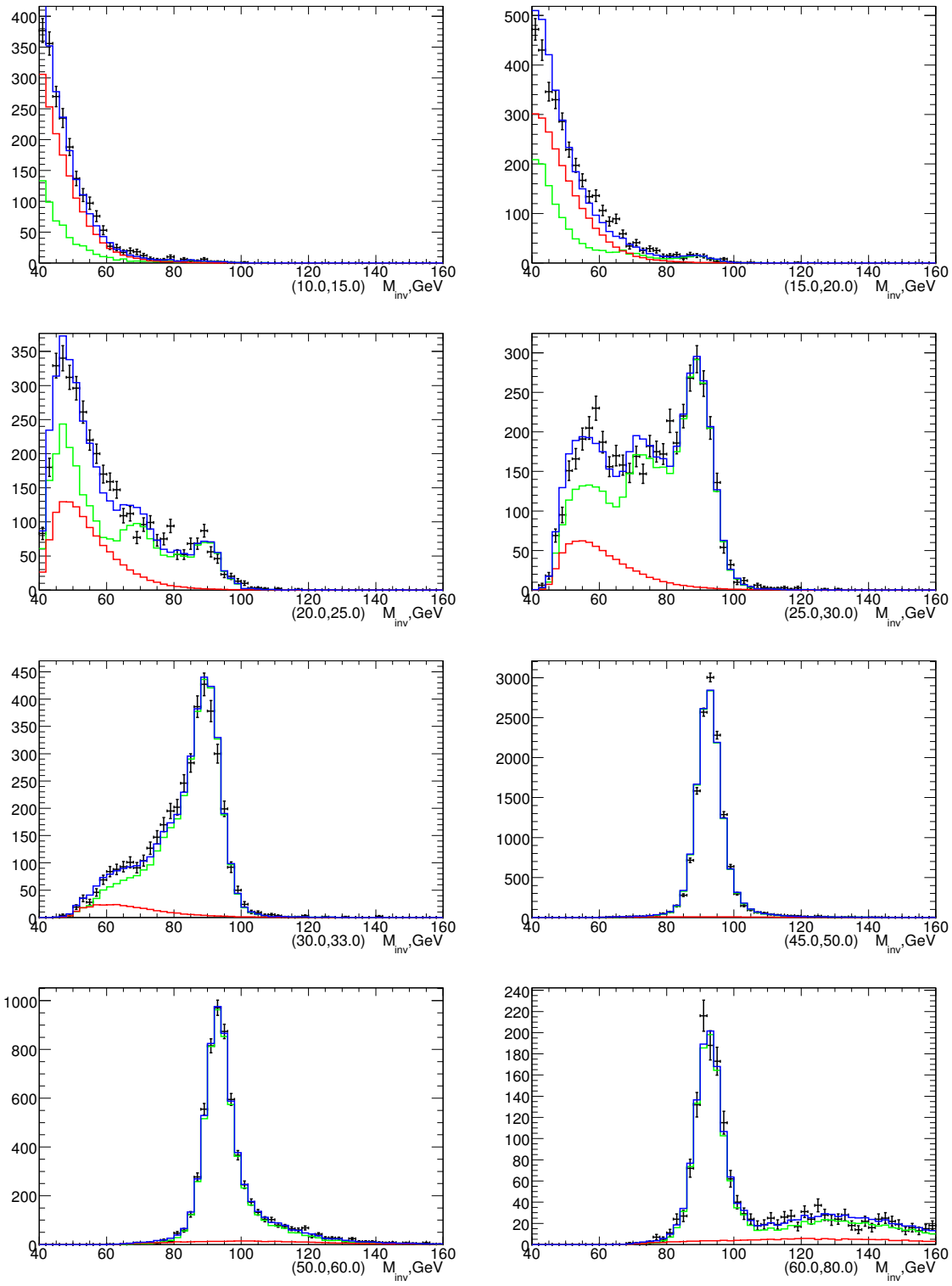

Figure C.33: The template fitting on the Z mass spectrum for the various p_T regions of CC-CC probe electrons in Run IIa data and MC [90].

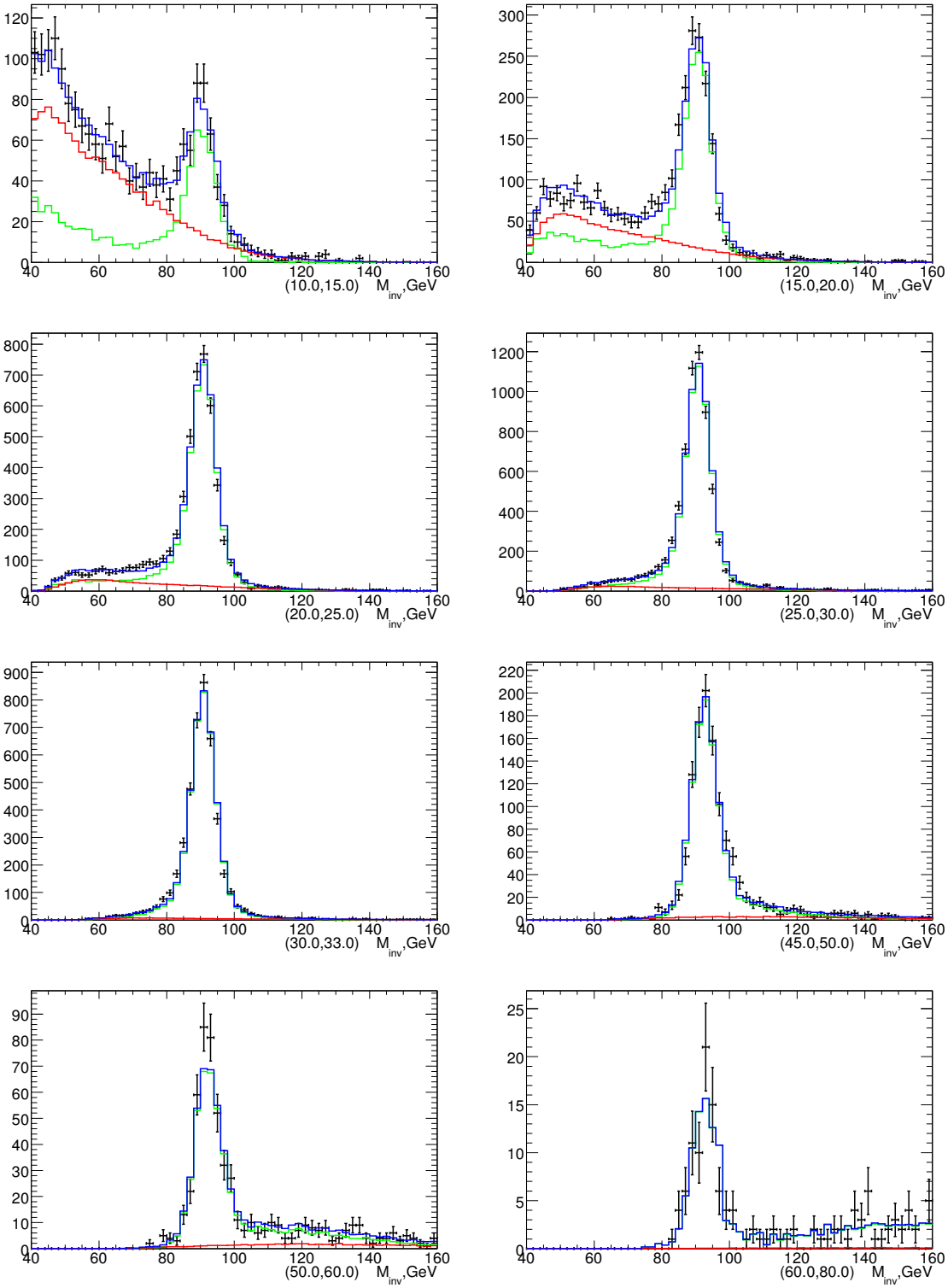

Figure C.34: The template fitting on the Z mass spectrum for the various p_T regions of CC-EC probe electrons in Run IIa data and MC [90].

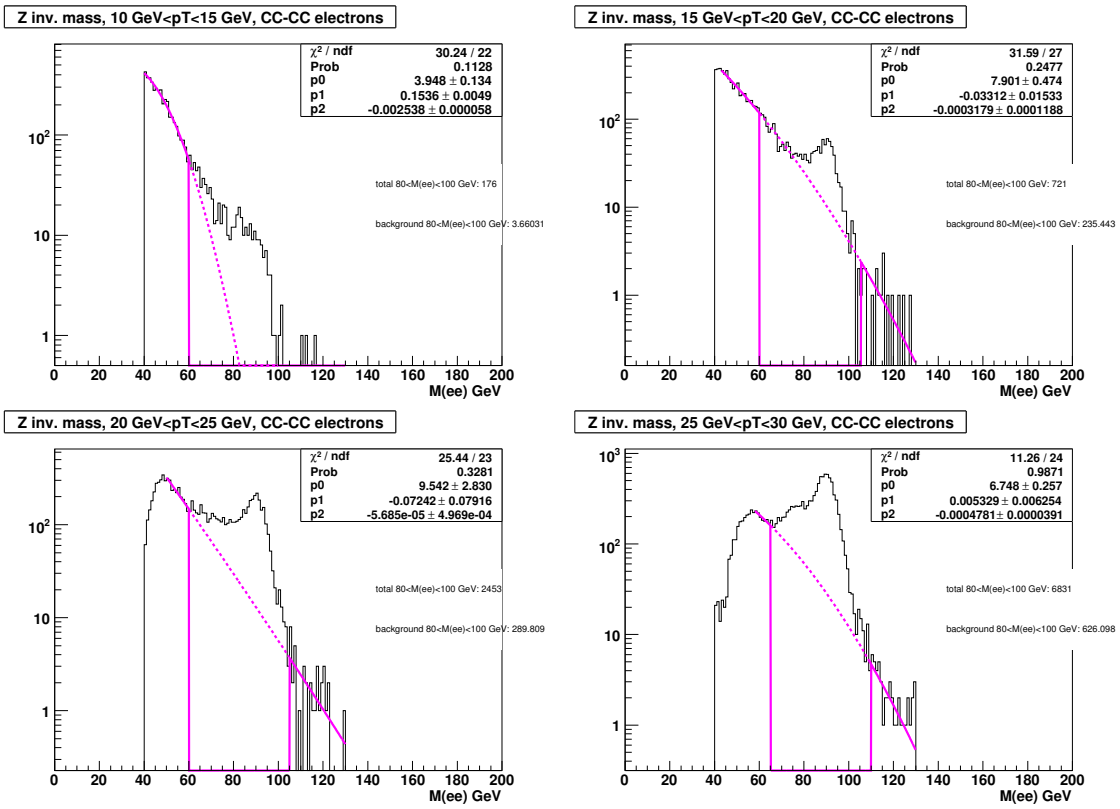

Figure C.35: The side-band fitting for the Preselection in CC: $10 < p_T < 15$ GeV (Top left), $10 < p_T < 15$ GeV (Top right), $20 < p_T < 25$ GeV (Bottom left), $25 < p_T < 30$ GeV (Bottom right) [90].

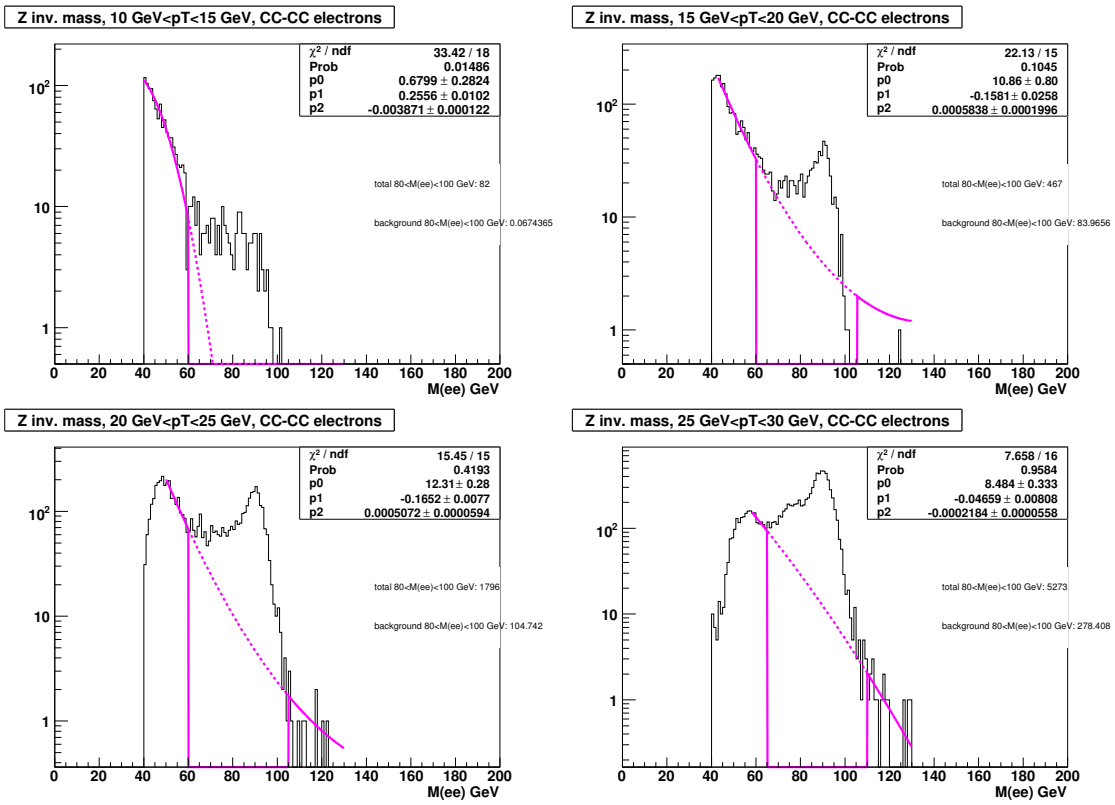

Figure C.36: The side-band fitting for the CCcore0: $10 < p_T < 15$ GeV (Top left), $10 < p_T < 15$ GeV (Top right), $20 < p_T < 25$ GeV (Bottom left), $25 < p_T < 30$ GeV (Bottom right) [90].

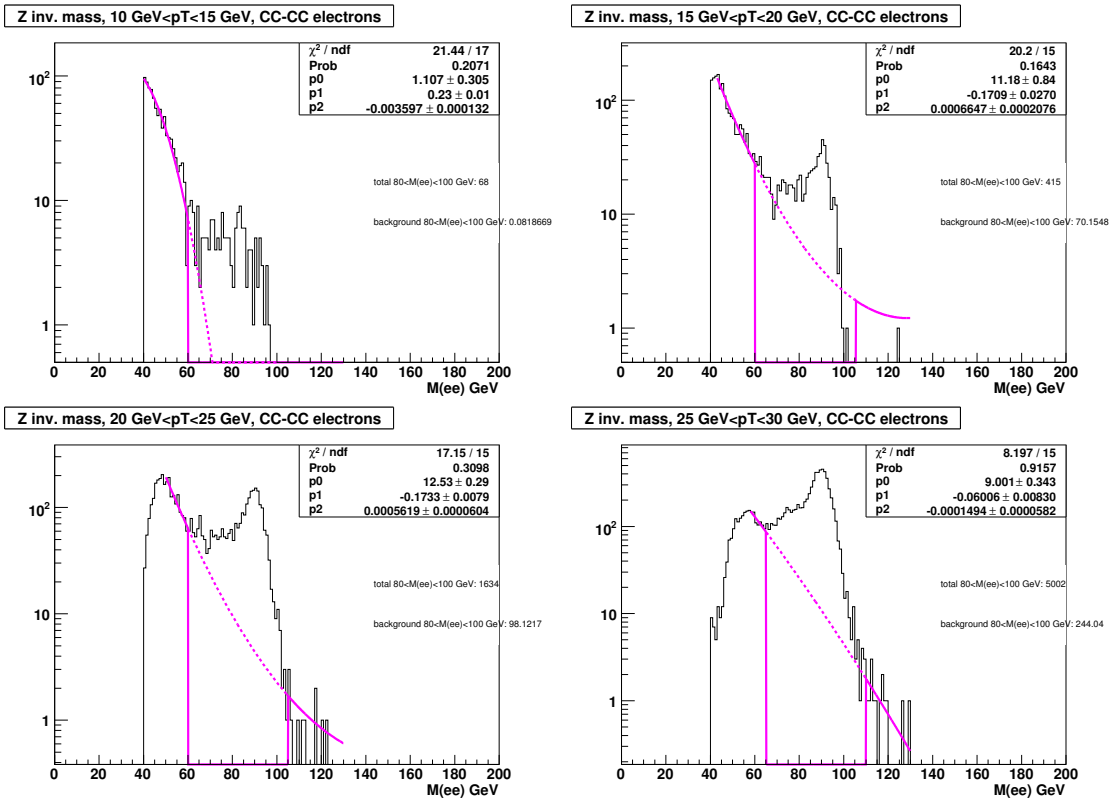

Figure C.37: The side-band fitting for the CCcore1: $10 < p_T < 15$ GeV (Top left), $10 < p_T < 15$ GeV (Top right), $20 < p_T < 25$ GeV (Bottom left), $25 < p_T < 30$ GeV (Bottom right) [90].

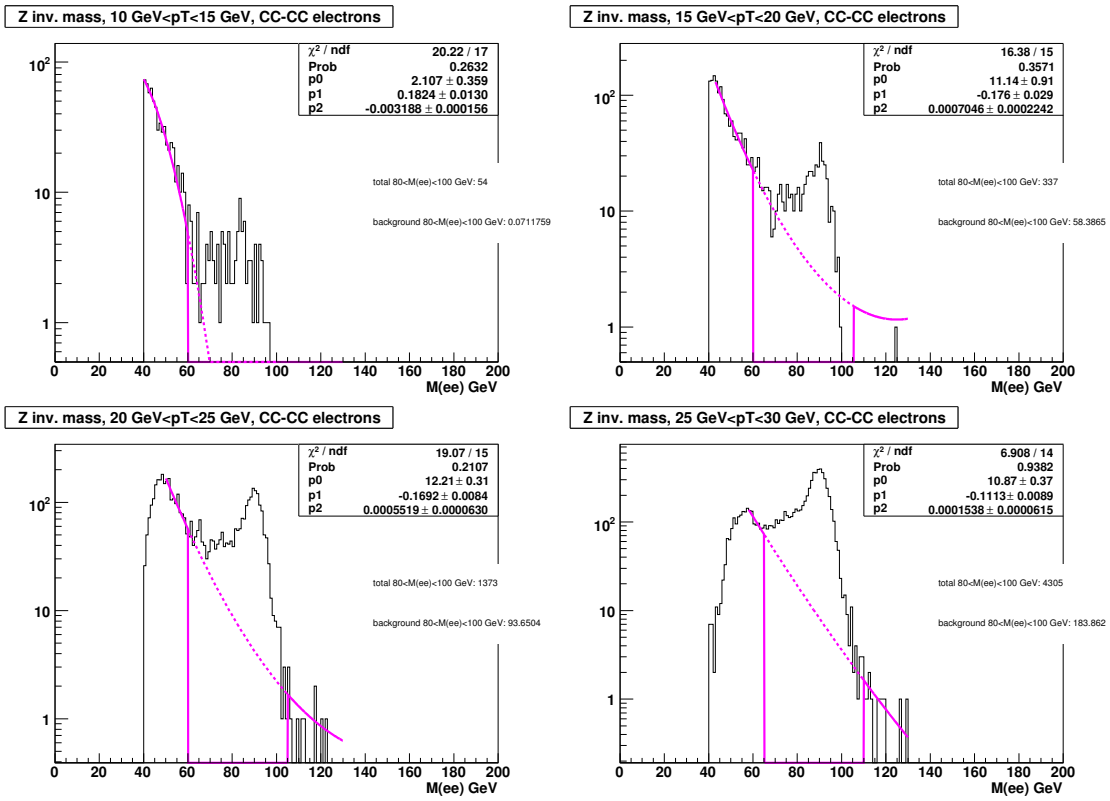

Figure C.38: The side-band fitting for the CCcore0: $10 < p_T < 15$ GeV (Top left), $10 < p_T < 15$ GeV (Top right), $20 < p_T < 25$ GeV (Bottom left), $25 < p_T < 30$ GeV (Bottom right) [90].

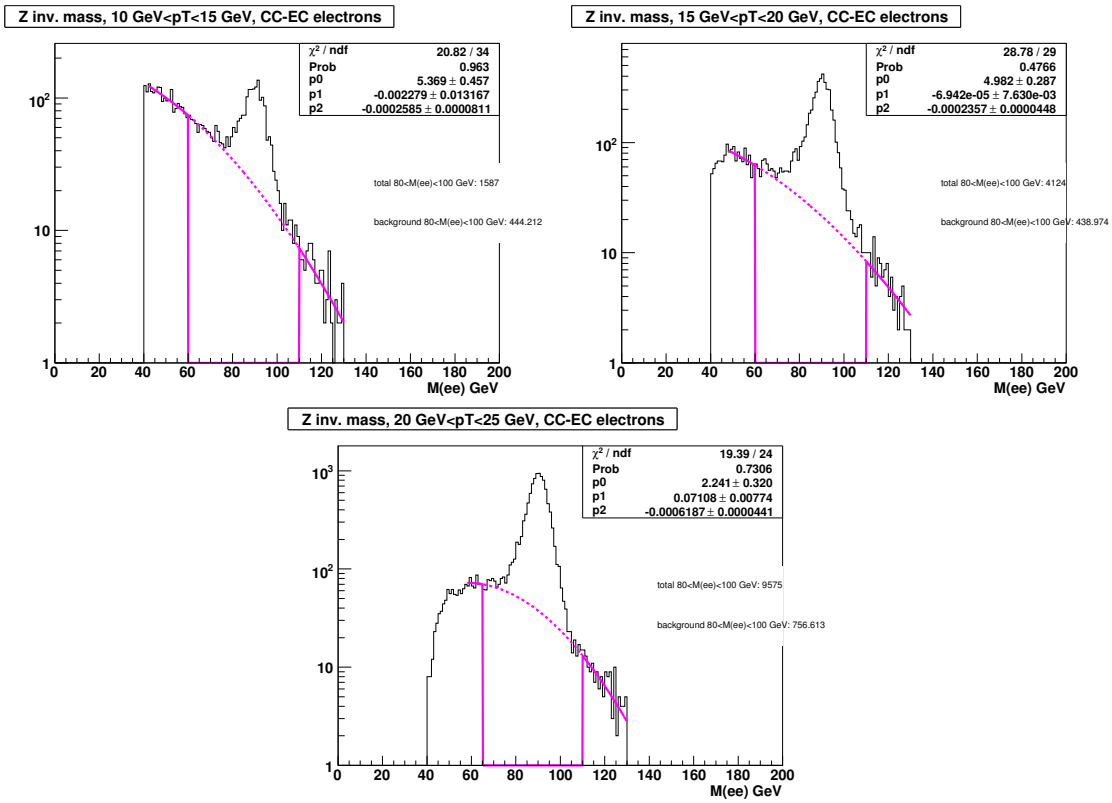

Figure C.39: The side-band fitting for the Preselection in EC: $10 < p_T < 15$ GeV (Top left), $10 < p_T < 15$ GeV (Top right), $20 < p_T < 25$ GeV (Bottom) [90].

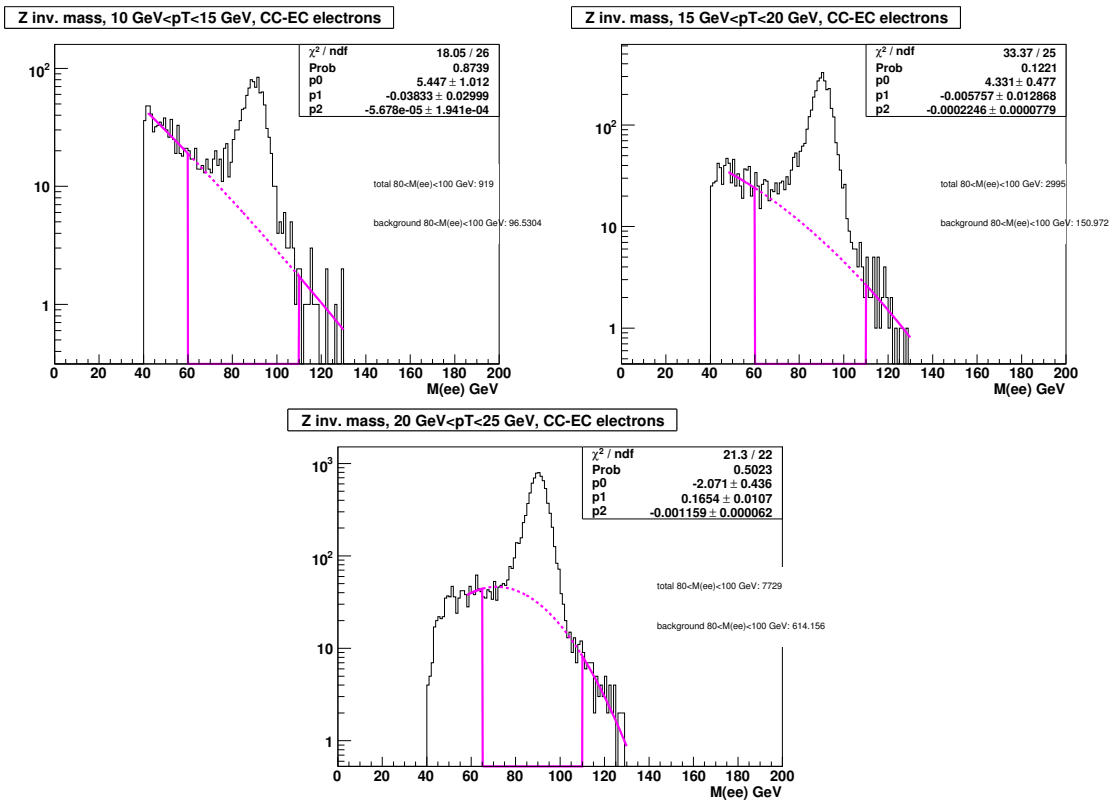

Figure C.40: The side-band fitting for the ECcore0: $10 < p_T < 15$ GeV (Top left), $10 < p_T < 15$ GeV (Top right), $20 < p_T < 25$ GeV (Bottom) [90].

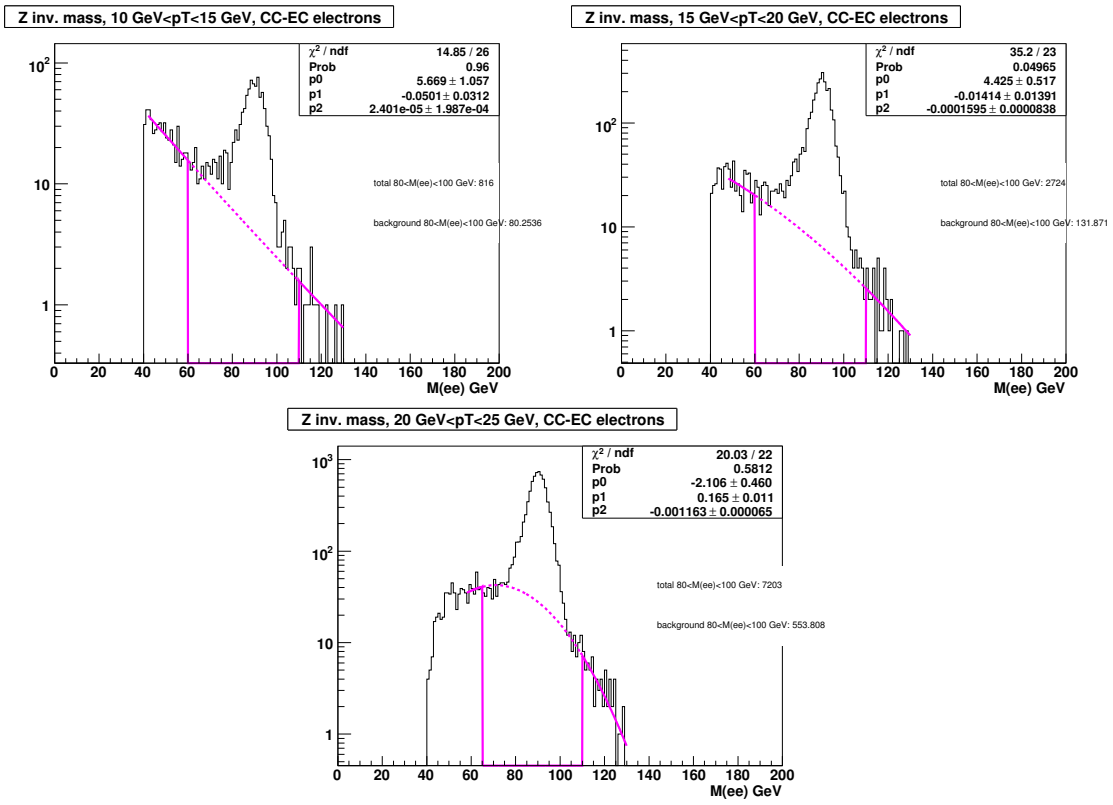

Figure C.41: The side-band fitting for the ECcore1: $10 < p_T < 15$ GeV (Top left), $10 < p_T < 15$ GeV (Top right), $20 < p_T < 25$ GeV (Bottom) [90].

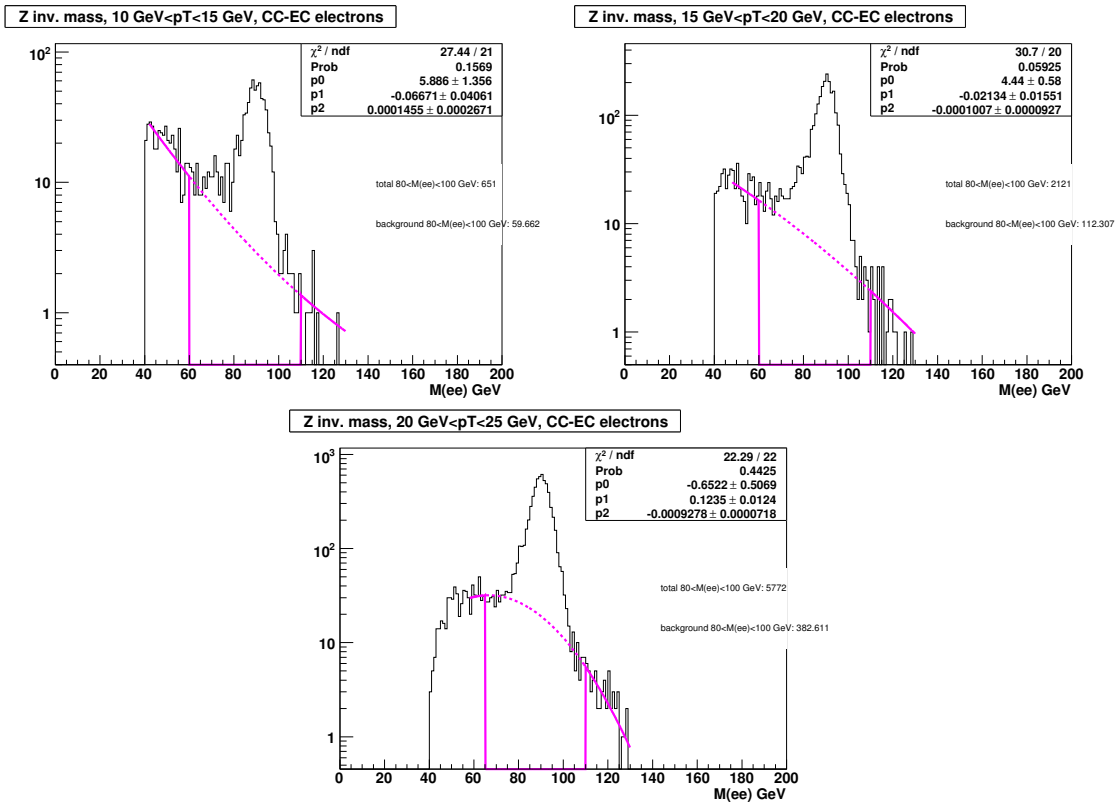

Figure C.42: The side-band fitting for the ECcore2: $10 < p_T < 15$ GeV (Top left), $10 < p_T < 15$ GeV (Top right), $20 < p_T < 25$ GeV (Bottom) [90].

C.8.2 Electron Passing "no-track" Matching Efficiency

Using electrons passed the core cuts, the efficiency that an electron passes the no-track requirement is measured, i.e. the efficiency that an electron fakes a photon is measured. Figures C.43 - C.54 show no-track matching efficiencies as function of p_T, η_{det} and ϕ_{det} in Run IIa and IIb data, and MC. The scale factors corresponding to them are also shown in Figures. In the CC ($-1.1 < \eta_{det} < 1.1$) region, the scale factors have ϕ_{det} dependence, thus they are parameterized as function of ϕ. The functions are fitted with the third order polynomial function ($p0 + p1 \cdot \phi_{det} + p2 \cdot \phi_{det}^2 + p3 \cdot \phi_{det}^3$). The parameters in the polynomial function are shown in Table C.14, and the systematic uncertainty of 15% is assigned to cover the one standard deviation of the scale factor fluctuation (bottom right plots in Figures C.43 - C.45, and C.49 - C.51). In the EC ($1.5 < |\eta_{det}| < 2.5$) region, the scale factors have dependence of both η_{det} and ϕ_{det}, and 10% is assigned to their systematic uncertainties. The no-track matching efficiencies of electrons passing ECcore cuts and their scale factors are shown in Figures C.46 - C.48, and C.52 - C.54.

Table C.14: Parameters for the scale factor function of the electron no-track matching efficiency ($p0 + p1 \cdot \phi_{det} + p2 \cdot \phi_{det}^2 + p3 \cdot \phi_{det}^3$) in the CC region [90].

	Run IIb			Run IIa		
Parameters	CCcore0	CCcore1	CCcore2	CCcore0	CCcore1	CCcore2
$p0$	1.40805	1.56334	1.6503	2.11331	2.09394	2.13796
$p1$	0.496714	0.799907	0.817676	-0.274626	-0.255502	-0.289944
$p2$	-0.297867	-0.441342	-0.460075	-0.0258044	-0.0320524	-0.0189376
$p3$	0.0363113	0.0522431	0.0547057	0.0101667	0.0107348	0.00938735

C.8.3 Study the Rate of Quark and Gluon Jets Faking Photon

By splitting the emjet MC samples into quark and gluon jets samples, the rates that quark and gluon jets fake photons are investigated. According to Table C.15, the quark jets have a higher fake rate by a factor of two than the gluon jets. For this case, the rate is calculated by the ratio of quark or gluon jets passing the core cuts after requiring the preselection cut to those passing the preselection cut. Figure C.55 shows the fake rates in the CC and EC

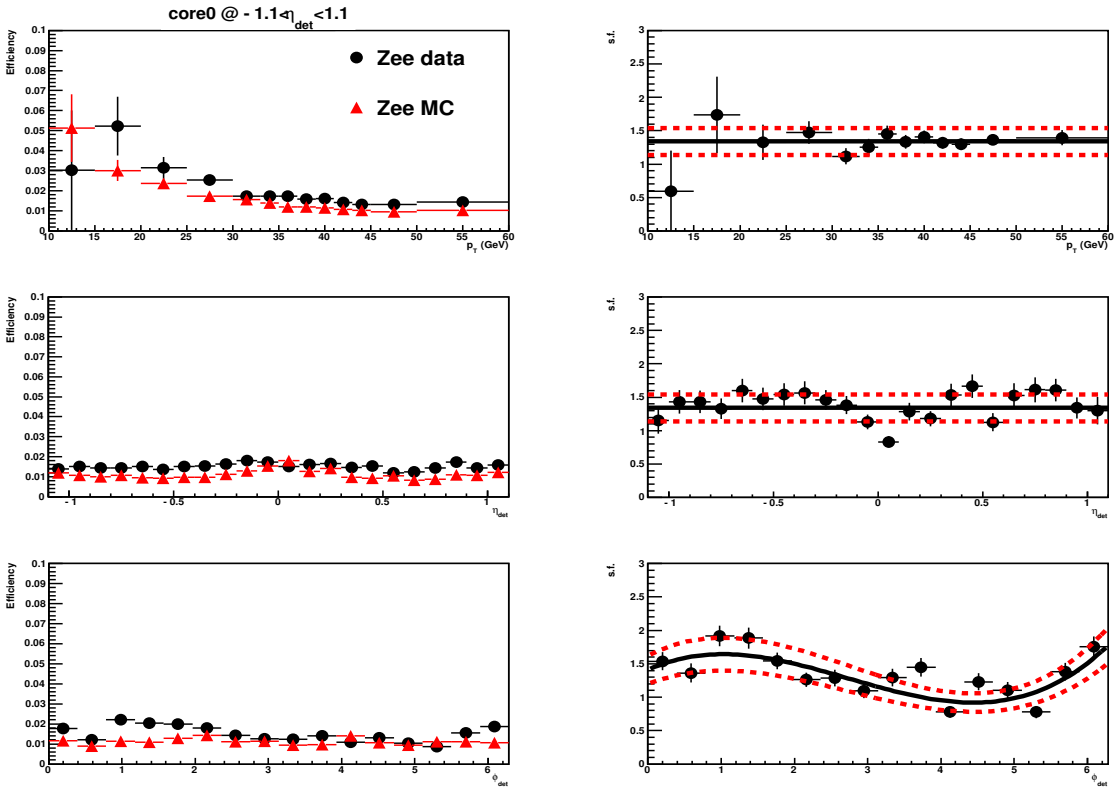

Figure C.43: The no-track matching efficiencies of electrons passing CCcore0 for p_T, η_{det} and ϕ_{det}, and their scale factors for Run IIb [90].

regions. But no significant difference of fake rate between the quark and gluon jets are found after requiring O_{NN} (NN output) > 0.6 (Table C.16 and Figure C.56). For this case, the rate is found by the ratio of quark or gluon jets passing O_{NN} (NN output) > 0.6 after requiring the core cuts to those passing the core cuts.

Table C.15: Mean efficiencies for the quark and gluon jets passing core cuts. The statistical uncertainty is considered [90].

Jet	CCcore0	CCcore1	CCcore2	CCcore0	CCcore1	CCcore2
Quark	0.071 ± 0.001	0.037 ± 0.001	0.025 ± 0.001	0.123 ± 0.001	0.065 ± 0.001	0.042 ± 0.001
Gluon	0.057 ± 0.001	0.012 ± 0.001	0.007 ± 0.001	0.081 ± 0.001	0.019 ± 0.001	0.012 ± 0.001

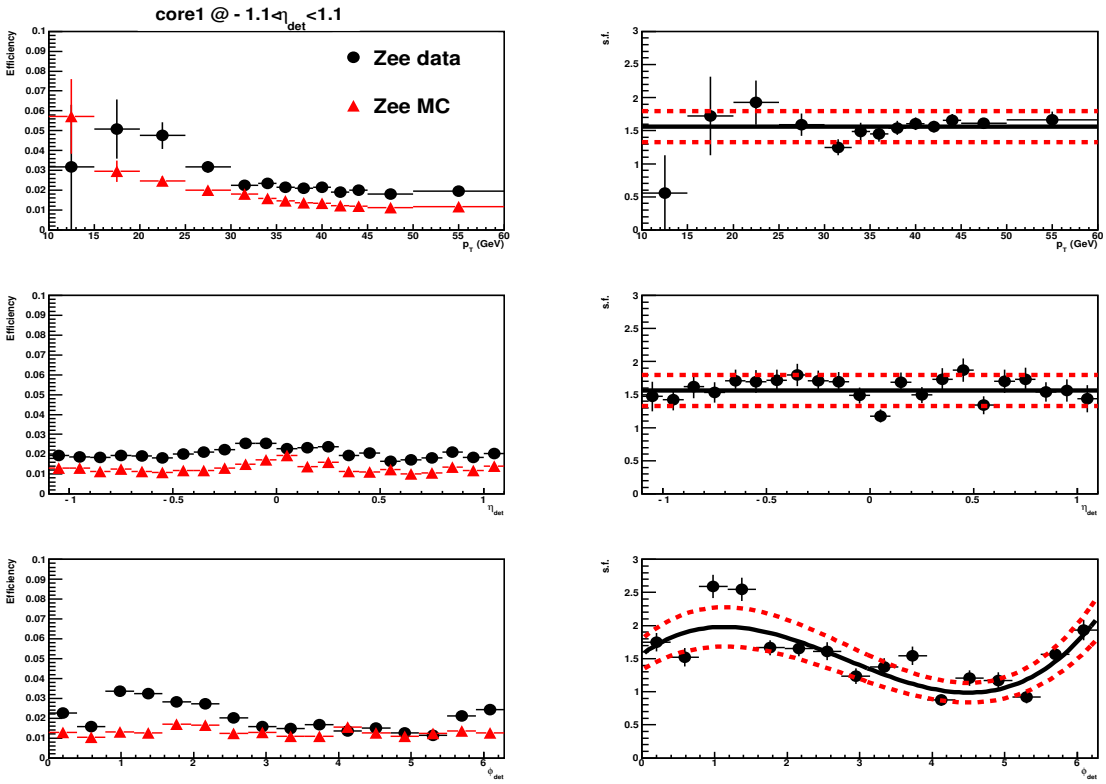

Figure C.44: The no-track matching efficiencies of electrons passing CCcore1 for p_T, η_{det} and ϕ_{det}, and their scale factors for Run IIb [90].

Table C.16: Mean efficiencies for the quark and gluon jets passing core cuts and O_{NN} (NN output) > 0.6. The statistical uncertainty is considered [90].

Jet	CCcore0	CCcore1	CCcore2	CCcore0	CCcore1	CCcore2
Quark	0.535 ± 0.004	0.512 ± 0.006	0.675 ± 0.007	0.479 ± 0.004	0.467 ± 0.005	0.659 ± 0.006
Gluon	0.545 ± 0.010	0.502 ± 0.022	0.670 ± 0.026	0.568 ± 0.016	0.493 ± 0.034	0.710 ± 0.040

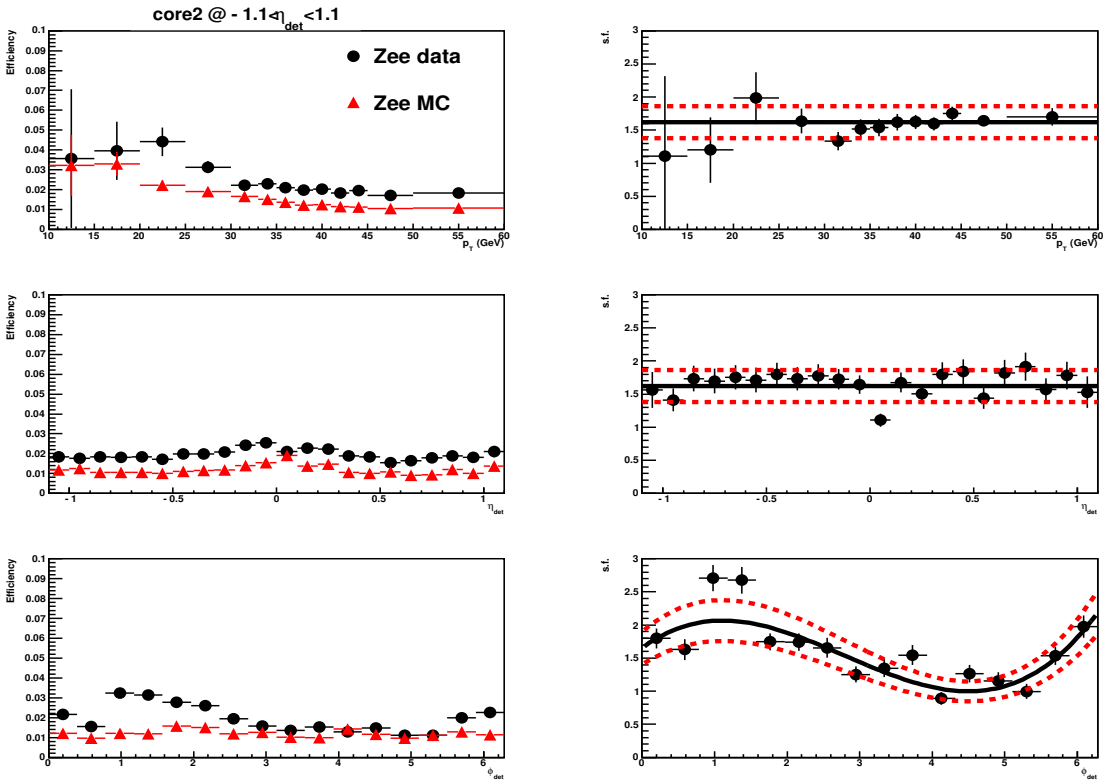

Figure C.45: The no-track matching efficiencies of electrons passing CCcore2 for p_T, η_{det} and ϕ_{det}, and their scale factors for Run IIb [90].

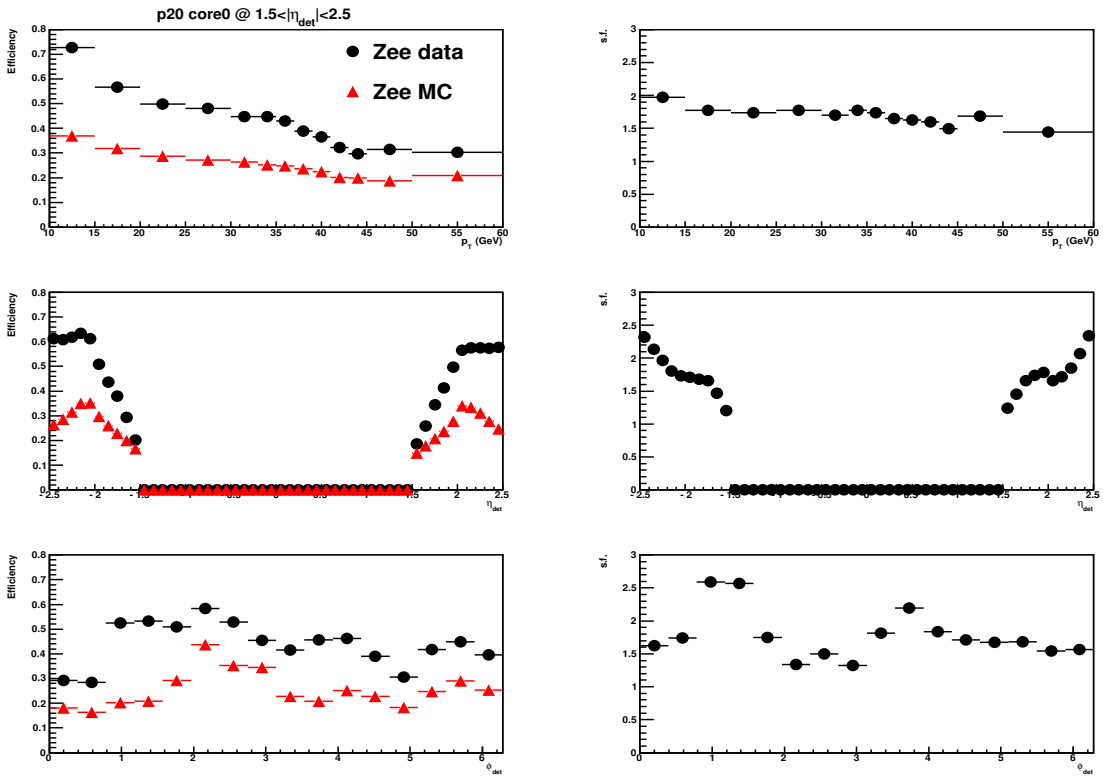

Figure C.46: The no-track matching efficiencies of electrons passing ECcore0 for p_T, η_{det} and ϕ_{det}, and their scale factors for Run IIb [90].

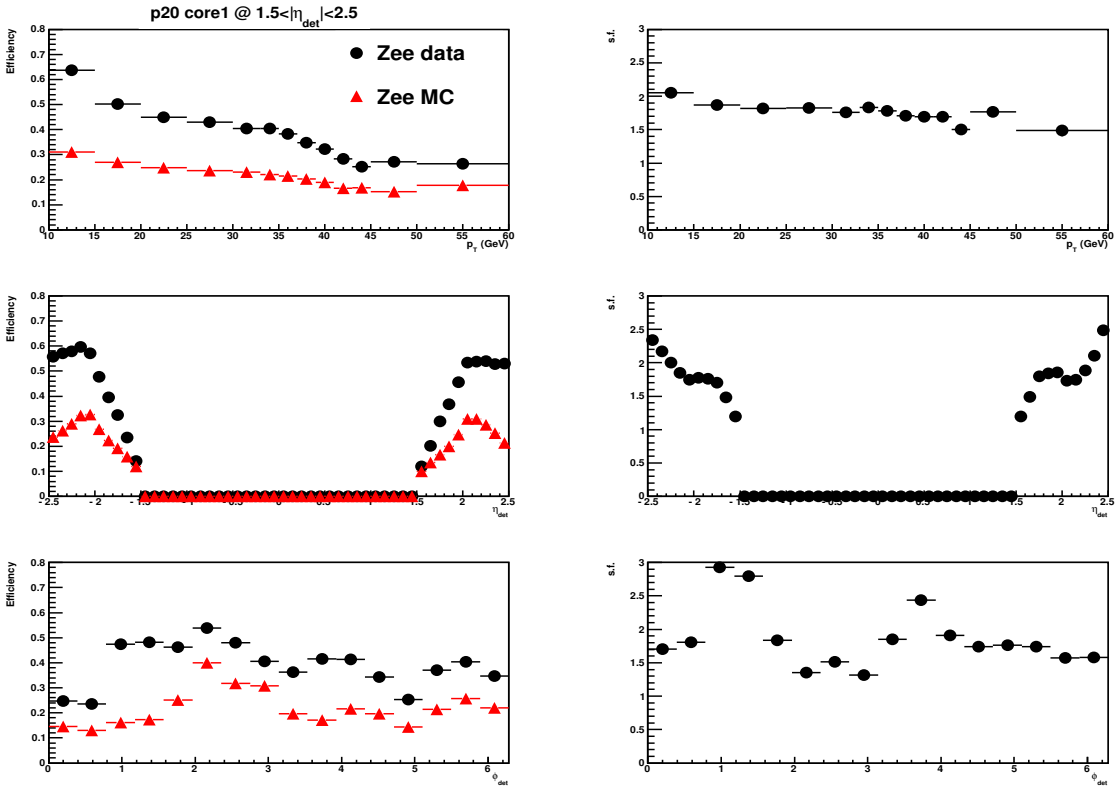

Figure C.47: The no-track matching efficiencies of electrons passing ECcore1 for p_T, η_{det} and ϕ_{det}, and their scale factors for Run IIb [90].

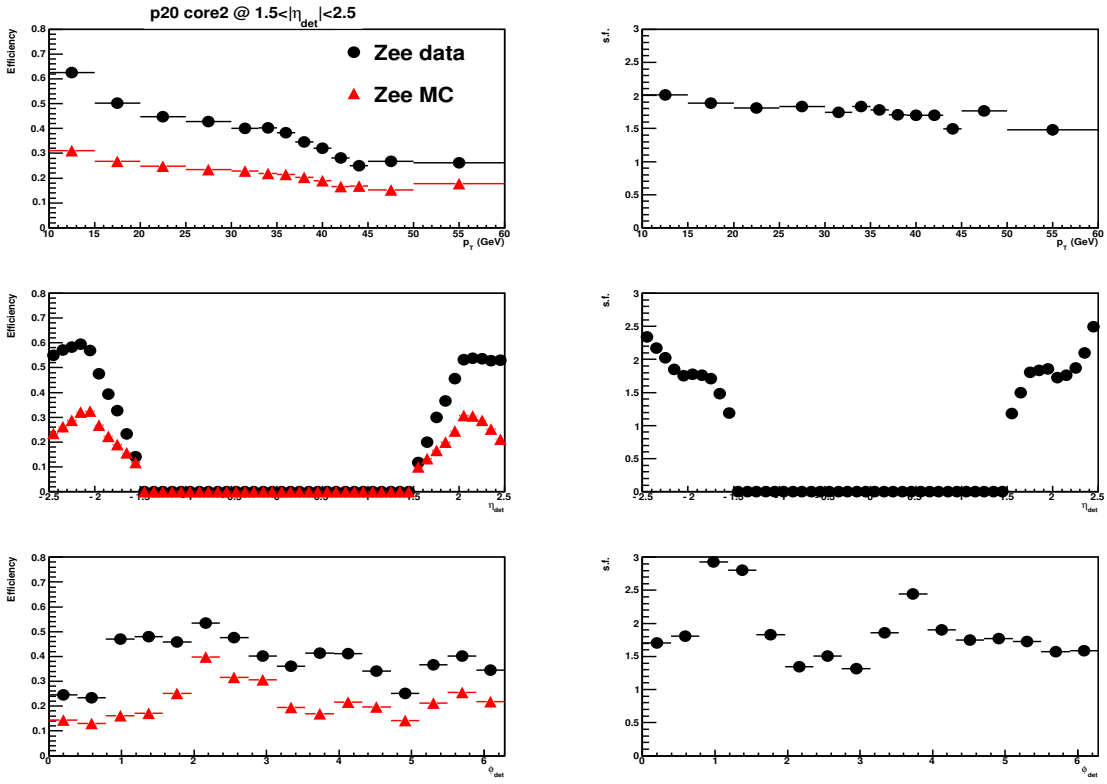

Figure C.48: The no-track matching efficiencies of electrons passing ECcore2 for p_T, η_{det} and ϕ_{det}, and their scale factors for Run IIb [90].

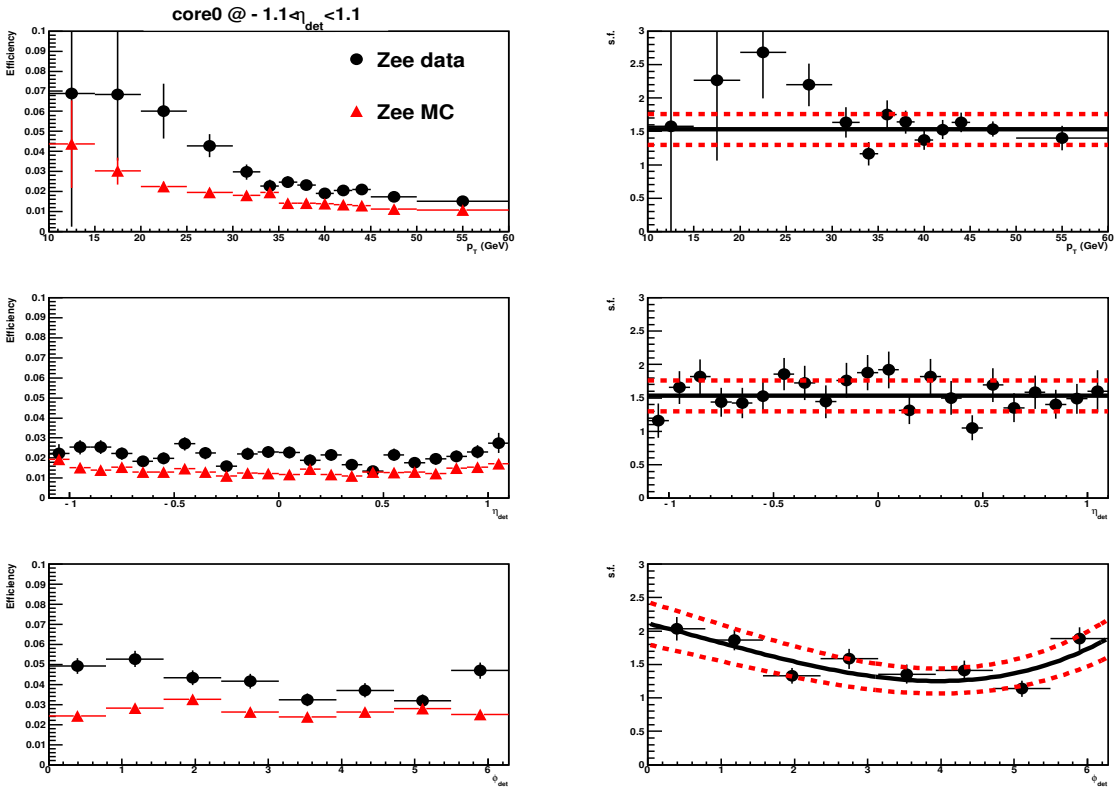

Figure C.49: The no-track matching efficiencies of electrons passing CCcore0 for p_T, η_{det} and ϕ_{det}, and their scale factors for Run IIa [90].

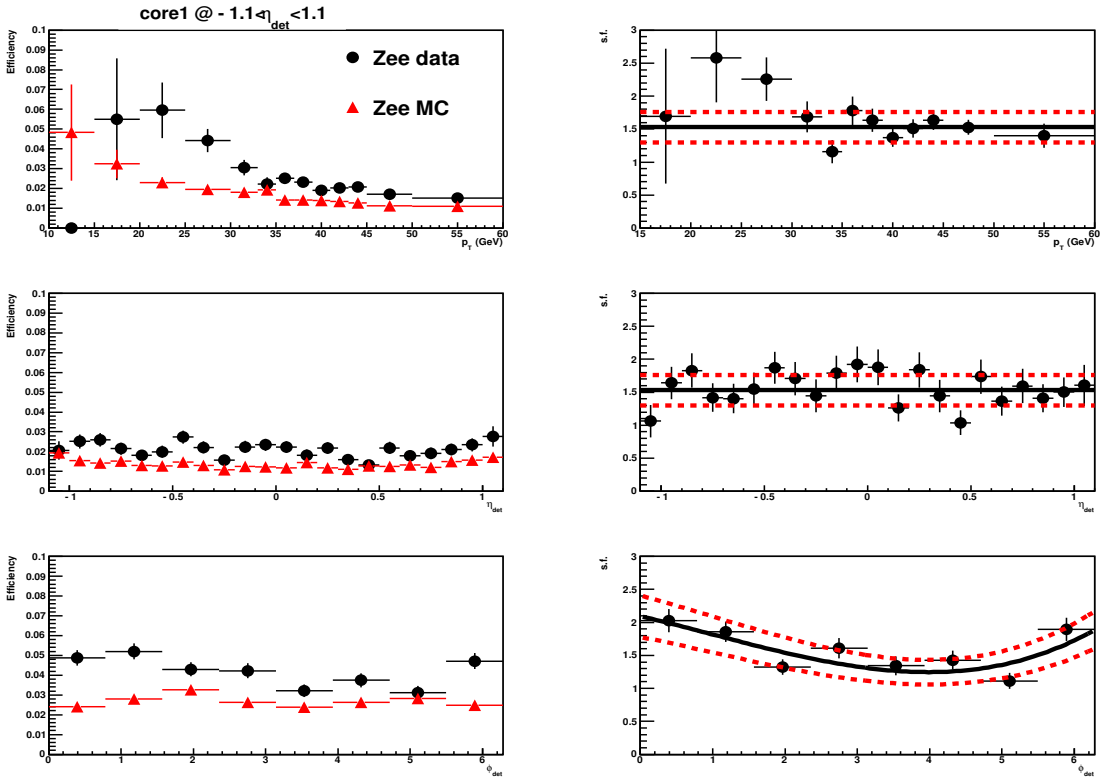

Figure C.50: The no-track matching efficiencies of electrons passing CCcore1 for p_T, η_{det} and ϕ_{det}, and their scale factors for Run IIa [90].

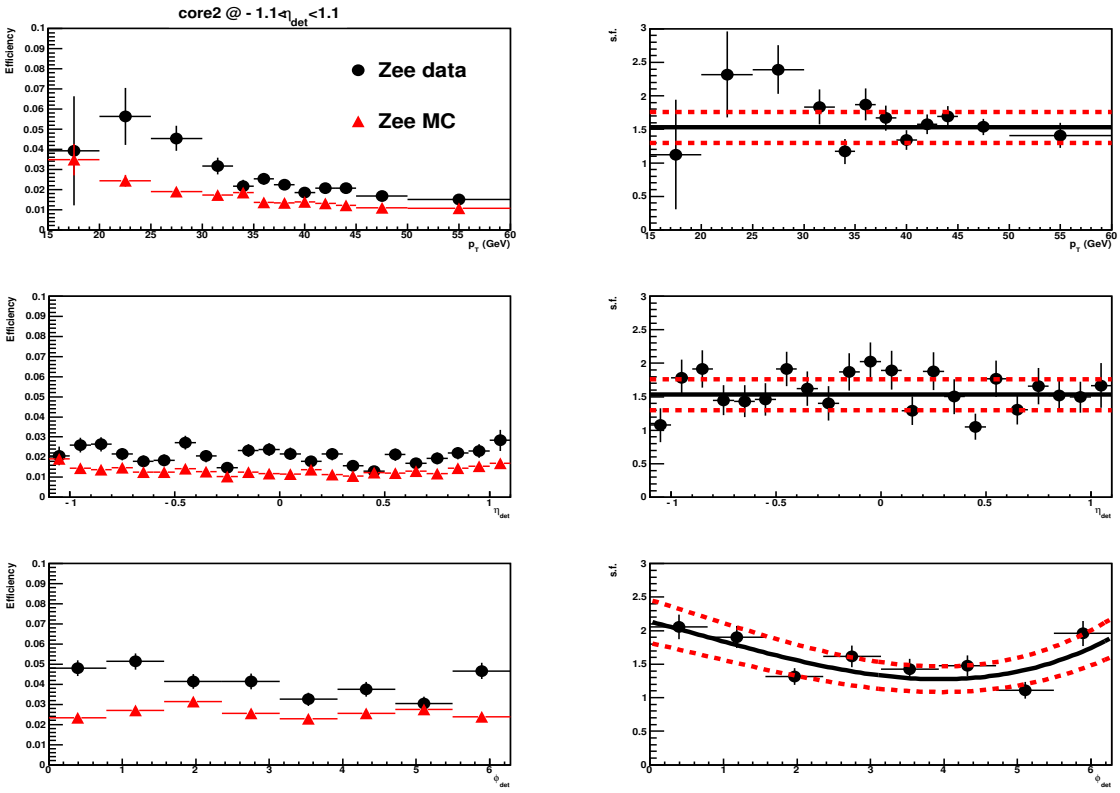

Figure C.51: The no-track matching efficiencies of electrons passing CCcore2 for p_T, η_{det} and ϕ_{det}, and their scale factors for Run IIa [90].

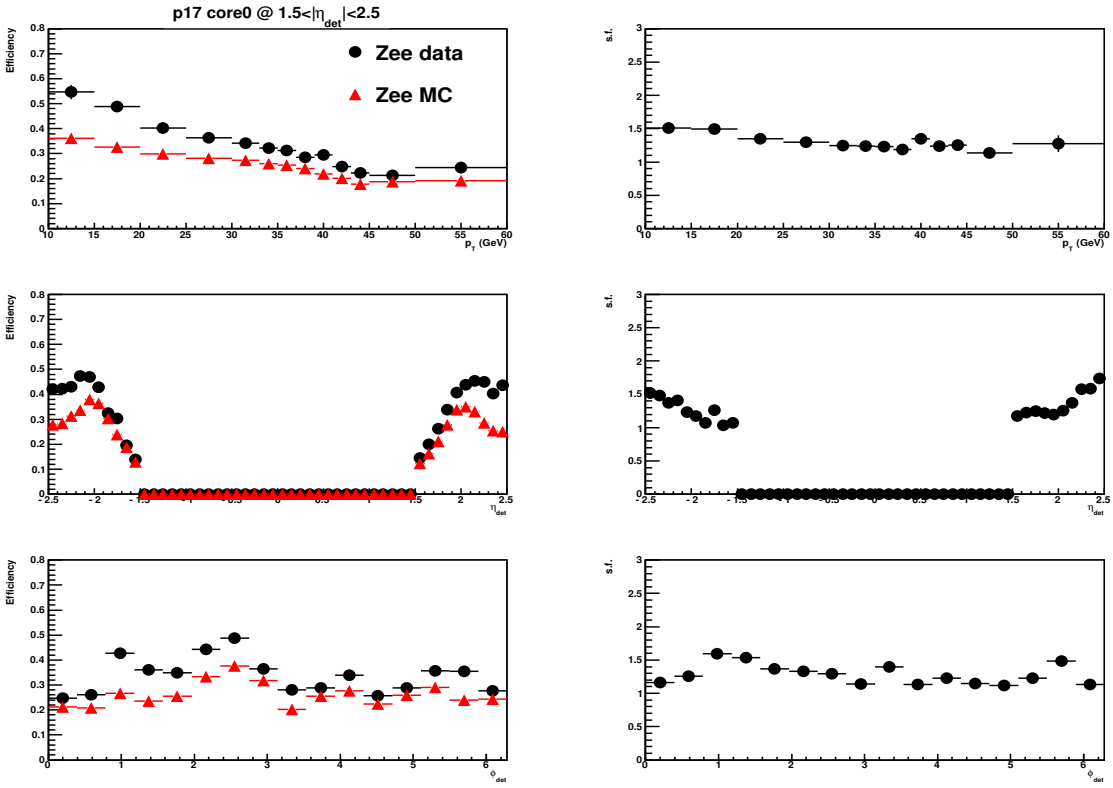

Figure C.52: The no-track matching efficiencies of electrons passing ECcore0 for p_T, η_{det} and ϕ_{det}, and their scale factors for Run IIa [90].

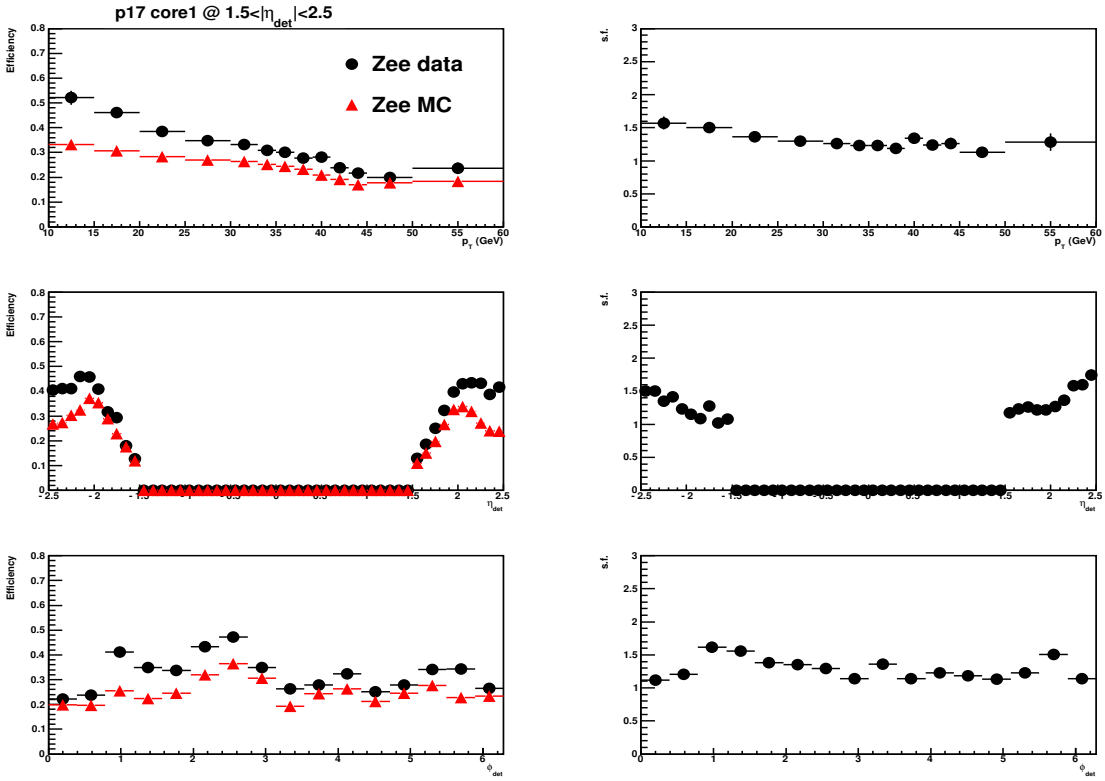

Figure C.53: The no-track matching efficiencies of electrons passing ECcore1 for p_T, η_{det} and ϕ_{det}, and their scale factors for Run IIa [90].

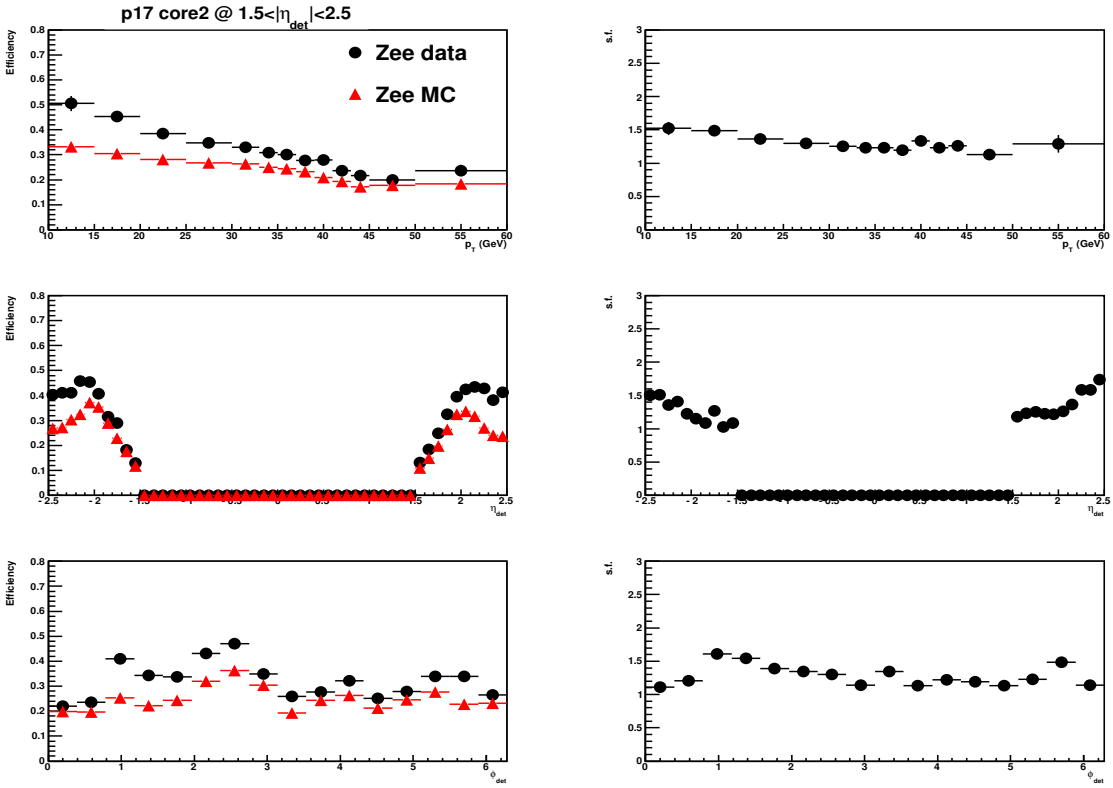

Figure C.54: The no-track matching efficiencies of electrons passing ECcore2 for p_T, η_{det} and ϕ_{det}, and their scale factors for Run IIa [90].

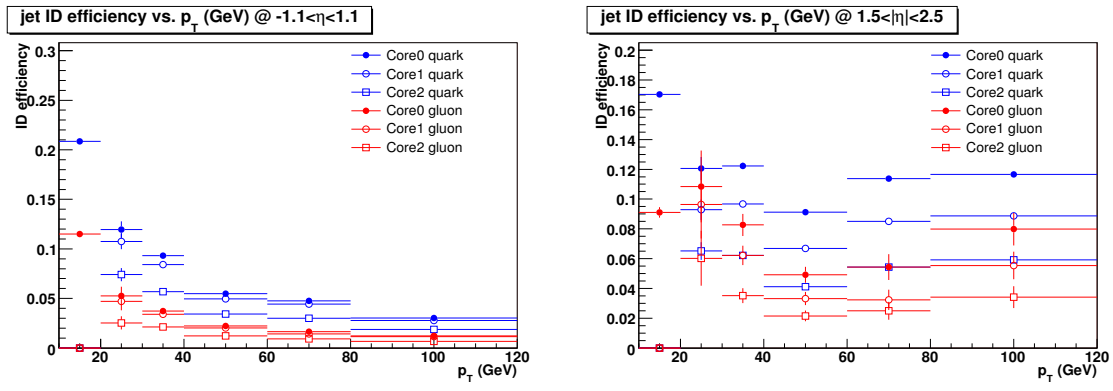

Figure C.55: The efficiency that quark and gluon jets pass the core cuts after satisfying the preselection cuts in the CC (left) and EC (right) regions. This efficiencies are parameterized in p_T [90].

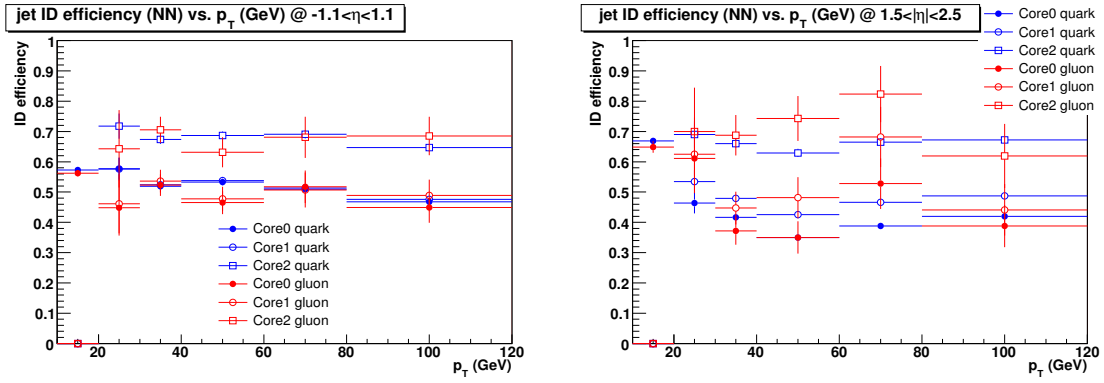

Figure C.56: The efficiency that quark and gluon jets pass O_{NN} (NN output) > 0.6 after satisfying the core cuts in the CC (left) and EC (right) regions. This efficiencies are parameterized in p_T [90].

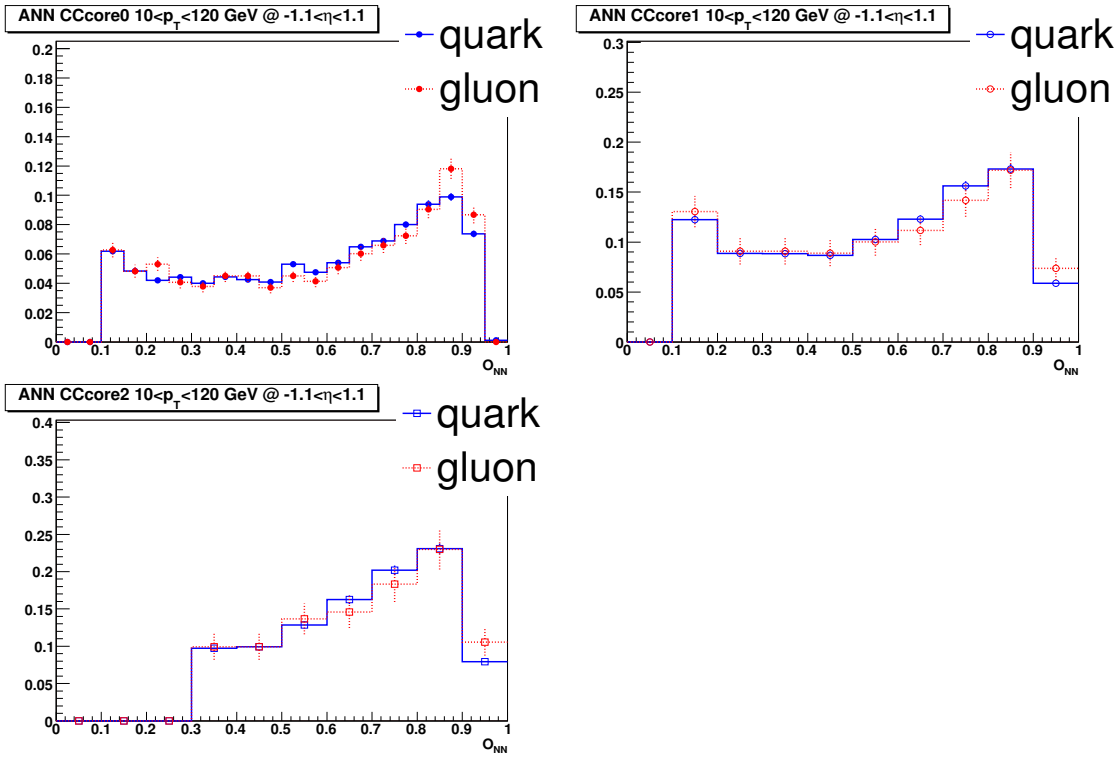

Figure C.57: The distributions of NN output for quark and gluon jets after satisfying the core cuts in CC [90].

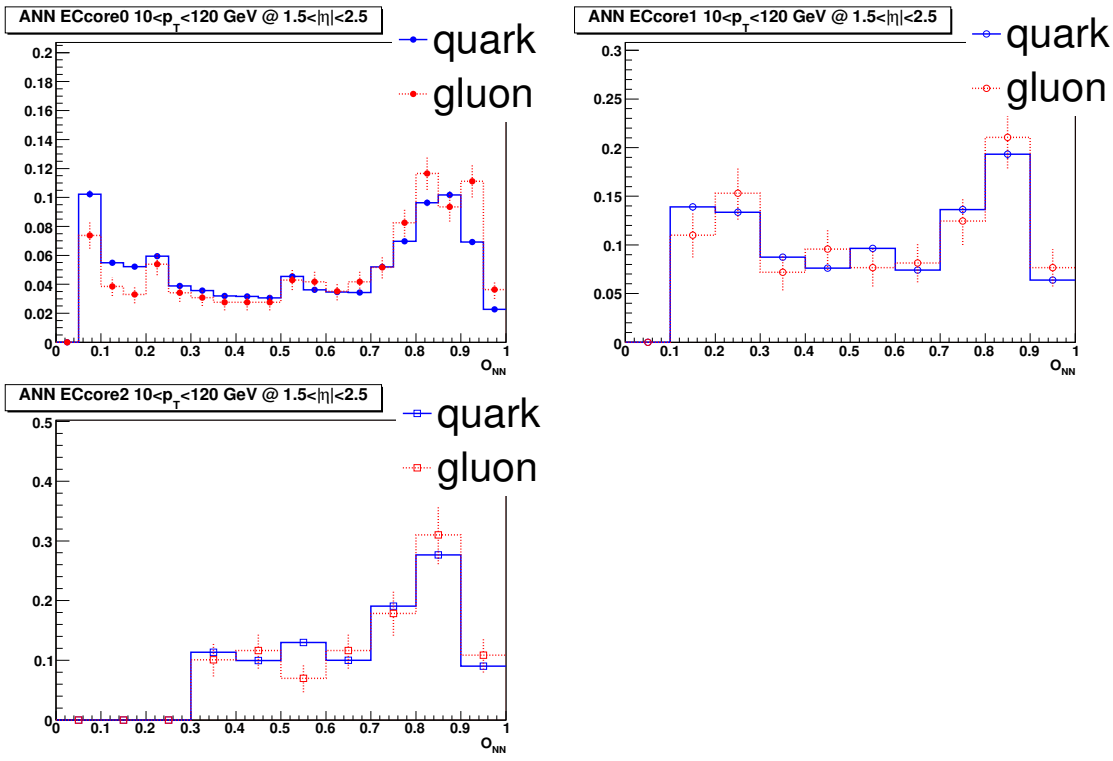

Figure C.58: The distributions of NN output for quark and gluon jets after satisfying the core cuts in EC [90].

APPENDIX D. Discrimination of a Single Photon and a Photon Doublet from π^0 Decay

The neutral pion is the most important background for the selection of single photons due to $\pi^0 \rightarrow \gamma\gamma$ decay and the geometrical coalescing, or overlapping, of the two photons in the DØ calorimeter. Rejecting these $\pi^0 \rightarrow \gamma\gamma$ decay photons relative to single photons is important for raising the purity of a single photon sample. In this note, we introduce two new variables (the energy asymmetry A_E and the dispersion in energy of the two photons, D_z) to discriminate a single photon and a photon doublet from neutral pion decay with CPS detector information.

D.1 Introduction

In a $p\overline{p}$ collider experiment, the π^0 is the important background to high purity single photons. A photon is selected by cuts based on the calorimeter variables, and the DØ EM calorimeter recognizes the di-photon from π^0 decay above 10 GeV as one EM object instead of two due to the small opening angle of the di-photon. Thus this di-photon final state can fake a single photon and lower the purity of single photons. This affects analyses related to final states which have an isolated photon or photons such as H$\rightarrow \gamma\gamma$, SUSY, Zγ and so on. We developed two variables to discriminate a single photon and a photon doublet from π^0 decay using CPS detector information. In this note, we present CPS cluster selection and the performance of the two variables. One is the energy asymmetry (A_E) of two cps clusters and the other is the dispersion of the energies of two Central Pre Shower (CPS) clusters (D_z).

D.2 Data and Monte Carlo samples

D.2.1 Data Samples

For both $Z \to ee$ and $Z\gamma \to ee+\gamma$ event selections, we used the 2EMhighpt skims provided by Common Sample Group [86].

- CSG_CAF_2EMhighpt_PASS4_p21.10.00_p20.12.00
- CSG_CAF_2EMhighpt_PASS4_p21.10.00_p20.12.01
- CSG_CAF_2EMhighpt_PASS4_p21.10.00_p20.12.02
- CSG_CAF_2EMhighpt_PASS4_p21.10.00_p20.12.04
- CSG_CAF_2EMhighpt_PASS4_p21.12.00_p20.12.05_allfix

$Z\gamma \to \mu\mu + \gamma$ events were found in the 2MUhighpt skims [86].

- CSG_CAF_2MUhighpt_PASS4_p21.10.00_p20.12.00
- CSG_CAF_2MUhighpt_PASS4_p21.10.00_p20.12.01
- CSG_CAF_2MUhighpt_PASS4_p21.10.00_p20.12.02
- CSG_CAF_2MUhighpt_PASS4_p21.10.00_p20.12.04
- CSG_CAF_2MUhighpt_PASS4_p21.12.00_p20.12.05_allfix

To check whether the correct invariant mass of the π^0 is reconstructed, the following QCD CSG skims were used [86].

- CSG_CAF_QCD_PASS4_p21.10.00_p20.12.00
- CSG_CAF_QCD_PASS4_p21.10.00_p20.12.01
- CSG_CAF_QCD_PASS4_p21.10.00_p20.12.02
- CSG_CAF_QCD_PASS4_p21.10.00_p20.12.04
- CSG_CAF_QCD_PASS4_p21.12.00_p20.12.05_summer2009

D.2.2 Monte Carlo Samples

First off, this study was conducted with single photons in the QCD direct gamma-gamma sample and π^0s which were extracted from emjet samples. The final states of those samples are apparently from the physics collisions.
Single photon samples are [87]:

- QCD direct gamma-gamma m=15-50 GeV

π^0 samples are [88]:

- p20-pythia_p17.06.02_qcd_emjet_Pt10_20_mcp17
- p20-pythia_p17.06.02_qcd_emjet_Pt20_30_mcp17
- p20-pythia_p17.06.02_qcd_emjet_Pt30_40_mcp17
- p20-pythia_p17.06.02_qcd_emjet_Pt40_60_mcp17
- p20-pythia_p17.06.02_qcd_emjet_Pt60_80_mcp17
- p20-pythia_p17.09.06_qcd_emjet_Pt80_120_mcp17

$Z/\gamma^* \rightarrow ee$ [89]

- $Z/\gamma^* \rightarrow ee$ (m=15-60GeV)

D.2.3 Event Selection

Section D.2.1 and D.2.2 listed data and MC samples that we used for the photon identification development.

D.2.3.1 The selection of photon candidates

In these samples, we required photon candidates in the CC region and three standard photon identification criteria, which are core0, core1 and core2 [90]. The z position of the primary vertex should be $|z| < 60\ cm$.

The common criteria for photon candidates are:

- $-1.1 < \eta_{det} < 1.1,\ \eta$ fiducial region
- The p_T of EM cluster > 10 GeV
- id $= \pm$ 11 or 10

The additional criteria for core0 photon candidates are:

- Isolation < 0.15
- EMfrac > 0.9
- Track isolation < 2.0
- Sigphi < 18
- ANN5 > 0.1

The additional criteria for core1 photon candidates are:

- Isolation < 0.10
- EMfrac > 0.95
- Track isolation < 2.0
- Sigphi < 18
- ANN5 > 0.1

The additional criteria for core2 photon candidates are:

- Isolation < 0.07
- EMfrac > 0.97
- Track isolation < 1.5
- Sigphi < 18
- ANN5 > 0.3

D.2.3.2 CPS cluster selection

The CPS detector plays an important role in distinguishing a single photon and a di-photon final state from π^0 decay. Thus, selecting cps clusters associated with a photon candidate found in the EM calorimeter is the important step in this study. The following paragraph explains how we selected cps clusters.

CPS cluster selection:

- we found all cps clusters in a event.
- The 3D cps clusters whose dR from the selected photon candidate in the EM calorimeter was bigger than 0.1 were rejected.
- Tight cps clusters were selected to reduce fake cps clusters. Tight cps cluster selection was described well in the [91].
  - matchEQ < 1.5.
  - matchQ < 0.7.
  - samlles number of SLC strips is above 2.
  - smallest energy of SLC must exceed 0.007 GeV.
- We selected one or two most energetic cps clusters in accordance with how many 3D cps clusters a photon candidate left in the CPS detector while it passed through the detector.

.

D.3 Validation of the CPS cluster selection

In this section, we would like to validate the CPS cluster selection by investigating reconstructed invariant mass in the π^0 MC samples and measure the opening angle between two CPS clusters to confirm what π^0 energies we can reconstruct correctly.

In Fig. D.1 we show the two-body decay diagrams in the center of mass frame and in the lab frame, respectively.

Figure D.1: The 2-body particle decay in the center of mass frame (left) and in the lab frame (right).

The relation between angles in the center-of-mass frame and the lab frame can be written Eq. D.1, D.2

$$\tan\theta_1' = \frac{\sin\theta_1}{\gamma(\frac{\beta}{\beta^*} + \cos\theta_1)} \tag{D.1}$$

$$\tan\theta_2' = \frac{\sin\theta_2}{\gamma(\frac{\beta}{\beta^*} + \cos\theta_2)} = \frac{\sin\theta_1}{\gamma(\frac{\beta}{\beta^*} - cos\theta_1)} \tag{D.2}$$

If we consider the π^0 rest frame, γ and β can be derived from the energy and the mass of the π^0. $\beta^* = 1$ for photons. If we follow the notation in the Eq. D.1, the opening angle α between two photons from the π^0decay will be $\alpha = \theta_1' + \theta_2'$. Let us look into the opening angle of the di-photon final state from the π^0 decay. If $\cos\theta_1 = 1$, one of the photons goes forward and the other goes backward because the mass of the photon is zero, its backwards velocity is c and the boost of the π^0 to the lab frame can not overcome this. In this case, the opening angle between the two photons is π. This is maximum opening angle of this system. On the other hand, the minimum opening angle occurs for the symmetric decay, $\cos\theta_1 = \cos\theta_2 = 0$ or $\theta_1 = \theta_2 = 90°$. Section D.7 verifies where the minimum opening angle occurs. The table D.1 shows the minimum opening angles corresponding to the individual π^0 energies.

In Figs. D.2, D.3 are shown the distribution of the invariant mass reconstructed by two most energetic CPS clusters and the opening angle of them. The opening angle was found by

Table D.1: The minimum opening angle between the two photons corresponding to each π^0 energy

π^0 energy	θ_1 (rad)	θ_2 (rad)	The min. opening angle α (rad)
10 GeV	0.013	0.013	0.026
20 GeV	0.067	0.067	0.0134
30 GeV	0.0045	0.0045	0.009
40 GeV	0.0034	0.0034	0.0068
50 GeV	0.0027	0.0027	0.0054
60 GeV	0.0023	0.0023	0.0046

the vector dot product.

$$\cos\theta = \frac{\vec{a}\cdot\vec{b}}{|a||b|} \tag{D.3}$$

Let's assume that two photons left two traces as two 3D CPS clusters in the CPS detector when they passed through the detector. We know the positions of two CPS clusters and the primary vertex. If we let two CPS cluster positions and the primary vertex position be (a'_x, a'_y, a'_z), (b'_x, b'_y, b'_z) and $(x_{vtx}, y_{vtx}, z_{vtx})$ respectively, the two vectors $\vec{a}$ and $\vec{b}$ w.r.t. the primary vertex for two CPS clusters will be

$$\vec{a} = (a'_x - x_{vtx})\hat{i} + (a'_y - y_{vtx})\hat{j} + (a'_z - z_{vtx})\hat{k} \tag{D.4}$$

$$\vec{b} = (b'_x - x_{vtx})\hat{i} + (b'_y - y_{vtx})\hat{j} + (b'_z - z_{vtx})\hat{k} \tag{D.5}$$

$$\tag{D.6}$$

and finally, the opening angle measured by the CPS detector will be

$$\theta = \arccos\frac{\vec{a}\cdot\vec{b}}{|a||b|} \; or \; \cos\theta = \frac{\vec{a}\cdot\vec{b}}{|a||b|} \tag{D.7}$$

Due to very small opening angle between two photons from the decay of the π^0 above 10 GeV, they deposit energy as only one EM object in the calorimeter. Thus the energy of the EM object E_{EM} can be assumed to be the π^0energy. From this, we estimate the energy of the individual photon candidates E_i by scaling the EM object energy using the energies of

the CPS clusters E_{CPS1} and E_{CPS2} associated with the EM object as Eq. D.8 .

$$E_i = E_{EM} \frac{E_{CPSi}}{E_{CPS1} + E_{CPS2}} \tag{D.8}$$

where i = 1, 2. The invariant mass of the π^0can be found by the Eq. D.9

$$m_{\gamma\gamma} = \sqrt{2E_1E_2(1 - \cos\theta)} \tag{D.9}$$

The $\cos\theta$ is calculated using Eq. D.7.

The fig. D.2, D.3 show the opening angle and the invariant mass distributions derived by Eq. D.7, D.9

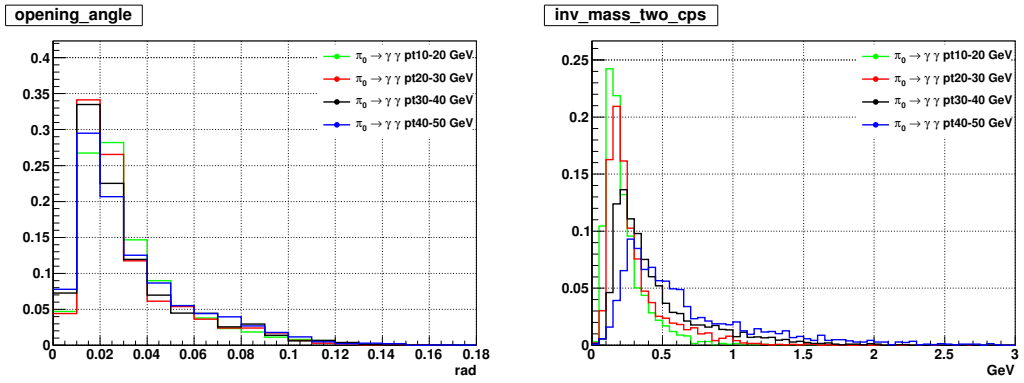

Figure D.2: The opening angles distributions (left) and the invariant mass distributions (right) for the individual π^0energies. The **core0** photon candidates and **no tight cut** for CPS clusters were required.

The core0 photon candidates were selected and we didn't required the tight cut for CPS clusters in fig. D.2 but the tight cut for CPS clusters was included in the fig. D.3. Also fig. D.4 was plotted with the core1 and no tight CPS cut, fig. D.5 with the core1 and the tight CPS cut, fig. D.6 with the core2 and no CPS cut and fig. D.7 with the core2 and the tight CPS cut. If we compare the opening angle distributions to Table D.1, the opening angle of the π^0 between 10 GeV and 30 GeV is well measured by the CPS detector for both the tight CPS cut and no tight cut but the other energy range of the π^0 has the same angle peak in 0.01 rad. According to Table D.1, the opening angles should be less than 0.01 rad for the π^0 energy above 30 GeV. This explains why we have reasonable invariant mass peaks below 30 GeV for both the tight

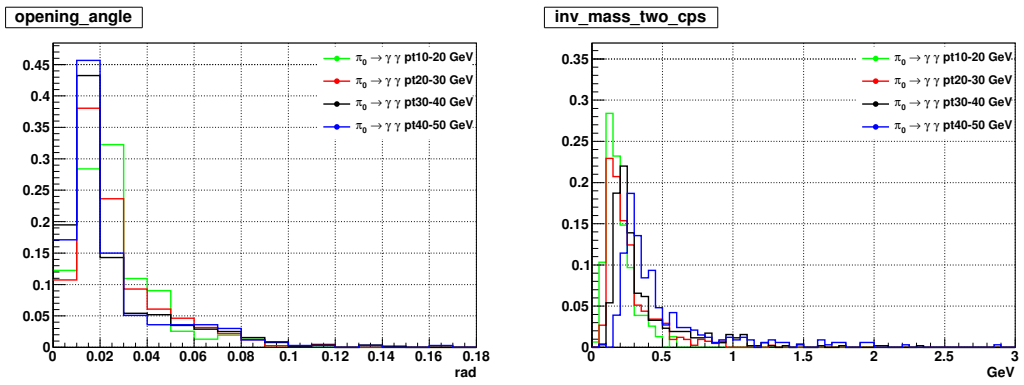

Figure D.3: The opening angles distributions (left) and the invariant mass distributions (right) for the individual π^0energies. The **core0** photon candidates and **tight cut** for CPS clusters were required.

CPS cluster cut and no tight cut but invariant mass peaks are above the π^0 mass when its energies are above 30 GeV. This demonstrates that we can reconstruct the π^0 mass correctly for the π^0energy below 30 GeV. Thus we will consider the acceptance of single photons and the rejection for the π^0 between 10 GeV and 30 GeV for the tight CPS cluster cut and no tight cut.

The final step for the CPS cluster validation is to check the performance in QCD data. We reconstructed the invariant mass with core0 photon candidates in the CC region between 10 and 30 GeV. Both tight and no tight CPS cluster cut were considered. The invariant mass distributions are shown in the fig. D.8. The invariant mass peaks for both tight and no tight CPS cluster cut are located in the π^0 mass. We could conclude that these CPS cluster selection worked well for the extraction of the π^0candidates. We go forward to the discrimination of single photons and photon doublets from the π^0decay with the energy asymmetry and the energy dispersion of two selected CPS clusters.

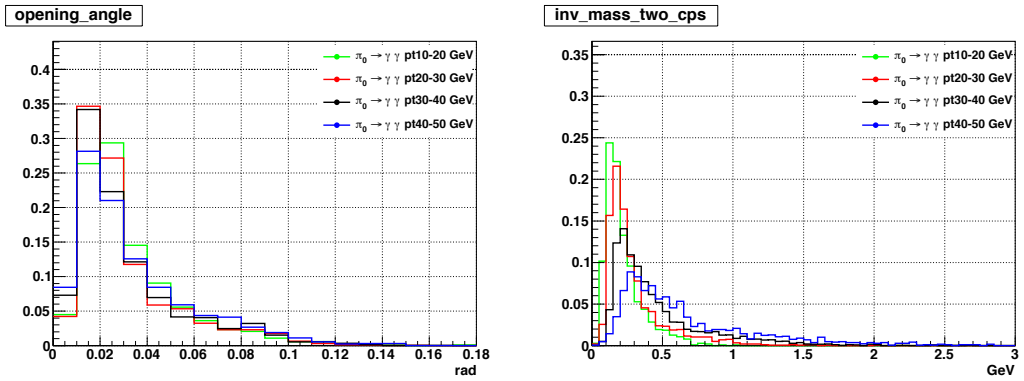

Figure D.4: The opening angles distributions (left) and the invariant mass distributions (right) for the individual π^0energies. The **core1** photon candidates and **no tight cut** for CPS clusters were required.

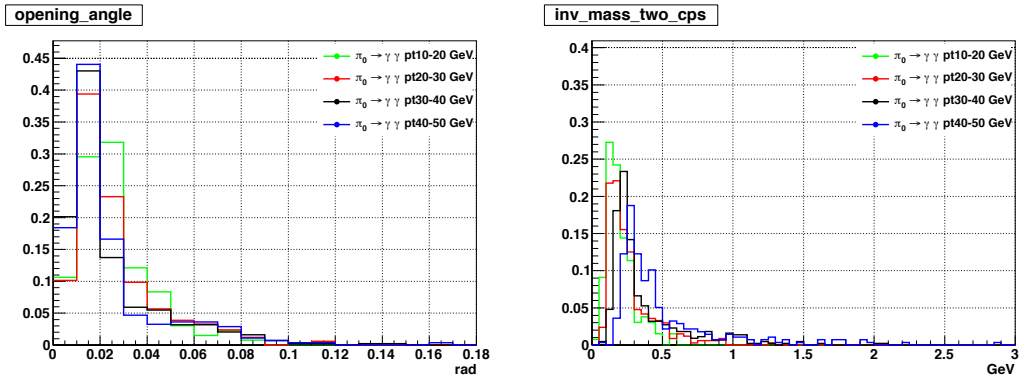

Figure D.5: The opening angles distributions (left) and the invariant mass distributions (right) for the individual π^0energies. The **core1** photon candidates and **tight cut** for CPS clusters were required.

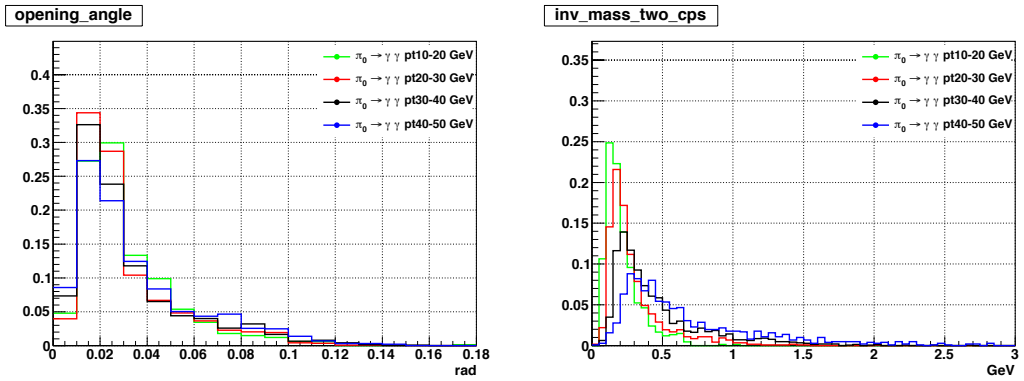

Figure D.6: The opening angles distributions (left) and the invariant mass distributions (right) for the individual π^0energies. The **core2** photon candidates and **no tight cut** for CPS clusters were required.

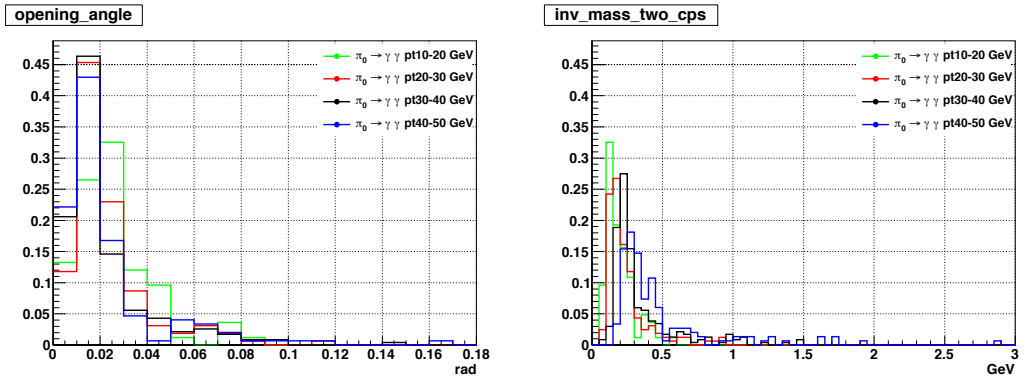

Figure D.7: The opening angles distributions (left) and the invariant mass distributions (right) for the individual π^0energies. The **core2** photon candidates and **tight cut** for CPS clusters were required.

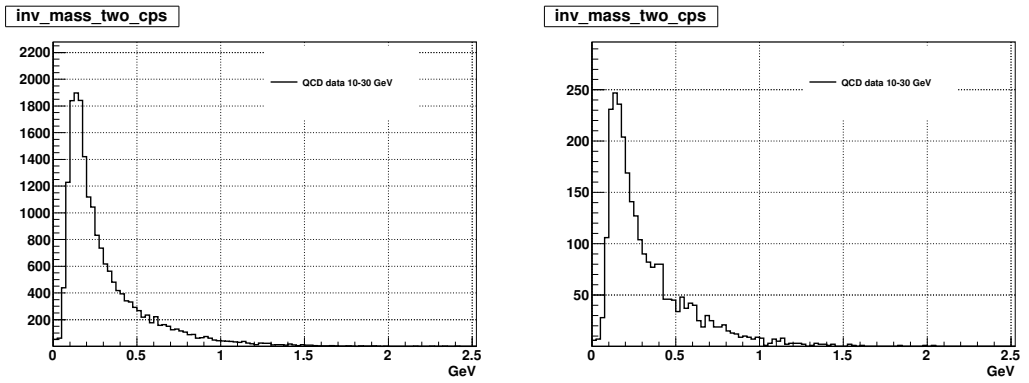

Figure D.8: Invariant mass distributions by two CPS clusters in QCD data described in the section D.2.1. Photon candidates are **core0 in the CC region** and $10 < p_T < 30GeV$. The **tight CPS cluster cut was not required (left) and required (right)**.

D.4 The performance of the new variables

We consider two variables for discriminating single photons and a photon doublets from the π^0 decay, which are the energy asymmetry of one or two CPS clusters and the dispersion of CPS clusters energy.

The fig. D.9 are the number of CPS clusters before and after the tight CPS cluster cut for 10 - 20 GeV single photons and π^0s which were selected as core0 photon. The fig. D.9 tells the number of photon candidates which have two or more CPS clusters is reduced significantly by the tight CPS cluster cut. For example, if we assume that a photon candidate has two cps clusters, it has two CPS clusters before the tight CPS cluster cut. After applying the tight cut, only one of two clusters passes the cut but the other CPS cluster is rejected by cut. Thus this event comes to have only one CPS cluster. This is why the tight CPS cluster cut reduces the number of photon candidates which have two or more CPS clusters.

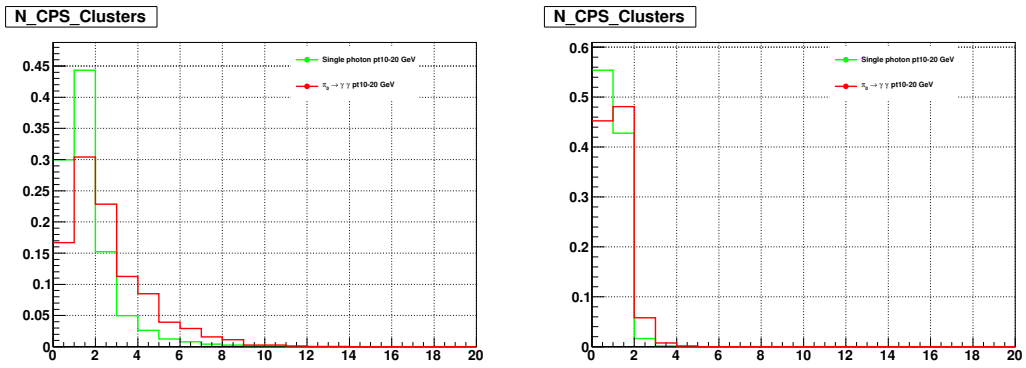

Figure D.9: The number of CPS clusters before the tight CPS cluster cut (letf) and after the tight cut (right). The core0 photon candidates between 10 and 20 GeV were used.

To verify this statement, we investigated the number of photon candidates before and after the tight CPS cluster cut with the CCcore0 photon candidates. In the Table D.2, the first row in the 10-20 GeV row is the number of photon candidates before the tight CPS cluster cut. The total number of photon candidates is 1943, the number of photon candidates which have only 1 CPS cluster and 2 or more CPS clusters are 709 and 1234, respectively. The second

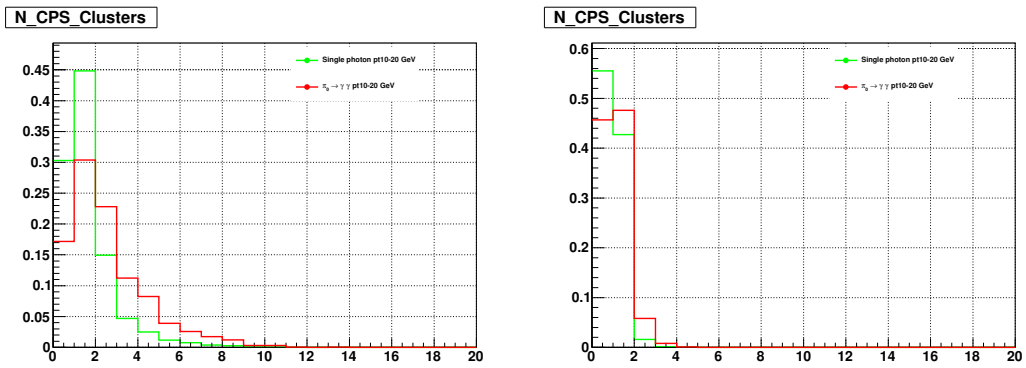

Figure D.10: The number of CPS clusters before the tight CPS cluster cut (letf) and after the tight cut (right). The core1 photon candidates between 10 and 20 GeV were used.

row shows rejected number of photon candidates by the tight CPS cluster cut. 482 photon candidates which have only one CPS cluster and 184 which have 2 or more CPS clusters were thrown away by the tight CPS cluster cut. Subtracting the second row (2) from the first row (1) results in the third row. These numbers in the third row are the reduced number by the cut. By the way, as we can know in the fig. D.9, we can anticipate some photon candidates which have 2 or more CPS clusters become those which have only one CPS cluster by the cut. The fourth row tells about this number of photon candidates. 895 photon candidates which have 2 or more CPS clusters become those which have only one CPS cluster. Finally, the total number of photon candidates is 1277 and the number of photon candidates which have one and 2 or more CPS clusters are 1122 and 155 after the tight CPS cluster cut. 895 out of 1234 photon candidates come to have one CPS cluster from 2 or more. 72.5 % of photon candidates which have 2 or more CPS clusters was changed to photon candidates which have one CPS cluster. The row for the 20-30 GeV can be understood like the row for the 10-20 GeV. For this 20-30 GeV, 83.5 % is changed to photon candidates which have one CPS cluster. These 72.5 % and 83.5 % are not small number and the tight CPS cluster cut will reduce the discrimination power of the variables significantly that we would like to use, which will be shown in the section D.4.1, D.4.2. The core1 and the core2 photon candidates also have same behavior as the core0 according to the fig. D.10, D.11. However, as we could see the plots in

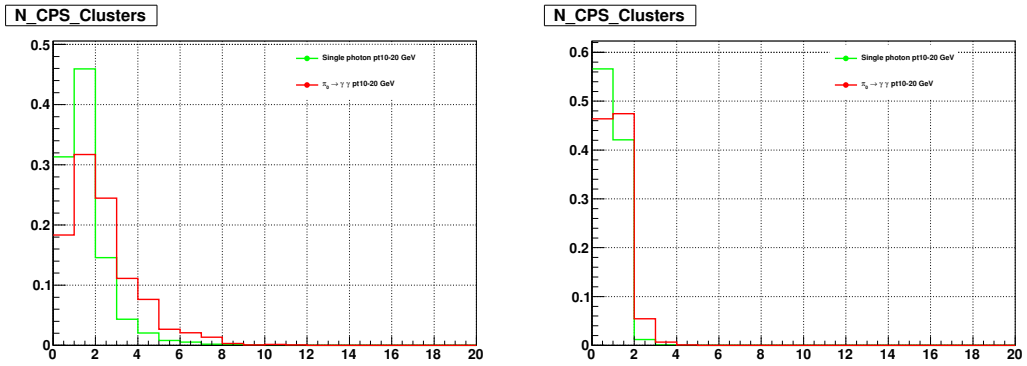

Figure D.11: The number of CPS clusters before the tight CPS cluster cut (letf) and after the tight cut (right). The core2 photon candidates between 10 and 20 GeV were used.

Table D.2: The number of photon candidates before and after the tight CPS cluster cut for the π^0 sample.

Energy		Total	1 CPS cluster	≥2 CPS clusters
10-20 GeV	Before the tight CPS cluster cut — (1)	1943	709	1234
	Rejected # of photon candidates by the tight CPS cluster cut — (2)	666	482	184
	(1) - (2)	1277	227	1050
	# of photon candidates whose # of CPS clusters are changed from ≥2 to 1		+895	-895
	# of photon candidates after the tight CPS cluster cut	1277	1122	155
20-30 GeV	Before tight CPS cluster cut — (3)	3962	1480	2482
	Rejected # of photon candidates by the tight CPS cluster cut — (4)	1116	1116	0
	(3) - (4)	2846	364	2482
	# of photon candidates whose # of CPS clusters are changed from ≥2 to 1		+2072	-2072
	# of photon candidates after the tight CPS cluster cut	2846	2436	410

the section D.3, both the tight and no tight CPS cluster cuts gave us reasonable opening angle and invariant mass distributions in the range of 10 - 30 GeV. So we consider the acceptance of single photons, π^0 rejection rate and compare efficiencies for both cases.

D.4.1 The energy asymmetry of one or two CPS clusters

As explained in the section D.2.3.2, we selected one or two most energetic CPS clusters. When a photon candidate has one CPS cluster, the asymmetry is 1 and if there are two CPS

clusters associated with a photon candidate, it is derived by the Eq. D.10.

$$A_{CPS} = \frac{E_{CPS1} - E_{CPS2}}{E_{CPS1} + E_{CPS2}} \tag{D.10}$$

As we can anticipate, naively, a single photon would leave one CPS cluster in the CPS detector while the π^0 two CPS clusters. This means that a single photon have mostly the asymmetry 1 but the π^0less than 1. By this anticipation and considering all of the asymmetry distributions, we picked 0.99 as a cut value to reject π^0s and then calculated the acceptance of single photons and the rejection of π^0s using Eq. D.11. Single photons above 0.99 were accepted and π^0s below 0.99 rejected.

$$Acceptance\ of\ single\ photon \quad = \frac{the\ number\ of\ accepted\ single\ photons\ by\ a\ cut\ value}{the\ total\ number\ of\ single\ photons} \tag{D.11}$$

$$Rejection\ of\ \pi^0 \quad = \frac{the\ number\ of\ rejected\ \pi^0 s\ by\ a\ cut\ value}{the\ total\ number\ of\ \pi^0 s} \tag{D.12}$$

The Table. D.3 classifies the energy range of photon candidates, which core cut and whether the tight CPS cluster cut are applied or not. The Table. D.4 includes the acceptance of single photons and the rejection of photon doublets from the π^0decay for all cases which are mentioned in the Table. D.3.

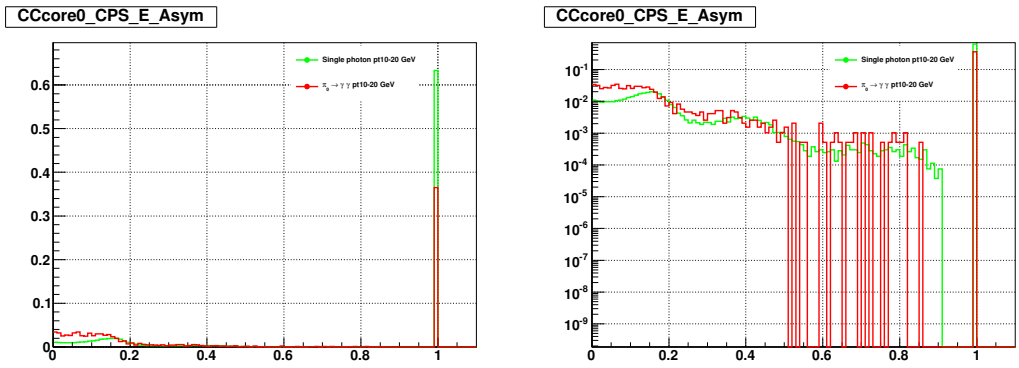

Figure D.12: The asymmetry distribution of cps clusters energies (letf) and the log scaled plot of the left (right). The tight CPS cluster was not required. CCcore0, 10 GeV $< p_T <$ 20 GeV.

The acceptance of single photons and the rejection of photon doublets from the π^0 decay are in the Table D.4. On average over all energy range and photon IDs, the acceptance of

Table D.3: Energy range and applied cuts for the asymmetry distribution figures.

	Energy	Photon ID cut	Tight CPS cluster
Fig.D.12	10-20 GeV	core0	No
Fig.D.13	10-20 GeV	core0	Yes
Fig.D.14	20-30 GeV	core0	No
Fig.D.15	20-30 GeV	core0	Yes
Fig.D.16	10-20 GeV	core1	No
Fig.D.17	10-20 GeV	core1	Yes
Fig.D.18	20-30 GeV	core1	No
Fig.D.19	20-30 GeV	core1	Yes
Fig.D.20	10-20 GeV	core2	No
Fig.D.21	10-20 GeV	core2	Yes
Fig.D.22	20-30 GeV	core2	No
Fig.D.23	20-30 GeV	core2	Yes

single photons is 63.5 % and the rejection of the π^0 is 61.8 % for the no tight CPS cluster cut but they are 95.5 % and 12.7 % for the tight CPS cluster cut, respectively. The tight CPS cluster cut kills the fake CPS clusters but it reduces the π^0rejection significantly. It rejects the second CPS cluster although it is a real CPS cluster from the π^0 decay and many π^0s come to have only one CPS cluster. This results in single photons can be contaminated seriously by $\pi^0$when we apply the tight CPS cluster cut as we can know from the fig. D.9, D.10, D.11 and the π^0rejection in the Table D.4. However, the tight CPS cluster cut will select EM-like cps clusters with higher probability instead that we select fake ones. This helps reconstruct purer π^0 invariant mass.

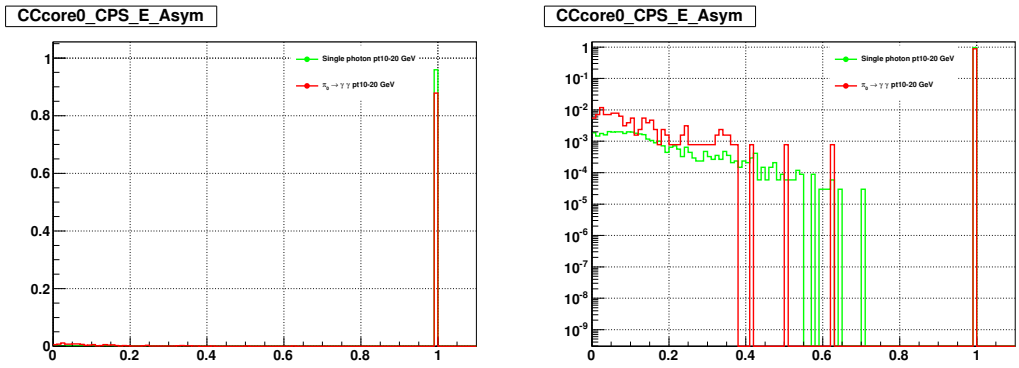

Figure D.13: The asymmetry distribution of cps clusters energies (letf) and the log scaled plot of the left (right). The tight cut for cps clusters was required. CCcore0, 10 GeV $< p_T <$ 20 GeV.

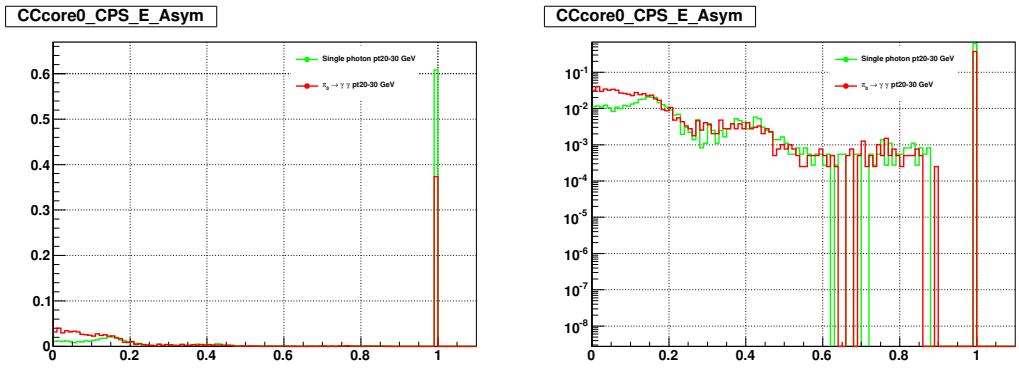

Figure D.14: The asymmetry distribution of cps clusters energies (letf) and the log scaled plot of the left (right). The tight cut for cps clusters was not required. CCcore0, 20 GeV $< p_T <$ 30 GeV.

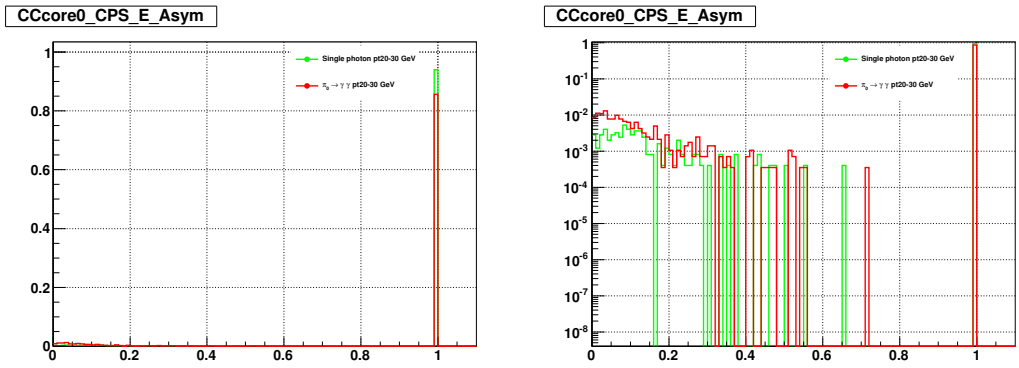

Figure D.15: The asymmetry distribution of cps clusters energies (letf) and the log scaled plot of the left (right). The tight cut for cps clusters was required. CCcore0, 20 GeV $< p_T <$ 30 GeV.

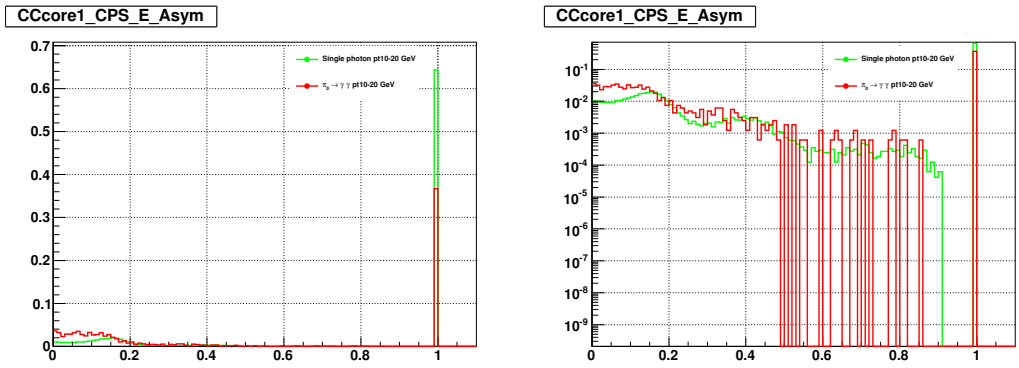

Figure D.16: The asymmetry distribution of cps clusters energies (letf) and the log scaled plot of the left (right). The tight cut for cps clusters was not required. CCcore1, 10 GeV $< p_T <$ 20 GeV.

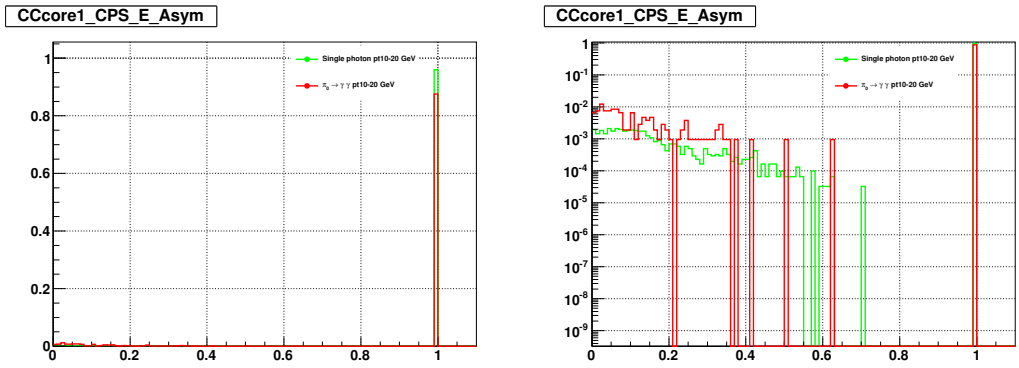

Figure D.17: The asymmetry distribution of cps clusters energies (letf) and the log scaled plot of the left (right). The tight cut for cps clusters was required. CCcore1, 10 GeV $< p_T <$ 20 GeV.

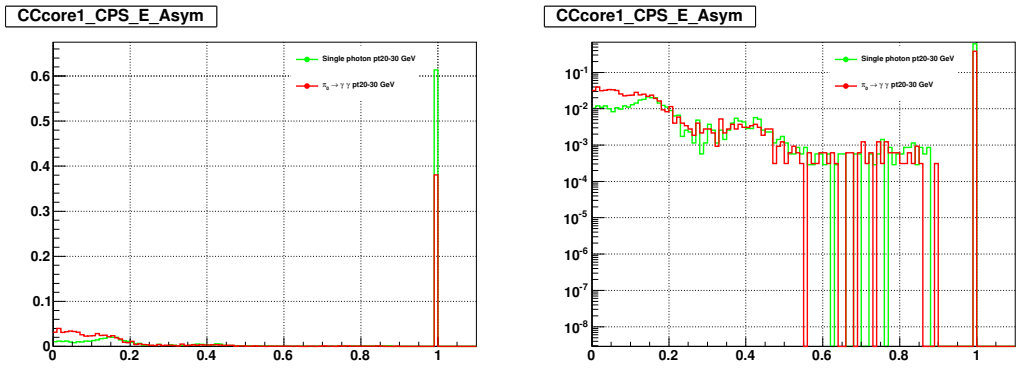

Figure D.18: The asymmetry distribution of cps clusters energies (letf) and the log scaled plot of the left (right). The tight cut for cps clusters was not required. CCcore1, 20 GeV $< p_T <$ 30 GeV.

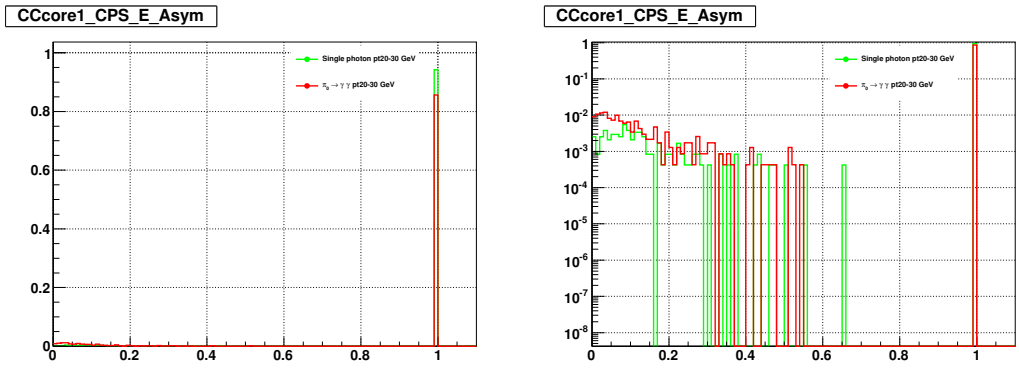

Figure D.19: The asymmetry distribution of cps clusters energies (letf) and the log scaled plot of the left (right). The tight cut for cps clusters was required. CCcore1, 20 GeV $< p_T <$ 30 GeV.

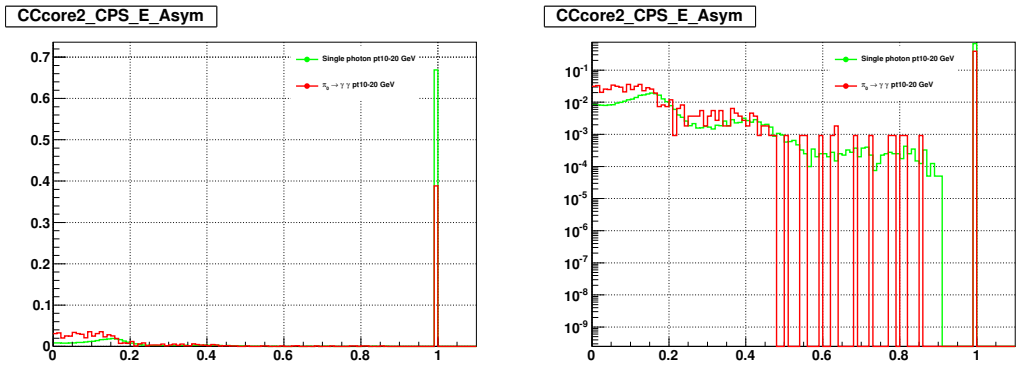

Figure D.20: The asymmetry distribution of cps clusters energies (letf) and the log scaled plot of the left (right). The tight cut for cps clusters was not required. CCcore2, 10 GeV $< p_T <$ 20 GeV.

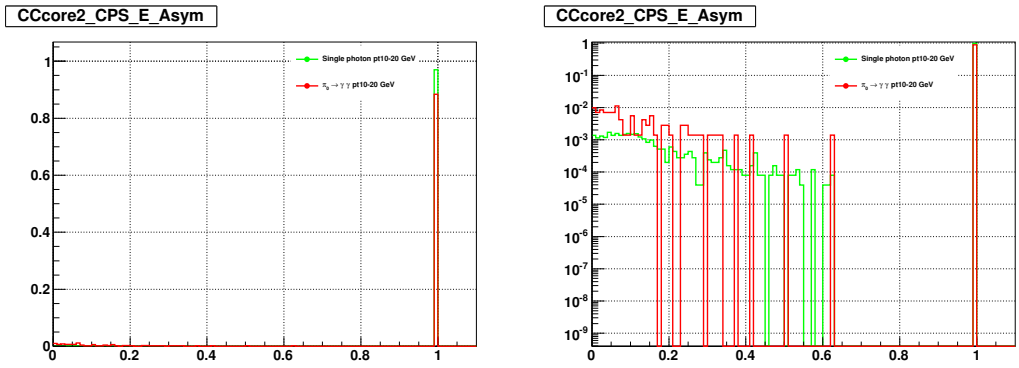

Figure D.21: The asymmetry distribution of cps clusters energies (letf) and the log scaled plot of the left (right). The tight cut for cps clusters was required. CCcore2, 10 GeV $< p_T <$ 20 GeV.

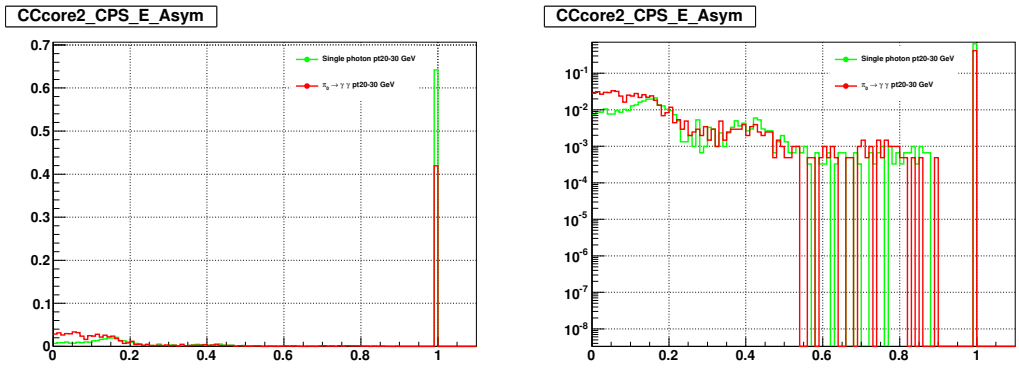

Figure D.22: The asymmetry distribution of cps clusters energies (letf) and the log scaled plot of the left (right). The tight cut for cps clusters was not required. CCcore2, 20 GeV $< p_T <$ 30 GeV.

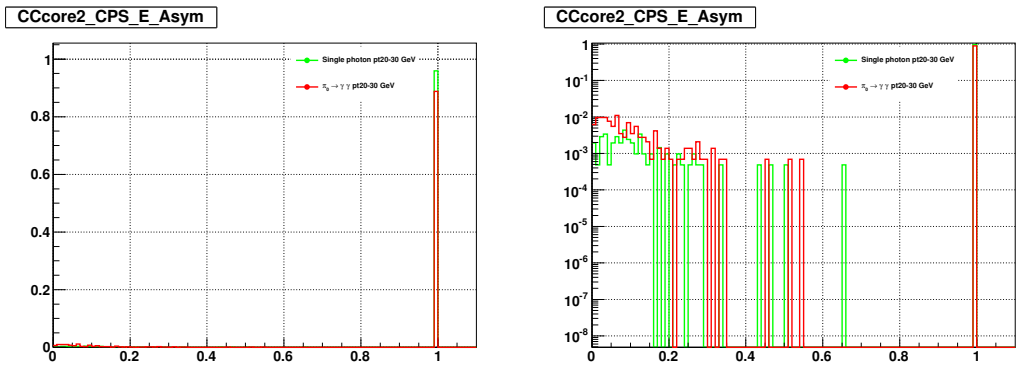

Figure D.23: The asymmetry distribution of cps clusters energies (letf) and the log scaled plot of the left (right). The tight cut for cps clusters was required. CCcore2, 20 GeV $< p_T <$ 30 GeV.

Table D.4: The acceptance of single photons and the rejection of the $\pi^0$by the asymmetry of the CPS clusters energies

Energy	Photon ID	Tight CPS cluster	The acceptance of single photons (%)	The rejection of the π^0 (%)
10-20 GeV	core0	No	63.3	63.5
10-20 GeV	core0	Yes	95.9	12.1
20-30 GeV	core0	No	60.8	62.6
20-30 GeV	core0	Yes	94.0	14.4
10-20 GeV	core1	No	64.3	63.3
10-20 GeV	core1	Yes	96.0	12.4
20-30 GeV	core1	No	61.4	61.9
20-30 GeV	core1	Yes	94.2	14.4
10-20 GeV	core2	No	66.9	61.2
10-20 GeV	core2	Yes	97.0	11.6
20-30 GeV	core2	No	64.2	58.1
20-30 GeV	core2	Yes	95.9	11.2

D.4.2 The dispersion of CPS cluster energies

The second variable for the discrimination of single photons and π^0s is the dispersion, D. The dispersion that we looked in this note represents the energy distribution of the CPS clusters along a selected axis.

$$D = \frac{\sum E_i x_i^2}{\sum E_i} - (\frac{\sum E_i x_i}{\sum E_i})^2 \tag{D.13}$$

where E_i is the energy of the i_{th} cluster, x_i is the x position of the i_{th} cluster. The x can be extended to y or z coordinates. The Eq. D.13 tells that D will have bigger value if the CPS clusters are dispersed broadly. In other words, the π^0which has two photons final state would have bigger D than a single photon. The figures in this section show that the second peak occurs for the π^0. Even though the height of the second peak is not high as compared with the first peak at 0, the second peak of the $\pi^0$is higher than that of single photon. This also give us a discrimination power. We picked 0.25 for cut value, which distinguishes the first peak and the second peak. The acceptance of single photons and the rejection of the π^0s were found by Eq. D.11 The Table. D.5 classifies the energy range of photon candidates, which core cut and whether the tigh CPS cluster cut were applied or not.

Table D.5: Energy range and applied cuts for the asymmetry distribution figures.

	Energy	Photon ID cut	Tight CPS cluster
Fig.D.24	10-20 GeV	core0	No
Fig.D.25	10-20 GeV	core0	Yes
Fig.D.26	20-30 GeV	core0	No
Fig.D.27	20-30 GeV	core0	Yes
Fig.D.28	10-20 GeV	core1	No
Fig.D.29	10-20 GeV	core1	Yes
Fig.D.30	20-30 GeV	core1	No
Fig.D.31	20-30 GeV	core1	Yes
Fig.D.32	10-20 GeV	core2	No
Fig.D.33	10-20 GeV	core2	Yes
Fig.D.34	20-30 GeV	core2	No
Fig.D.35	20-30 GeV	core2	Yes

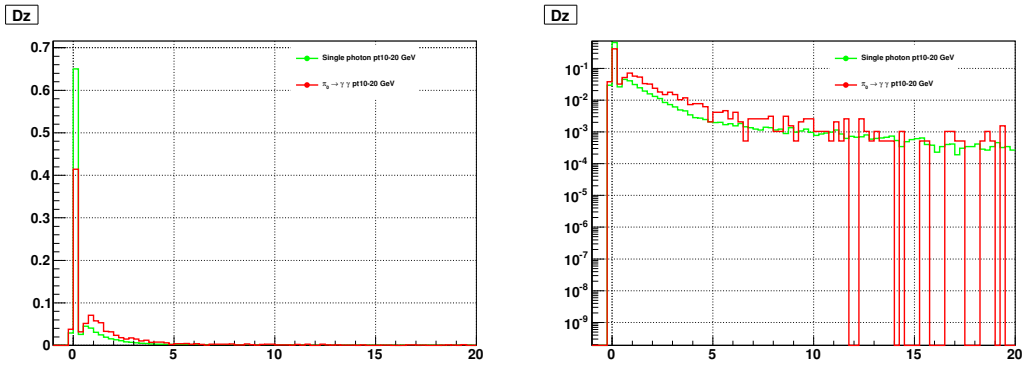

Figure D.24: The dispersion of cps clusters energies (letf) and the log scaled plot of the left (right). The tight cut for cps clusters was not required. CCcore0, 10 GeV $< p_T <$ 20 GeV.

The acceptance of single photons and the rejection of photon doublets from the π^0 decay are in the Table D.6. On average over all energy range and photon IDs, the acceptance of single photons is 67.4 % and the rejection of the π^0 is 53.2 % for the no tight CPS cluster cut but they are 95.5 % and 12.7 % for the tight CPS cluster cut, respectively. In this case, we can see the tight CPS cluster reduces the rejection of the π^0 too like the case of the asymmetry of the energy of the CPS clusters.

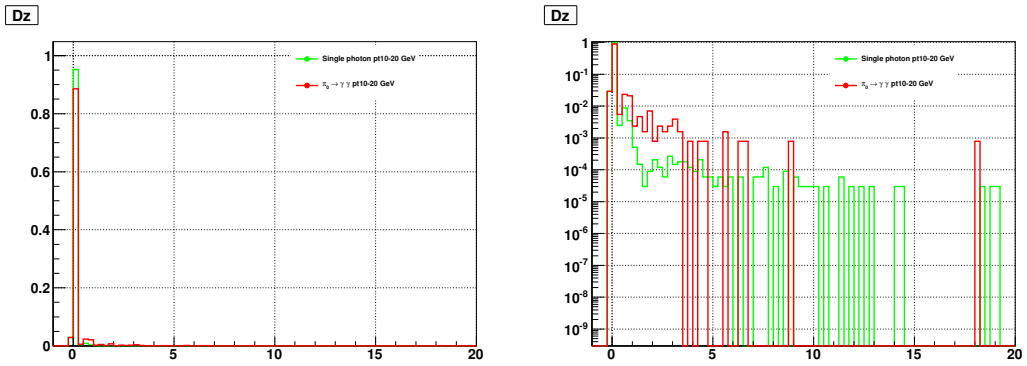

Figure D.25: The dispersion of cps clusters energies (letf) and the log scaled plot of the left (right). The tight cut for cps clusters was required. CCcore0, 10 GeV $< p_T <$ 20 GeV.

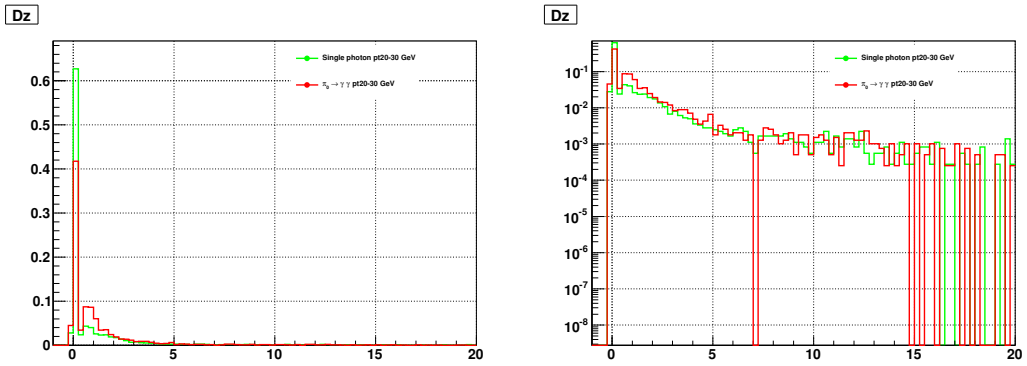

Figure D.26: The dispersion of cps clusters energies (letf) and the log scaled plot of the left (right). The tight cut for cps clusters was not required. CCcore0, 20 GeV $< p_T <$ 30 GeV.

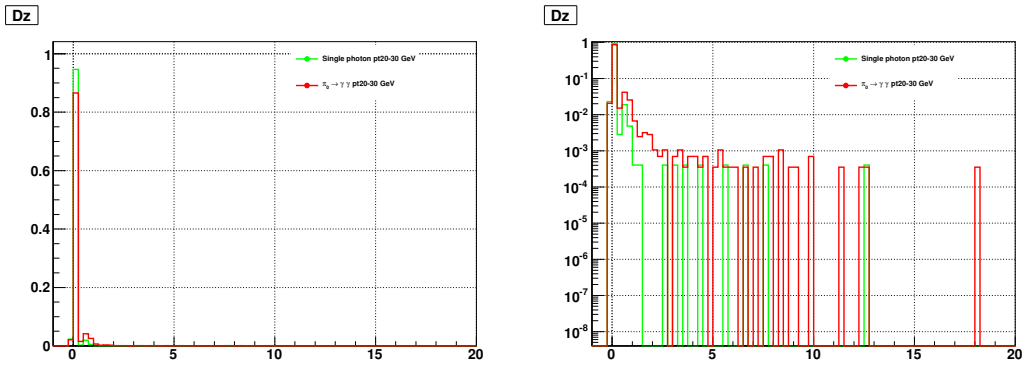

Figure D.27: The dispersion of cps clusters energies (letf) and the log scaled plot of the left (right). The tight cut for cps clusters was required. CCcore0, 30 GeV $< p_T <$ 30 GeV.

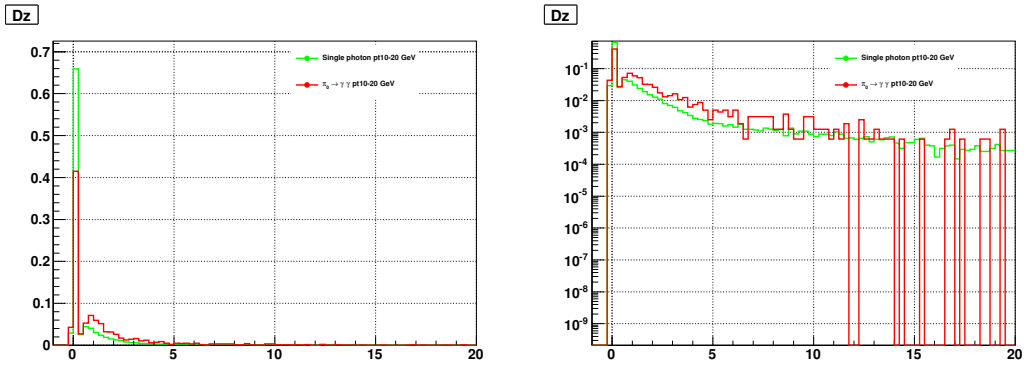

Figure D.28: The dispersion of cps clusters energies (letf) and the log scaled plot of the left (right). The tight cut for cps clusters was not required. CCcore1, 10 GeV $< p_T <$ 20 GeV.

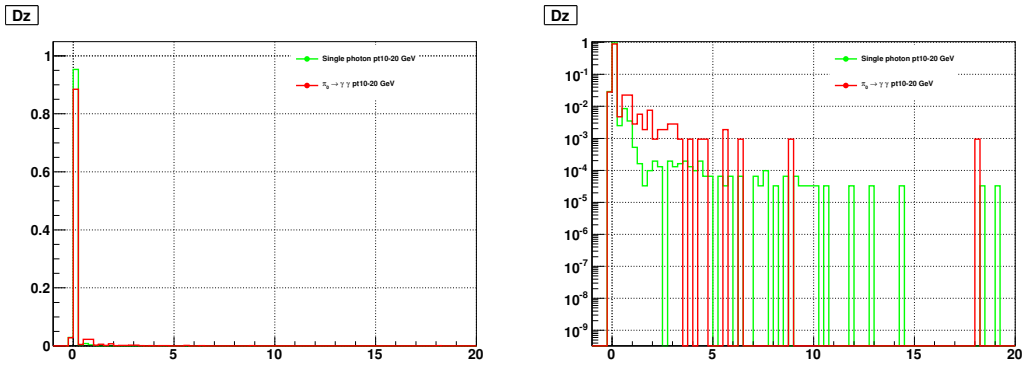

Figure D.29: The dispersion of cps clusters energies (letf) and the log scaled plot of the left (right). The tight cut for cps clusters was required. CCcore1, 10 GeV $< p_T <$ 20 GeV.

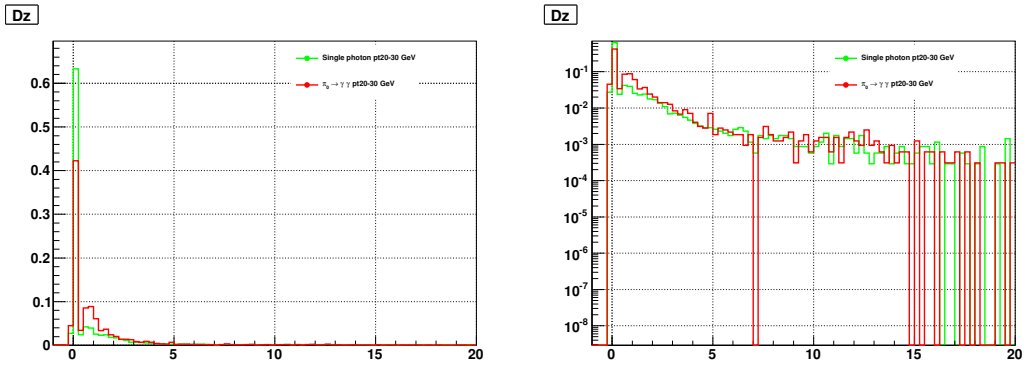

Figure D.30: The dispersion of cps clusters energies (letf) and the log scaled plot of the left (right). The tight cut for cps clusters was not required. CCcore1, 20 GeV $< p_T <$ 30 GeV.

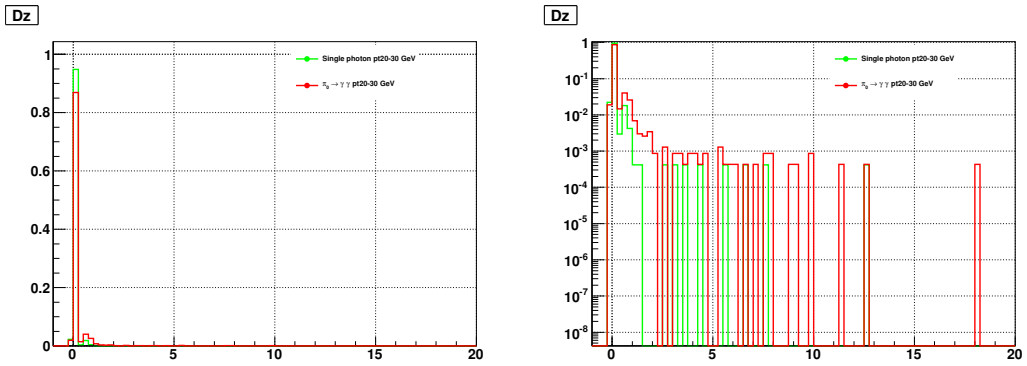

Figure D.31: The dispersion of cps clusters energies (letf) and the log scaled plot of the left (right). The tight cut for cps clusters was required. CCcore1, 20 GeV $< p_T <$ 30 GeV.

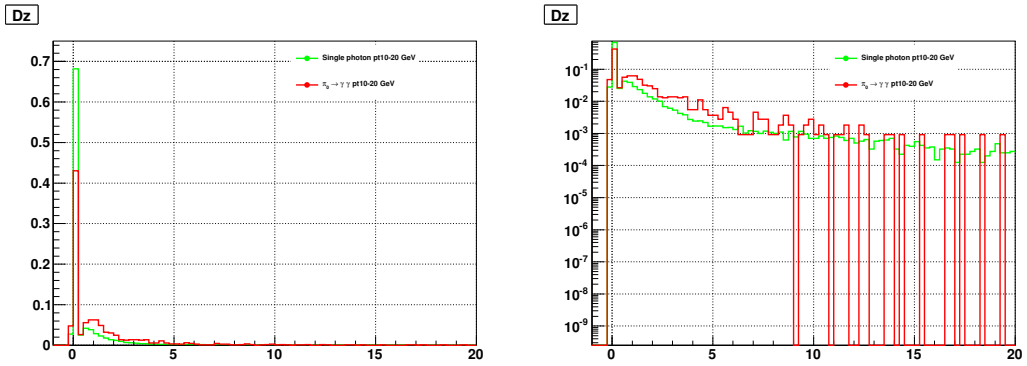

Figure D.32: The dispersion of cps clusters energies (letf) and the log scaled plot of the left (right). The tight cut for cps clusters was not required. CCcore2, 10 GeV $< p_T <$ 20 GeV.

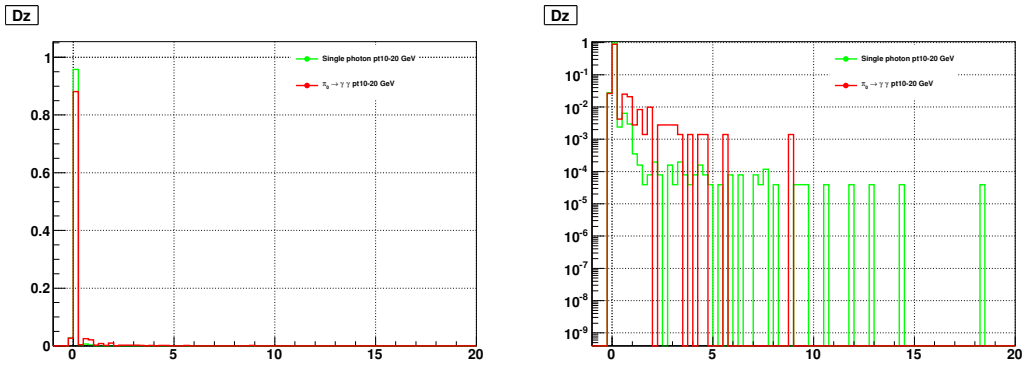

Figure D.33: The dispersion of cps clusters energies (letf) and the log scaled plot of the left (right). The tight cut for cps clusters was required. CCcore2, 10 GeV $< p_T <$ 20 GeV.

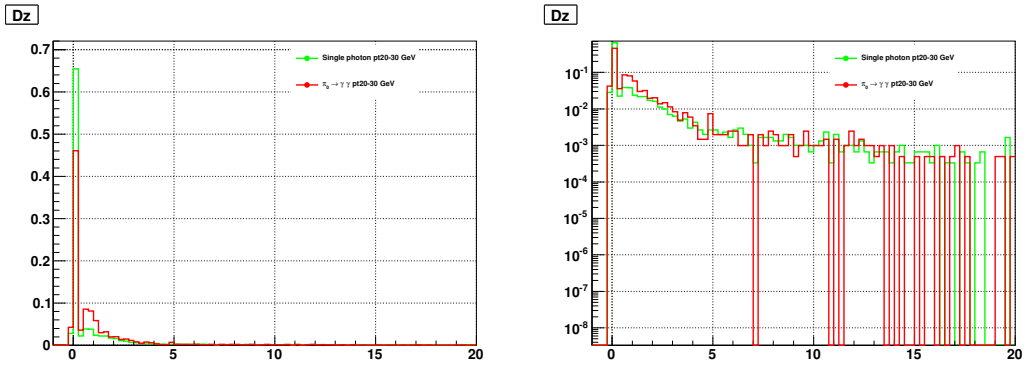

Figure D.34: The dispersion of cps clusters energies (letf) and the log scaled plot of the left (right). The tight cut for cps clusters was not required. CCcore2, 20 GeV $< p_T <$ 30 GeV.

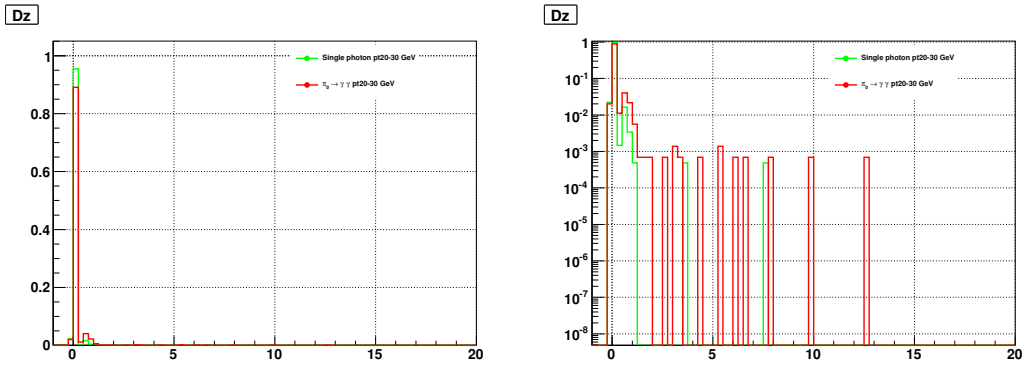

Figure D.35: The dispersion of cps clusters energies (letf) and the log scaled plot of the left (right). The tight cut for cps clusters was required. CCcore2, 20 GeV $< p_T <$ 30 GeV.

Table D.6: The acceptance of single photons and the rejection of the $\pi^0$by the dispersion of the CPS clusters energies

Energy	Photon ID	Tight CPS cluster	The acceptance of single photons (%)	The rejection of the π^0 (%)
10-20 GeV	core0	No	67.4	55.0
10-20 GeV	core0	Yes	98.2	8.6
20-30 GeV	core0	No	65.0	54.0
20-30 GeV	core0	Yes	96.9	11.3
10-20 GeV	core1	No	68.4	54.4
10-20 GeV	core1	Yes	98.2	8.8
20-30 GeV	core1	No	65.5	53.5
20-30 GeV	core1	Yes	97.1	11.2
10-20 GeV	core2	No	70.5	52.4
10-20 GeV	core2	Yes	98.6	9.3
20-30 GeV	core2	No	67.8	49.9
20-30 GeV	core2	Yes	97.7	8.9

D.5 The response of the new variables in Data

In this section, we would like to show the performance of the new variables in $Z\gamma \to ee + \gamma$ and $Z\gamma \to \mu\mu + \gamma$ as well as Zee Data and MC. According to the section D.4, the tight CPS cluster cut tends to change photon candidates which have two CPS clusters into those which have one CPS cluster. The second CPS cluster is rejected by the tight CPS cluster cut even thought it is real one generated by one of two photons from the π^0 decay. Finally, we could see the tight CPS cluster cut reduced the rejection of the π^0. To avoid this situation in the looking of real data and since we could confirm that the invariant mass reconstruction and the measurement of opening angle for the π^0worked well without the tight CPS cluster cut, we didn't require the tight CPS cluster cut and selected just one or two most energetic CPS clusters and the core0 photon candidates for better statistics. However, we also show the result by the tight CPS cluster cut.

D.5.1 The performance of the new variables in Zee Data and MC

As described in the section D.2.1and D.2.2, the 2EMhighpt data and the $Z/\gamma^* \to ee$ MC sample were used.

Table D.7: The acceptance of Zee Data and MC by the energy asymmetry (>0.99) and the Dz (<0.25). The tight CPS cluster cut was not required.

		Energy	Photon ID	Tight CPS cluster	The acceptance (%)
The energy asymmetry of CPS clusters	Data	10-30 GeV	core0	No	51.4
	MC	10-30 GeV	core0	No	57.8
The dispersion of CPS clusters energy	Data	10-30 GeV	core0	No	59.1
	MC	10-30 GeV	core0	No	63.8

The number of CPS clusters, the invariant mass distributions, the energy asymmetry and the dispersion of CPS clusters in fig. D.36, D.37 have fair Data and MC agreement. Based on this agreement, we measured the acceptances using the energy asymmetry and the dispersion of CPS clusters. Table. D.7, D.8 show the acceptances by the energy asymmetry and the dispersion of CPS cluster in Data and MC. When we required the tight CPS cluster cut, the

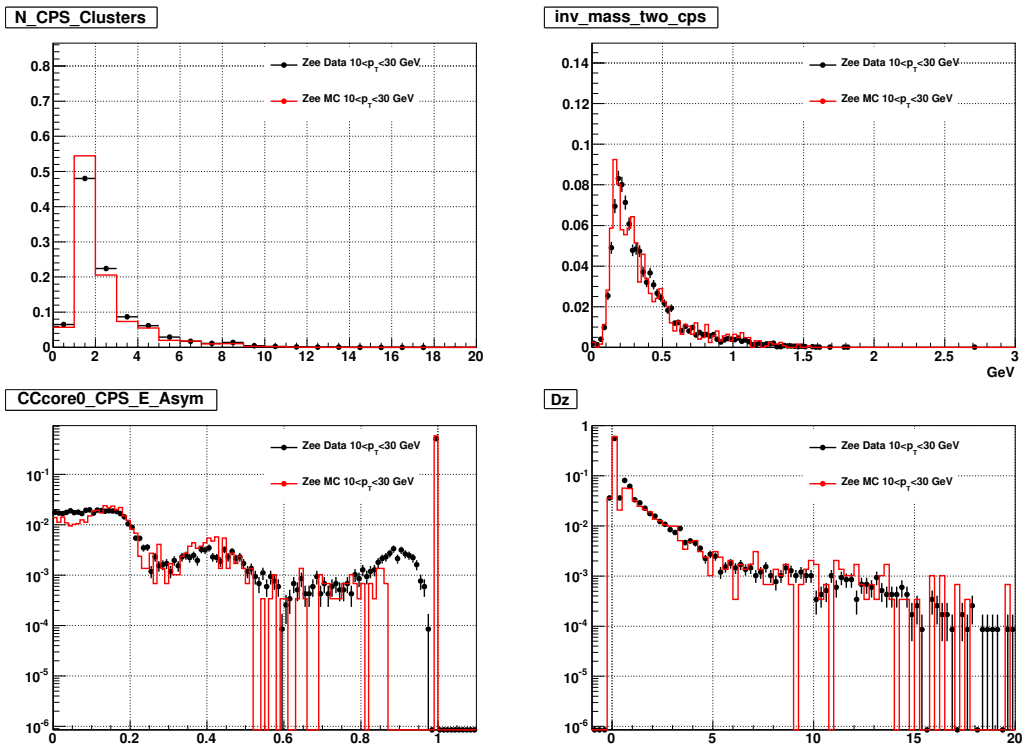

Figure D.36: The comparison of Zee Data and MC. The number of CPS clusters (upper left). The invariant mass distributions (upper right). The energy asymmetry of CPS clusters (lower left). The dispersion of the CPS clusters energy (lower right). The tight CPS cluster cut was not required.

acceptance is definitely higher as we mentioned in the section D.4. Also we demonstrated why the tight CPS cluster cut made the acceptance rise in the beginning of section D.4.

D.5.2 The response of the new variables in $Z\gamma \to ee + \gamma$ and $Z\gamma \to \mu\mu + \gamma$ events

Fig. D.38 is drawn with $Z\gamma \to ee + \gamma$ events selected in data and Fig. D.39 $Z\gamma \to \mu\mu + \gamma$. In fig. D.38, D.39, the upper and lower left are the energy asymmetry of CPS clusters, the upper and lower mid the dispersion of CPS cluster energy and the upper and lower right the invariant mass distributions by two CPS clusters. We required the tight CPS cluster cut for the lower plots and no tight CPS cluster cut for the upper plots. According to fig. D.38, D.39, the tight CPS cluster cut seems to let us have purer $Z\gamma$ events and give higher acceptance that

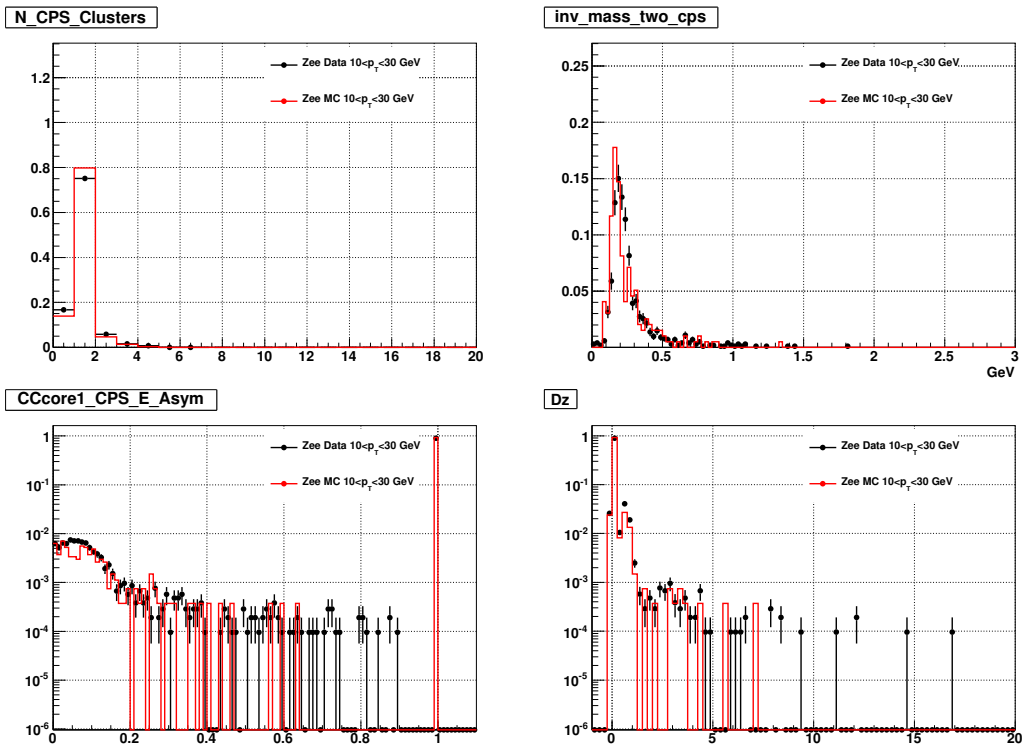

Figure D.37: The comparison of Zee Data and MC. The number of CPS clusters (upper left). The invariant mass distributions (upper right). The energy asymmetry of CPS clusters (lower left). The dispersion of the CPS clusters energy (lower right). The tight CPS cluster cut was required.

are shown in Table. D.9, D.11. But Table. D.10, D.12 tell us that photon candidates which have two or more CPS clusters become those which have one CPS cluster because the number of photon candidates which is higher than the asymmetry 0.99 increases after the tight CPS cluster cut. The section D.4.1 explained that the asymmetry 1 means photon candidates have only one CPS cluster. Also the section D.4 showed that after applying the tight CPS cluster cut, most photon candidates which have two or more CPS clusters became those which have only one CPS cluster in the π^0samples. The same situation happens in the $Z\gamma$ events samples. Thus although the tight CPS cluster cut seem to give purer single photon candidates, we have to consider that these can be from the π^0.

Table D.8: The acceptance of Zee Data and MC by the energy asymmetry (>0.99) and the Dz (<0.25) cuts. The tight CPS cluster cut was not required.

		Energy	Photon ID	Tight CPS cluster	The acceptance (%)
The energy asymmetry of CPS clusters	Data	10-30 GeV	core0	Yes	90.3
	MC	10-30 GeV	core0	Yes	92.7
The dispersion of CPS clusters energy	Data	10-30 GeV	core0	Yes	91.9
	MC	10-30 GeV	core0	Yes	94.5

Table D.9: The acceptance of $Z\gamma \rightarrow ee + \gamma$ by the energy asymmetry (>0.99) and the Dz (<0.25) cuts

	Energy	Photon ID	Tight CPS cluster	The acceptance (%)
The energy asymmetry of CPS clusters	10-30 GeV	core0	No	57.4
	10-30 GeV	core0	Yes	98.8
The dispersion of CPS clusters energy	10-30 GeV	core0	No	60.2
	10-30 GeV	core0	Yes	100

D.6 Conclusion

In MC, we have looked into the invariant mass, opening angle, the number of CPS clusters and the performance of the two new variables. From the consideration of all of these, we could show the acceptance of single photons and the rejection of the π^0 in the Tables. D.4, D.6. The tight CPS cluster cut reduces the π^0 rejection and makes single photons have higher possibility that they can be contaminated by π^0. The selection of CPS clusters using one or two most energetic without the tight CPS cluster cut have better performance for filtering π^0.

In $Z \rightarrow ee$ Data and MC, the fair agreement between Data and MC was demonstrated and based on this, we measured the acceptance for both Data and MC. In all Data samples showed in the section D.5, the tight CPS cluster cut gave higher acceptance but those photon candidates accepted by the asymmetry or the dispersion cut after applying the cut can have higher possibility to come from the π^0 than accepted photon candidates without the tight CPS cluster cut. We need more study about CPS cluster selection.

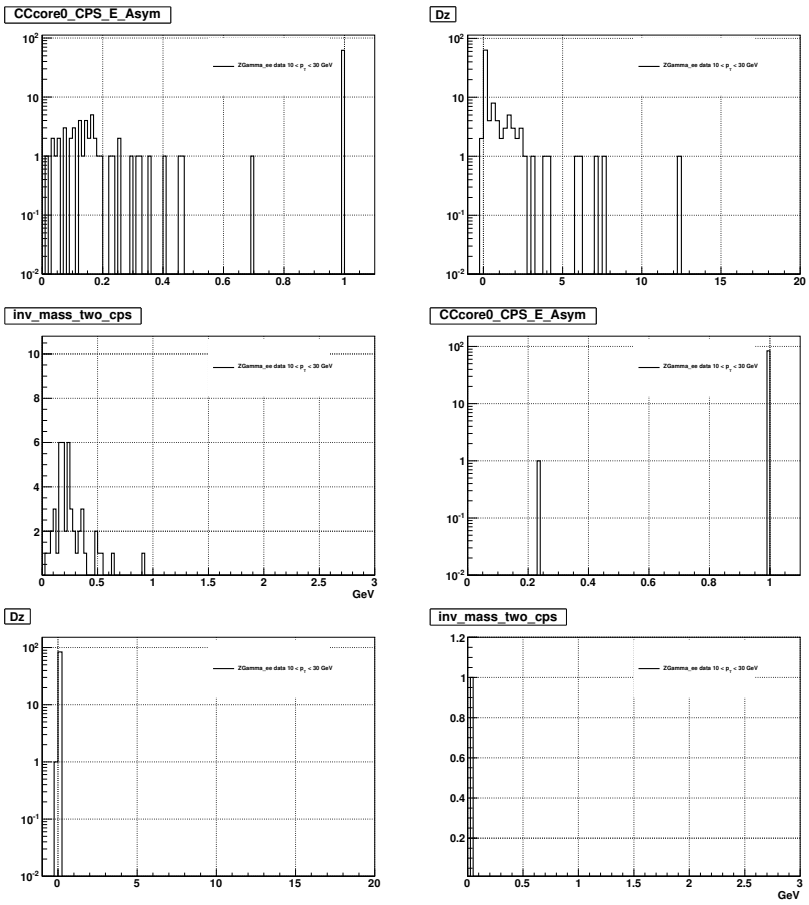

Figure D.38: The energy asymmetry of CPS clusters (upper and lower left), the dispersion of CPS cluster energy (upper and lower mid), the invariant mass of two CPS clusters (upper and lower right). The tight CPS cluster was not required in the upper row but required in the lower row. These distributions came from $Z\gamma \to ee + \gamma$.

D.7 The minimum opening angle of a photon doublet from the π^0decay

We can derive the opening formula using Eq. D.1, D.2 in Section D.3. The opening angle in the lab frame α is

$$\alpha = \theta_1' + \theta_2' = \arctan \frac{\sin\theta_1}{\gamma(\frac{\beta}{\beta^*} + \cos\theta_1)} + \arctan \frac{\sin\theta_1}{\gamma(\frac{\beta}{\beta^*} - cos\theta_1)} \tag{D.14}$$

The fig. D.40 is the opening angle in the lab frame as function of θ_1 in the center of mass frame for the 10 GeV π^0. The π^0 mass is 134.9766 MeV. For a 10 GeV π^0, the $\gamma = \frac{E_\pi}{m_\pi} = 74.09$,

Table D.10: The number of photon candidates by the energy asymmetry cut for the tight and the no tight CPS cluster cut in $Z\gamma \to ee + \gamma$ events

The energy asymmetry of CPS clusters	Total	>0.99	<0.99
No tight CPS cluster cut	108	62	46
Tight CPS cluster cut	85	84	1

Table D.11: The acceptance of $Z\gamma \to \mu\mu + \gamma$ by the energy asymmetry (>0.99) and the Dz (<0.25) cuts

	Energy	Photon ID	Tight CPS cluster	The acceptance (%)
The energy asymmetry of CPS clusters	10-30 GeV	core0	No	62.7
	10-30 GeV	core0	Yes	95.8
The dispersion of CPS clusters energy	10-30 GeV	core0	No	64.5
	10-30 GeV	core0	Yes	98.3

$\beta = \frac{P_\pi}{E_\pi} = 0.9991$ and $\beta^* = 1$ for the photon. Fig.. D.40 shows that the minimum opening angle occurs at $\theta_1 = 90^\cdot$. The minimum opening angle for other energy of the pion will also occur at $\theta_1 = 90^\cdot$ since the boost of the π^0 to the lab frame can not overcome the speed of the photon.

D.8 The π^0 detection in the DØ EM calorimeter

In this section, we will explain why we can not use EM calorimeter variables to discriminate single photons from the di-photon of the π^0decay. The 10-20 GeV single photon and π^0samples are used since 10 GeV π^0 has largest opening angle in the energy what we are interested in. First off, we need to look into the basic properties of the π^0at 10 GeV and 20 GeV. The mass of the $\pi^0$is 135 MeV and the life time $8.7 \times 10^{-17}s$. The π^0whose energy is higher than 10 GeV is relativistic so a distance d between two photons from the decay can be estimated by Eq. D.15 assuming that the length from the production vertex to the calorimeter is D [92]. m

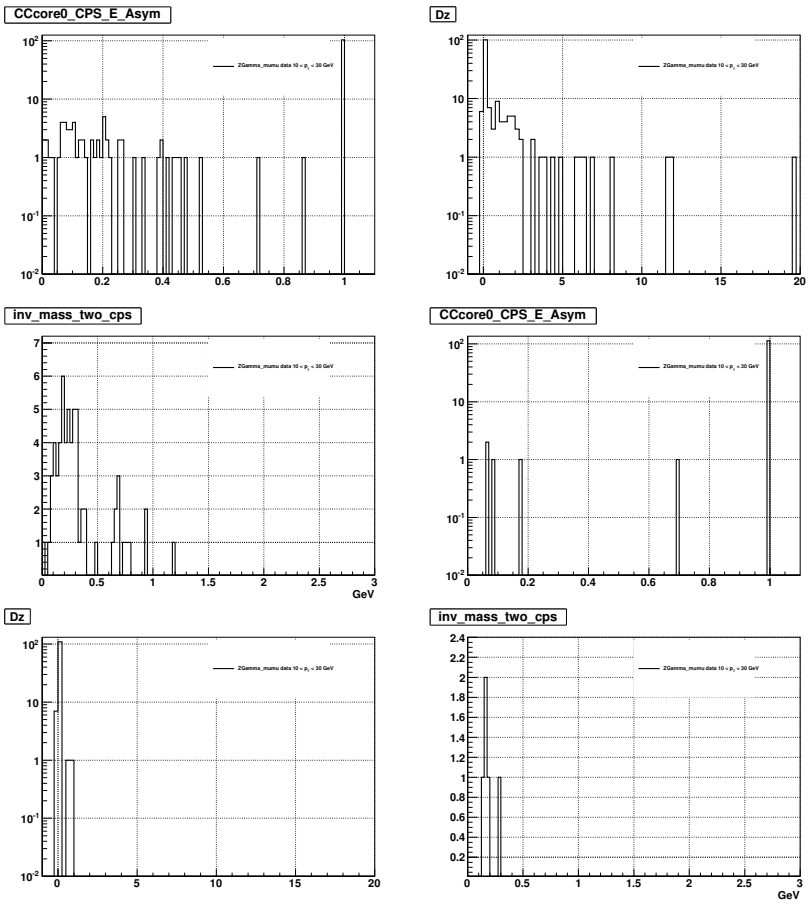

Figure D.39: The energy asymmetry of CPS clusters (upper and lower left), the dispersion of CPS cluster energy (upper and lower mid), the invariant mass of two CPS clusters (upper and lower right). The tight CPS cluster was not required in the upper row but required in the lower row. These distributions came from $Z\gamma \to \mu\mu + \gamma$.

and E are the mass and energy of the π^0, repectively.

$$d \approx \frac{Dm}{E} \tag{D.15}$$

From Table D.13, the π^0s definitely decay to two photon before entering the CPS detector and the EM calorimeter due to their short decay length.

As the fig. D.41 shows, each calorimeter tower covers η 0.1 and the length for the first tower at the beginning of the EM calorimeter is $\sim$ 7.5 cm due to the distance from the center to the EM calorimeter is $\sim$75 cm. ds are 10.13 mm and 5.06 mm for 10 GeV and 20 GeV π^0,

Table D.12: The number of photon candidates by the energy asymmetry cut for the tight and the no tight CPS cluster cut in $Z\gamma \to \mu\mu + \gamma$ events

The energy asymmetry of CPS clusters	Total	>0.99	<0.99
No tight CPS cluster cut	166	104	62
Tight CPS cluster cut	118	113	5

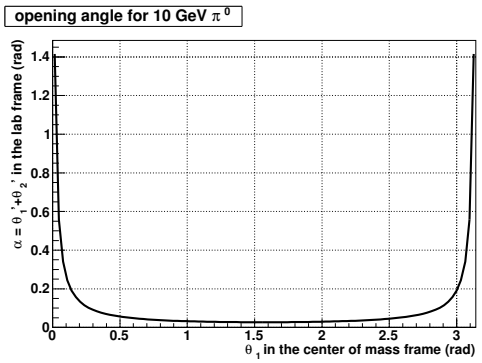

Figure D.40: The relation of the opening angle in the lab frame and θ_1 in the center of mass frame

respectively. Thus one tower in the Central Calorimeter is wide enough to contain two photons as one EM object. The energy of each photon coming from the π^0decay is not deposited to each tower. These two photons are detected as one EM object and deposit energy through one, two or more EM calorimeter towers. The asymmetry distribution of single photons and photon doublets from the $\pi^0$by one or two most energetic towers are very similar each other and this is not useful to discrimination of single photons and photon doublets from the π^0. This is shown in the fig. D.42.

$$A_{tower} = \frac{E_{tower1} - E_{tower2}}{E_{tower1} + E_{tower2}} \tag{D.16}$$

From the dispersion of EM object energy in the fig. D.42 which were found by Eq. D.17, what we can see are that the dispersion distributions of single photons and photon doublets are very similar and two explicit peaks are there. This means that both single photons and

Table D.13: Decay length and separation distance between two photons.

	10 GeV π^0	20 GeV π^0
γ	74.1	148.1
Time dilation	$6.4 \times 10^{-15} s$	1.3^{-14}
Decay length	$1.92^{-6} m$	3.9×10^{-6} m
D (from center to EM calorimeter)	$\sim$ 75 cm	$\sim$ 75 cm
d (distance between two photons)	10.13 mm	5.06 mm

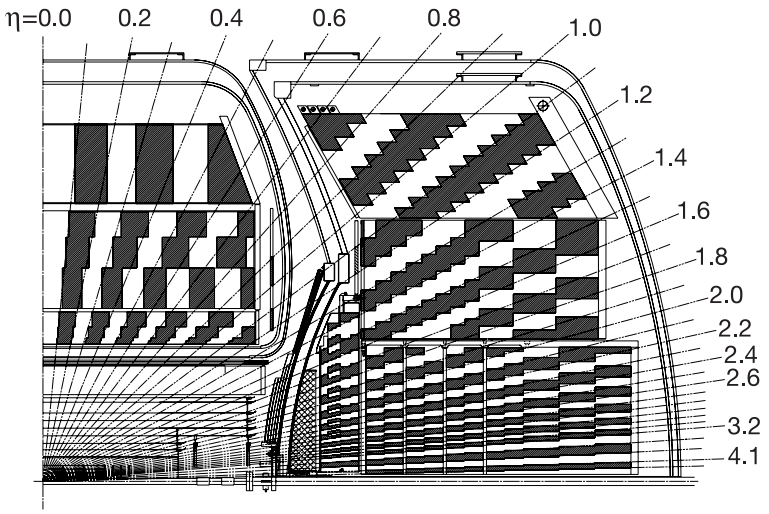

Figure D.41: The first quadrant of DØ calorimeter.

photon doublets are detected as one EM object in the EM calorimeter and these EM objects deposit most energy through two towers and the rest of energy is deposited beyond the second tower.

$$D = \frac{\sum E_i x_i^2}{\sum E_i} - (\frac{\sum E_i x_i}{\sum E_i})^2 \tag{D.17}$$

where E_i is energy in the ith cell and $x_i$is the cell position in η or ϕ.

In conclusion, the behavior of photon doublets coming from the π^0decay is very similar to single photons. Thus the asymmetry of two tower energies can not be good discriminator.

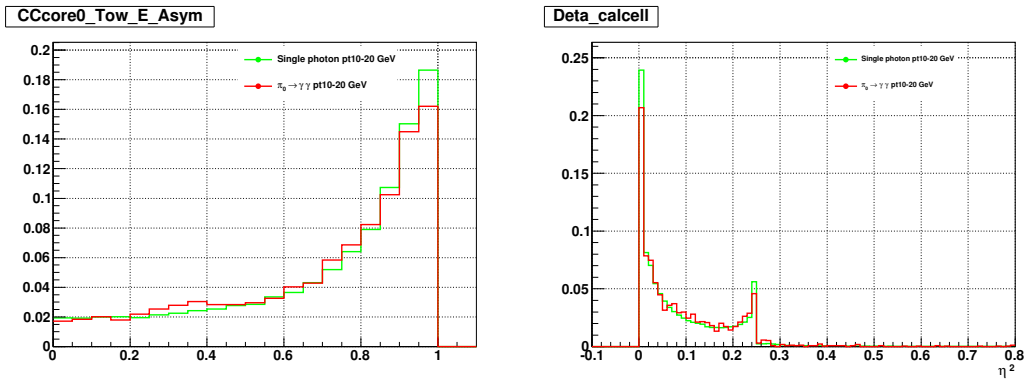

Figure D.42: The asymmetry of on or two most energetic towers (left) and the dispersion of EM object energy (right).

BIBLIOGRAPHY

[1] David Griffiths (1987) *Introduction to Elementary Particles*, John Wiley & Sons, Inc.

[2] Gordon Kane (1993) *Morden Elementary Particle Physics*, Addison-Wesley.

[3] Wolfgang Wagner (2007) *Top quark physics in hadron collisions*, arXiv:hep-ph/0507207v2.

[4] P. Nason, S. Dawson, R. K. Ellis (1987) *The total cross section for the production of heavy quarks in hadronic collisions*, FERMILAB-Pub-87/222-T.

[5] S. Moch and P. Uwer (2008) *Theoretical status prospects for top-quark pair production at hadron colliders*, arXiv:0804.1476v2 [hep-ph].

[6] Particle Data Group (2010) *Review of Particle Physics*, Journal of Physics G (Nuclear and Particle Physics) Volume 37 .

[7] Top Physics group at DØ *http://www-d0.fnal.gov/Run2Physics/top/top_public_web_pages/top_feynman_diagrams.html*

[8] David Atwood, Shaouly Bar-Shalm, Gad Eilam and Amarjit Soni (2000) *CP Violation in Top Physics*, arXiv:hep-ph/0006032v2.

[9] Donald H. Perkins (2000) *Introduction to High Energy Physics*, Cambridge University Press.

[10] S. Bethke (2008) *Experimental Tests of Asymptotic Freedom*, arXiv:hep-ex/0606035v2.

[11] Lynne H. Orr (1984) *Decay versus hadronization for top quarks produced in hadron colliders*, Phys. Rev. D 44 (1991) 88.

[12] Francis Halzen, Alan D Martin (1984) *Quarks and Leptons:An Introudctory Course in Modern Particle Physics*, John Wiley & Sons, Inc.

[13] Yannis K. Semertzidis (2004) *Electric Dipole Moments of Fundamental Particles*, arXiv:hep-ex/0401016v1.

[14] Y. Sumino (2000) *Probe of CP violation in* $e^+e^- \rightarrow t\bar{t}$ *Near Threshold*, arXiv:hep-ph/0007326v1.

[15] Oleg Antipin, G. Valencia (2009) *T-odd correlations from CP violating anomalous top-quark couplings revisited*, arXiv:0807.1295v3.

[16] Sudhir Kumar Gupta, G. Valencia (2010) *CP-odd correlations using jet momenta from* $t\bar{t}$ *events at the Tevatron*, arXiv:0912.0707v2.

[17] V.M. Abazov et al. (2006) *The Upgraded DØ Detector*, Nucl. Instrum. and Methods A 565, 463-537.

[18] The Beams Division at the Fermilab (2010) *http://www-bdnew.fnal.gov/operations/rookie_books/Concepts_v3.6.pdf*

[19] The Beams Division at the Fermilab *http://www-bd.fnal.gov/public/multiturn.html*

[20] The Beams Division at the Fermilab (2010) *http://www-bdnew.fnal.gov/operations/rookie_books/LINAC_v2.pdf*

[21] The Beams Division at the Fermilab (2010) *http://www-bd.fnal.gov/public/antiproton.html#target*

[22] DØ Luminosity ID group (2011) *http://d0server1.fnal.gov/Projects/Operations/D0RunII_DataTaking.htm*

[23] John Hauptman (2011) *Particle Physics Experiments at High Energy Colliders*, Wiley-VCH.

[24] A. Khanov (2000) *HTF: histogramming method for finding tracks. The algorithm description*, DØ note 3778.

[25] G. Borissov (2003) *Status of DØ Track Reconstruction*, presented at All DØ Meeting, Feb. 14.

[26] G. Borissov (2003) *Ordering a Chaos or... Technical Details of AA Tracking*, presented at All DØ Meeting, Feb. 28.

[27] A. Schwartzman, C. Tully (2005) *Primary Vertex Reconstruction by Means of Adaptive Vertex Fitting*, DØ note 4918.

[28] Ariel Schwartzman, Meenakshi Narain (2002) *Probabilistic Primary Vertex Selection*, DØ note 4042.

[29] O. Atramentov, D. Bandurin, X. Bu, B. Calpas, E. Carrera, D. Duggan, A. Ferapontov, M. Takahashi, T. Uzbyakova, H. Yin (2008) *Electron and Photon Identification with p20 data*, DØ note 5761.

[30] EM ID group (2010) *https://plone4.fnal.gov/P1/D0Wiki/object-id/emid/emcert/Redo_Winter2009Summer2009/*

[31] The DØ Muon ID group (2010) *Muon Identification Certification for the Summer 2009 Extended Dataset (Run IIb-1 and -2)*, DØ note 6025.

[32] Gerald C. Blazey (2000) *Run II Jet Physics*, arXiv:hep-ex/0005012.

[33] G. Bernardi, E. Busato and J.-R Vlimant (2004) *Improvements from the T42 Algorithm on Calorimeter Objects Reconstruction*, DØ note 4335.

[34] K. DeVaughan et al. (2008) *Jet Energy Scale Determination for DØ RunIIb (final p20 version)*, DØ note 5801.

[35] S. Calvet et al. (2005) *Towards MissingET Certification and Unclustered Energy Studies*, DØ note 4927.

[36] R. Demina, A. Khanov, F. Rizatdinova (2002) *b-Tagging with Counting Signed Impact Parameter Method*, DØ note 4049.

[37] D. Bloch, B. Clement (2005) *Update of the JLIP b-tagger Performance in p14/pass2 with Jes 5.3*, DØ note 4824.

[38] D. Boline, L. Feligioni, M. Narain (2005) *Update on b-quark jet identification with Secondary Vertex reconstruction using DØ reco version p14-Pass2 Samples*, DØ note 4796.

[39] Thomas Gadfort et al. (2009) *Performance of the D NN b-tagging Tool on Lepton-Photon 2009 Run IIb Data*, DØ note 5803.

[40] Miruna Anastasoaie et al. (2007) *Performance of the D NN b-tagging Tool on p17 Data*, DØ note 5213.

[41] N. Makovec, J. Grivaz (2005) *Shifting, Smearing and Removing Simulated Jets*, DØ note 5914. C. Ochando and J.-F. Grivaz (2008) *SSR for p17*, DØ note 5609.

[42] Common Sample Group *http://www-d0.fnal.gov/Run2Physics/cs/index.html*

[43] Recommended setup for Summer 2009 extended analysis by V+jets group *https://plone4.fnal.gov/P1/D0Wiki/physics/VplusJets/CAFtools/vjets_cafe_v3*

[44] Laurent Duflot, et al. (2004) *cal_event_quality package*, DØ note 4614.

[45] M. L. Mangano et al. (2003) *a Generator for Hard Multiparton Processes in Hadronic Collisions*, JHEP 0307:001.

[46] Törbjorn Sjöstrand, Stephen Mrenna, Peter Skands *http://projects.hepforge.org/pythia6/*

[47] O. Brandt et al. (2010) *Measurement of the $t\bar{t}$ Cross Section in the leption+jets Channel with 5.3 fb^{-1}*, DØ note 6028.

[48] J. Campbell and R.K. Ellis *http://mcfm.fnal.gov/*, MCFM - Monte Carlo for FeMtobarn processes.

[49] E.Boos et al, [CompHEP Collaboration] (2004) *CompHEP 4.4: Automatic computations from Lagrangians to events*, Nucl. Instrum. Meth. A534 250.

[50] Wade Fisher, Joe Haley, Darren Price (2009) *Studies of Alpgen Parameter Corrections and Uncertainties*, DØ note 5966.

[51] J.F. Grivaz *http://www-d0.hef.kun.nl//askArchive.php?base=agenda&categ=a08266&id=a08266s1t4/transparencies*

[52] V.Sharyy *How to reweight MC according to the luminosity profile in data,https://plone4.fnal.gov/P1/D0Wiki/comp/caf/caffaq/LumiReWeight*

[53] H. Schellman (2006) *The longitudinal shape of the luminous region at DØ*, DØ note 5142.

[54] Y. Peters, M. Begel, K. Hamacher, D. Wicke (2007) *Reweighting of the fragmentation function for the DØ Monte Carlo*, DØ note 5325.

[55] Daren Price, and W. fisher, J. Haley, D. Price (2009) *Studies of Alpgen Parameter corrections and uncertainties*, DØ note 5966.

[56] S. Snyder (1995) *Measurement of the Top Quark mass at DØ*, Doctoral Thesis, State University of New York at Stony Brook.

[57] Marc-André peier (2007) *Measurement of the Electron and Muon Fake Rates in Lepton+jets Datasets*, DØ note 5469.

[58] O. Brandt, A. Jung, Y. Peters (2010) *Fake rate measurement - estimation of* ϵ_{sig} *and* ϵ_{qcd}, DØ note 6055.

[59] E. Barberis et al. (2004) *The Matrix Method and its Error Calculation*, DØ note 4564.

[60] Hwidong Yoo (2008) *Top Quark Production Cross Section in the Lepton+jets Channel Using b-tagging at DØ.*

[61] A. Schartzman, M. Narain (2001) *A New 3_Dimensional Cone Track-Clustering Algorithm*, DØ note 3885.

[62] Dmitry Bandurin, Maiko Takahashi (2009) *electron charge misidentification for p17 and p20 data and Monte Carlo*, DØ note 5927.

[63] Samuel Calvet (2009) *Taggability scale factors for the dijet topology for summer conferences 2009*, DØ note 5944.

[64] M. Besancon et. al. (2010) *Measurement of the $t\bar{t}$ production cross-section in dilepton final state using RunIIb1 and RunIIb2 dataset for winter '10 conferences* , DØ note 6027.

[65] Oleg Brandt et. al. (2010) *Measurement of the Mass Difference Between Top and Antitop Quarks in the Lepton+Jets Channel Using the Matrix Element Method on 3.6 fb^{-1} of Run IIb Data* , DØ note 6105.

[66] Daniel Boline (2010) *Top quark mass in events with two charged leptons at the DØ experiment.*

[67] T. Andeen et al. (2007) *FERMILAB-TM-2365.*

[68] S.-J. Park, M. Begel (2007) *Efficiency of the Data Quality Calorimeter Flags*, DØ note 5324.

[69] H. Schellman et al. (2008) *Measurement of the cross section for $Z/\gamma \to e^+e^-$ production at DØ*, DØ note 5627.

[70] B. Martin et al. (2007) *Measurement of the $t\bar{t}$ production cross section at $\sqrt{s} = 1.96$ TeV in the ee final state using p17 data set*, DØ note 5386.

[71] O. Brandt, S.W. Cho, M. Cookc, M. Eads, D. Hedin, A. Santos, B. Tuchming, Y. Yatsunenko, S.W. Youn (2010) *Muon Identication Certication for the Summer 2009 Extended Dataset (Run IIb-1 and -2)*, DØ note 6025.

[72] F. Déliot et al. (2010) *Systematic Uncertainties in Top Quark Measurements*, DØ note 6024.

[73] *http://www-d0.fnal.gov/Run2Physics/top/d0 private/top private web pages/top cross sections.html*

[74] Tim Scanlon and Thomas Gadfort (2008) *Performance of the DØ NN b-tagging Tool on 3 fb^{-1} Run IIb Data*, DØ note 5803.

Tim Scanlon and Andrew Kobach (2008) *Measurement of a Fake-Tag Rate Scale Factor in p20 Data*, DØ note 5605.

T. Gadfort et al. (2007) *Performance of the DØ NN b-tagging Tool on p20 Data*, DØ note 5554.

[75] A. Harel (2008) *Data over MC, b over light jet response corrections for Run IIa JES*, DØ note 5654.

[76] Y. Peters, E. Shabalina, D. Wicke (2007) *Simultaneous measurement of* $B(t \to Wb)/B(t \to Wq)$ *and* $\sigma(p\bar{p} \to t\bar{t}) * B(t \to Wq)^2$, DØ note 5422.

[77] Y. Peters, M. Begel, E. Shabalina, D. Wicke(2007) *Study of the W+Jets heavy flavor scale factor in p17*, DØ note 5406.

[78] Stephen Mrenna (2007) *http://home.fnal.gov/ mrenna/lutp0613man2/node234.html*

[79] Grant R. Fowles (1975) *Introduction to Modern Optics, Second Edition*, Holt, Rinehart and Winston, Inc., pp. 164-168.

[80] DØ Collaboration (2009) *Search for Resonant Diphoton Production with the DØDetector*, Phys. Rev. Lett. 102, 231801.

[81] D. Bandurin (2005) *The Isolated Photon Cross Section in the Central Rapidity Region at 1.96 TeV*, DØ 4672.

[82] EMID Variables *http://www-d0.fnal.gov/phys id/emid/d0_private/variables.html*

[83] X. Bu, Yanwen Liu (2007) *Artificial neural network for Run IIb electron and photon identification*, DØ note 5545.

[84] X. Bu et. al. (2008) *Artificial neural network using central preshower detector information for electron and photon selection*, DØ note 5650.

[85] Oleksiy Atramentov, Yurii Maravin (2004) *Utilizing CFT and SMT hit count for photon and electron reconstruction*, DØ note 4444

[86] Common Sample Group *http://www-d0.fnal.gov/Run2Physics/cs/skimming/p20_pass4.html*

[87] Common Sample Group *http://www-d0.fnal.gov/Run2Physics/cs/MC/mccaf_www_p211100/pythia-diphoton-incl_sm.direct.html*

[88] Common Sample Group *http://www-d0.fnal.gov/Run2Physics/cs/MC/mccaf_www_p211100/unknown-unknown.html*

[89] Common Sample Group *http://www-d0.fnal.gov/Run2Physics/cs/MC/mccaf_www_p211100/pythia-gam-z-ee_sm.m15-60.html*

[90] Dmitry Bandurin et. al. (2010) *Photon Identification for Run II* , DØ note 6004.

[91] Yurii Maravin (2004) *Reconstruction of* π^0 *in di-photon final state* , DØ note 4446.

[92] Richard Wigmans (2000) *Calorimetry: Energy Measurement in Particle Physics*, New York: Oxford University Press.